NC STATE UNIVERSITY

PRECISION ENGINEERING CONSORTIUM

2019 & 2020 ANNUAL REPORT
VOLUME XXXIV

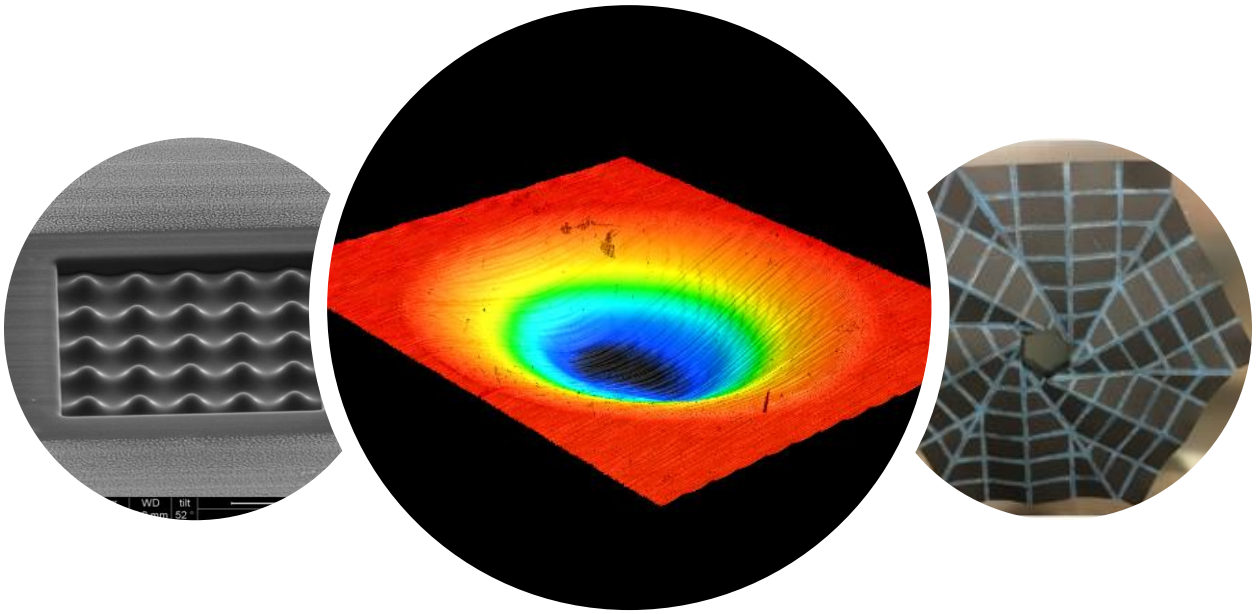

2019 & 2020
ANNUAL REPORT
VOLUME XXXIV
July 2021












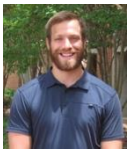

Faculty:	Mark Pankow
	Scott Ferguson
	Paul Cohen
	Thomas Dow
Graduate Students:	Usama Alfarid Dingankar
	Sumit Gundyal
	Noa McNutt
	Jacob Guymon
	Parker Eaton
	Tyler Young
Staff:	Kenneth Garrard
	Jacob Marx
Consultants:	Karl Falter
	Stephen Furst

Sponsors

Table of Contents

Letter from the Director

In January of 2020, we celebrated the retirement of our founding director, Dr. Thomas Dow. Since establishing the Precision Engineering Center in 1982 he has helped guide the PEC through multiple decades of continued success and we cannot thank him enough for all that he has done. I was named as the new director of the center with the intent of continuing the current work and maintaining the center's core ideologies Dr. Dow had established. A couple short months later we were all trying to figure out how handle the COVID-19 pandemic as it raced across the world. The past year had been exceptionally difficult, and everyone has been impacted by COVID. We hope that everyone is doing well and healthy and that things are starting to improve. As the pandemic continued to worsen, North Carolina State University suspended on-campus work and research on March 20th, 2020. The PEC is built around hands-on research that was indefinitely interrupted and delayed during that time. This presented new challenges for students and staff as it was pertinent to maintain progress despite the interruption to normal operations.

Students were committed to maintaining progress in their work and explored means to transfer their experimental work to modeling and designing experiments as access to the lab was limited. This avoided any large-scale setbacks and allowed them to easily pick their work back up from where they left off once limited access to the facilities was restored in the beginning of June, 2020. I am proud of our students, staff, and faculty's dedication to their work through this unprecedented period. As we continue to adhere safety standards set by the university, I would like to assure our sponsors and collaborators that the advancement of our research projects remains our top priority.

The PEC also underwent staff changes as it hired Dr. Jacob Marx to the Research Assistant position replacing Anthony Wong who recently began his work with the Army Research Office. The addition of new staff broadens the current research focus and resources of the PEC as we continue to open our doors to potential opportunities for collaboration. The past year proved exceptionally difficult for recruiting new students. Yet, we are excited to welcome new graduate and undergraduate students joining us in the fall with the ability to perform research in the labs.

In the report that follows we are excited to also include chapters covering work that occurs in the Blast Lab also under the direction of Dr. Pankow. The recent changes in director and staff do not change the fact that the PEC will continue its research focus on metrology, precision manufacturing, and actuation controls for industry and national laboratories.

Mark Pankow
Director of the PEC

Summary

The goals of the Precision Engineering Consortium (PEC) are: 1) to develop new technology in the areas of precision metrology, actuation, manufacturing and assembly; and 2) to train a new generation of engineers and scientists with the background and experience to transfer this technology to industry. Because the problems related to precision engineering originate from a variety of sources, significant progress can only be achieved by applying a multidisciplinary approach; one in which the faculty, students, staff and sponsors work together to identify important research issues and find the optimum solutions. Such an environment has been created and nurtured at the PEC for 34 years and the 100+ graduates attest to the quality of the results.

The 2020 Annual Report summarizes the progress over the past two years by the faculty, students and staff in the Precision Engineering Consortium. During the past two years, this group included 4 faculty, 6 graduate students, 7 undergraduate students, 2 technical staff members, and 1 administrative staff member. The diverse group of scientists and engineers provides a wealth of experience to address precision engineering problems. The format of this Annual Report separates the research effort into individual projects but there is significant interaction that occurs among the faculty, staff and students. Teamwork and group interactions are a hallmark of research at the PEC and this contributes to both the quality of the results as well as the education of the graduates.

A brief abstract follows for each of the projects and the details of the progress in each is described in the remainder of the report.

1. **Sub Aperture Polishing of Millimeter Sized Polymer Optics**

   Sub aperture polishing is a deterministic polishing process in which the polishing tool produces a contact patch that is smaller than overall dimension of the workpiece, such it is able to carry out localized polishing action and corrections within the body of the workpiece in specific areas of interest, whilst at the same time not altering the noninterest regions. The objective of this research project is to design and setup a sub aperture polishing system utilizing a soft silicone rubber based polishing tool attached to a high speed spindle drive, in order to produce a polished surface with a RMS surface roughness measuring 2 nm, and the ability to create and correct a free form feature on the workpiece surface measuring 6x6 mm in area, with a form PV of 15 microns. Polycarbonate (PC) and Polymethylmethacrylate (PMMA) are the two polymers that have been studied as workpieces, and Alumina suspension was utilized as the polishing abrasive. The effects of input variables namely – RPM, feed rate, normal load, polishing passes, toolpath strategy on the surface roughness RMS were studied and the results were reported.

2. **Sub Aperture Polishing Optimization**

   Elastic emission machining (EEM) is a high-accuracy sub-nanometer polishing process that is useful for removing unwanted material and refining surface finish. While many prior studies have examined aspects of EEM and tested its polishing ability, few have gone in depth on

how different paths impact the surface finish or how those effects relate to a wide range of EEM polishing parameters. This study investigates the effects of the tool path determine the optimal parameters achieve a desired finish without compromising the portions of the surface that are already within the specified margin. This work couples tool pathing with a study on how different combinations of parameters such as lubrication viscosity, applied force, and rotation speed can affect surface finish. EEM of polycarbonate is investigated in this study using a silicone ball and alumina slurry. The resulting surface is imaged using an optical interferometer to measure the surface finish. The applied load is found to have a direct impact on the machining process and final surface roughness.

3. Multi-Lens Array: Modeling of the Microindentation Process to Create Lens Array Features on a Mold

This report addresses the design of multi-indenter die and development of indentation strategies to create the negative features of a microlens array on a mold. A material parameter study is performed using the commercial finite element analysis software Abaqus™ to understand the effects of different indent patterns and processes on the pile-up and the maximum force required and shape error. Al 1100 is selected as the mold material based on this study. Glassy carbon is used as the die material. Multiple Indentation strategies are explored to understand the best die shape to reduce form error.

4. Novel Manufacturing Methods of Microscale Lens Arrays

In order to build off of the work outlined in the previous chapter, this work explores manufacturing a mold and die that can be used to create an optimal indent pattern for microlens arrays. This study details the steps taken to manufacture a mold and die from aluminum and diamond, respectively. The Al 1100 H14 was first characterized through nanoindentation and diamond turning. Indentation grids were effectively created using a Berkovich and conical nanoindenter. The diamond die was FIB milled and analyzed using surface interferometry. The FIB dwell time for 1 nA and 0.50 nA beam currents used to create a consistent parabolic array is documented.

5. Reducing Microlens Array Indentation Form Error via Testing and Simulation

This report addresses the initial methods involved in reducing the geometric form errors that occur when indenting microlens arrays. The microlens arrays are rapidly indented on a variety of metallic negative molds. A proprietary indent force and indent depth measurement technique is employed to aid in the characterization and control of the microindenting process. Insights from form error analysis and finite element simulations can then be used to make informed decisions to redefine die geometry and microindentation strategies in the pursuit of minimized geometric form error.

6. **Mechanical and Electrical Properties of Single Crystal Silicon under External Electric Fields using Nanoindentation**

   Silicon is widely used for electronics and modern day technology. Phase changes within the silicon structure can reduce machining forces and reduce material springback for electronics manufacturing. Single crystal silicon was tested under electrical contact nanoindentation at voltages between -10 and 10 V. The modulus and hardness of the silicon is measured during indentation and the effect of the voltage is used to determine potential phase changes in the single crystal silicon wafer. Large negative voltages have been shown to increase the reduced modulus of the silicon. The external electric field was found to have no effect on the hardness. Future work can focus on measuring the topography of the indented regions and resistivity while also exploring other materials.

7. **Development of a Novel Modular Monopolar and Bipolar Forceps**

   Electrosurgery devices can offer multi-use capabilities when paired with a surgical forceps design. Such a device can reduce surgical time by limiting the need to transfer between surgical tools. This project is set out to design, manufacture, and test a surgical forceps tool that can act as both a mono- and bipolar electrosurgery tool. Initial ideas were analyzed using a design matrix and with consultation with medical professionals. First steps have been taken to prototype and determine the next steps for material manufacturing and electronics. Future work will include manufacturing, wiring, and testing of the device followed by iterative improvements to the design.

8. **Deployable Structures**

   This report addresses the development of various deployable technologies for aerospace systems and their current status. There are two main research areas: Deployable booms with different mechanisms: both powered and unpowered, and Deployable Composite Origami. This work discusses the manufacturing and testing of each system. Both systems have or have ongoing zero-gravity flight demonstrations to understand their deployment characteristics in a relevant space environment. The Boom project has an ongoing collaboration with NASA Langley.

1 SUB APERTURE POLISHING OF MILLIMETER SIZED POLYMER OPTICS

Usama Alfarid Dingankar
Graduate Student, Department of Mechanical Engineering
Dr. Thomas Dow
Dean F. Duncan Distinguished University Professor
Department of Mechanical Engineering

ABSTRACT

Sub aperture polishing is a deterministic polishing process in which the polishing tool produces a contact patch that is smaller than overall dimension of the workpiece, such it is able to carry out localized polishing action and corrections within the body of the workpiece in specific areas of interest, whilst at the same time not altering the noninterest regions. The objective of this research project is to design and setup a sub aperture polishing system utilizing a soft silicone rubber based polishing tool attached to a high speed spindle drive, in order to produce a polished surface with a RMS surface roughness measuring 2 nm, and the ability to create and correct a free form feature on the workpiece surface measuring 6x6 mm in area, with a form PV of 15 microns. Polycarbonate (PC) and Polymethylmethacrylate (PMMA) are the two polymers that have been studied as workpieces, and Alumina suspension was utilized as the polishing abrasive. The effects of input variables namely – RPM, feed rate, normal load, polishing passes, toolpath strategy on the surface roughness RMS were studied and the results were reported.

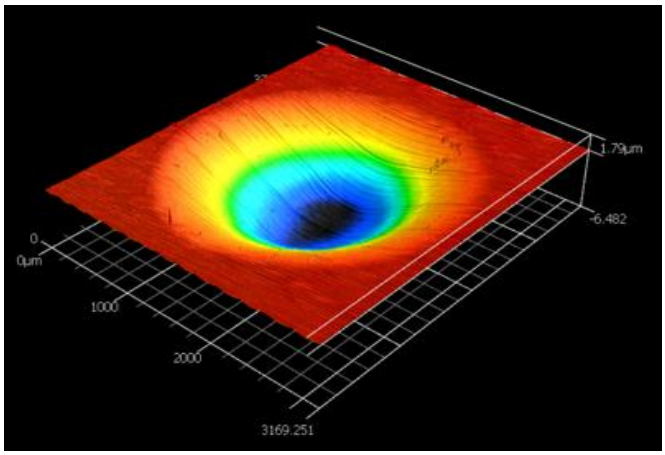

1.1 INTRODUCTION

Optical devices such as lenses are crucial with a varied usage in differing industries ranging from microscopy, laser processing equipment, imaging, defense sector, aerospace, medical and bio industry, projection visual devices like virtual reality headsets and in usual corrective spectacles [1]. The basic functionality of a lens, is to change the path profile of light by converging, diverging, or dispersing, magnifying to form an image of the object being viewed [2]. Optical lenses can be in many forms including convex, concave plano concave, plano convex etc. In today's advanced technical environment, many new technologies, such as concept of virtual reality, have started making a solid mark in the industry. The advent of such industries has led to a meteoric rise of the quality standards in the manufacturing and precision processing of optical devices. Two key metrics to measure the quality of the lenses are surface finish and surface form. A better surface finish and exacting form of these lenses will improve the overall performance of the lenses.

Many optical lenses are manufactured from polymer plastics like PMMA (Polymethylmethacrylate) and PC (Polycarbonate) and use manufacturing processes like injection molding or compression molding. Utilizing polymer optics is advantageous because they offer design flexibility in terms of cost, weight, shape, design, and transmittance of light, as compared to glass optics. The fabrication of glass optics is a slow and costly affair as compared to the polymer counterparts [1], [3]. But being an optical device, these lenses need to have a high level of surface finish, form and optical properties. These parameters can be achieved by utilizing the polishing process as a key finishing step in the lens manufacturing process. Polishing is routinely performed to improve the finishing of surfaces, to remove scratches and to reduce the surface roughness [4]. In layman's terms, polishing is the process of creating an improved surface by the means of mechanical or chemical interaction between the polishing tool and the workpiece, either in the presence of a free or fixed abrasive. Any given surface on a magnified scale has a system of crests and troughs present on it. The frequency of these features and the difference in the heights of these crests and troughs can be used as the description for the surface roughness.

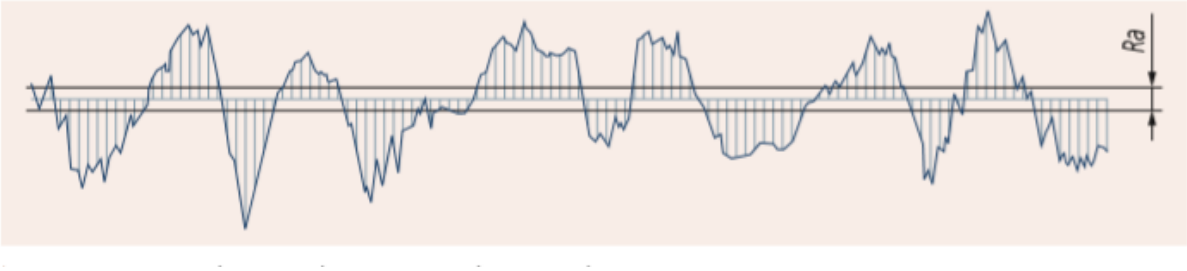

Figure 1-1: Sample measurement depicting the surface roughness profile in a trace [5].

1.2 DETAILS OF THE PROJECT

This research project deals with the computer controlled sub-aperture polishing process for polymers like Polycarbonate (PC) and Polymethylmethacrylate (PMMA). Sub-aperture polishing refers to the type of polishing in which the polishing contact patch which is the zone in which the actual polishing takes place, is much smaller than the overall lens diameter and dimension and allows the polishing of selective areas of the workpiece without affecting the form and finish of the noninterest regions. In the case where we need to polish flat, plano, or spherical surfaces, full aperture polishing is a preferred process, but since this project deals with the creation of a free form 3D sine wave surface, sub aperture polishing process is most effective, as due to the change of local curvature full aperture polishing is not a possible measure [6]. It provides a deterministic approach to obtain an improved surface finish and desired surface form in specific areas on the lens surface without any kind of damage to the remaining lens areas.

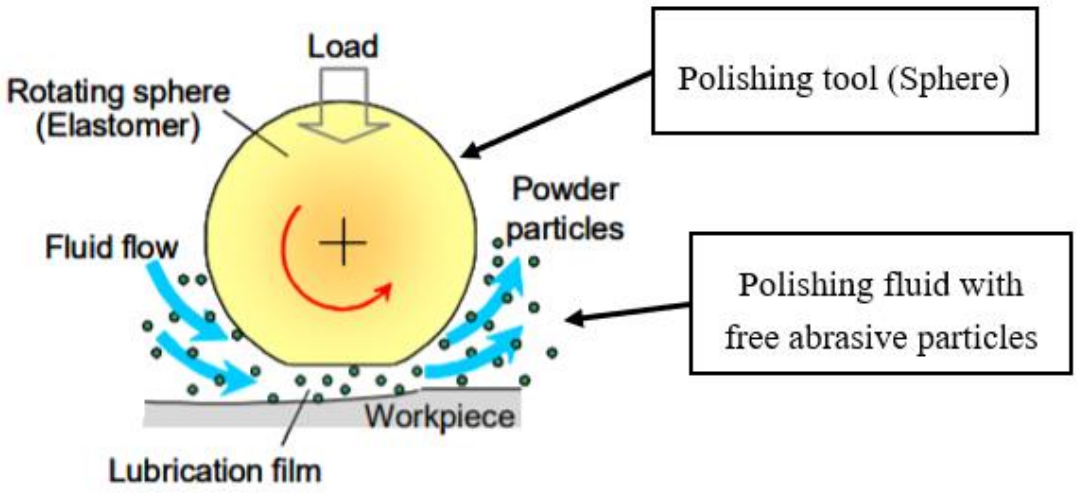

Figure 1-2: Diagrammatic representation of the elastic emission polishing process [7].

The process of sub aperture polishing can be described by using the concepts of elastic emission machining. Elastic emission machining is a non-contact machining process that utilizes a three way contact between the polishing tool, the abrasive grain, and the workpiece surface. The polishing process depends on the contact between abrasive particles and the workpiece surface [7]. A diagrammatic representation of the elastic emission polishing process is shown above in Figure 1-2. The polishing process is based on the free abrasive model wherein an abrasive fluid containing suspended abrasive particles is utilized which consists of a mixture of deionized water that acts as a vehicle to sustain and transport the aluminum oxide grains (abrasive) into the polishing zone. The polishing tool is a silicone rubber ball in this project. It is the driver of this system as shown above in the Figure 1-2, in the sense that it directs the abrasive fluid to the polishing zone and facilitates the motion of the polishing fluid (thereby the abrasive grains) on the workpiece thereby causing the material removal action, hence polishing the surface.
In this research, the effects of the sub-aperture polishing on surface roughness and surface form in Polycarbonate (PC) and Polymethylmethacrylate (PMMA) are studied and analyzed.

PMMA is an optically clear thermoplastic with a high impact strength, relatively low density, and is shatter-resistant. It has a low elongation at break point and has a high Young's modulus [8] compared to the polishing tool i.e. the silicone ball. These outstanding properties also include high optical clarity, weather resistance and scratch resistance. A refractive index of 1.490, and a high resistance to sunshine exposure (UV resistance) making PMMA a promising polymer for optical applications. PMMA also displays an inherent dependency on temperature in the case of material deformation. As the temperature increases the Young's modulus of the material decreases and thereby the material deforms easily [9]. PC is highly transparent, transmitting approximately 90% of visible light. It displays exceptional impact resistance, tensile strength, ductility, dimensional stability, and optical clarity. It is marketed under trademarks such as Lexan and Makrolon [10]. Polycarbonate is manufactured primarily as a transparent material and has very good light transmission and optical properties. Just like PMMA, Polycarbonate has a temperature dependent deformation mechanism. As the temperature is increased the material gets relatively easy to deform. As the temperature goes higher, the Young's modulus decreases and the material hence becomes easier to deform. The characteristics of Polycarbonate (PC) are quite like those of Polymethylmethacrylate (PMMA), but PC is stronger and more expensive, though its more prone to surface scratches, thereby making the precise handling of this polymer imperative.

1.3 EXPERIMENTAL SETUP

In the experimental setup, a silicone rubber ball of diameter 3 mm and shore hardness value of 70A was utilized, Figure 1-3. The silicone rubber ball was mounted on a brass spindle shaft to form the polishing tool head, shown in Figure 1-4 and 1-5.

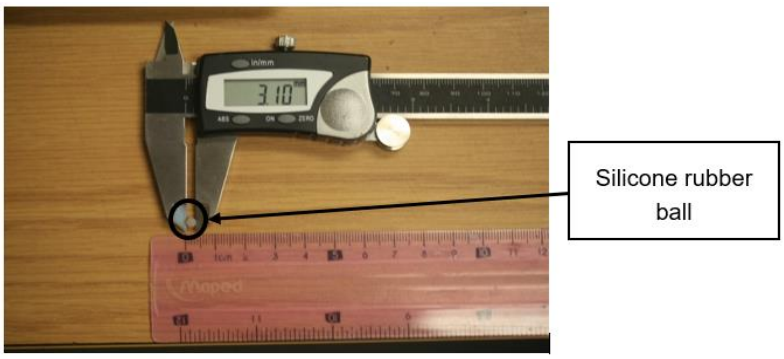

Figure 1-3: Silicone rubber tool size representation.

Silicone Rubber is a thermoset elastomer, and is usually non-reactive, stable, and resistant to extreme environments and temperatures. It is also stable at low and high temperatures [11]. The working temperature range for Silicone rubber is from −55 °C to 300 °C. The material has a Young's modulus of 50 MPa, with a yield strength of 7 MPa. The size of the silicone rubber ball was chosen based on the overall size of the features to be created.

The polishing fluids utilized in the project were supplied by Baikowksi International, Universal Photonics, and Buehler. Baikowksi Baikalox Aluminum Oxide (Al_2O_3) based fluid with a varying abrasive grain size of 0.05 µm, 0.1 µm, 0.3 µm, 0.5 µm was utilized to carry out the primary surface improvement experiments. Kontax 602 – an ultra-pure alumina polishing powder was also used for polishing experiments as it is known to give excellent results with Polycarbonate workpieces. The Kontax was used in 3 types of slurries with a varying abrasive concentration of 10%, 15%, 40% on the Baume scale.

The measurement of the surface finish and the surface form are of prime importance in the research project, as these output parameters form the backbone of the research objectives. An accurate and precise measurement of these parameters is needed to characterize the polishing process. Three different apparatuses have been used in order to obtain and record these measurements. In order to measure the surface roughness and form on a 3D scale the Zygo NewView 5000 3D surface profiler is used and the Keyence VKX1100 3D laser scanning confocal microscope, for the 2D cross sectional measurements the Taylor - Hobson Talysurf apparatus has been utilized.

To satisfy the sub aperture concept of the project, a polishing tool was required that was inherently smaller than the areas of interest to be polished. Since these areas of interest were in the range of 2 mm circular spots for surface roughness module and a 6x6 mm area for the form generation module, a polishing tool that would have a contact patch of less than 2 mm under the maximum loading conditions. Keeping in mind this size constraint, a Silicone ball of diameter 3 mm which provided a 0.26 mm contact patch under 1 N normal load and 30 degree polishing angle was selected as the main polishing head. The 30 degree polishing angle gave us enough freedom to move the tool along the workpiece without the risk of the tool crashing into the surface. This silicone ball was attached to a brass spindle shaft that was 15 mm long and 2 mm diameter. It was constrained onto the tip of the brass shaft by making a tapered groove at the tip of the brass shaft, such that it provided a line contact between the ball and the shaft as shown below in Figures 1-4 & 1-5.

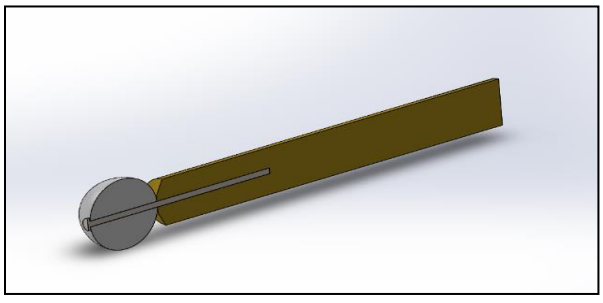

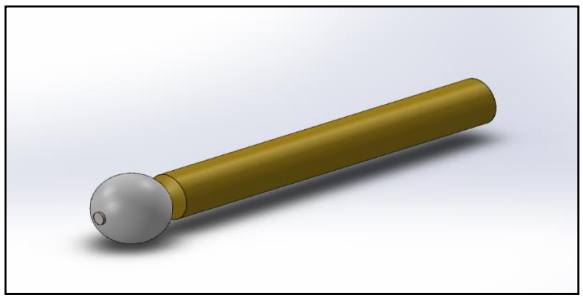

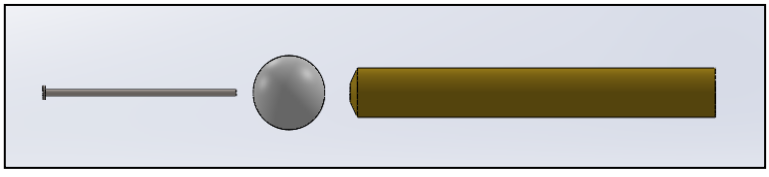

Figure 1-4: Image showing the a) cross section view, b) isometric view and c) exploded view of the polishing tool head assembly.

This assembly of the brass shaft, the silicone ball, and the stainless steel pin was attached to the spindle of a Medicool devices Pro-Power 40K dentist's drill, providing a working RPM range from 1000 to 40000. This RPM range covered all the experimental needs of the project. The drill had a control system that could be used to vary the RPM's in increments of 1000 RPM.

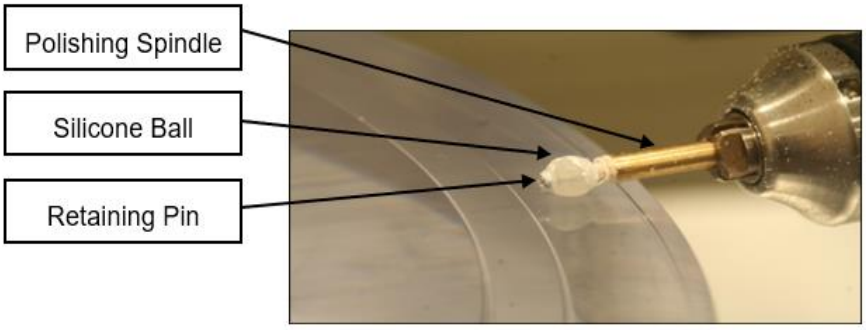

Figure 1-5: The 3mm Silicone Ball attached to the Brass spindle shaft.

A 3-axis micro-mill CNC machine was deemed feasible to be utilized as the main control setup. The mill provided access to the 3 degrees of freedom – namely the X, Y, Z axis. To ensure a sub aperture polishing of free form surfaces, a degree of freedom in the Θ axis was required as well, the Θ axis being the one that controlled the precess angle or the spindle angle with respect to the contact point on the workpiece surface. The fixture shown in Figure 1-6 was designed to satisfy these needs of obtaining 4 degrees of freedom for the polishing system.

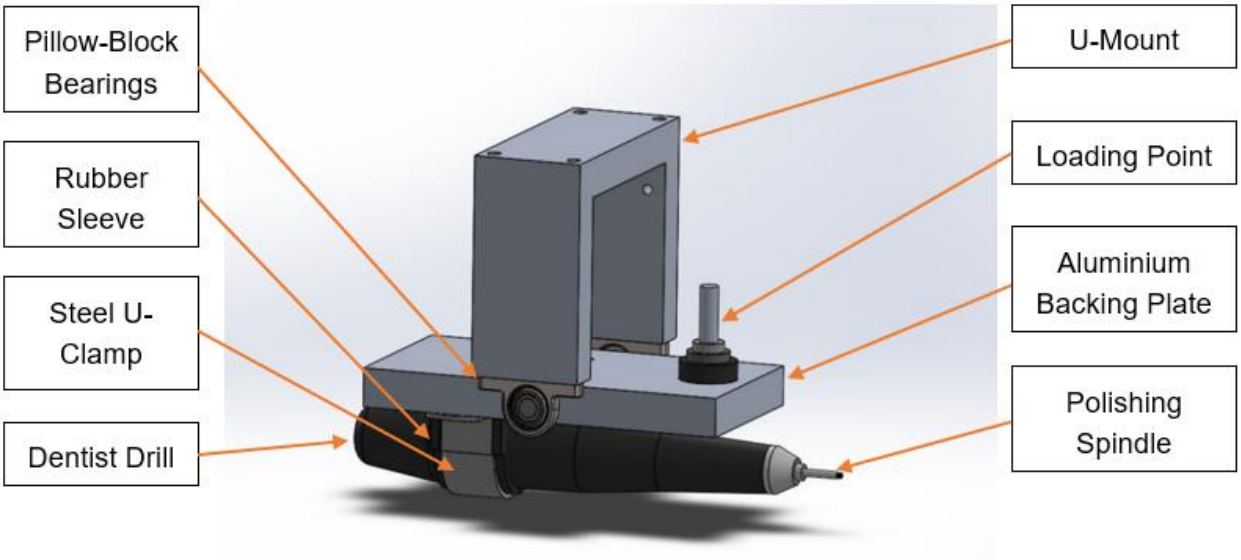

Figure 1-6: CAD Model of the polishing fixture.

1.4 **ANALYTICAL APPROACH**

In the case of sub aperture polishing the basic arrangement is that a polishing sphere is made to contact a workpiece (that could be flat, concave, convex) a force is applied on the polishing sphere to maintain the contact and the sphere is then rotated in a polishing slurry to carry out the polishing action. In order to model this contact the Hertzian contact theory has been utilized in this research. A few assumptions that need to be made to study the contact model are that the contact is non adhesive, meaning the contacting bodies can be separated without adhesion forces acting between them. Another important assumption is that the polishing tool is considered to be a sphere of a given diameter, and the workpiece is considered to be flat to begin with, hence has a diameter amounting to ∞. When these two solid bodies of are pressed together with a force F, a circular area of contact of radius ‘a’ is obtained, which leads to our next assumption that the contact area formed between the spherical polishing sphere and the flat workpiece is circular.

The next assumption is the normal loading force acting on the polishing sphere/tool. Hertzian contact model is based on the logic that pressure (contact stress) is developed when two curved bodies are brought in contact with each other and undergo slight deformation when the normal force is applied. This deformation is directly proportional to the Young’s modulus of the materials in contact.

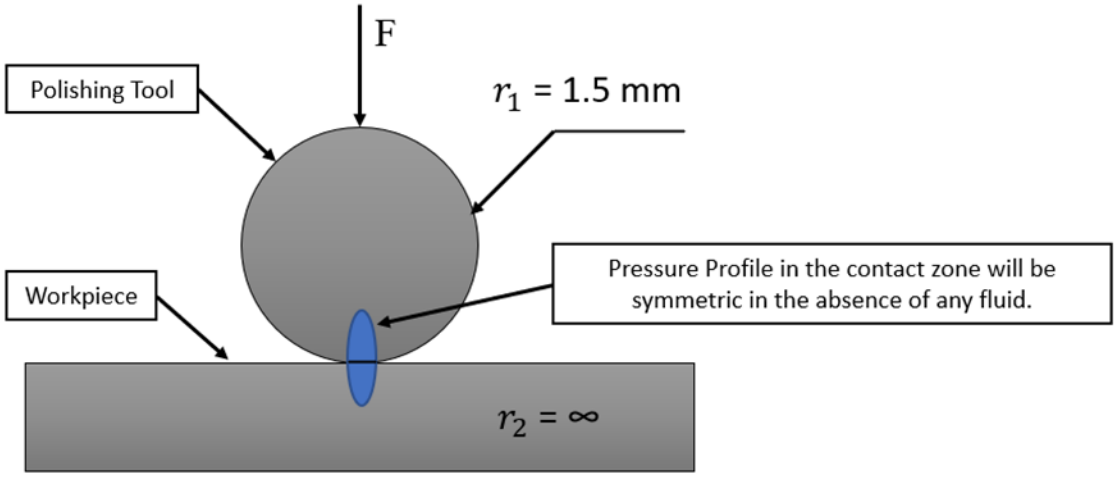

Figure 1-7: Image depicting the Hertzian contact between polishing sphere and workpiece

In the experimental setup a deadweight loading system has been used to maintain a constant force throughout the polishing process. The contact pressure (contact stress) is what determines the polishing action on the workpiece rather than the direct force which is exerted on the surface [12]. Meaning although the force applied might be constant, but the pressure and stresses developed might vary due to change in geometry shape being polished [12]. The contact stress values can be calculated about z -axis. The deformation of the polishing tool is one of the crucial factors in the polishing process, at it is hinged on the material properties of the polishing tool, since the Young's modulus of the polishing tool (Silicone Rubber) is 60 times lower than that of the workpiece (PMMA), the workpiece has been assumed to be rigid, whereas the polishing tool is deformable, this causes the polishing tool to flatten out on the workpiece when it is in contact and a normal load is applied to it. The more it flattens out the higher will be the contact radius and at a constant normal load, a higher contact patch radius would lead to a decrease in the contact pressure, directly reducing the polishing rates in the contact zone and increasing the polishing times. In a study carried out by Su et al. [13] it was discussed that the hardness of the polishing tool and the elastic deflection it undergoes determines the lubrication regime for the polishing process. It was observed that if the tool were made out of a soft material as compared to the workpiece and the loading is on the lower side in terms of magnitude the lubrication regime would lie in the IE or IR regimes. Hence it is imperative to figure out the deflection of the polishing tool itself as it rotates and contacts the surface.

1.4.1 **Polishing Tool Contact Analysis – Theoretical**

Now moving onto the case where the tool makes contact with the workpiece surface. According to the Hertzian contact model, the contact patch size is quantified by using the radius metric, the

radius of the contact patch is based upon the effective Young's modulus of the contacting bodies, E, effective diameter of the contacting bodies, d, and normal force acting in the contact situation, F [14]. The contact patch radius 'a' can be calculated as follows in equation 1 –

$$a = \sqrt[3]{\frac{3 * F * E_{effective}}{8 * (1/d_{effective})}} \quad (1)$$

$$E_{effective} = \frac{(1-\nu_1^2)}{E_1} + \frac{(1-\nu_2^2)}{E_2} \quad (2)$$

$$d_{effective} = \left(\frac{1}{d_1} + \frac{1}{d_2}\right) \quad (3)$$

In this research the polishing tool that has been used is a Silicone rubber based ball and Polycarbonate (PC), Polymethylmethacrylate (PMMA) workpieces. The calculations have been shown for Polycarbonate (PC).

Contact patch radius - $a = \sqrt[3]{\frac{3 * 1 * 0.0168}{8 * 0.333}}$ = 0.266 mm

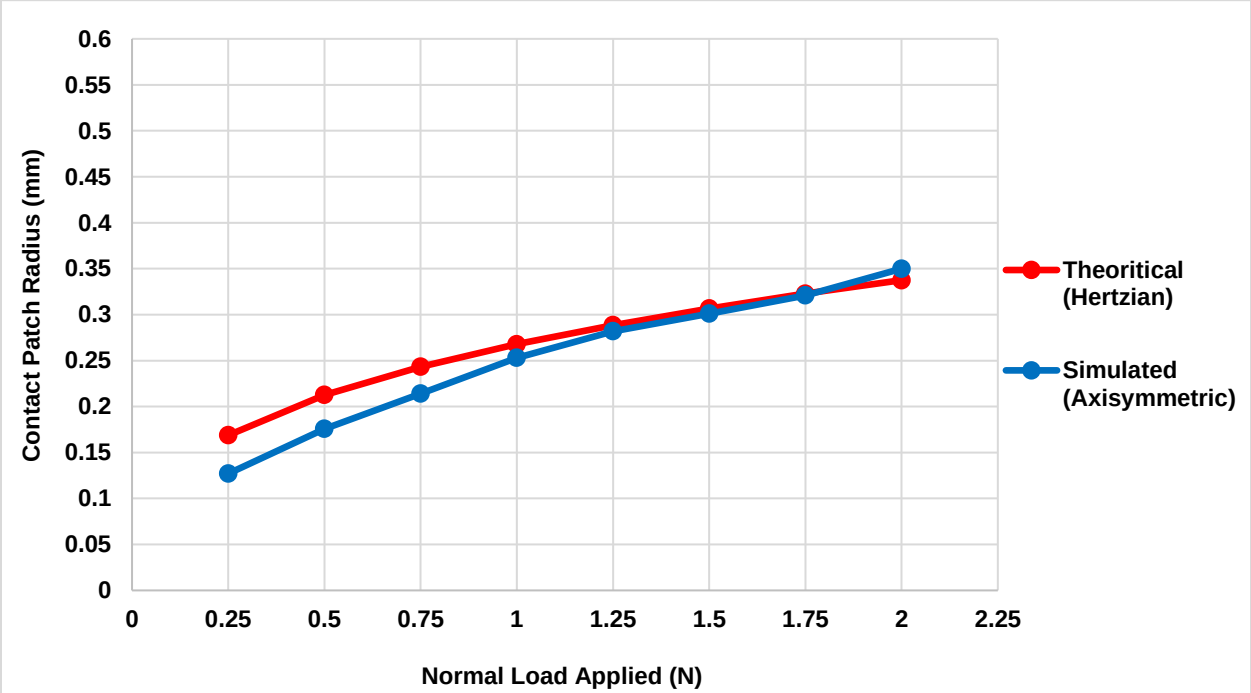

Figure 1-8: Plot depicting variation in the contact patch radius for differing normal loads.

According to the calculations at 10000 rpm, at a 1 N normal load, the theoretical contact patch would measure 0.266 mm in radius, and as the normal loading is increased, meaning as the force applied on the polishing tool is increased, it compresses more against the workpiece, and contact patch begins to flatten out, thereby causing an increase in the contact patch radius. The trend for the variation of the contact patch radius with the normal load as shown above in Figure 1-8 is

comparable to the results achieved by Dintwa et al. in their analysis of Hertzian theory for elastic sphere contact [15].

Now for any given contact the peak pressure value is calculated below using equation (4) –

$$P_{max} = \frac{3 * F}{2 * \pi * a^2} = 6.74 \text{ MPa} \quad (4)$$

Where – F – Normal force applied on the polishing tool

a – Contact patch radius

P_{max} – Peak pressure in contact zone.

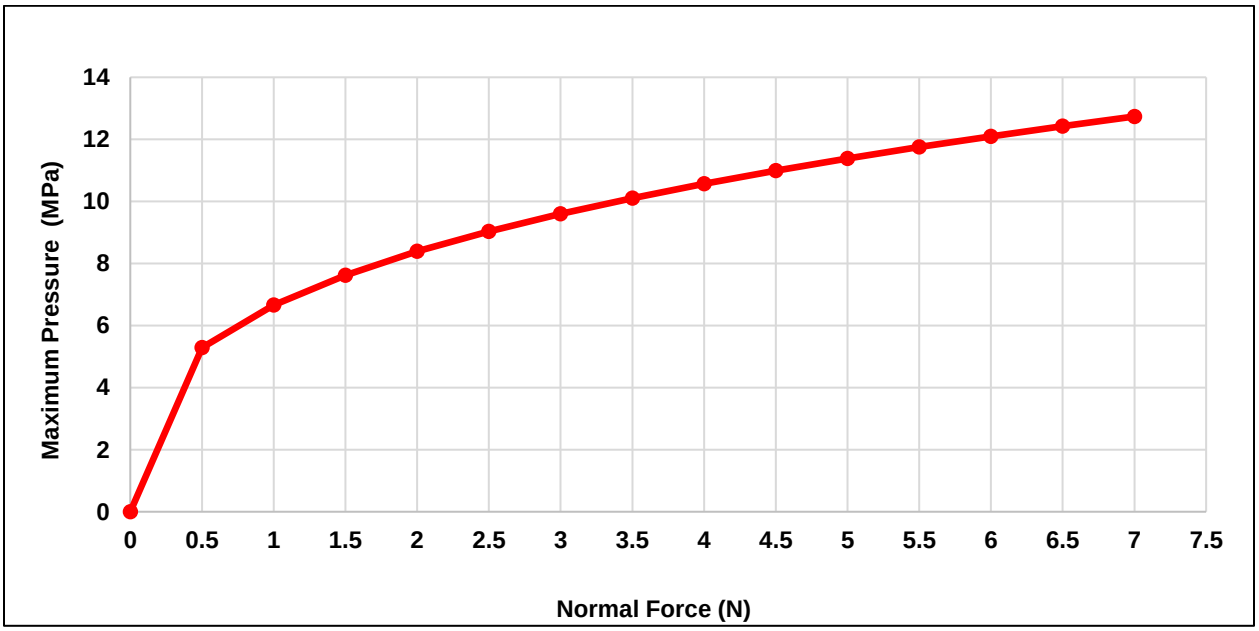

Figure 1-9: Plot depicting variation in maximum Hertzian pressure with normal loads.

According to the Hertzian contact theory the pressure variation across the contact patch is in accordance with Gaussian distribution. Now under a contact scenario between the two bodies in contact, the pressure distribution is symmetric about a centerline passing through the center of the point of contact in the XY plane [14]. In this research work the normal load range that is being utilized is from 0.25 N to 1.5 N as this range provides a small enough contact patch that is in line with overall size of the features that are being polished. This would give an expected peak pressure range of 5.28 MPa to 7.62 MPa. The pressure distribution along the contact patch [16] is given by equation (5) below –

$$\sigma_z = 1.5 * P_{mean} * \sqrt{1 - \frac{r^2}{a^2}} \quad (5)$$

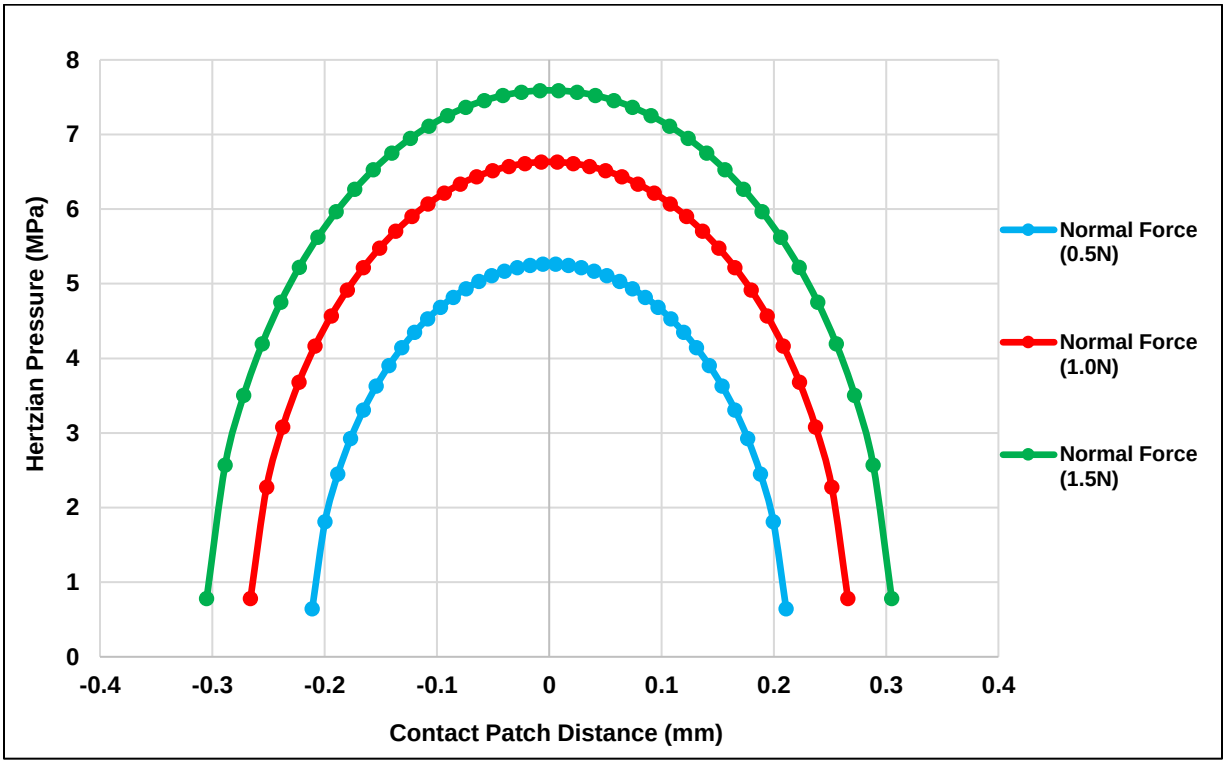

Figure 1-10: Plot depicting theoretical Hertzian contact pressure for varying normal loads.

Using a normal load (F) of 1 N and corresponding contact patch radius of 0.266 mm, a peak pressure of 6.65 MPa is obtained at the center of the contact zone. The Hertzian contact pressure distribution acts equally across the contact zone and with opposing directions on the polishing ball and the workpiece [14][16]. The theoretical pressure distribution across the contact patch for the case of varying normal loads was plotted as shown above in Figure 1-10. As it can be seen from the pressure distribution, it is distributed symmetrically across the contact patch.

1.4.2 **Polishing Tool Contact Analysis – Simulation**

Next moving onto the case wherein the polishing tool deflection is studied when the tool is normally loaded and rotated at the same time. Theoretically for the general case of a non-rigid workpiece and a non-rigid polishing tool (sphere), for a Hertzian contact, Fischer-Cripps et al. [16] stated that the deformation can be obtained by using the following equation (6) –

$$u_z' + u_z = \left[\frac{(1-\nu_1)}{E_1} + \left(\frac{(1-\nu_2)}{E_2}\right] * \frac{\pi}{(4*a)} * 1.5 * P_{mean} * ((2 * a^2 - r^2) \quad (6)$$

Where u_z' and u_z as the deflections of the polishing tool (sphere) and the workpiece, respectively. Since the polishing tool is made out of Silicone rubber and the workpiece is made out of PC/PMMA, the polishing tool (sphere) is taken as deformable and the workpiece is assumed to be rigid. Thus u_z would equal to zero, hence the equation (6) can be re written as follows, and this would provide us the theoretical deflection profile along the contact patch.

$$u_z = [\frac{(1-\nu_1)}{E_1} + (\frac{(1-\nu_2)}{E_2}] * \frac{\pi}{(4*a)} * 1.5 * P_{mean} * (2 * a^2 - r^2) \quad (7)$$

A finite element study was performed using the ANSYS Workbench suite to gauge the deflection of the polishing tool when the tool is modelled as a hyperelastic material and is made to contact the polishing work. The tool was angled at 30 degrees and allowed to rotate at an RPM of 10000, and a normal load of 1N was applied in a contact zone as a reaction force acting against the ball.

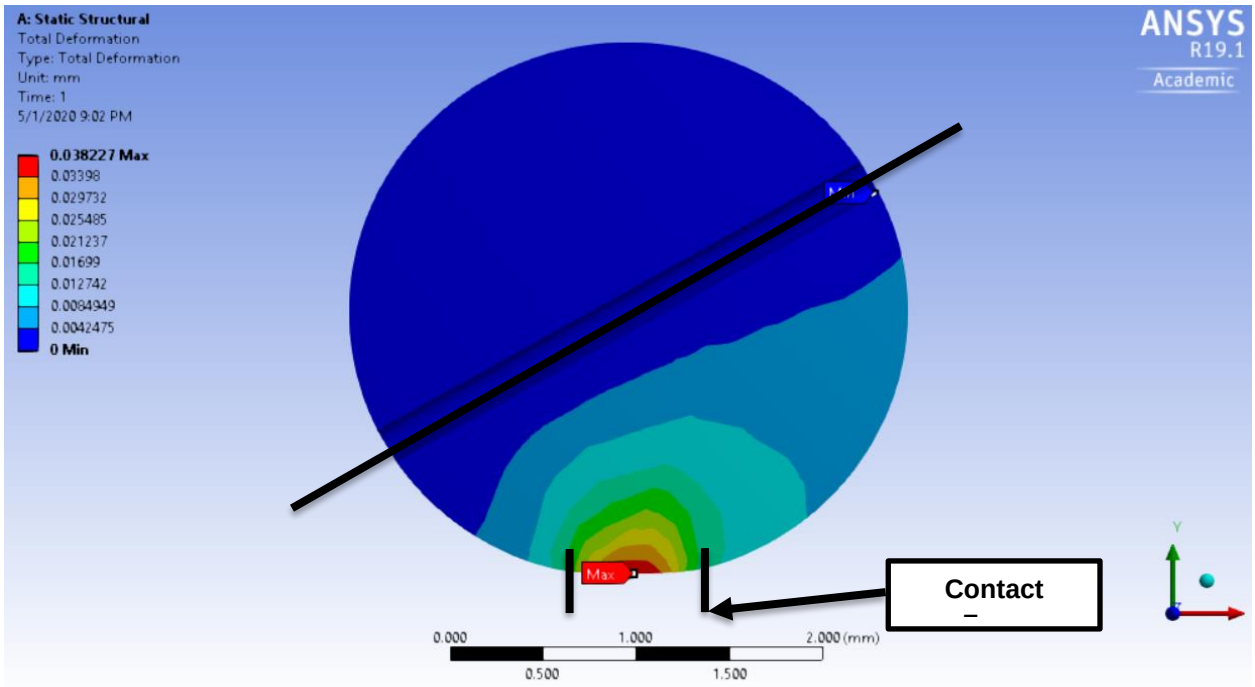

Figure 1-11: Side view of the finite element result for polishing tool deflection.

The below plot represents the variation in the deflection profile of the soft polishing tool along the contact patch – wherein the blue line is indicative of the deflection profile obtained by using the equation (7), and the red line in the Figure 1-12 is the finite element result of the deflection. The difference in the value between the two results can be attributed to the fact that the theoretical formulation does not consider the polishing tool rotation, it only considers the deflection due to the application of the normal force on the ball. Whereas the finite element model considers both the rotation of the tool and the normal force being applied, while also utilizing the hyperelastic properties of Silicone.

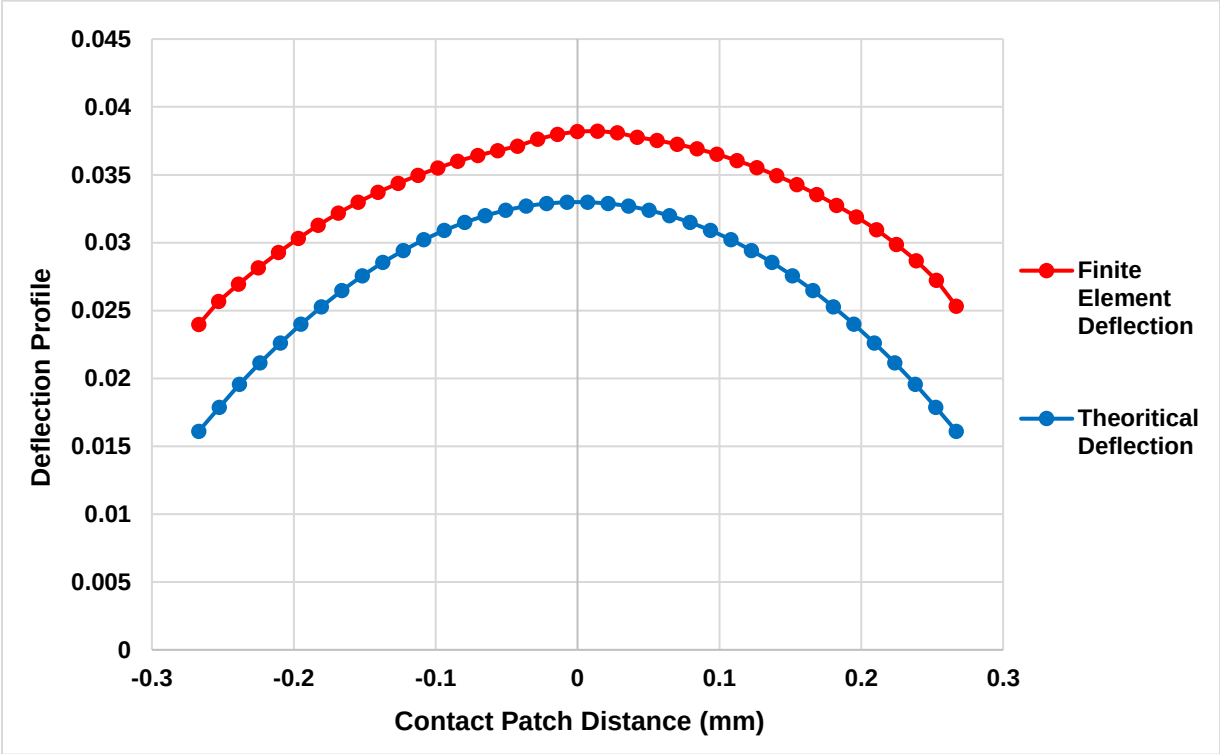

Figure 1-12: Plot depicting the deflection values for the polishing ball along contact patch.

In the process of sub aperture polishing there is a presence of three distinct systems, the polishing tool, the workpiece to be polished and the polishing slurry that separates the tool and the workpiece. Now the material removal in the polishing process takes place predominantly in the contact zone. The Hertzian theory of calculating the contact area doesn't involve the presence of a fluid film in the contact zone. However, a study done by Loewenthal et al. suggested that it can be assumed that even though the fluid film separates the two surfaces of the tool and the workpiece, the conjunction zone or the contact zone can be calculated using Hertzian theory, and the zone can then be projected through the film thickness of the polishing slurry and would determine the material removal

In order to simulate the Hertzian contact, a finite element analysis was modelled using a nonlinear solver by MSC Corporation called Marc/Mentat. The Hertzian contact was simulated in 2D first, in order to save computation time, and then was run in 3D to analyze the differences between the result. Within 2D the contact was analyzed using both the popular plain strain model for contact, and the axisymmetric model which would be more applicable for this project. The overall polishing system was reduced to a basic model for the FEA analysis. It is a clear observation that the overall model can be reduced to an axisymmetric model and also since the PMMA/PC workpiece is orders harder than the soft polishing tool, it can be assumed to be a rigid body it will not undergo

any noticeable deformations or stresses due to pressing of the soft tool and can be neglected from the model for contact analysis and is modelled as a geometric entity instead.

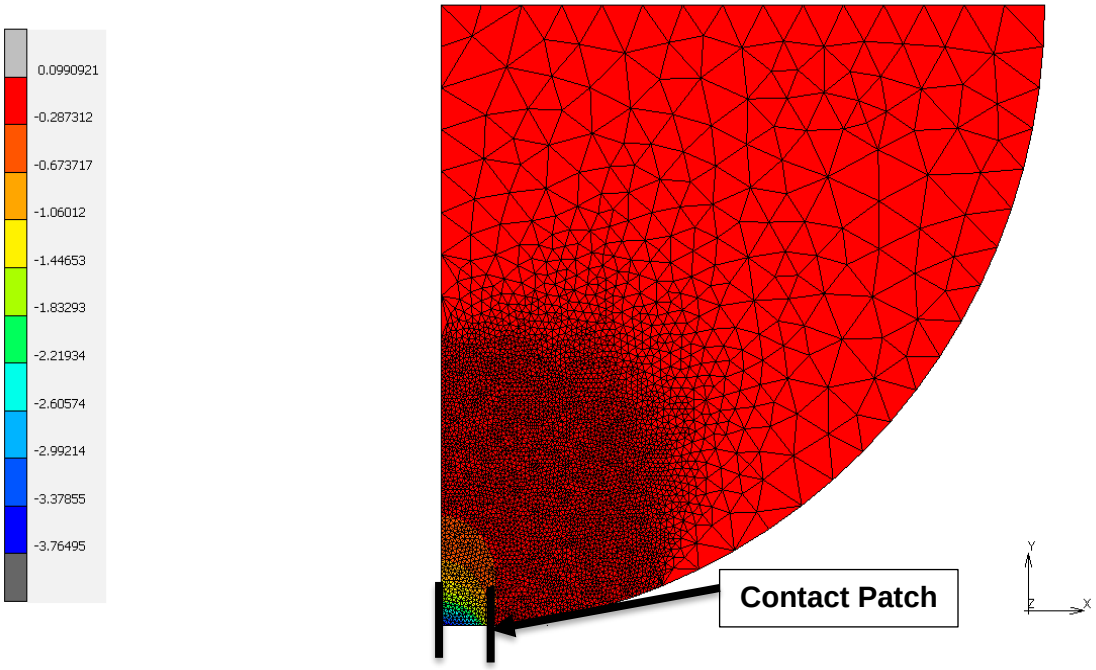

Figure 1-13: Contour plot for contact pressure at 0.25 N normal load.

Figure 1-13 above shows the contour plot of the contact pressure at 0.25 N normal load, which is loading range of the experiment set. It can be observed from the plots that the ball deflection and the contact pressure is proportional to the normal load applied on the polishing tool. The contact pressure distribution follows a Gaussian curve across the contact patch. The simulation result as shown in the Figure 1-14 vary slightly as compared to the maximum pressure values which were obtained using the Fischer Cripps model [16] for Hertzian contact of deformable tools, this can be explained as the simulation for the polishing tool considers the large strains and hyperelastic properties that associated with a soft material like Silicone Rubber, whereas the Fischer Cripps model for Hertzian contact doesn't account for the hyperelastic properties of the polishing tool.

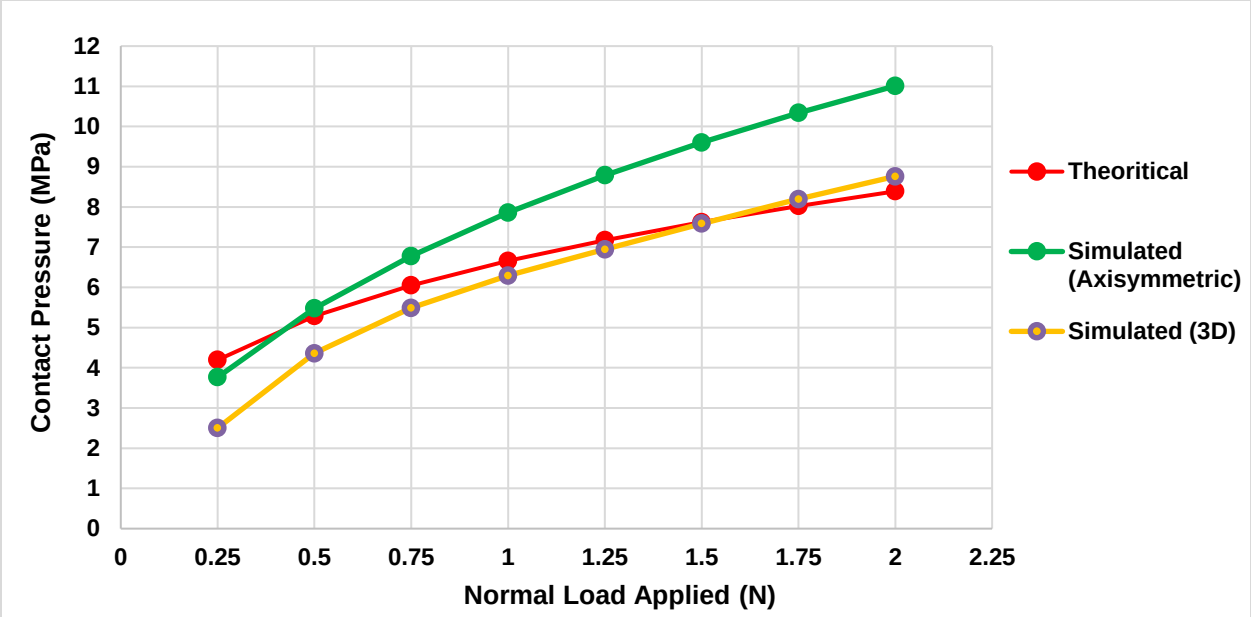

Figure 1-14: Plot depicting maximum contact variation with normal load.

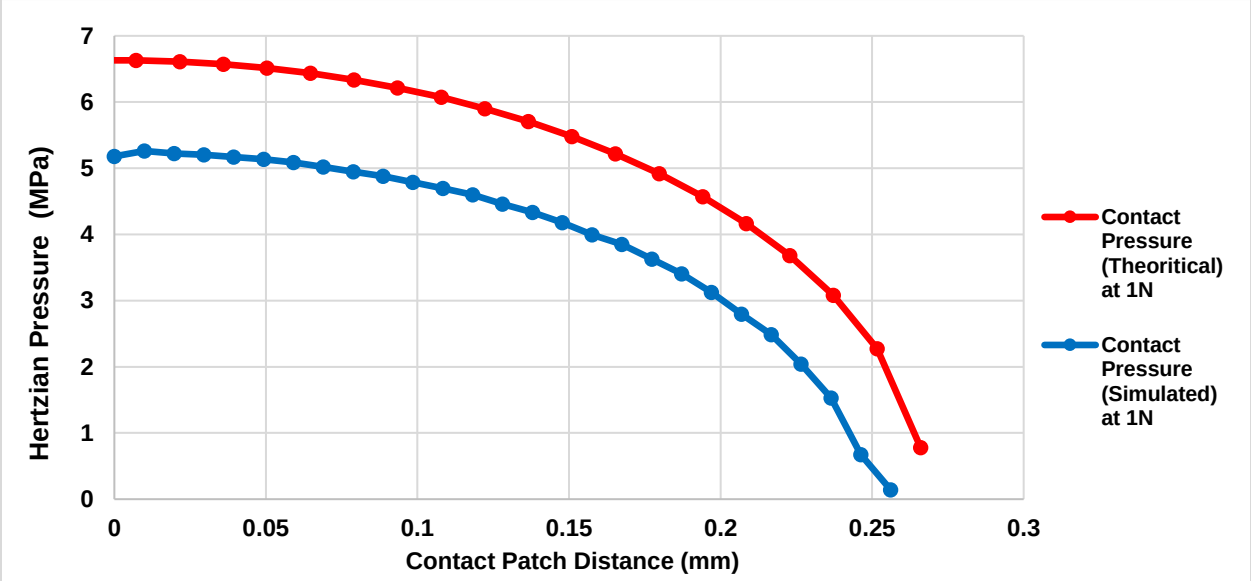

Figure 1-15: Plot depicting contact pressure profile along the half contact width.

The contact pressure profiles for the contact of the polishing were obtained from the simulations and the result were compared to the theoretically calculated pressure profiles the maximum contact pressure was found to be 6.65 MPa theoretically, while at the same normal load the contact pressure was found to be 7.86 MPa through the FEA simulation, that gives us an error percent of around 18%. This difference in the pressure profiles can be accounted by the fact that the due to the softness and the hyper elastic nature of the Silicone rubber tool, as the normal load

is applied it compresses more than what can be expected from a general elastic material, meaning the compression of the body of a hyperelastic material will be larger than normal elastic body, and will have a lower body stiffness. As the polishing tool compresses more readily, it will lead to a lower pressure profile than a standard elastic tool.

The 3D model was setup in the same way as the axisymmetric model, with the polishing tool defined as a deformable body and assigned the material properties of Silicone Rubber. The polishing workpiece was setup as a rigid body and assigned the material properties of PMMA for the sake of the simulation. The workpiece base in this case was fixed in the x,y,z directions, and the polishing ball was constrained to move freely in the y axis. A normal load was applied on the ball as per the volumetric loading criteria.

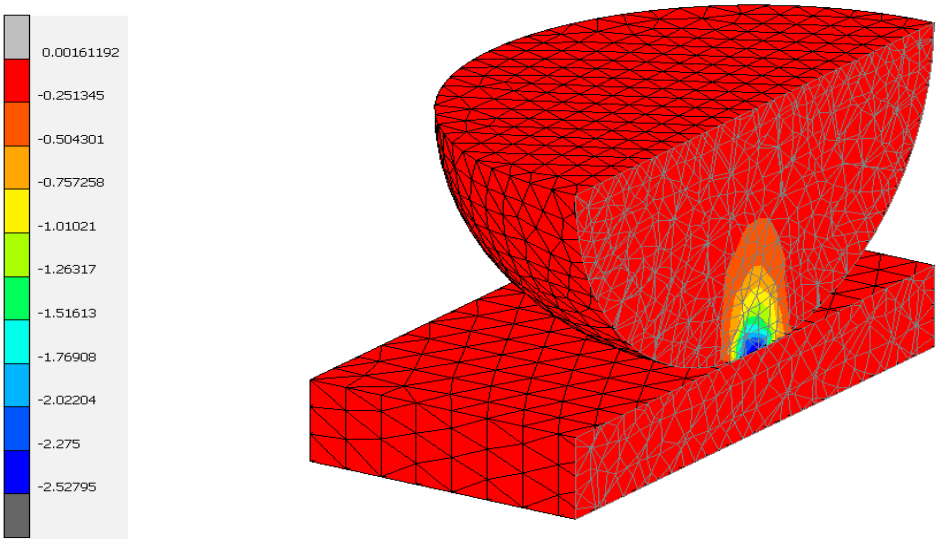

Figure 1-16: Figure depicting the contour plot for contact pressure at 0.25 N normal load.

From the simulation result it was observed that the maximum contact pressure at 1N was found to be 6.29 MPa as compared to the theoretical contact pressure value which was 6.65 MPa which is in good agreement with each other.

1.4.3 **Abrasive Fluid Film Analysis**

In the process of sub aperture, the polishing fluid film is what separates the rotating polishing tool from the workpiece. In a usual experiment the area of interest, which is to be polished, is flooded with the polishing fluid to ensure complete coverage of the polishing zone. As the polishing tool starts rotating and feeding into the polishing zone, it pulls in and drags the polishing fluid into the

polishing zone. This polishing fluid forms a thin layer between the tool and the workpiece, the film thickness of which is paramount, as it affects what type of contact there will be between the tool and the workpiece, and it also affects what type of lubrication regime would be present in the process. Loewenthal et al. in their work suggested that the lubrication regime of elastohydrodynamic applies to the process of elastic emission polishing, since the polishing tool that is being used is made up of a soft material with a low Young's modulus. In this project the polishing tool is made out of Silicone rubber which has a Young's modulus of 50 MPa, which is orders less as compared to the workpiece (PMMA/PC). Dowson et al. [17] in their study presented a discussion on the effect of the deflection of soft polishing tool on the polishing fluid in the contact region. The following equation (8) derived from the Dowson et al. [17] was used to calculate the minimum film thickness H_{min} for the contact of a spherical polishing tool with a low elastic modulus on a flat surface –

$$H^{min} = 7.43 * U^{0.65} * W^{-0.21} * (1 - 0.85 * e^{-0.31*K}) * R \quad (8)$$

H^0_{min} – Dimensional minimum film thickness parameter

H_{min} – Minimum film thickness (mm)

K – Ellipticity parameter

R – Radius of the polishing tool

U – Dimensionless speed parameter

W – Dimensionless load parameter

The minimum film thickness value was calculated to be H_{min} = 0.014 mm at 10000 rpm and 1N normal load for the Aluminium Oxide (Alumina) polishing fluid with an abrasive grain size of 0.01 µm (the Aluminium Oxide abrasives are dispersed in a deionized water solvent medium.

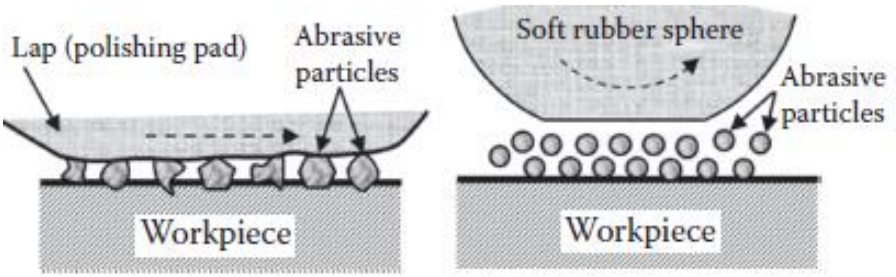

Figure 1-17: Figure depicting the two modes of polishing contacts [18].

The minimum film thickness value has to be greater than the size of the polishing abrasives and the inherent surface roughness of the workpiece so that the abrasives will be able to flow in and out of the zone with ease, and lead to effective polishing action as shown above in Figure 1-17B. In this project the polishing abrasives measure 0.01 µm which makes them small enough to flow through the thin film created in the contact zone. If the film thickness is smaller than the abrasive

particle size it could lead to the indentation and damage of the surface as shown above in Figure 1-17A. The polishing tool surface roughness was measured using the Keyence laser confocal microscope, the average surface roughness value was found to be 9.8 µm over a sampling length of 1.6 mm and a cutoff frequency of 0.8 mm.

Figure 1-18: Laser image depicting the polishing tool surface at 10X magnification.

With a minimum film thickness value of 14 µm, which is greater than the surface roughness of the polishing ball, it can be said that the lubrication type is synonymous to Elasto-Hydrodynamic lubrication in accordance with the Stribeck curve. The metric used was the comparison of the film thickness height to the surface roughness value and was adapted from a study done by Bart et al. [19].

It can also be said that when the polishing tool used has a low Young's modulus value and the loads applied are on the lower magnitude, in accordance with the study performed by Su et al. [13], the fluid can either lie in IE (isoviscous elastic) or IR (isoviscous rigid) regime. Now to figure out whether the regime would be in IE or IR, the polishing tool deformation which is an important metric that defines the lubrication [13]. From prior simulations carried out on the polishing tool which can be seen in the Hertz contact section of chapter 5, the deflection of the polishing tool was found out to be 0.03 mm, which is significant and comparable to the film thickness calculated which was 0.011 mm, it can be said the fluid film between the polishing tool and the workpiece would lie in the IE (isoviscous elastic) regime From equation (12) it can be said that the minimum film thickness is greatly affected by the polishing tool rotation, as is evident by the dimensionless velocity parameter which has the highest power in the formulae. As shown in the Figure 1-19 below the minimum film thickness increases almost linearly as the polishing tool rotational velocity is increased, this is in line with results obtained in studies done by Loewenthal et al.

From the Figure 1-19 below it can be seen that the minimum fluid film thickness decreases the most when the load is increased from 0.1 N to 0.8 N, with minimum film thickness decrease of 33.33% observed from the plot, thereafter as the load is further increased it doesn't affect the film thickness by much.

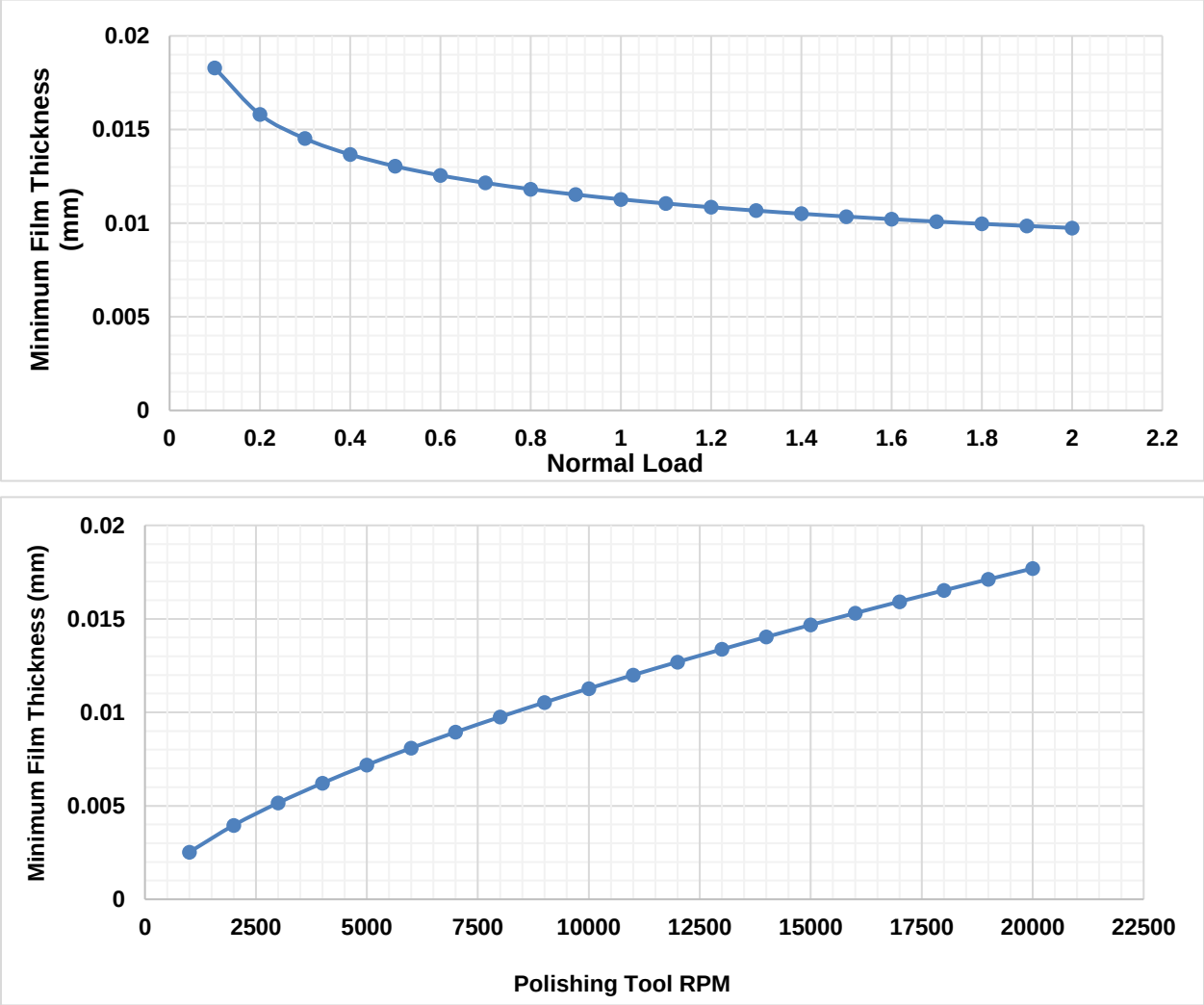

Figure 1-19: Plot depicting the variation of minimum film thickness with polishing tool RPM and normal load.

Coming over to the FEA analysis of the setup of polishing tool, fluid film and the workpiece, this is an integral simulation as it will help to obtain an understanding of how the soft polishing tool deflects real time in the presence of a flowing abrasive fluid and will help to analyze the fluid pressure, flow velocity profiles across the contact zone during polishing. In order to do this, a coupled 2 way fluid – structural interaction (FSI) simulation was carried out using the ANSYS software package. For this the entire polishing system was reduced down to the main components

(which are the polishing tool, abrasive fluid, workpiece). The free body diagram with the main forces for the system can be seen below in the Figure 1-20.

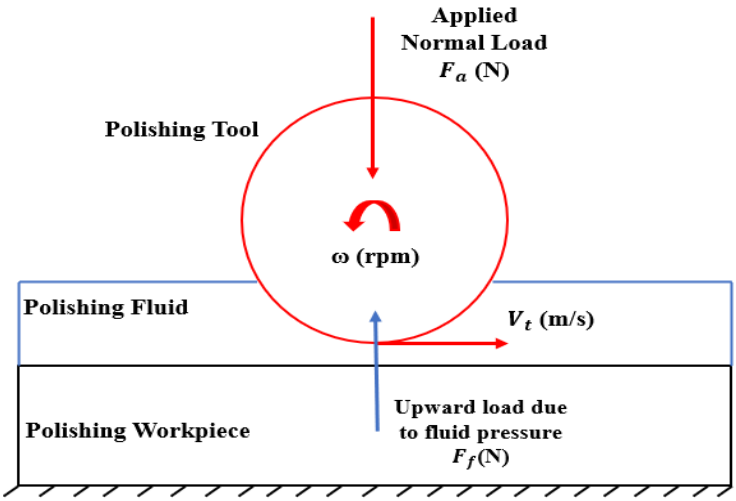

Figure 1-20: Free body diagram for the polishing system showing the main forces.

In order to carry out the simulation the full 3D model was further reduced to a half model and was made symmetric along the X-Y plane. The basic idea behind a FSI analysis is to carry out a coupled analysis wherein the deformations and stresses developed in the structural (solid bodies) are transmitted to the fluid flow around those solid bodies, and the complimentary reaction forces developed in the fluid like fluid pressure, shear stresses are transmitted to the structural side. In this project the polishing tool and workpiece form the structural side of the simulation and the polishing fluid flowing through the contact patch forms the fluid side of the simulation. In the Figure 1-21 below we can observe the fluid velocity profiles, as the abrasive fluid flows in the polishing zone, due to the rotational velocity of the polishing tool, a centrifugal force acts on the polishing fluid thereby pulling the fluid along the surface of the tool. We have the peak velocity of the fluid on the center line of the tool, with a maximum fluid velocity of 1.549 m/s at the polishing tool wall boundary, which is equivalent to the surface velocity of the rotating tool at 10,000 rpm.

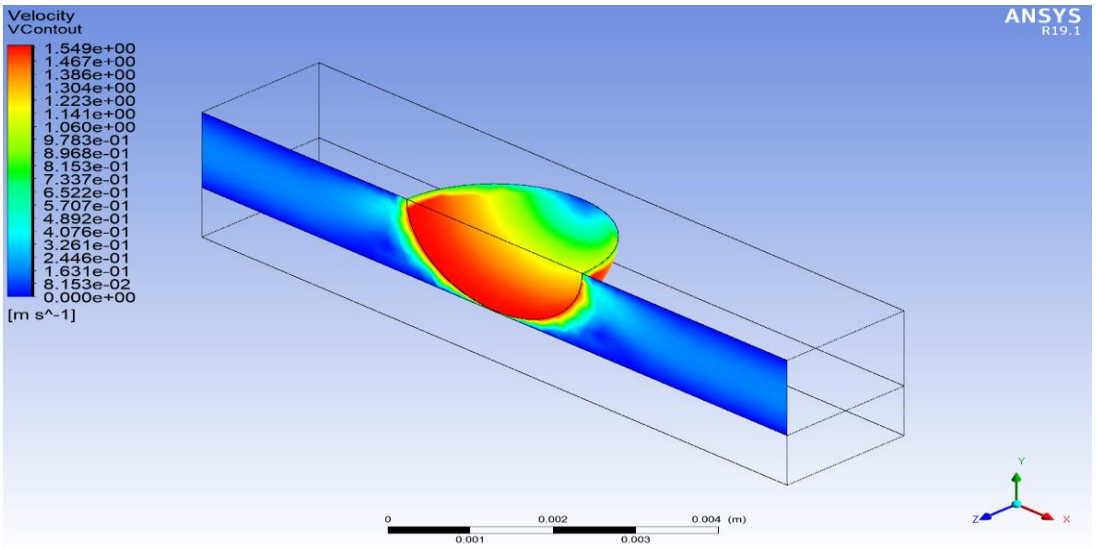

Figure 1-21: Image depicting the polishing fluid velocity contour.

Now as the fluid flows through the contact zone, it can be imagined as the fluid being forced through a narrow opening, which has a converging inlet and a diverging outlet. As the fluid enters this contact zone between the rotating tool and the workpiece, we see an increase in the velocity of the fluid – same as when a fluid enters a converging section, and as per the Bernoulli equation, the velocity increases the pressure should reduce, but since the fluid impacts the rotating tool at the inlet, and since the boundary wall of the fluid isn't stationary, but is the rotating tool boundary, the pressure value goes up as the fluid starts applying an upward pressure on the soft tool surface.

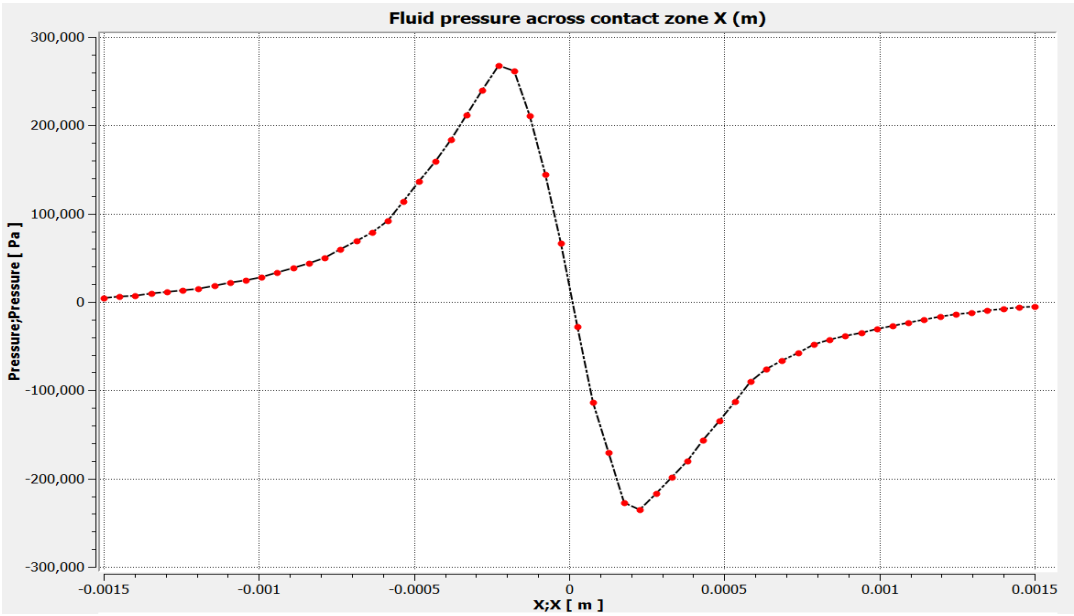

Figure 1-22: Image depicting the fluid pressure distribution along the contact zone

In the center of the contact zone, as expected the fluid velocity is at its peak, while the pressure value reduces as seen in Figure 1-22. Then as the fluid starts exiting the contact zone, the fluid velocity starts to drop, and the pressure value starts to increase (on the exit side of the contact), we observe a negative pressure value on the exit side, this is due to the fact that as the fluid is exiting the contact at a high velocity, it tends to create a pressure gradient that pulls on the polishing tool surface, i.e. a fluid pressure acting downward away from the polishing tool body is generated, as it can be observe the pressure profile across the contact zone in Figure 1-22.

The result of this kind of pressure distribution can be observed in the section 1.5.2 we see flat profile tool influence profiles (which were made by allowing the tool to rotate at a given spot, for a given time t), which are indicative of the pressure distribution observed in Figure 1-30. Figure 1-23 depicts the contour map of the pressure distribution just discussed, in the contour maps it can be seen that the pressure undergoes an inflection at the center point of the contact, wherein it changes the direction. In the contour map in Figure 1-23 the red and blue regions are regions with a highest pressure magnitude, but opposite directions.

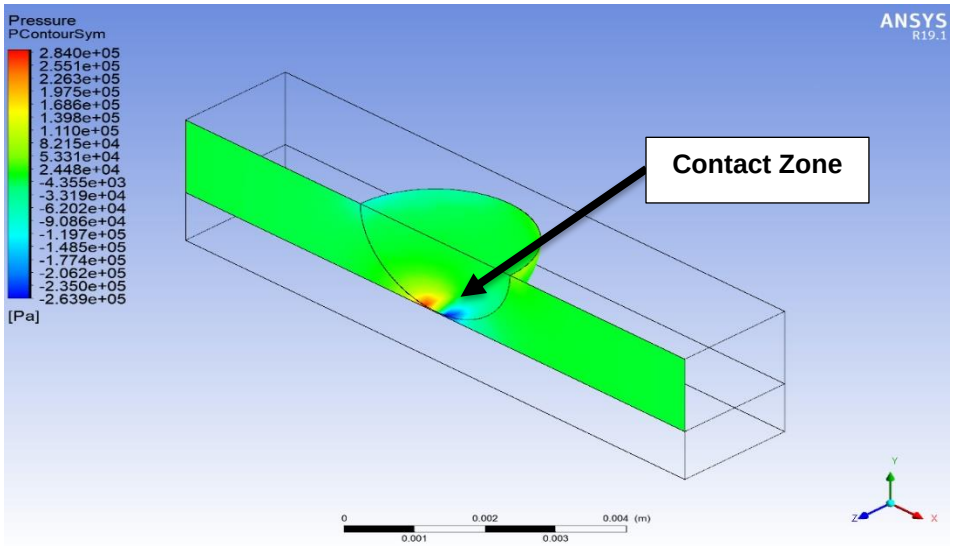

Figure 1-23: Image showing the fluid pressure contours.

Now discussing the fluid film characteristic in the contact zone, the average fluid film thickness was calculated using the Dowson and Higgins film thickness formulae. In this project the polishing tool is made out of a soft material Silicone rubber, and the workpiece is Polycarbonate which is orders harder as compared. When the polishing fluid flows through the contact zone, it imparts an upward normal force on the soft polishing tool due to pressure of the fluid, hence causing it to deflect and leading to the development of a film thickness profile as seen below in Figure 1-24. It can be observed in Figure 1-24 that there is a deflection in the tool surface towards the outlet side of the flow, this deflection causes the further constricting of the fluid film at the outlet side thereby leading to spike in the reducing pressure as it can be observed in the pressure gradient plot. This result is in line with previous work done by Dowson et al. on EHL film analysis. The film more or

less maintains a constant central film thickness except for the deflection of the film on the outlet side of the polishing fluid flow.

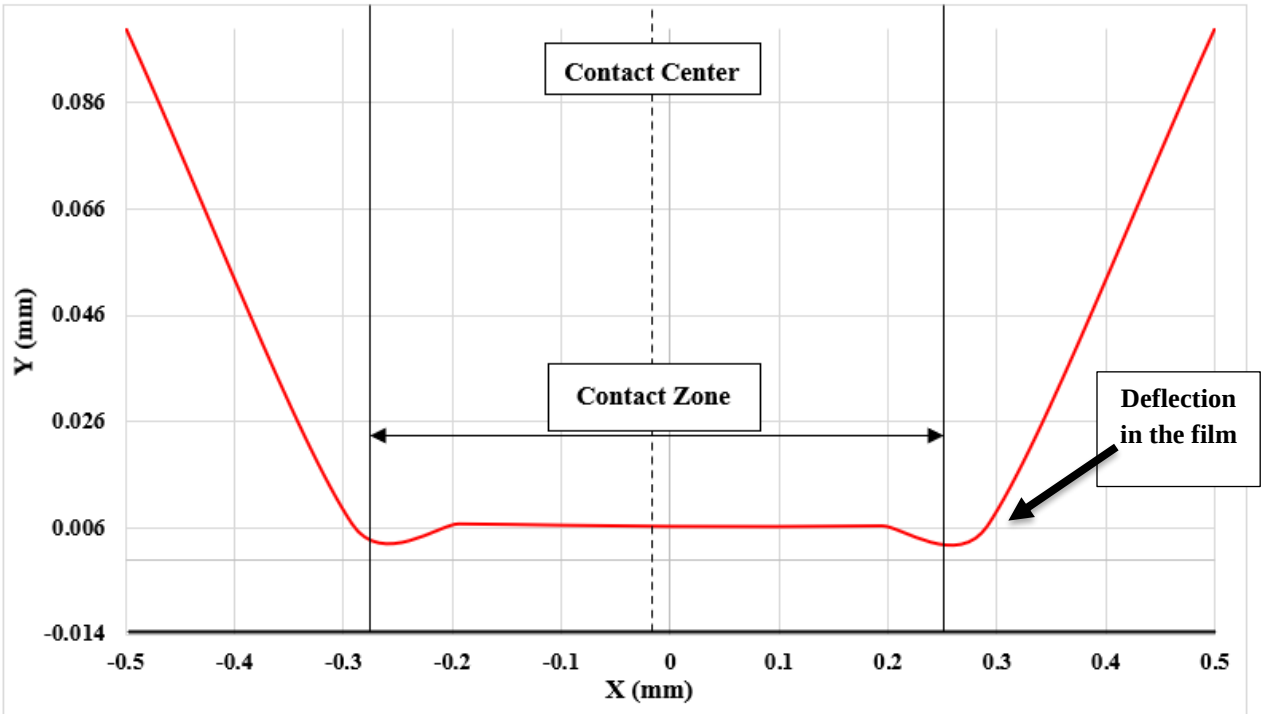

Figure 1- 24: Plot depicting fluid film thickness profile on the zoomed in contact zone scale.

The deflection of the polishing tool is an integral part of the elastohydrodynamic polishing principle as was discussed in the works of Dowson et al. [17] and also governs the regime of the fluid lubrication as discussed in the works of Su at al [13]. The advantage of running this kind of simulation (2 way FSI) is that we can couple the pressure values generated by the fluid flow right back onto the solid body in contact with fluid, thereby causing the deflection in real time. It was seen in the simulation that the polishing tool deflects maximum in the contact zone, although the deflection value in itself is small, measuring about 0.006228 mm in the upward direction as seen below in Figure 1-25.

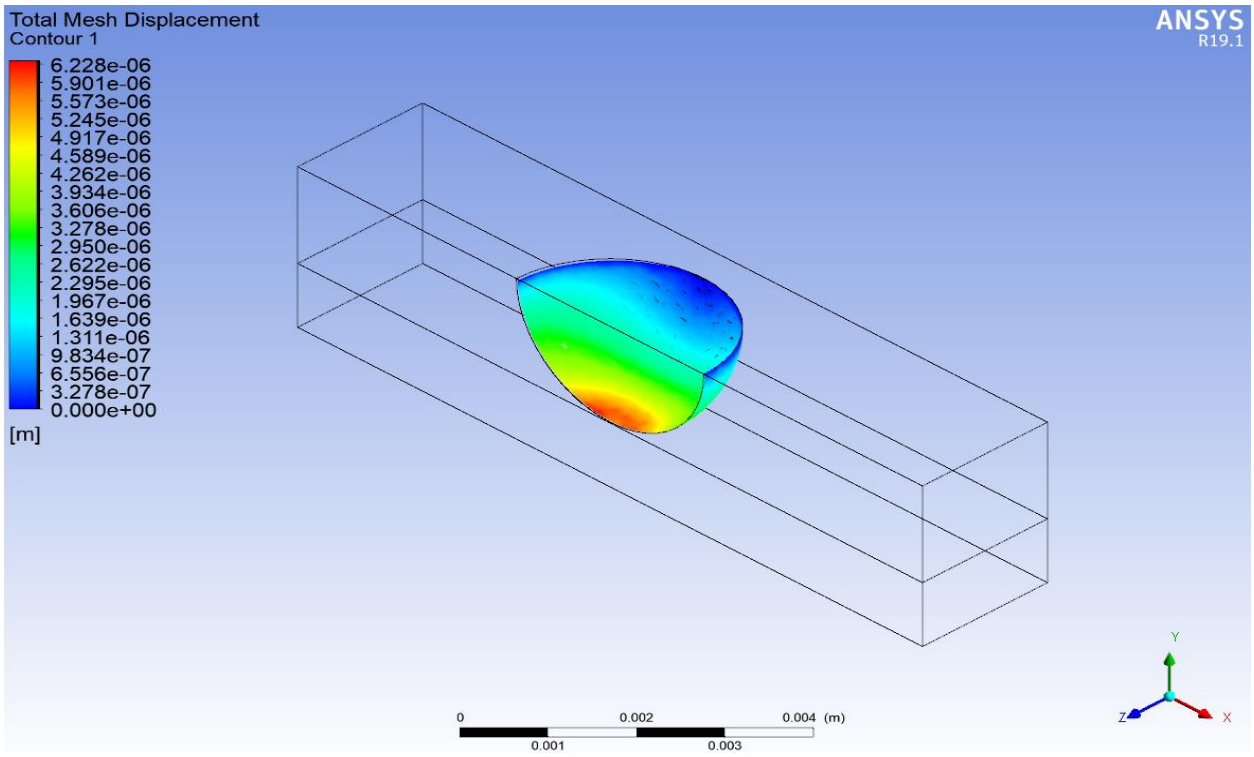

Figure 1-25: Contour map of the polishing tool deflection due to fluid pressure.

1.5 **EXPERIMENTAL RESULTS**

The basis of this project was to create an initial knowledge base for the sub aperture polishing project line at the Precision Engineering Center, NCSU. The problem statement was to carry out sub aperture polishing of polymer lenses in order to attain a surface roughness finish of 2-3 nm in RMS scale and to showcase the ability to be able to create a surface form spread over a 6x6 mm area with a max amplitude measuring 5 µm peak to valley. In this project, the study was performed on two polymers – Polycarbonate and Polymethylmethacrylate. The input parameters were selected and their effect on the surface roughness and the material removal rates were characterized. Studies were also carried out to gauge the effect different toolpaths used in the polishing have on the surface roughness improvement of the polymer surfaces.

1.5.1 **Polishing Tool Influence without Abrasive Fluid**

The first experiment carried out to was analyze the effect the material removal when the Silicone ball is made to touch the workpiece surface naked, without the presence of any polishing fluid. It was observed that when the contact occurs without the presence of the polishing fluid, due to the high rotational velocity of the polishing tool, there is a lot of heat generated due to the friction present between the rotating polishing tool and the workpiece, which leads to a rise in

temperature, as the temperature rises above the heat deflection temperature of the polymer, the surface melts, which leads to very high and uncontrolled material removal rate, this molten layer on the surface is smeared across the indent and then is displaced to the outlet region of the indent as observed in Figure 1-26 below. The molten material along with the worn off material from the polishing tool aggregates near the outlet region of the feature created, forming a bead like structure.

At the inlet region of the indent, there was also the presence of a heat affected zone, where the heat generated due to the initial contact of the rotating tool with the workpiece takes place, the initial contact causes generation a lot of heat, that causes blister like features prior to inlet zone.

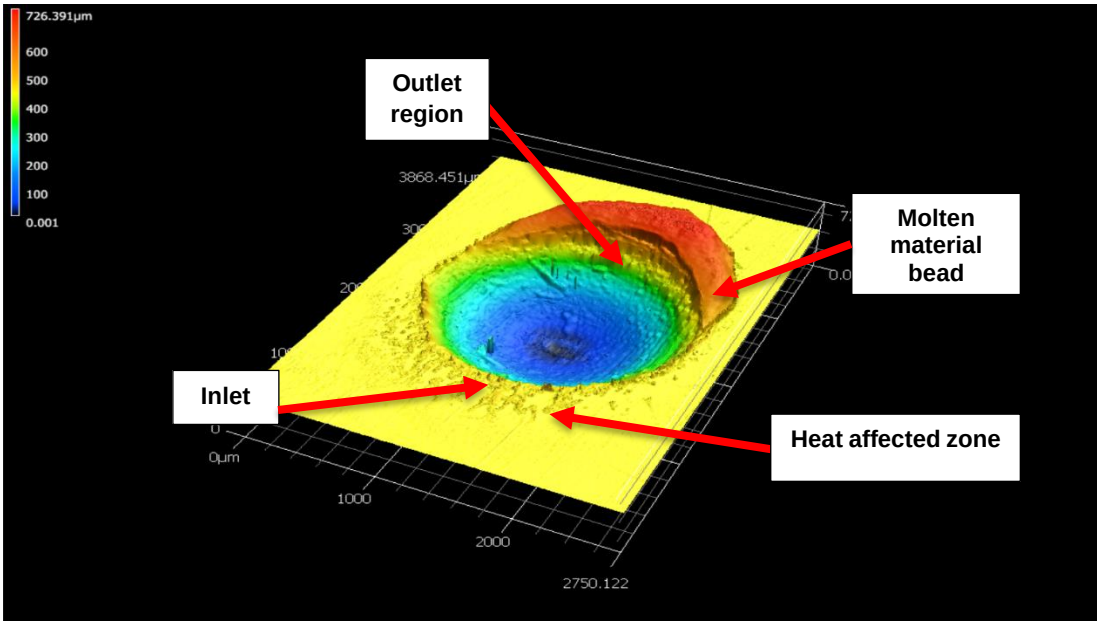

Figure 1-26: Image depicting the material removal in an indent A for a naked contact of the rotating polishing tool on the workpiece at 25000 RPM.

In the image above it can be observed that the profile of the indent is deeper in the middle and assumes a concave shape, which is in line of what is to be expected. When the rotating tool contacts the polymer surface, the contact pressure would be maximum in the center of the contact as per the Hertzian contact criteria. The volume of the molten bead which is formed in the outlet zone was found out to be 0.232 mm^3, while the volume of the material removed (i.e. the cavity) was found out to be 0.59 mm^3. The molten bead has a lower volume as compared to the volume removed from the cavity, this can be attributed to the fact that some of the material which gets heated up in the contact zone gets smeared on in the indent itself, which would raise the height of the indent cavity.

The major disadvantage for running an experiment set without any abrasive fluid is that the polishing tool will get worn quickly and is not feasible for multiple runs. Three experiment sets were performed at varying loads to gauge the effect of naked contact of the polishing tool with the

workpiece surface. The Table 1-1 below shows the input parameter levels utilized for the naked contact of the polishing tool.

SET	RPM	DWELL TIME (seconds)	LOAD (grams)	SPINDLE ANGLE (Θ)
A	25000	10	150	15
B	25000	10	100	15
C	25000	10	50	15

Table 1- 1: Data set for the naked contact experiment set.

The surface roughness was measured at the base of all the 3 indent sets. The average surface roughness was measured at 10 different points, and the points were spaced at 5 pixel points from each other.

Set	Load	Ra (Average surface roughness) (μm)	Std Dev
A	150	5.608	0.45
B	100	5.899	0.512
C	50	7.496	0.713

Table 1- 2: Surface roughness measurement for the naked contact.

It was observed from the surface roughness measurements in Table 1-2, that the surface roughness values obtained are not in the acceptable range and are on the higher side. It should also be noted that the surface roughness values increase as the normal load goes down, which leads to a contact pressure reduction and in turn leads to an increase in the roughness.

A study was also performed gauging the surface roughness variation along the polished indent. From Figure 1-27 below it can be seen that the average surface roughness is best (lowest) at the center of the indent, as the center of the contact has the peak contact pressure, causing maximum polishing action that zone, as the tool moves away from the center towards the periphery the surface roughness keeps worsening (increases) this observation is in line with prior studies carried out by Hu et al. [20].

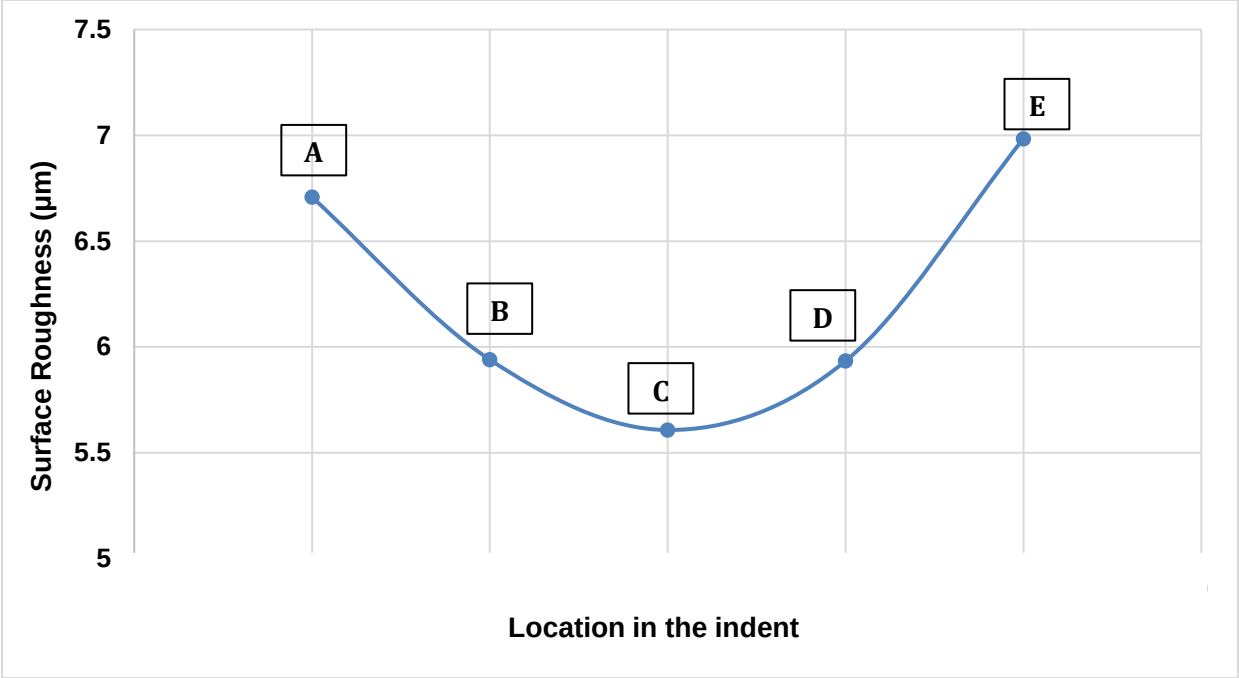

Figure 1-27: Plot depicting the variation of surface roughness variation along the indent.

Polishing Tool Influence with Abrasive Fluid

Next the experiment set was performed using the abrasive fluid, the rotating polishing tool was made to contact the polymer surface in the presence of an abrasive fluid, in the scope of this project the abrasive fluid used was Aluminum Oxide solution, which consisted of Al_2O_3 grains suspended in a deionized water medium, manufactured and supplied by Baikowski Inc.

When a polishing tool is made to rotate at a high RPM value, and is made to contact the surface, it tends to leave behind an indent at the point the contact was made, this region/indent is basically the footprint of the polishing tool which is unique to that tool, in technical terms this is referred to as the tool influence function of the polishing tool. The tool influence function can be of two types: Static tool influence and Dynamic tool influence function, where the static functions are basically allowing the tool to rotate at a given spot for time interval t. The tool influence function is also a way of measuring how much material is being removed by the polishing tool per unit time.

Figure 1-28 below shows the tool influence function (TIF) of a worn ball. The worn ball TIF tends to leave behind a set of significant ridges in the TIF. The deepest ridge measured was found to be 1 µm, as compared to the overall depth of the TIF which was measured to be 3 µm thereby the ridges were around 33% of the total depth of the profile of the TIF which is not acceptable, as

it means that the ridges are significant but unwanted. The case of tool influence function of a new ball (unused), there were still some ridges present but in this case the deepest ridge measured was around 0.08 µm, as compared to the overall depth of the TIF which was measured to be 1µm, thereby the ridges were 8% of the total depth, which can be neglected.

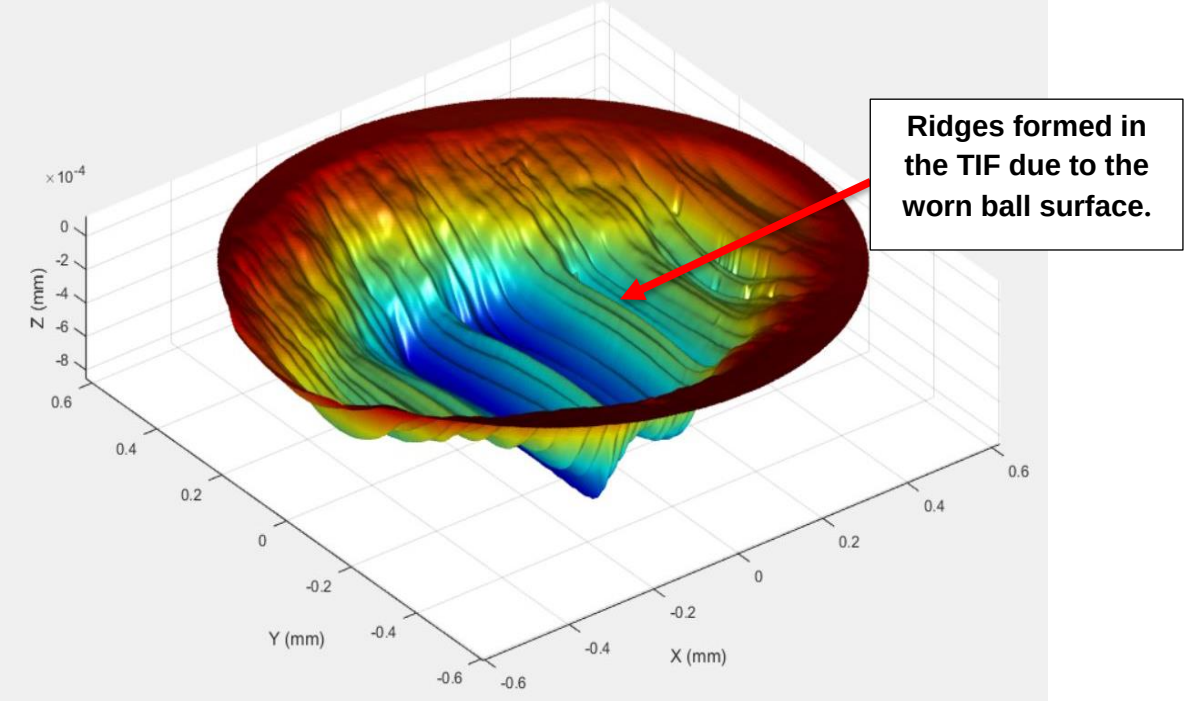

Figure 1-28: Tool influence function of a worn ball at 10 seconds dwell time.

The tool influence experiments were run for differing dwell times to measure the material removal rates, and to gauge the effect of dwell time of the polishing tools on the profile of the material removed. The experiment set was performed at selected time intervals of 5, 10, 15, 20 seconds. Table 1-3 below shows the parameter set selected for running the experiments.

Set	RPM	Load (N)	Abrasive Size (µm)	Ball Type	Dwell Time (s)
A	10000	1	0.05	Old	5
B	10000	1	0.05	Old	10
C	10000	1	0.05	Old	15
D	10000	1	0.05	Old	20

Table 1- 3: Table depicting the parameters levels for the dwell time TIF experiment set.

In the below Figure 1-29 it can be seen that, as the dwell time of the polishing tool increases, so does the depth of the TIF created. As the tool is allowed to stay at the spot for a larger duration the polishing action of the tool increases, meaning it removes more material at a higher time interval leading to deeper TIF profiles. This explanation matches the work done by Yamauchi et al. and Su et al. [18], [13] in their study of sub aperture polishing. This explanation is in line with the Preston's equation for material removal –

$$\Delta h = k_p * P * V_r * \Delta t \quad (1)$$

From the Preston's equation (1) above it can be inferred that the material removal is directly proportional to the contact pressure, relative velocity, and the dwell time.

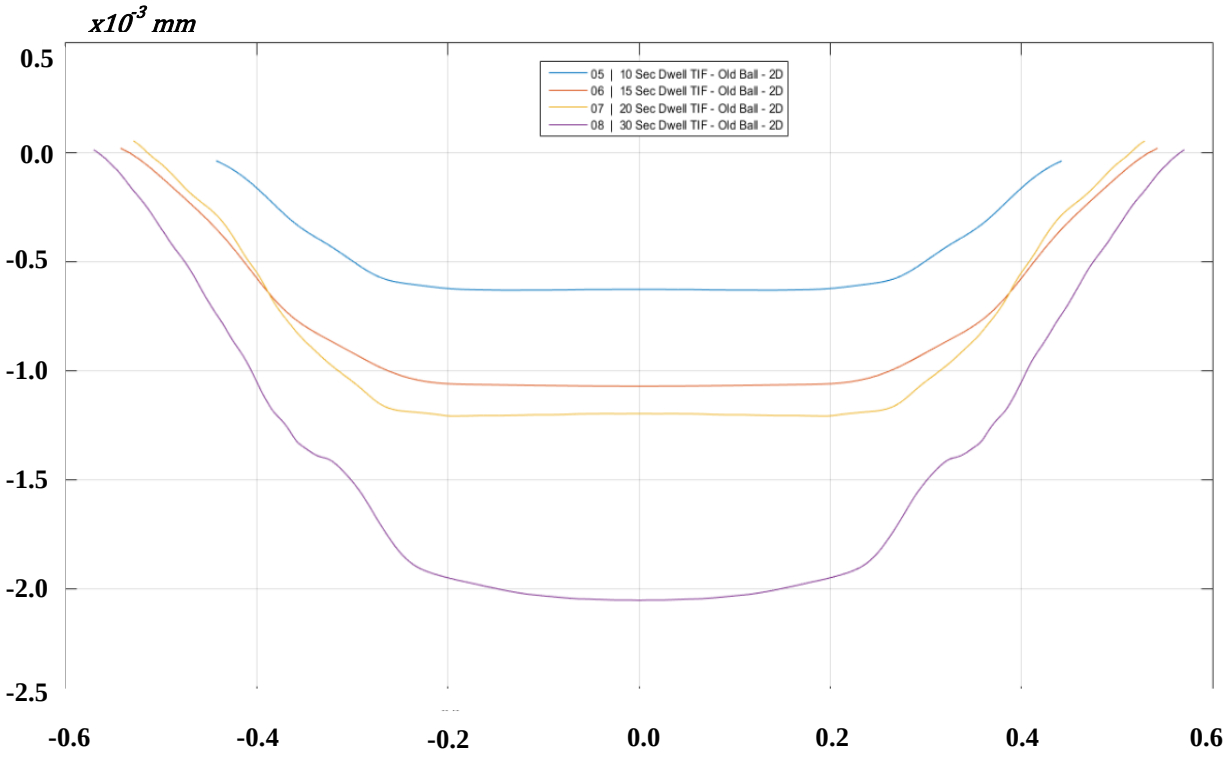

Figure 1-29: Averaged out 2D profiles of TIF of worn tool at varying dwell times showing the material removal variation.

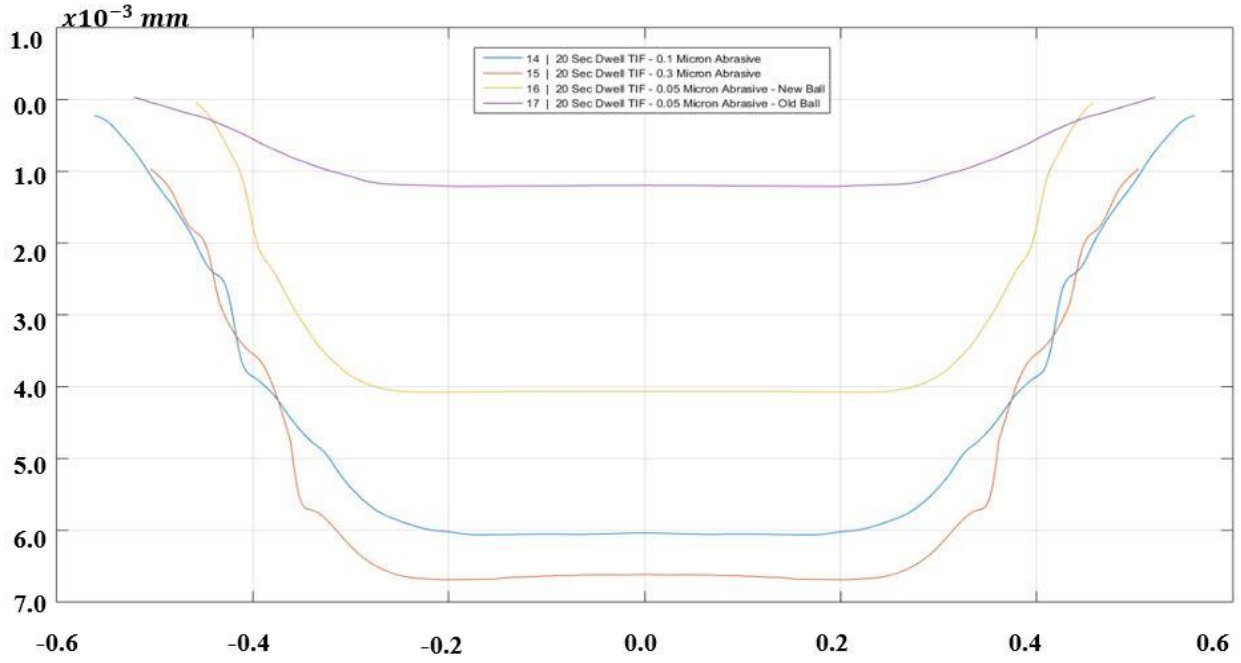

Figure 1-30: Averaged out 2D profiles of TIF of worn tool at varying abrasive sizes.

Figure 1-30 above shows the profiles of the TIF created using varying abrasive grain sizes, the abrasive grain sizes used were 0.05 µm, 0.1 µm, and 0.3 µm Al_2O_3 polishing abrasive fluids. It was observed that as the grain size of the abrasive increases the depth of the TIF profile increases and the contact patch grows wider.

Now there is a lot of contradicting literature that diverges into two theories, the first theory being that as the abrasive grain size increases it causes a decrease in the material removal rate, this was stated in the works done by Jianfeng et al., Bielmann et al., and Bhasin et al. [21], [22]. The theory behind that being, as the grains become bigger in size at a given abrasive fluid concentration the number of abrasive grains entering the contact zone reduces if the film thickness is smaller than the abrasive size, thereby reducing the removal rates. But in our case the film thickness is bigger than the abrasive size, so it doesn't hamper the particles from entering the contact zone during polishing.

The second theory states that as the abrasive grain size increases the material removal rates also increases. This was stated in the works done by Yongsong et al, Tamboli et al. and Lie et al. [23]–[25]. This is because of the fact in the case of larger abrasive particles the material removed per single grain of larger abrasive is more as compared to the material removed per single grain of smaller abrasive. This contradiction is due to the fact that the material removal mechanisms

vary greatly in sub aperture polishing process and depend on the materials being used as polishing tool and workpiece, the abrasive fluid being used and the abrasive grain type [26].
Next an experiment set was performed at the same dwell time levels of 5, 10, 15, 20 seconds but using a new polishing tool ball, to see the difference in the tool influence profiles between the worn tool and the new polishing tool. In the case of the new tool, it was observed that the TIF profiles generated were deeper as compared to the ones generated using a worn ball. This result was in line to what was seen in the studies carried out by Pan et al. [27]. This was attributed to the fact that due to continuous use of over 25 experimental runs the old polishing tool had undergone a reduction in size. When measured using a micrometer this reduction was found out to be of the order of 0.001 mm. Another aspect that is being postulated in this work is that due to undergoing multiple cycles of polishing runs, the surface of the polishing tool itself undergoes a reduction in the surface roughness value – smoothens out, and as the tool surface roughness directly relates to the fluid film thickness as proven by the works of Loewenthal et al. When the surface roughness of the tool increases the film thickness decreases, which in turn reduces the amount of abrasives entering the polishing region and thereby causing a lesser polishing action. This is evident from Figure 1-29, as one can notice that the TIF's of the new tool are much deeper as compared to the TIF's of the worn tool which were seen in Figure 1-31.

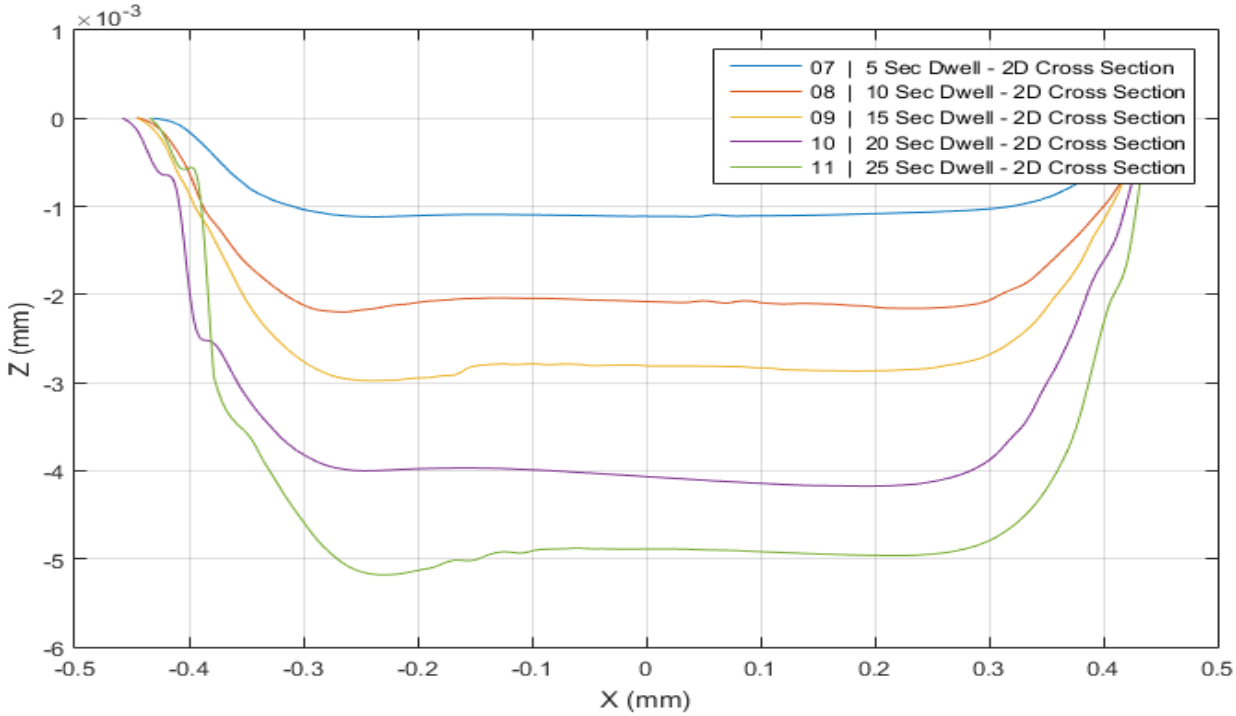

Figure 1-31: Image depicting the 2D profiles for the TIF of the new tool.

1.5.2 **Surface Roughness Improvement Experiments**

In the previous section a discussion was presented on the generation of the tool influence functions of the soft polishing tool and have analyzed how it is affected by the abrasive grain size, dwell time of the polishing tool, the presence of the abrasive fluid, and the effect of using a new tool over a worn tool, the next section would deal with the characterization of the input parameters, and the effect they have on the surface roughness of the polished surface. The input parameters selected for the study were the polishing tool RPM, feed rate, normal load, abrasive grain size, abrasive grain concentration, polishing tool offset (path overlap), polishing tool type.

The experiment sets were performed individually for each of the input parameters as a separate study. The materials studied in this experiment set were Polycarbonate (PC) and Polymethylmethacrylate (PMMA). The experiments were also duplicated on both the diamond turned surfaces and as manufactured surfaces. In order to maintain a standardized study, all experiments for the input parameters were performed utilizing the spiral toolpath to polish a 3 mm area on the polymer workpiece.

1.5.3 **Toolpath Planning for Surface Roughness Improvement**

In the process of sub-aperture polishing, toolpaths form an important part of the polishing strategy. The toolpaths decide which area is to be polished, how the area of polishing would be covered during the polishing process. The basic requirement for a polishing toolpath is to ensure a total coverage of the desired area of interest [28]. In the case of an automated polishing process, the trajectory of the toolpath is a vital factor affecting the quality and form of the surface being produced [29]. The toolpath strategy employed is integral to the process in the sense that it affects the amount of material removal in the polishing zone [28], and affect the surface finish attained. It helps to maintain a uniform material removal rate over the polishing area. This is achieved by making sure that the toolpath uniformly covers the polishing region and is well distributed, also the direction of the toolpath lines should be balanced throughout the surface in order to achieve a uniform material removal rate [29]. Also the polishing toolpath strategy should be devised such that it provides a multidirectional coverage of the surface, as it ensures that majority of the asperities are processed by the polishing grains [30]. Each of the toolpath strategy have their own sets of advantages and disadvantages associated with them, and some of them are utilized in specific applications.

The toolpath strategies that are studied in this project are the unidirectional raster, bidirectional raster, cross hatching scan, spiral scan, and special space covering fractal toolpaths like the Hilbert's fractal toolpath strategies. All the toolpaths are studied and compared at a constant stepover or offset distance. A finer step or offset size would lead to a more uniform polishing of the surface, as the toolpath passes will start blending or overlapping with the adjacent passes/grooves, although a finer offset value would increase the overall toolpath length and polishing time, but the area coverage would be the same irrespective of the offset value. Using a

finer offset size would lead to denser toolpath, which provides a surface with lower peak to valley values over the polished surface as was found in the works of Hon-Yuen Tam et al. [28].

A regular toolpath like spiral and raster toolpath tend to leave behind a repetitive tool signature on the polished surface when used over a large cycle time, or when utilized over a large number of polishing passes which is a direct result of the imposition of the Gaussian tool influence functions as the tool passes over the same tracks repeatedly as in the case of a spiral or a raster toolpath [31]. This effect was also observed in few of the experiment sets where the spiral toolpath was utilized at a high number of polishing passes as seen below in Figure 1-32. Such signatures can cause unwanted diffraction effects in critical applications [31].

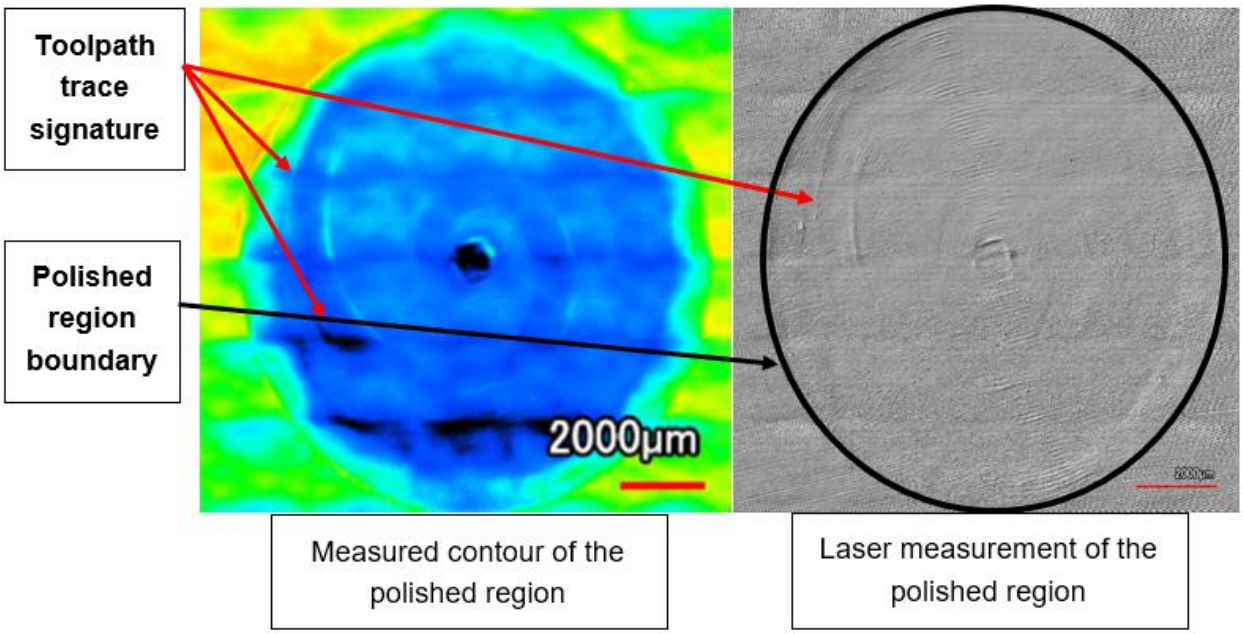

Figure 1-32: Image showing the trace signature of the toolpath in the case of using a spiral toolpath for multiple polishing passes.

In the case of the space filling fractal toolpaths, which are paths that cover the entire area of interest by the means of non-intersecting lines. Hilbert fractal toolpaths were studied for the scope of this project. It has been also been noted that the use of Hilbert and Peano polishing strategies is better than conventional raster toolpaths as these toolpaths maintains a balanced direction over the surface as compared to the usual raster scan strategies which usually go back and forth over the area of interest [32]. The Hilbert's toolpath is a result of extrapolation of a repeating unit over the entire polishing area of interest, this is explained in Figure 1-33 below, where the repeating unit shape is the same.

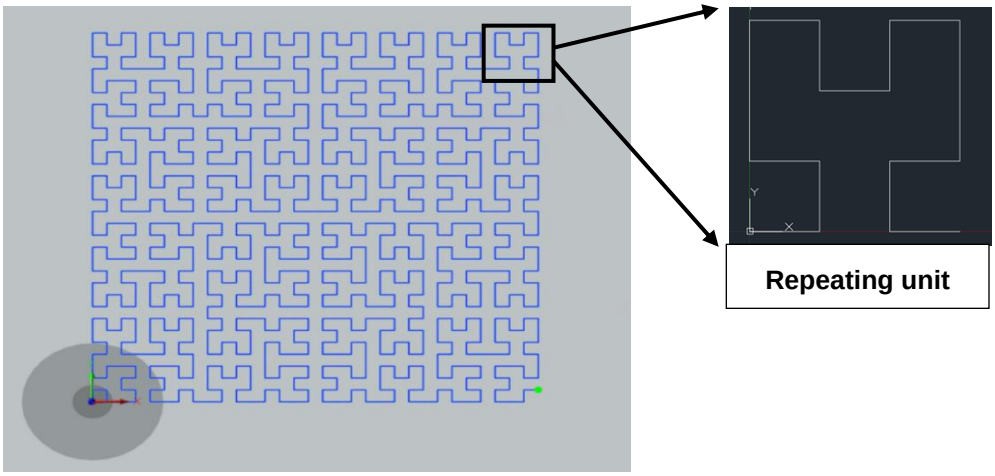

Figure 1-33: Image showing the Hilbert's toolpath and the repeating unit.

The Hilbert's toolpath density can be modified as shown in Figure 1-34 depending on the magnitude of polishing action which is needed during the polishing run. A higher density toolpath would tend to cover a specific region on the workpiece a larger number of times thereby causing an increased polishing action.

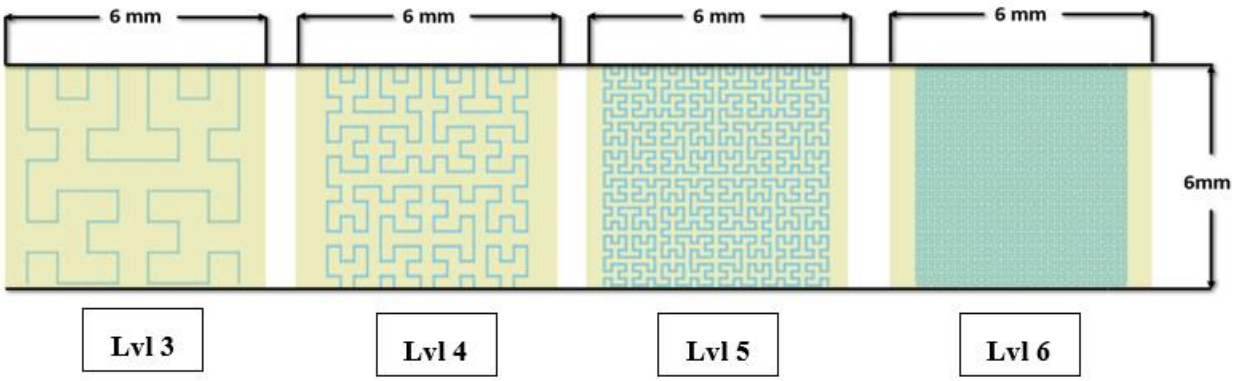

Figure 1-34: Image showing Hilbert's toolpath at various toolpath density levels.

The levels of the Hilbert's toolpath are directly related to how dense the toolpath is, as is seen in Figure 1-34 above, a level 3 iteration of Hilbert's is very sparse as compared to a level 6 Hilbert's which is very dense – both being spread over the same area measuring 6x6 mm. In the subsequent experimental runs for surface roughness improvement the spiral toolpath has been utilized extensively, specific experiments have also been carried out using the linear raster toolpath and Hilbert's toolpath strategy.

1.5.4 **Effect of RPM on the Surface Roughness**

It can be seen in Figure 1-35 that for a diamond turned surface, as the RPM increases, the surface roughness starts improving. The best finish recorded was 6.6 nm for Polycarbonate (PC) down from the initial roughness value of 45 nm, and 4.733 nm for Polymethylmethacrylate (PMMA) down from the initial roughness value of 25 nm. The inverse proportionality which was seen in the case of both PC and PMMA could be attributed to the fact that, as the RPM of the polishing tool increases, it causes the increase the relative surface velocity of the polishing system, and as the relative surface velocity increases, the number and frequency of particles entering the polishing zone increases and hence the polishing action increases and a better surface finish is obtained, this result is in line with the study done by Singh et al. [33].

At high rotational velocities, the fluid film thickness increases [17], as the fluid film thickness increases the conjunction region where the polishing also increases, leading to larger zone where the abrasive grains can enter easily, as a result the better surface finishes are achieved. Another phenomenon that allows to achieve better surface finished at higher RPM's is the friability and evolution of abrasive grains during polishing. Cumbo et al. [34] in their work discussed the evolution of abrasive grains during polishing, the alumina abrasive grains are friable in nature which leads to the grains breaking into smaller particles and achieving finer cuts on the surface, on account of which a better surface finish is achieved. It was also observed in the experiment that as the RPM keeps on increasing, the surface finish peaks and then starts to deteriorate, which can be attributed to the fact that at very high RPM values, there is a tendency of the polishing fluid to spill and spray away from the contact, leading to a possible naked contact of the polishing tool on the workpiece surface leading to a worse surface finish.

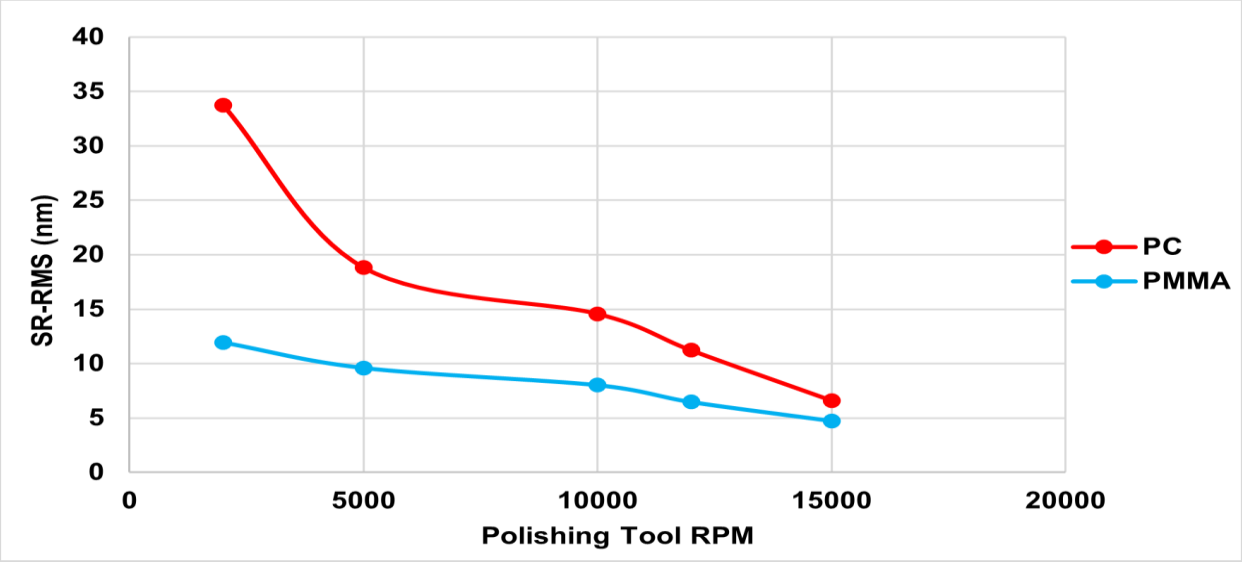

Figure 1-35: Plot depicting the surface roughness variation with the polishing tool RPM for a diamond turned surface.

Figure 1-36 below shows the trend of the surface roughness improvement as the polishing tool RPM is increased on an already smooth surface. It can be seen that the result contradicts the trend that was seen in the case of polishing diamond turned surfaces. This can be explained as – as manufactured surface is already smooth and doesn't have distinct peaks and valleys as observed on a diamond turned surface, so when the polishing tool rotates on a smooth surface, the abrasive grains actual start attacking the smooth surface, and instead of improving it, start worsening it, leading to an increased surface roughness.

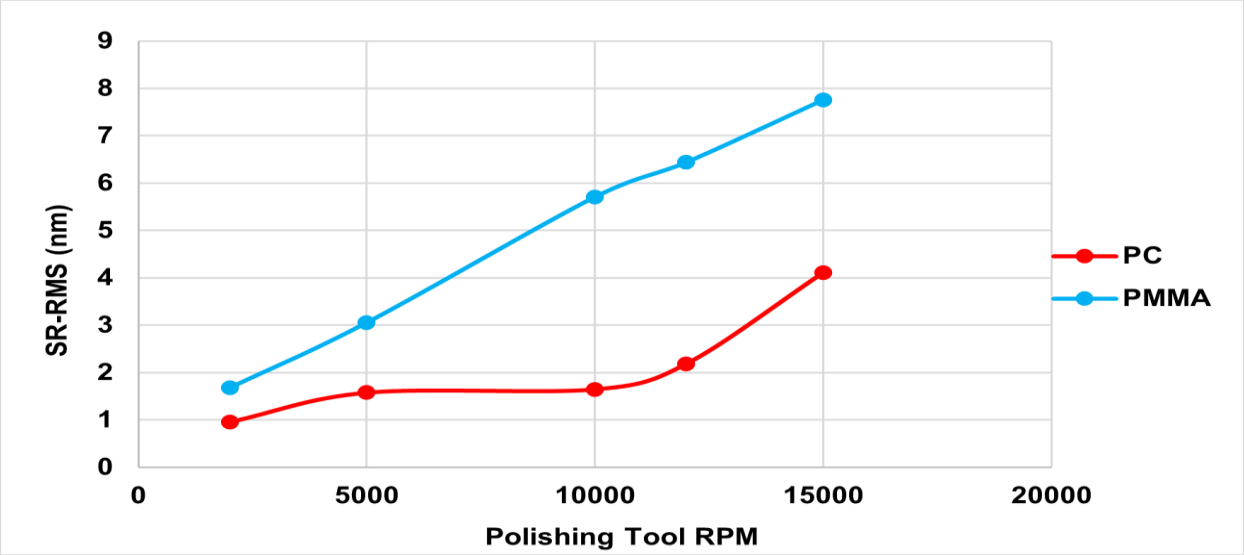

Figure 1-36: Plot depicting the surface roughness variation with the polishing tool RPM for as manufactured surface.

The diamond turned surface has peaks and valleys at constant frequencies, it can be observed from Figure 1-37 that as the polishing tool RPM is gradually increased the peaks on the surface start getting shaved off by the abrasive grains, at the low level of 2000 RPM almost no effect is seen on the peaks on the surface as observed, but as the RPM is increase to 15000, there is a major change as the peaks get almost shaved off and start blending into the flat surface as observed in Figure 1-37.

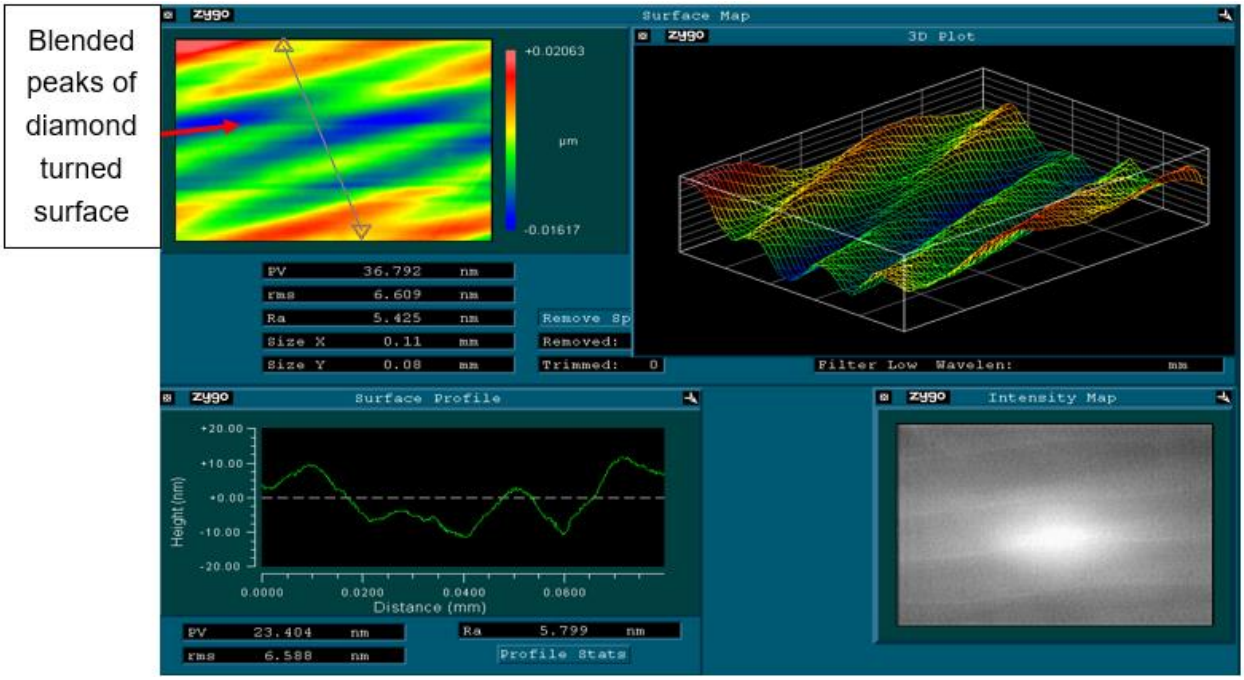

Figure 1-37: Image depicting the surface roughness measurement of the polycarbonate (PC) at 15000 rpm level of polishing.

1.5.5 **Effect of Normal Load on the Surface Roughness**

The normal load was varied from a minimum level of 0.25N all the way up to a maximum level of 1.5N. The abrasive fluid used was an Alumina based polishing suspension. The grain size of the abrasive used was 0.05 µm. There is an inverse proportionality which exists between the normal load and the surface roughness as it can be seen in Figure 1-38, it can be explained as, when the normal loading is increased, the contact pressure increases, this leads to a higher material removal rate as dictated by the Preston's equation, which states that the material removal rate is directly proportional to the normal load applied. In the study done on material removal model in polishing by Jiunyulai et al, microcutting due to abrasive particles occurs in process of polishing, In the work it was theorized that the surface roughness is directly proportional to the depth of the groove cut by the particles, this would relate to the fact that a deeper groove would have a superior finish at the groove center. Now the as the normal load applied increases the material removal rate goes up, and which leads to deeper grooves, and a better surface finish, which is what was observed in the experiment set.

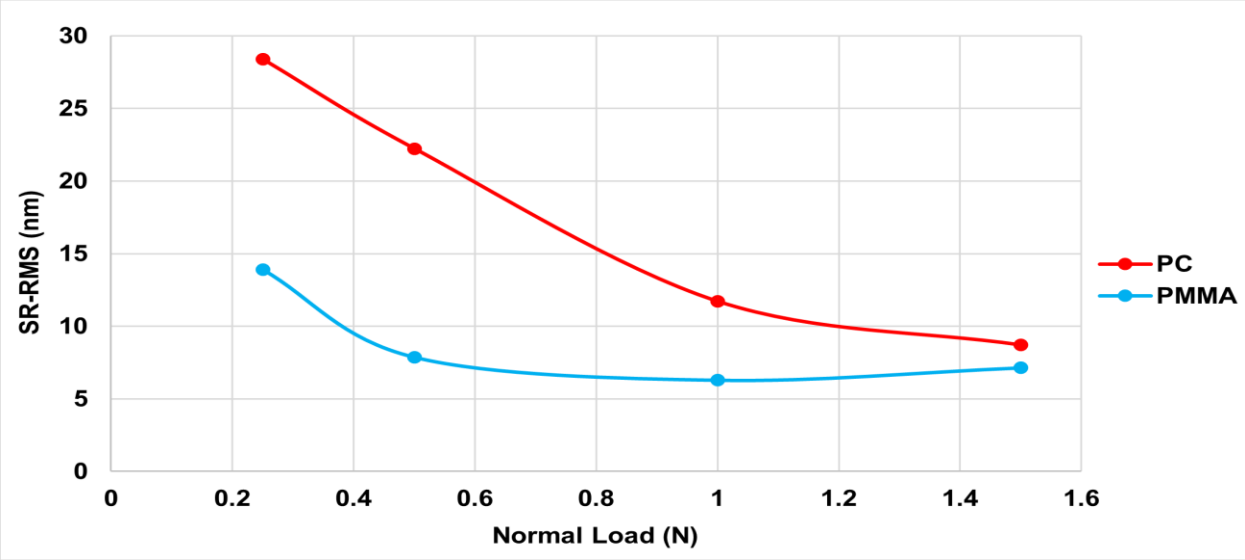

Figure 1-38: Plot depicting the surface roughness variation with the normal load for a diamond turned surface.

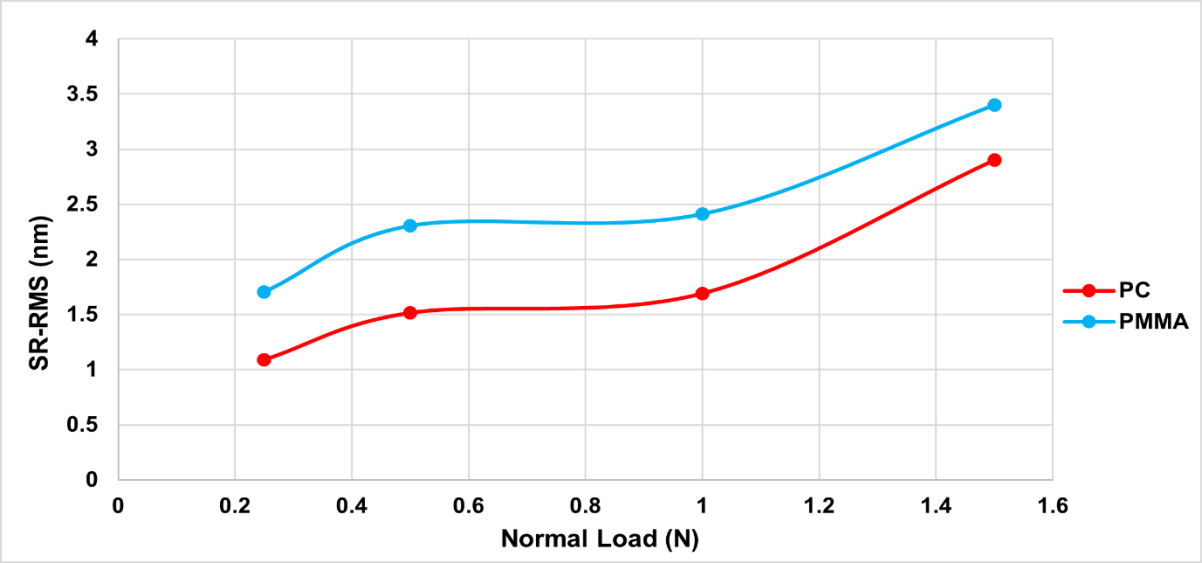

Figure 1-39: Plot depicting the surface roughness variation with the normal load for an as manufactured surface.

1.5.6 **Effect of Feed Rate on the Surface Roughness**

The feed rate was varied from a minimum level of 50 mm/min all the way up to a maximum level of 500 mm/min, the feed rate was capped at 500 mm/min, as above this value the polishing action reduces a lot, and in order to get measurable result, the number of passes would have to be

increased to get a region which is polished and can be measured. The abrasive fluid used was an Alumina based polishing suspension. The grain size of the abrasive used was 0.05 μm. It was seen from Figure 1-40, for a diamond turned surface, as the feed rate decreases the surface roughness starts improving. The best finish recorded was 4.661 nm for Polycarbonate (PC) down from the initial roughness value of 45 nm, and 3.558 nm for Polymethylmethacrylate (PMMA) down from the initial roughness value of 25 nm.

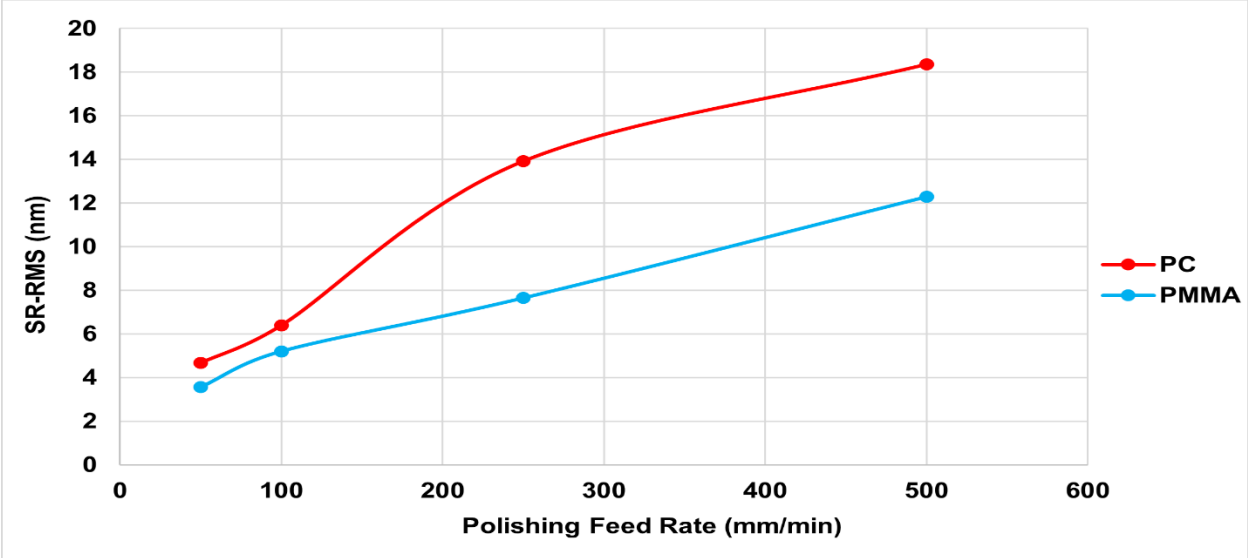

Figure 1-40: Plot depicting the surface roughness variation with the feed rate for a diamond turned surface.

The direct proportionality which was seen in the case of both PC and PMMA could be attributed to the fact the relative velocity is an influencing parameter in the Preston's equation, and is directly proportional to the material removed. The Preston's equation has a term for relative velocity in a polishing system –

$$\frac{\Delta h}{\Delta t} = K_p * P * V_r \quad (2)$$

The equation (2) can be rearranged to include the feed rate velocity as follows [35] –

$$\frac{\Delta h}{\Delta t} = K_p * P * \frac{(V_f + V_{rot})}{V_f} \quad (3)$$

Where V_f is the feed rate velocity, V_{rot} is the polishing tool rotational velocity and P is the contact pressure, and K_p is the Preston's coefficient.

From the equation (3) above it can be seen that the feed rate velocity is directly proportional to the material removal, now as the feed rate velocity is increased the material removed is increased,

this would lead to the diamond turned peaks on the surface to be removed and sheared off at a faster rate, this is the logical reasoning, but this reasoning contradicts the results that were obtained in the experiment. The results show that as the feed rate is increased, it reduces the dwell time per abrasive particle in the polishing zone, as its obvious that as the feed rate is increased, the relative velocity goes up, this means that the polishing abrasive grains are not allowed enough time to carry out the localized polishing in the area that specific grain covers, hence the surface isn't improved at higher feed rates. This result is in line with those obtained in the work performed by Tong et al. [36], the technical terminology for this phenomenon is termed as undercutting [35], or in scope of this project it can be referred to as under polishing. It is important to note that as you reduce the feed rate substantially, it could lead to overcutting, as the number of abrasive grains entering the polishing zone increase, this could possibly lead to the indentation of workpiece.

In Figure 1-41 below it depicts the result of the experiment on an already smooth surface, it can be seen that the result contradicts the trend that was observed in the case of polishing diamond turned surfaces. This can be explained as – as manufactured surface is already smooth and doesn't have distinct peaks and valleys as observed on a diamond turned surface, so when the feed rate is increased on a smooth surface the abrasive grains do not get enough time to actually polish the surface (under polishing) and normally in case of rough surfaces or like the diamond turn surfaces which have distinct peaks on the surface, this would lead to not enough polishing and surface roughness is not improved by a lot. But in the case of smooth as manufactured surfaces, this scenario of under polishing is advantageous, as at higher feed rates the abrasive grains don't get enough dwell time to worsen the surface. Hence when the feed rate is low in the case of smooth surface it results in the surface actually worsening and leading to high surface roughness values.

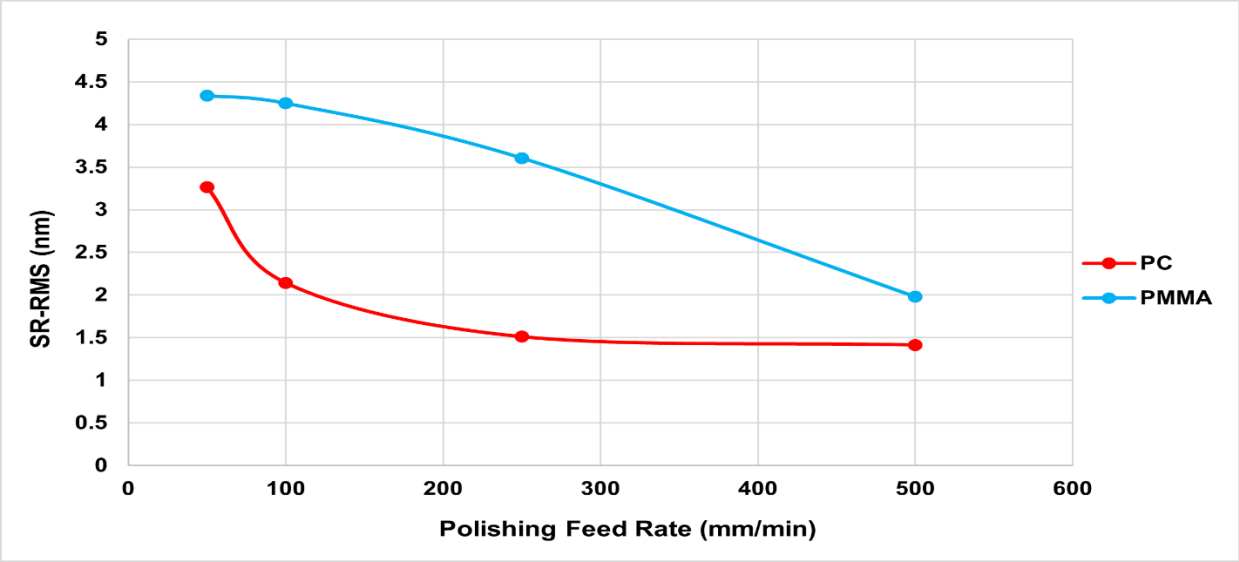

Figure 1-41: Plot depicting the surface roughness variation with the feed rate for an as manufactured surface.

In the Fig 1-42 below shows the measurement of the polished diamond turned surface for 50 mm/min feed rate. It can be seen that the peaks of the diamond turned surface are sheared off due to the polishing action as seen in the figure below.

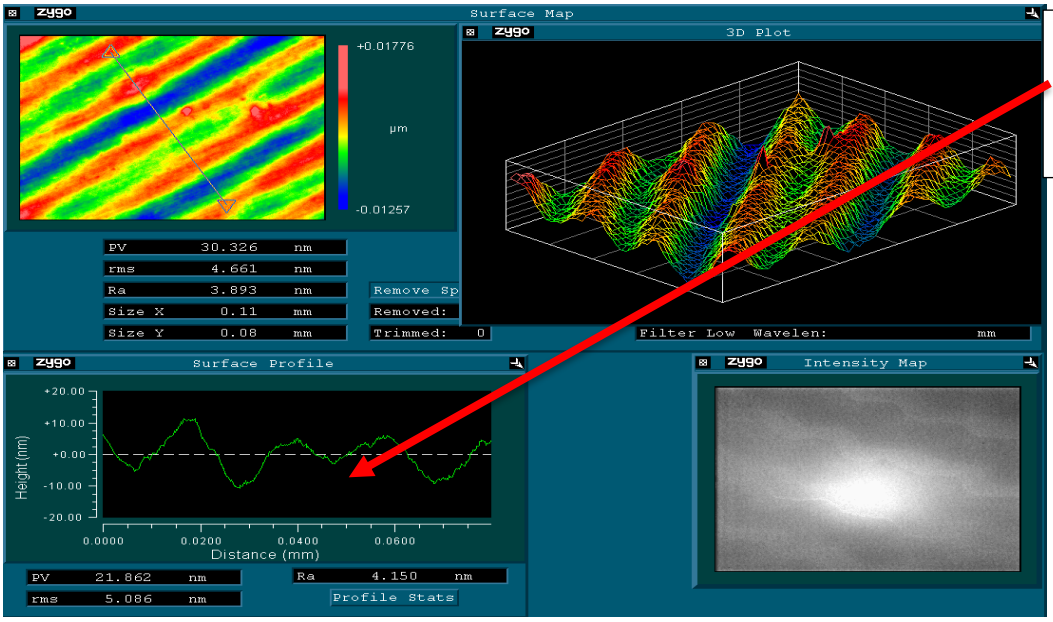

Figure 1-42: Image depicting the surface roughness measurement of the polycarbonate (PC) at 50 mm/min feed level of polishing.

1.5.7 **Effect of the Offset on the Surface Roughness**

The offset distance was varied from a minimum level of 0.01 mm all the way up to a maximum level of 0.3 mm. The offset distance was lower bound at 0.01mm as going below this would lead to an increase in polishing times by a lot and would also lead to over polishing, and the offset distance was capped at 0.3 mm as above this value the polishing action reduces a lot, and there would a few patches unpolished in the polishing region. The abrasive fluid used was an Alumina based polishing suspension. The grain size of the abrasive used was 0.05 µm. It can be seen from Figure 1-43 that for a diamond turned surface, as the offset distance is increased the surface roughness worsens. The best finish recorded was 1.805 nm for Polycarbonate (PC) down from the initial roughness value of 45 nm, and 1.95 nm for Polymethylmethacrylate (PMMA) down from the initial roughness value of 25 nm.

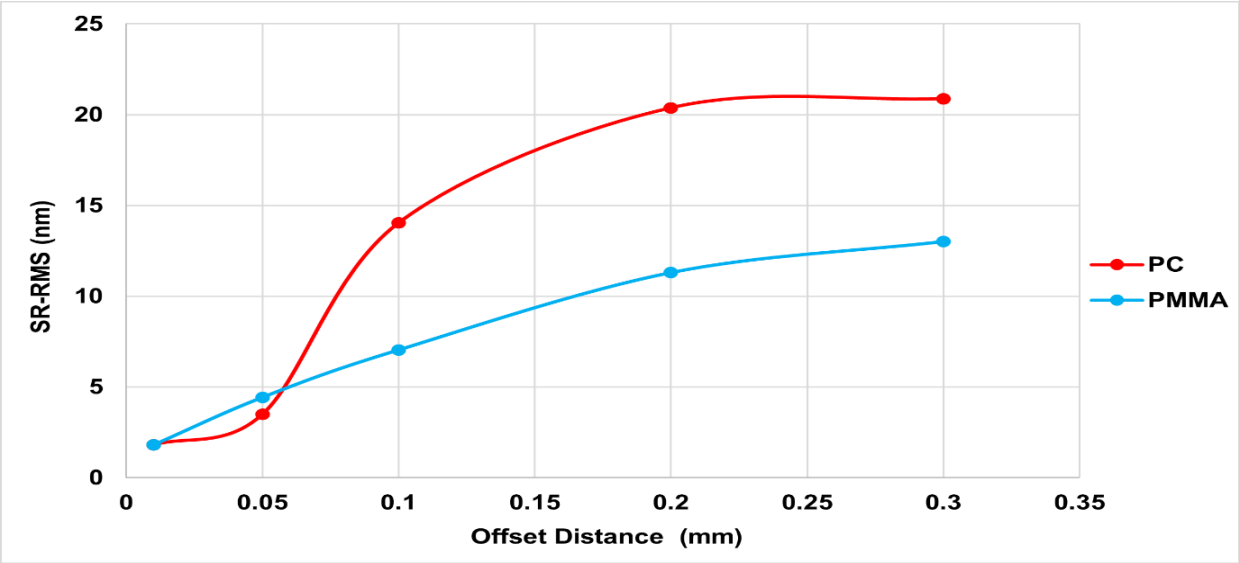

Figure 1-43: Plot depicting surface roughness variation with offset distance for a diamond turned surface.

It can be observed from Figure 1-43 above that as the offset distance is reduced, the surface roughness values decrease, and consequently when the offset distance is increased the surface roughness keeps on increasing. There is a sudden jump in the surface roughness in the case of Polycarbonate as the offset value was increased from 0.05 mm to 0.1 mm, this could be a result of the fact that at 0.5 mm there might be some region which was under polished during the process leading to an unusually higher roughness value, but this can be brushed aside as an anomaly.

When the polishing is done using a low offset value, this would result in the adjacent toolpath passes overlapping with each other, and this would in turn cause an increased polishing action in zone where the toolpath passes are overlapping and leading to the surface roughness reduction, because the polishing tool crosses the same area again and again. When higher offset values

are used, it would mean the toolpath are further spaced out from each other, meaning the overlaps between the adjacent polishing tool passes is lower leading to higher surface roughness values. Also, there always a cause of concern that using very high offset values could result in some patches in the area of interest to be unpolished. Figure 1-45 below depicts the polished surface measurement at 0.01 mm (low offset), and it can be seen that at lower offset values the peaks are sheared off and are completely blended into the surface and smoothened.

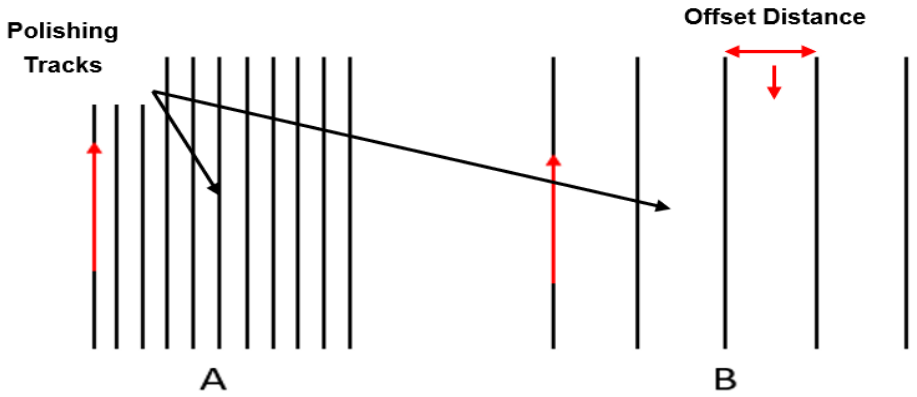

Figure 1-44: Image depicting the offset distance explanation A) depicting a low offset distance and B) depicting the higher offset.

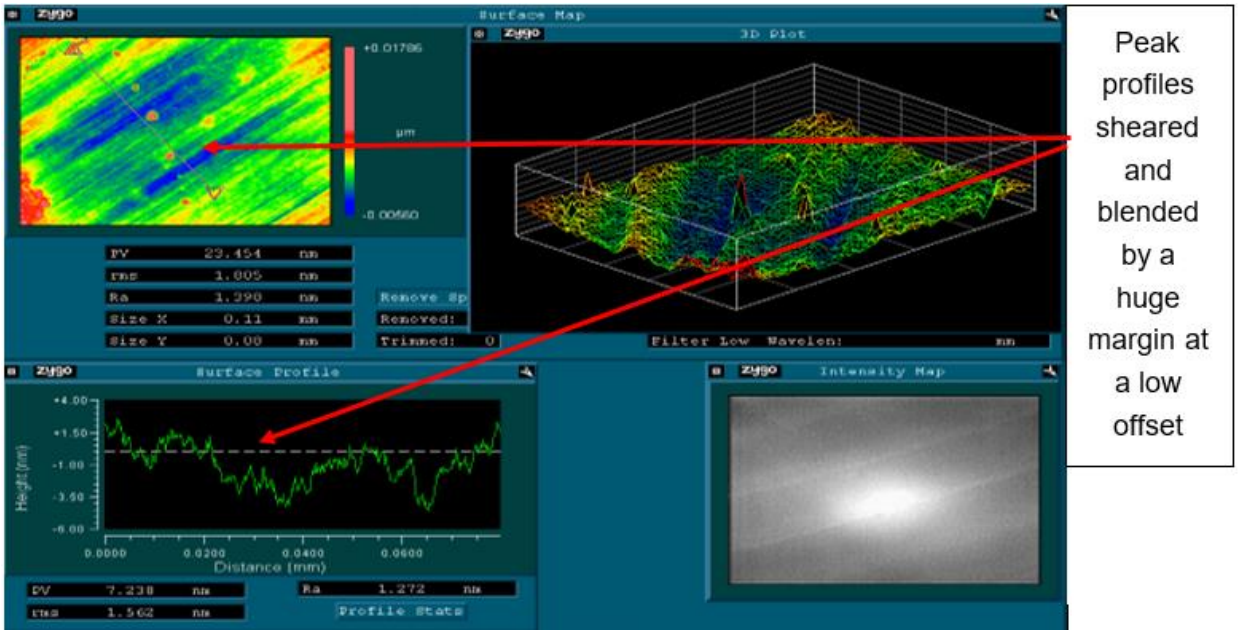

Figure 1-45: Image depicting the surface roughness measurement of the polycarbonate (PC) at 0.01 mm offset level of polishing.

1.5.8 **Effect of Number of Passes on Surface Roughness**

The number of passes was varied from a minimum level of 1 pass all the way up to a maximum level of 15 passes, the number of passes capped at 15 passes, as above this value the polishing action increases a lot, and as the number of polishing passes increase, the overall cycle time for the process increases by a huge margin. The abrasive fluid used was an Alumina based polishing suspension. The grain size of the abrasive used was 0.05 µm.

It was seen from Figure 1-46 that for a diamond turned surface, as the number of polishing passes increase, the surface roughness starts improving. The best finish recorded was 1.148 nm for PC using a raster toolpath, and 5.78 nm using a spiral toolpath down from 45 nm initial surface roughness finish. The best finish recorded was 1.027 nm for PMMA using raster toolpath, and 3.987 nm using a spiral toolpath.

The number of polishing passes dictate how many times the polishing tool will cross a given area and carry out the polishing action, higher the number of time the tool passes over a region, higher would be the polishing action, and better would be the surface finish, as the effectively the increase in the number of passes increases the overall dwell time the polishing tool get in a region, and as this effective dwell time increases, the material removal rates increase as per the Preston criteria. At a higher material removal rate the peaks of the diamond turned surface would be sheared off much easily and at a faster rate thereby improving the surface finish and smoothening capabilities of a polishing system. From Figure 1-46 it can be observed that major change in the surface roughness occurred when the number of passes were increased from 0 to 3 passes, the roughness dropped from 45 nm RMS finish to around 2.5 nm RMS finish in the case of Polycarbonate and using a Raster toolpath, which gave us a surface improvement percentage of 94%. After the 3rd pass the surface roughness still improves a bit, but the magnitude of improvement is greatly reduced, and is almost constant. This phenomenon occurs because of the fact that when we begin with the polishing process, the surface has distinct peaks and valleys from the diamond turning, so there is a lot of opportunity for the polishing tool and the abrasive grains to attack these high points, and shear them off, as the polishing passes continue the peaks continue to get sheared off, and consequently in the end almost get blended into the flat surface, this instance from the point where the peaks were at their maximum amplitude, to the point where they get blended into the surface, gives us the maximum surface improvement percentage. Once the peaks are almost sheared off and blended, there are no distinct high points which the tool can polish down to the surface level, hence after about 3-4 passes the change in the surface roughness is almost negligible.

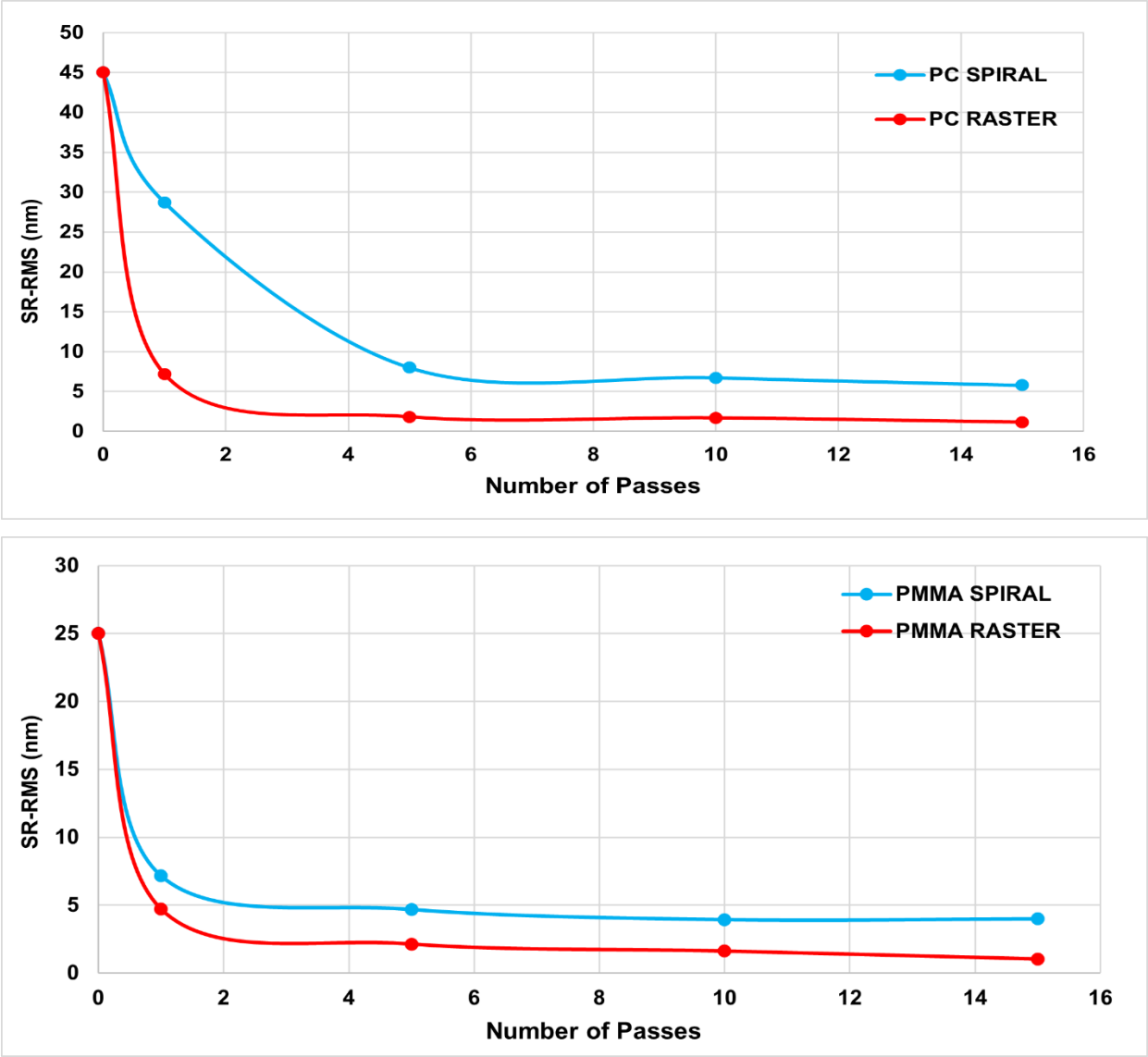

Figure 1-46: Plot depicting the surface roughness variation of PC and PMMA with number of passes for a diamond turned surface.

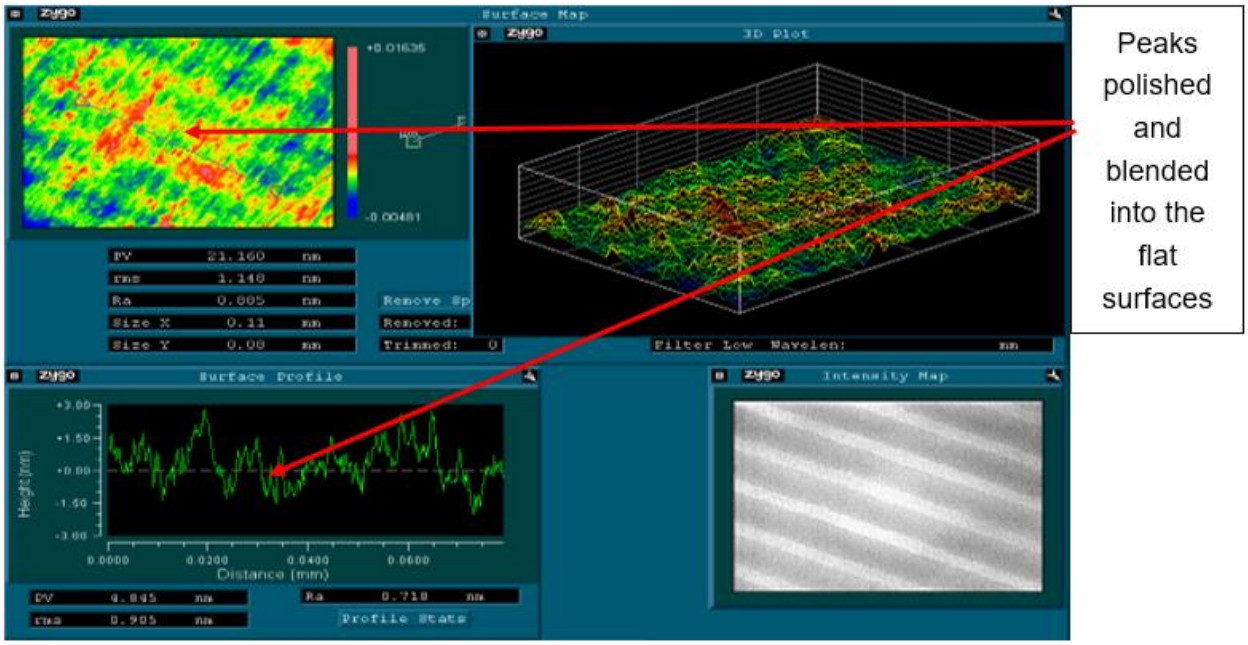

Figure 1-47: Image depicting the surface roughness measurement of the polycarbonate (PC) at 15 passes of polishing.

1.5.9 **Effect of the Abrasive Grain Size on Surface Roughness**

The abrasive suspension was supplied by Baikowski Inc. The abrasive grain size was varied from a minimum level of 0.01 μm all the way up to a maximum level of 0.3 μm. Figure 1-48 depicts the variation of the surface roughness variation along with the abrasive grain size.

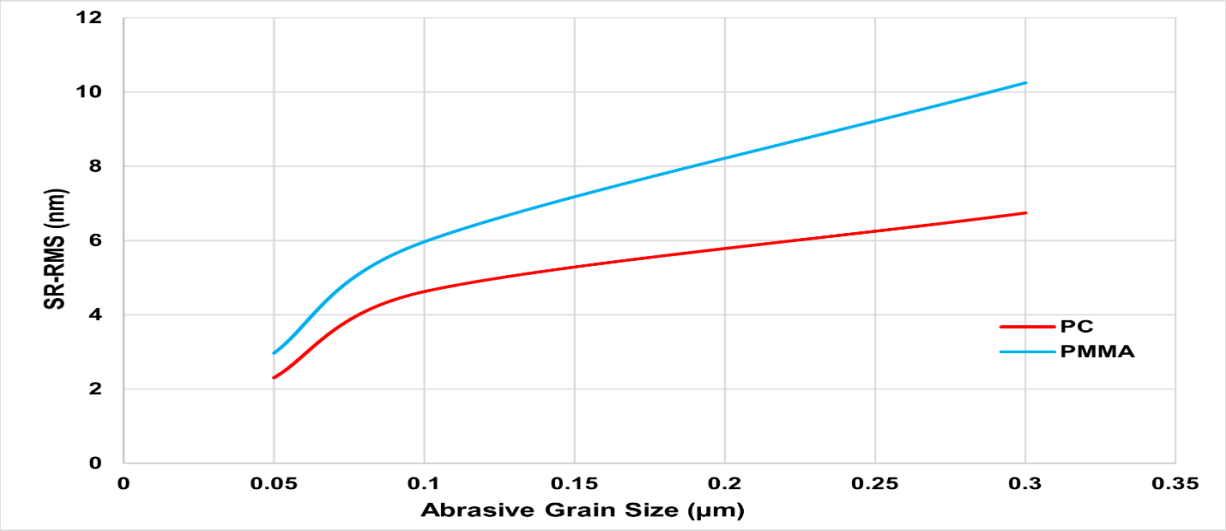

Figure 1-48: Plot depicting the surface roughness variation of PMMA with abrasive grain size for a diamond turned surface.

It can be observed that as the abrasive grain size decreases the surface roughness improves. The abrasive grain size dictates the number of the active abrasive grain in the given volume of the abrasive fluid, a smaller grain size abrasive will have a larger number of grains in a given fluid volume, at a given instantaneous time as hypothesized by Singh et al. Now under a given normal load and RPM, if we consider an amount of polishing fluid V, the smaller grain cause finer cuts on the surface, leading to low surface roughness values, and a better surface finish [33]. It can also be said that when smaller abrasive grains are used the effective surface area available for the chemical reaction between the slurry and the polymer workpiece surface increases, note that this will only be the case when the slurry used has either a basic or acidic pH value – in this project a neutral slurry [37] was used so as to focus only on the mechanical aspect of the polishing. This trend of the surface roughness increase along with the increase in the abrasive grain size was also previously documented in the works done by Yongsong et al. [23].

1.5.10 Surface Form Generation Experiments

The sub aperture polishing process can also be utilized to create specific surface forms and profiles. This can be done by using specific polishing toolpath strategies to create specific shapes like a concave or a concave surface can be generated by utilizing a spiral toolpath, and a raster toolpath or a Hilbert's fractal toolpath can be used to create flat surfaces with exceptional surface finish. Another way of generating a surface profile could be using the dwell time approach, wherein the shape is created by controlling how much time the polishing tool spends at a discrete point on the surface.

1.5.11 Toolpath Strategy

In the toolpath approach the tool will simply follow the profile shape to be generated, the material removal rate would be controlled by varying z – levels in accordance with the shape to be polished. Suppose if the shape to be polished is a concave shape, the z – level would have the maximum depth/ or maximum sag in the center of the concave shape, below the origin plane, this would result in the polishing tool being pushed down, as the tool is pushed down it will lead to the flattening of the soft tool, leading to a wider contact patch and a higher contact pressure leading to a higher material removal rate, which will create a deeper feature section. On the other hand, if say a convex shape needs to be polished onto a flat surface the maximum sag or the maximum depth would again be in the center of the profile but in this case above the origin plane, this would mean pulling up the tool to reduce the contact pressure and contact patch so that the material removal rate is reduced. Using this logic different toolpath strategies were used to create some basic shapes which are explained in the following section.

1.5.12 Hilbert's Fractal Toolpath Experiment

Hilbert fractal toolpath was utilized at different toolpath densities to run an experiment set to polish the diamond turned Polycarbonate surface in order to improve the surface. The area of interest was polished 3 times in a continual manner. It was observed that the polished surface didn't show a major change in the shape before and after being polished in terms of presence of major curvature, instead as expected this toolpath strategy resulted in the generation of a flat surface, in layman's terms the polished surface was observed to be pushed down from the original height uniformly throughout the polished region. Exceptional surface finish was observed in this case, with the polished surface measuring 0.823 nm RMS surface finish and had a PV value of 8.02 nm, down from the initial surface roughness of 45 nm RMS surface finish, which is an improvement of around 98% in terms of surface finish. The volume of material removed is 0.077 mm^3 for the case of level 6 Hilbert's path densities and goes down to 0.00861 mm^3 for the case of level 4 Hilbert's path density. At a higher path densities, the features produced are deeper and smoother. It can also be observed that the features produced using Hilbert's toolpath are smooth and flat with the best peak to valley achieved measuring 8.02 nm.

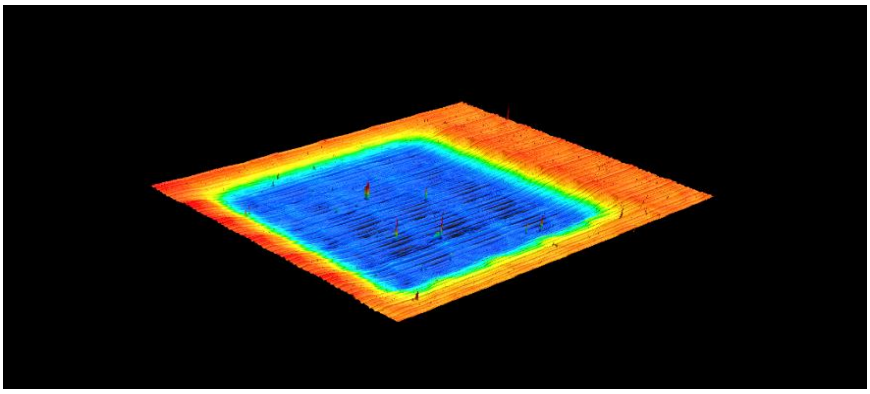

Figure 1-49: Image showing measurement of surface polished using Lvl 6 Hilbert path.

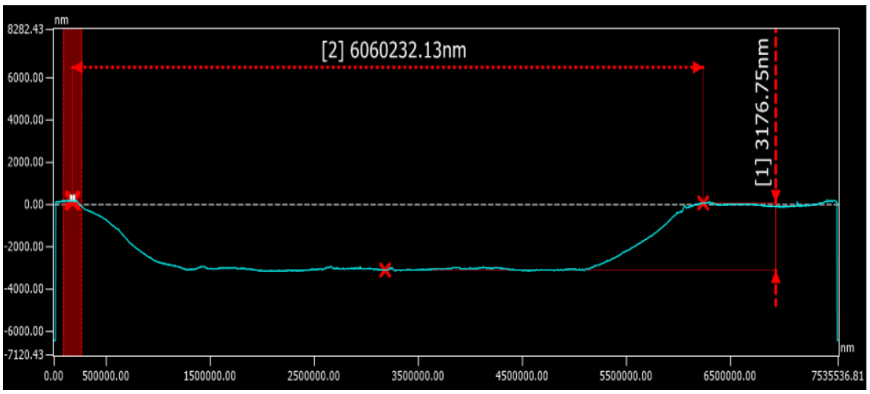

Figure 1-50: Image showing 2D cross section of the surface polished using Level 6 Hilbert.

1.5.13 Linear Raster Toolpath Experiment

Another polishing experiment set was also carried out using the linear raster toolpath. The area of polishing was a 3mm x 3mm square, and the area was polished 15 times in a continual manner. It was observed that the polished surface didn't show a major change in the shape before and after being polished in terms of presence of major curvature, instead as expected this toolpath strategy resulted in the generation of a flat surface. This profile is what was achieved even when the Hilbert's toolpath was utilized to carry out the polishing.

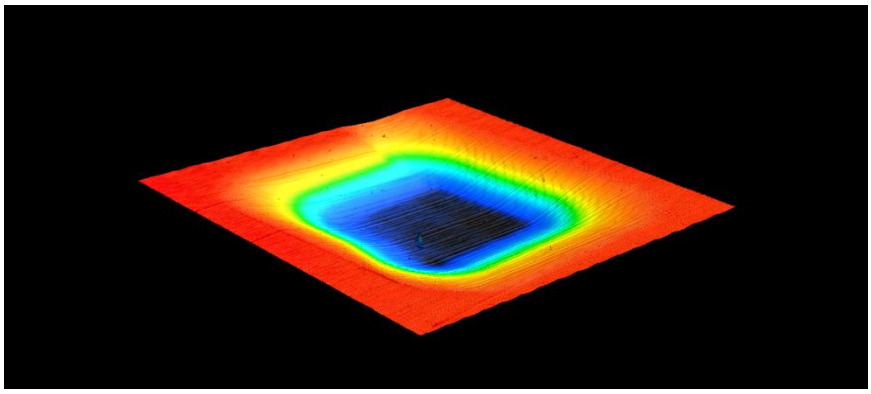

Figure 1-51: Image showing the measurement of surface polished using a raster toolpath.

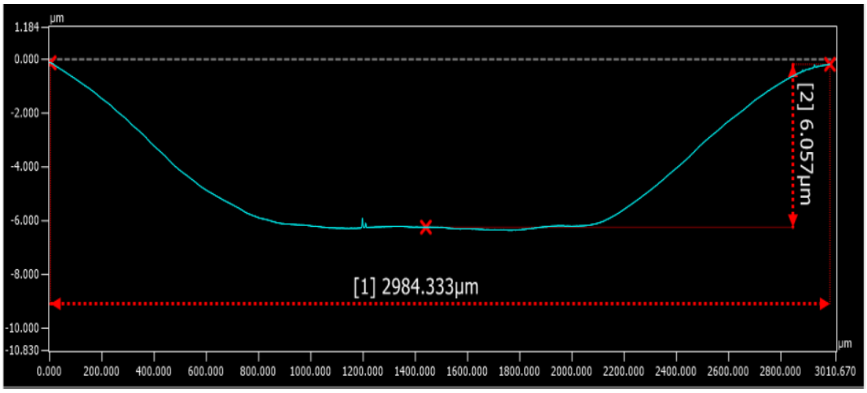

Figure 1-52: Image showing 2D cross section of surface polished using raster toolpath.

The designed shape of the profile for the linear raster strategy was a 3x3 mm square patch, which was supposed to have a depth of 15 µm. In the measured result it was observed that the depth of the polished surface achieved was around 6 µm after 15 polishing passes, which gives us a removal of around 0.4 µm depth per polishing pass. There was a difference of 9 µm in the expected depth and the polished depth. The volume of material removed during the polishing process was 0.03 mm^3 after 15 polishing passes, this volume removed is lesser than the volume removed when using Hilbert's toolpath which was 0.07 mm^3 after 3 polishing passes. The reason for this difference in the volumes removed could be attributed to the fact that the Hilbert's toolpath, has a very dense toolpath distribution over the same area as compared to a raster toolpath, leading to more material removal in lesser number of polishing passes. The surface finish of the polished surface measured 12 nm RMS surface finish and had a PV value of 22 nm, down from the initial surface roughness of 45 nm RMS surface finish, which is an improvement of around 73% in terms of surface finish. It can also be observed in Figure 1-51 and 1-52 that the features produced using a raster toolpath are smooth and flat with the best peak to valley achieved measuring 20 nm.

1.5.14 **Spiral Toolpath Experiment**

The next toolpath which was analyzed was the spiral toolpath. The area of polishing was a 3mm x 3mm area, and the area was polished 15 times in a continual manner. It was observed that the profile obtained for polished surface was a concave profile, this is to be expected as the toolpath used was spiral toolpath with the tool starting from the outside groove and moving inwards towards the center at a constant cross feed and up feed. Now at a constant feed, when the tool is on the outer diameter of the polished region it will tend to travel a larger distance, with the distance being equal to the circumference of the polished area, the larger distance the tool has to travel would mean a lower removal of material, as the tool spends less time per unit area on the outer periphery. Now as the tool is fed in towards the center the distance that the tool has to travel decreases and tends to zero at the center of the polished region, this would mean that as the tool moves towards the center the amount of time it spends per unit area increases leading to higher material removal and deeper profile in the center region as compared to the outer periphery, leading to the development of a concave profile.

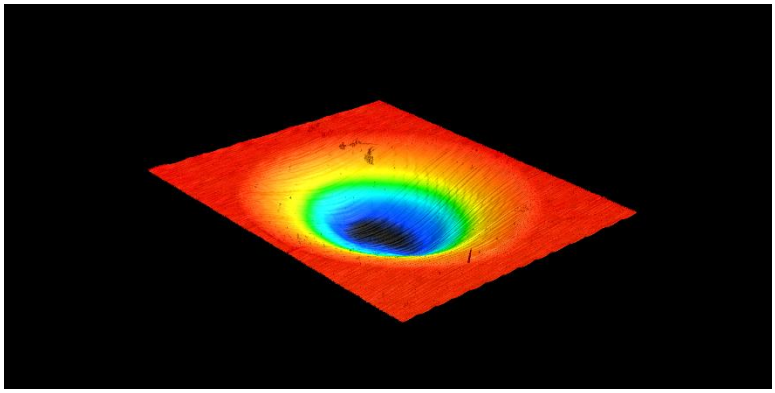

Figure 1-53: Image showing the measurement of surface polished using a spiral toolpath.

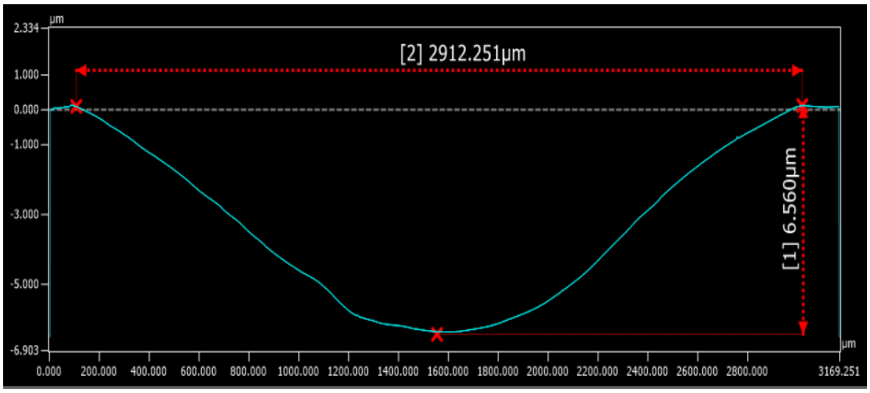

Figure 1-54: Image showing 2D cross section of surface polished using spiral toolpath.

The designed shape of the profile for the spiral toolpath strategy was a 3mm diameter patch, which was designed to have a depth of 15 μm. In the measured result it was observed that the depth of the polished surface achieved was around 6 μm after 15 polishing passes, this removal rate was similar to was what was observed in the case of a raster toolpath, which is a removal of around 0.4 μm depth per polishing pass. There was a difference of 9 μm in the expected depth and the polished depth. The volume of material removed during the polishing process was 0.017 mm^3 after 15 polishing passes, this volume removed is lesser than the volume removed when using Hilbert's toolpath which was 0.07 mm^3 after 3 polishing passes. The reason for this difference in the volumes removed could be attributed to the fact that the Hilbert's toolpath, has a very dense toolpath distribution over the same area as compared to a spiral toolpath, leading to more material removal in lesser number of polishing passes.

The surface finish of the polished surface measured 14 nm RMS surface finish, had a PV value of 38 nm, averaged over 10 measurements down, from the initial surface roughness of 45 nm RMS surface finish, which is an improvement of around 68% in terms of surface finish. It can also be observed in Figure 1-53 and 1-54 that the features produced using Spiral toolpath are smooth and flat with the best peak to valley achieved measuring 38 nm.

1.5.15 Groove Profile Polishing Experiments

Now as the polishing tool static influence profiles have been analyzed, an experiment set was carried out to study the effect of the dynamic influence of the tool, this was done by allowing the polishing tool to move along a straight line, and then the grooves generated are then analyzed for surface roughness. The experiment set was carried out both with and without any abrasive fluid present in the polishing zone. First analyzing the groove made by the polishing tool in the absence of any polishing fluid. The experiment was carried out by allowing the ball to rotate and then feeding it along the straight line, there were two test cases studied – one wherein the rotation and the feed of the ball were perpendicular to each other, second wherein the rotation and the feed of the ball were parallel to each other, as shown in Figure 1-55.

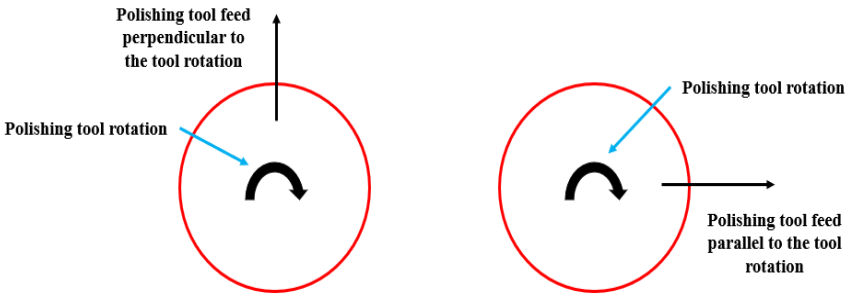

Figure 1-55: Image depicting the rotation and feed motion direction of the polishing tool.

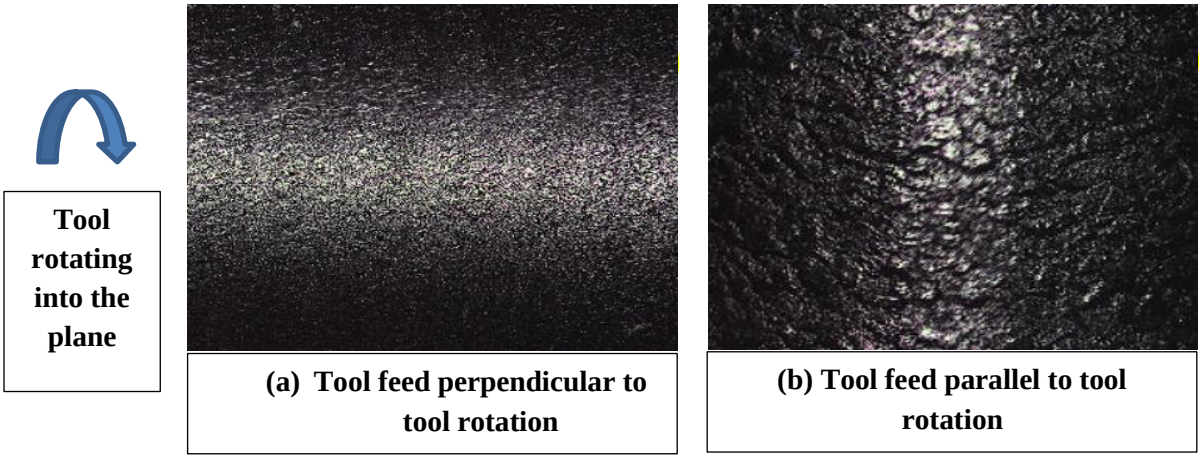

Figure 1-56: Image depicting the measured surface polished by using the (a) perpendicular and (b) parallel feed modes.

The surface generated by the two modes of the tool feeding perpendicular to the tool rotation direction and parallel to the rotation direction is shown above in Figure 1-56. It can be observed that the in the above Figure 1-56a the texture obtained is smoother, more uniform and is aligned to the direction of the rotation of the polishing tool, the surface texture appears to be blended due to the polishing tool moving perpendicular to the rotation direction. Whereas in Figure 1-56b it can be observed that the texture of the surface is visibly very rough, with presence of small scale like structures formed. This can be attributed to the fact that as this experiment set was performed in the absence of any polishing fluid, so as the tool feeds along the direction its rotating it heats up the polymer, and pushes it back as it moves forward, where the semi-solid polymer now cools down, creating the scale like structures. This observation was then verified by measuring the surface roughness of the two surfaces using the laser confocal microscope.

The surface roughness observed in the case of parallel tool feed was measured to be 2.8 microns, and the surface roughness in the case of perpendicular tool feed was measured to be 2.69

microns, meaning the surface generated using the perpendicular toolpath is around 6.5% smoother as compared to the one generated by using the parallel toolpath, but visually the surface texture was much better in case of the perpendicular tool feed.

Next an experiment set was performed to gauge the combined effect of the tool rotation and feed direction in the presence of abrasive fluid. The tool was fed parallel, perpendicular, and at 45 degree angle to the polishing tool rotation. From the measurements it was observed that the best surface finish was observed for the case of 45 degree tool feed, followed by perpendicular tool feed, and the worst finish was observed for the case of parallel tool feed. It was also observed in the case of parallel tool feed as seen in Figure 1-57, there were presence of small grooves artifacts at the bottom of the main groove, the smaller grooves were formed aligned to the tool rotation direction. These periodic small groove artifacts weren't observed in the case of 45 degree and perpendicular tool feed. One explanation for these small groove artifacts could be that there could be a small imperfection of the order of 10^{-5} mm on the ball surface, as a result when the tool rotates at a high RPM and feeds in, it imprints this imperfection onto the surface, leading to the formation of those small groovy artifacts on the base of the main groove. In the case of both the perpendicular and 45 degree feeds there was no presence of the periodic small groove artifacts observed in the measurements. In both cases the base of the measured grooves showed a flat profile, with no visible change in shape observed. In terms of the polishing depth the maximum depth of the profile was measured to be 0.35 microns which was observed in the case of perpendicular feed profile. The polishing depths were pretty much in the similar range for both the perpendicular and parallel tool feed. The lowest polished depth was found to be in the case of the 45 degree tool feed which was 0.3 microns.

Now a single groove can be imagined as a series of individual spots that have been polished at very short distances to each other, leading to the spots blending in together and forming a continuous groove. According to the Hertzian contact theory, for the operating conditions that were used to create these grooves, the contact patch should measure 0.52 mm in diameter – leading to the ideal groove width being 0.52 mm assuming that each groove is a series of very closely placed spots. Now in all the three cases of parallel, perpendicular and 45 degree tool feed it was observed that the actual width of the profile was higher than the expected width as shown below in the Table 1-4.

	Groove Type		
	Parallel Feed	**Perpendicular Feed**	**45 Degree Feed**
Measured Profile Width	0.86 mm	0.9 mm	0.88 mm
Expected Profile Width	0.61 mm		

Table 1- 4: Profile width comparisons between expected and measured results.

There is a difference of around 32% in the expected width and the measured width which can be accounted to the fact that the Hertzian formulation which was used to calculate the theoretical (expected) contact width doesn't account for the softness and the hyperelastic properties of the Silicone rubber tool. The properties of the Silicone rubber allow it compress more readily under an applied load leading to a wider contact patch – which is what was observed in the measured experimental results. One more observation made was that the grooves made by the perpendicular tool feed were the widest amongst the three types of tool feeds, this is because of the fact that during the tool rotation, the polishing tool tends to expand diametrically, and in the case of the perpendicular tool feed, the tool motion would be perpendicular to this tool expansion caused by the tool rotation, hence leading to a bigger contact patch. This expansion results in a wider groove, which is what was observed in the measurement. Hence to conclude this section it can be surmised that to obtain the best result it should be noted that the perpendicular feed type must be utilized, as it provides a profile which doesn't have any kind of periodic polishing artifact, and it has the best surface finish amongst all the other feed types tested in the experiment.

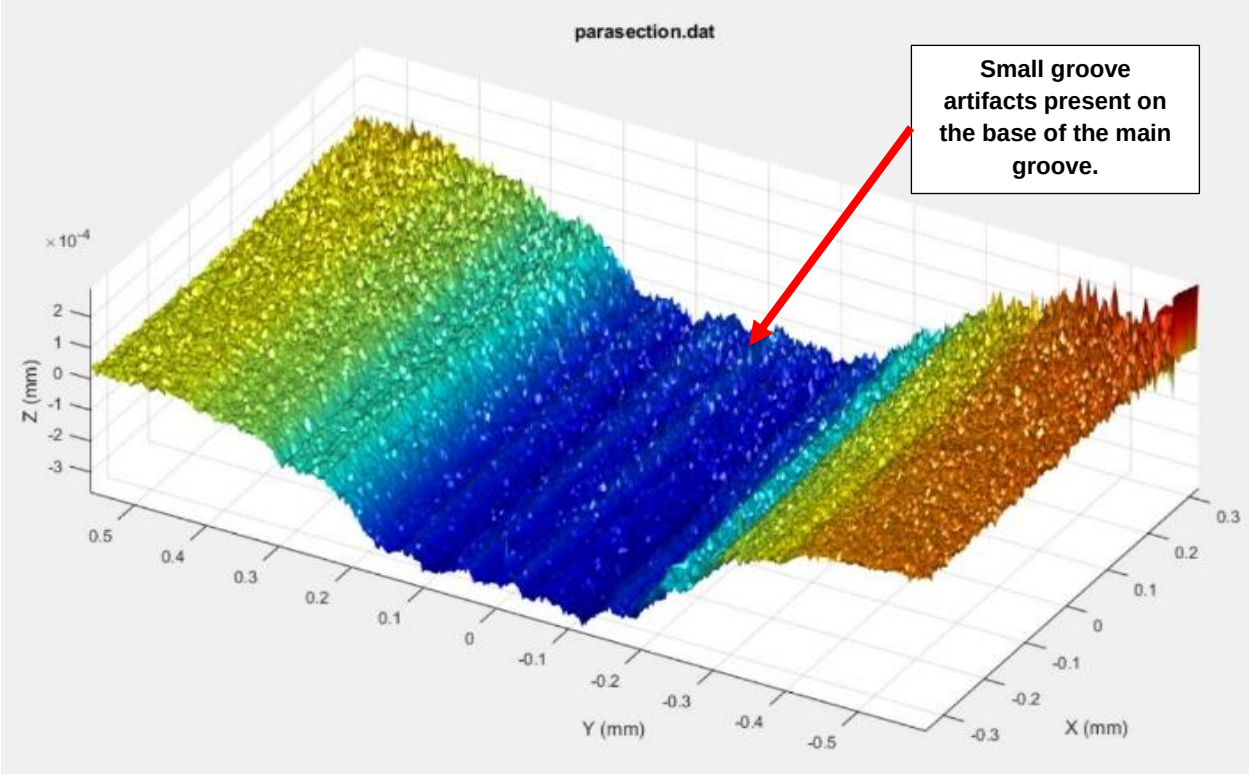

Figure 1-57: Image depicting measured surface polished using parallel tool feed.

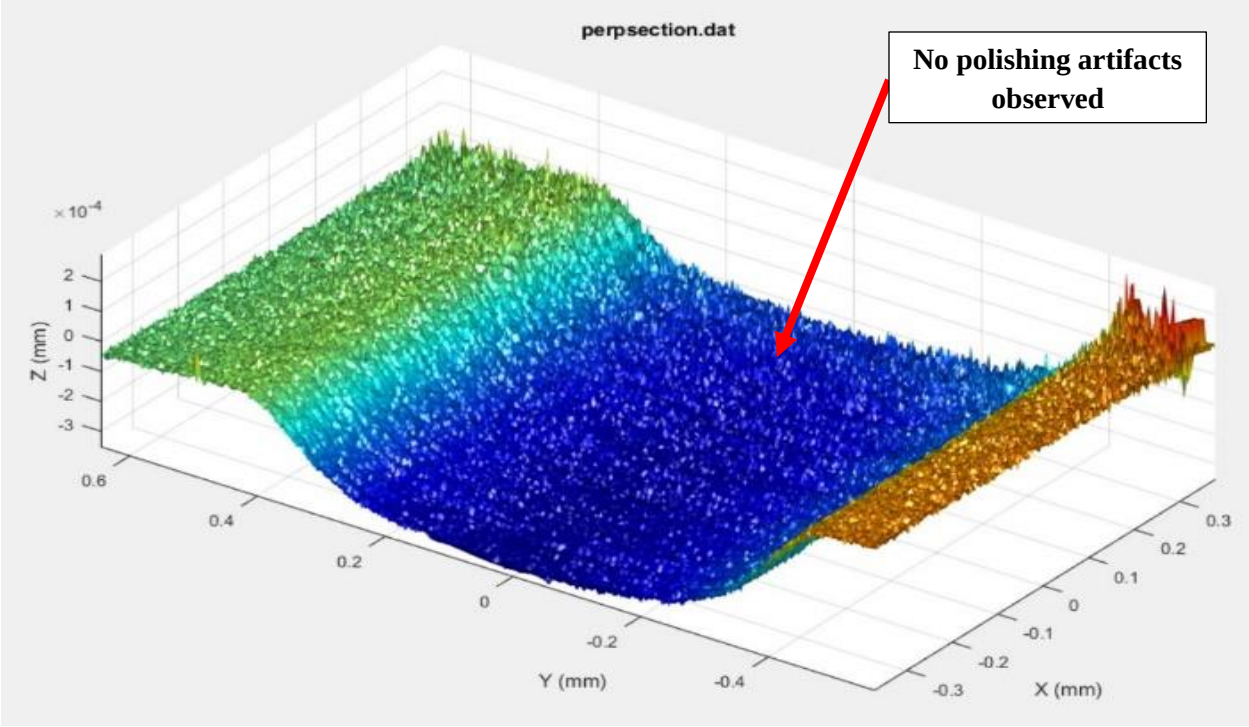

Figure 1-58: Image depicting measured surface polished using perpendicular feed.

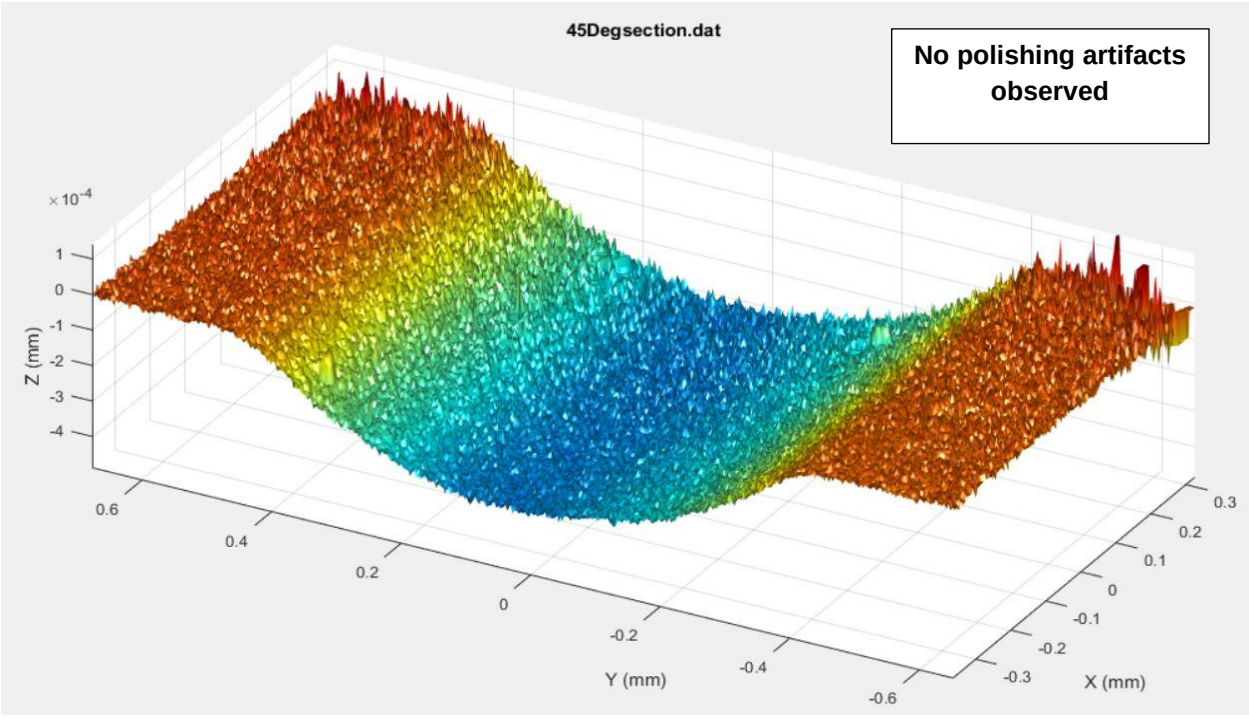

Figure 1-59: Image depicting measured surface polished using 45 degree tool feed.

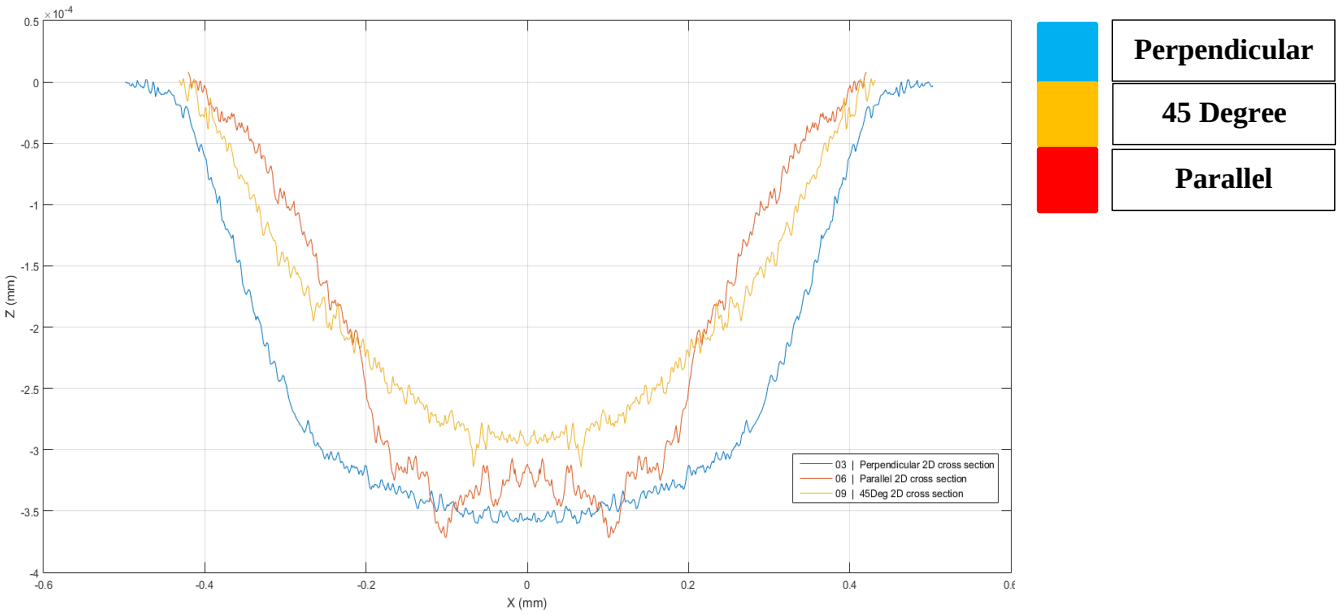

Figure 1-60: 2D cross section of the surface polished using differing feed direction type.

Next an experiment set was carried out to analyze the surface created when two grooves intersect with each other, for which the adjacent grooves were polished to the same length and were made to overlap each other by a fixed value, for the experiment set this value was chosen such as the grooves would be overlapping each other by 25%, 50% and 90% overlap in three distinct experiments. The toolpath for the experiment set was generated using Autodesk Fusion 360, the grooves were designed to be of 10 mm in total length, and the overlap between each adjacent groove was kept at a constant 0.25 mm which is around 25% overlap for a 1 mm groove width. 4 grooves were polished in the experiment set, and a feed perpendicular to the direction of tool rotation was utilized for this experiment.

In Figure 1-61 and 1-62 below, the cross section of the profile produced when the grooves are polished using a 25% overlap can be observed. It was seen in the figure that there are 3 distinct zones A, B, C wherein the adjacent grooves overlap. These zones are the region wherein the tool tends to pass twice due to the overlap causing a higher material removal, hence they are deeper than the surrounding regions which is what was expected. Another reason for this could be the fact that the pressure gradient is skewed towards the outlet side, and the fluid film tends to constrict towards the outlet side as explained in the fluid film section of this report. The pressure is on decline before these regions as they all lie on the outlet side of the polishing tool rotation,

but due to the ball deflection and the elastohydrodynamic effects of the fluid film, there is a slight pressure spike at the outlet. The deflection coincides with the reduction in the film thickness at the exact location (A, B, C – the deeper sections in Figure 1-62), leading to a higher material removal, and hence those deep set features are produced at the end point (side periphery of each groove).

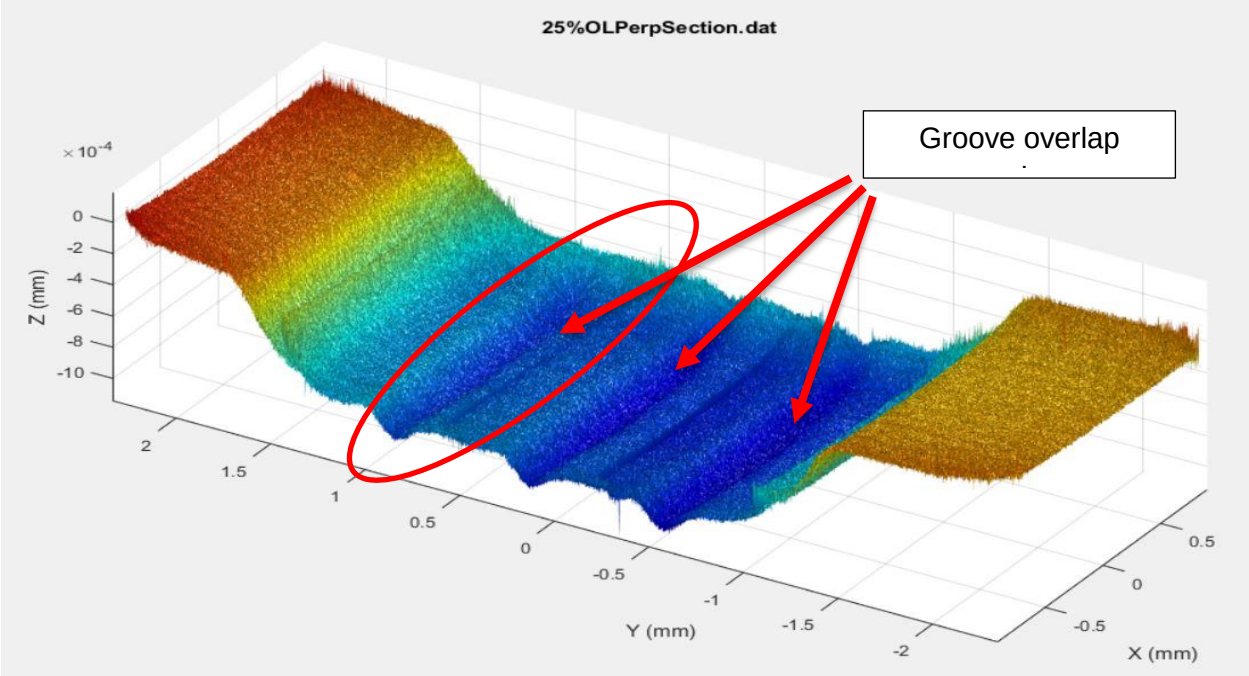

Figure 1-61: Image showing the measurement of surface polished with a 25% overlap.

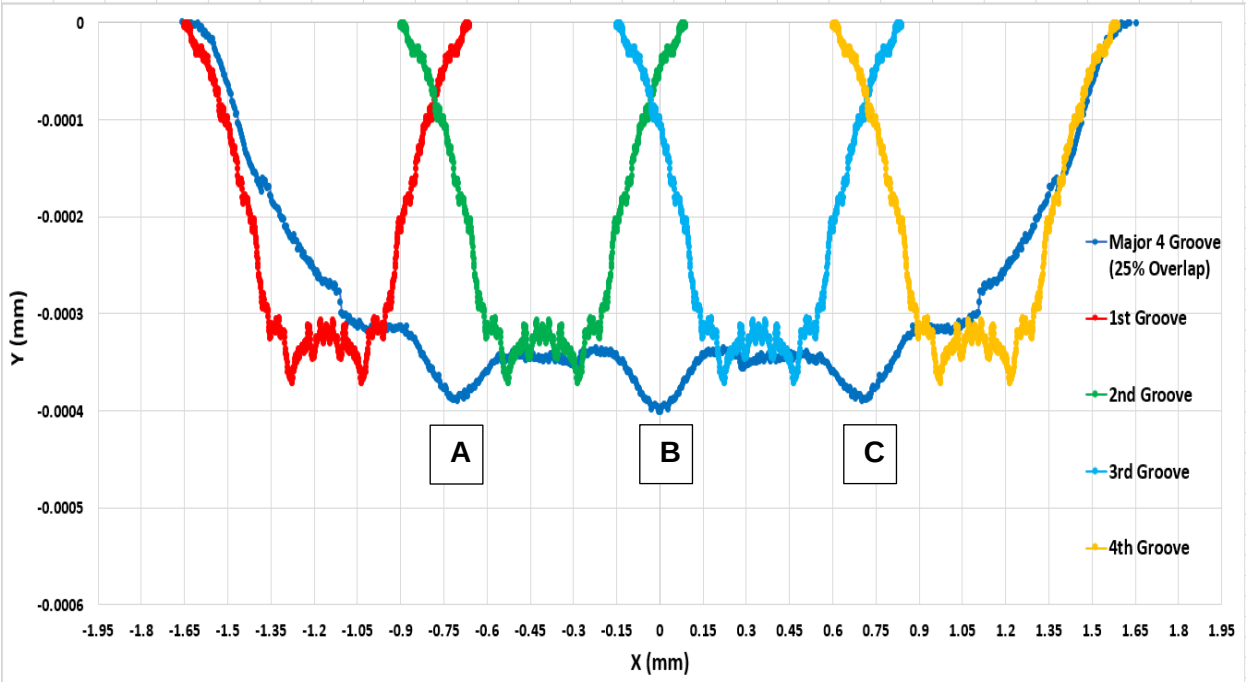

Figure 1-62: 2D cross section profile of entire polished patch with 25% groove overlap.

One more thing to notice are the extremities of the profile, both the beginning and the end section of the overall profile shows a curved boundary which is again indicative of the tool influence as it creates the first groove. One more thing to note is that when viewed on this page the tool is being fed into the page but is rotating in the plane of the page.

Now in order to further understand how exactly the grooves are overlapping each other so, another experiment set was run using a 50% overlap of the adjacent grooves, but this time the grooves were kept discontinuous, meaning the adjacent grooves weren't of the same length, but the overlap between each adjacent groove was kept at a constant 0.5 mm which is around 50% overlap for a 1 mm groove width. 4 grooves were polished in the experiment set, and a feed perpendicular to the direction of tool rotation was utilized for this experiment. Even in this case it can be seen from Figure 1-65 that there were deep regions observed in region A and B, as these were the regions where the tool overlapped the previous toolpath, similar to what was observed in the case of 25% overlap.

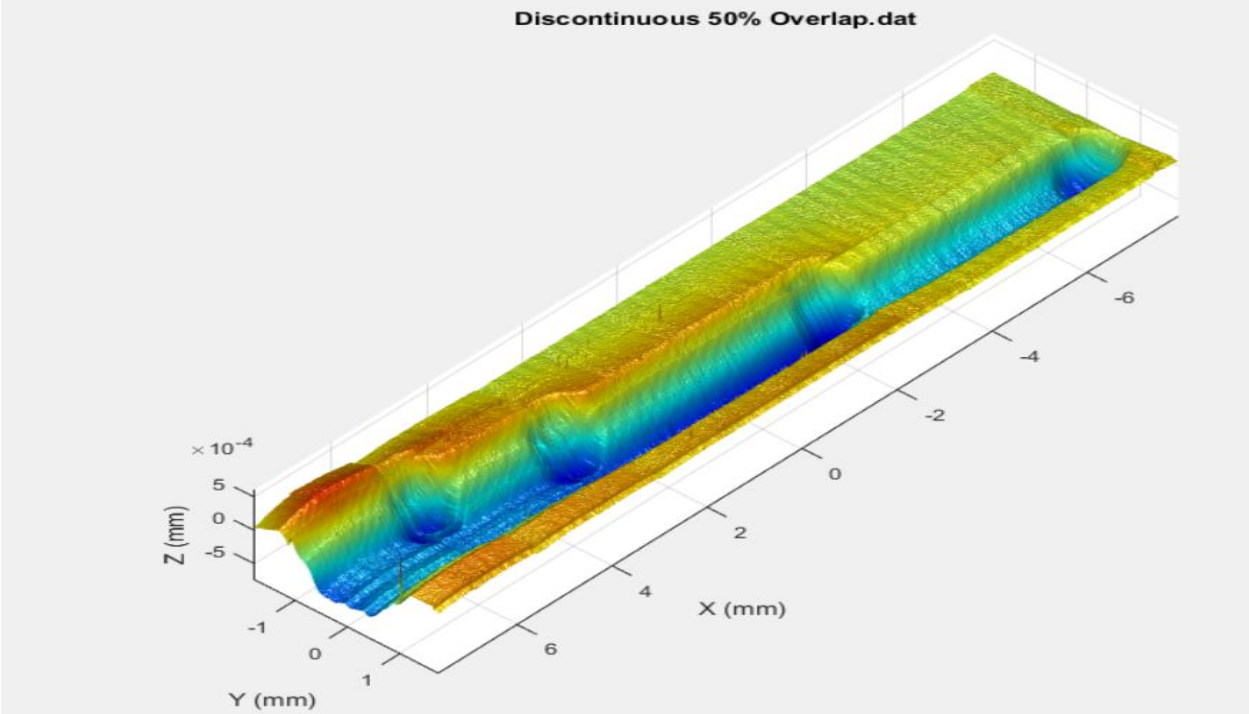

Figure 1-63: Image showing the measurement of surface polished with a 50% overlap.

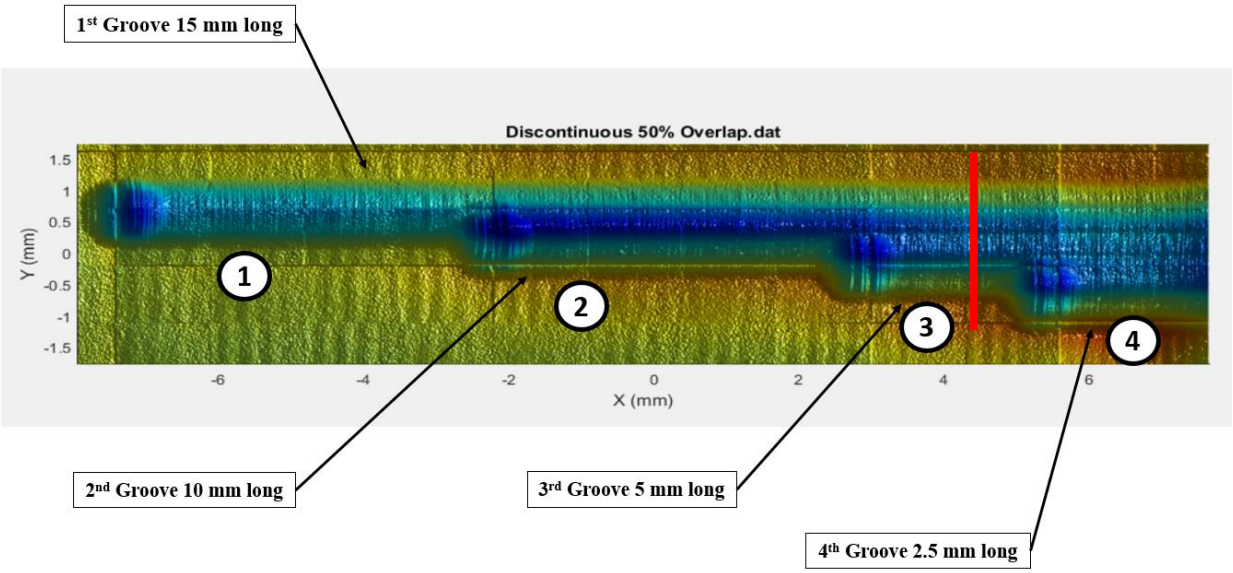

Figure 1-64: Top view of the polished discontinuous grooves showing the overlap.

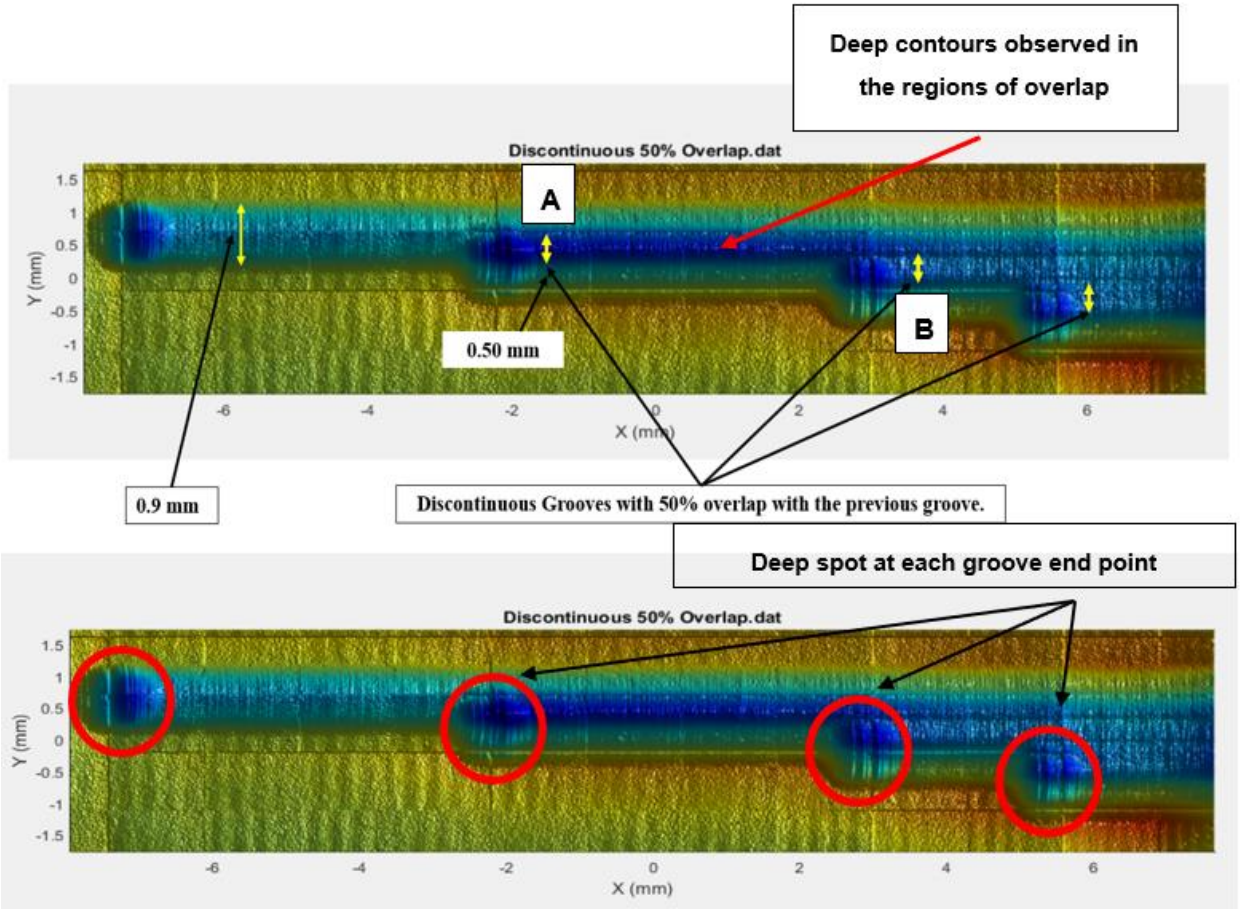

Figure 1-65: Image showing the region of overlap in the polished groove.

It can be observed from Figure 1-65 that the measurement clearly shows darker contour zones in the region of overlap between the adjacent grooves, which is indicative of the fact due to the polishing tool passing the overlap region multiple times, causes a higher material removal rate. Another thing which was observed is the presence of deep set features at the end of each groove as seen in Figure 1-65, these were attributed to the fact that the tool tends to sit at the end point for some time before lifting up to make a new groove, and this issue can be possibly solved by using a higher ramp feed, which will prevent the tool from stalling at the end points.

1.6 STATISTICAL ANALYSIS OF POLISHING PROCESS

In the previous sections a discussion was carried out on how the input parameters like RPM, normal load, toolpath offset, abrasive grain size, abrasive concentration, feed rate affect the surface roughness and the material removal rate during the polishing process, but one point to note is that those experiments were singular factor experiments wherein only a single input parameter was varied and its effect on the surface roughness and material removal rate was analyzed. But this approach doesn't give us an idea of how these input parameters interact with

each other, and how they affect the output variable when they are varied together. For this reason, a full statistical study was carried out so as to observe and analyze these multi variable interactions and their effect. Design of experiment theory was used to create the statistical model that was used to define the polishing process and its underlying parameters. Now a usual design of experiment study consists of two types of factors – controllable and uncontrollable input factors, as the name suggest the controllable factors are the ones which can be varied or controlled which in our case are RPM, normal load, feed rate, offset, abrasive concentration, and abrasive grain size. Uncontrollable factors could be the ambient temperature of the room, machine vibration etc. The statistical study in this project aims at creating a base for correlating the polishing input parameters with the surface roughness. The response which is the surface roughness was analyzed using the mean square value metric (R_q). The response surface method was chosen as the statistical study model. This method was chosen as it enabled the capturing of the quadratic effects of the input variable interactions. Response surface method enables the analysis of one or more input variable and their corresponding one or more responses or output variable, and also helps to include the quadratic terms in the interactions.

	LOW	**MID**	**HIGH**
RPM	5000	10000	15000
Normal Load (N)	0.5	1	1.5
Feed Rate (mm/min)	50	275	500
Toolpath Offset (mm)	0.01	0.105	0.2

Table 1- 5: Table depicting input parameters and parameter levels selected for the study.

The Minitab LLC package was used to design and analysis of the statistical model. As it can be seen in Table 1-5 above there are 4 factors to be studied, and each factor has 3 levels. Depending on this data we obtained 27 experimental runs using the Box Behnken design. In the 27 experiments there 3 center points were designed which were basically repeat experiments to check for variability, and the remaining 24 were the edge points.

After running the experiments an ANOVA (analysis of variance) was performed to figure out which parameter and which interactions are significant in the polishing process. It was observed that the linear term - Feed rate and the linear interaction between RPM and Tool offset are most significant terms in this polishing process, with p-values of 0.015 and 0.001 respectively, with both the values being less than 0.05 (using a 95% confidence level). It was also observed that the Feed rate affects the surface roughness by 47%, while the combination of RPM and Offset affects the surface roughness the highest by 69%, indicating that each of these parameters have a significant effect on the surface roughness quality.

In Figure 1-66 below shows the Pareto chart for the polishing parameters, this chart is used to confirm the ANOVA results. The Pareto chart shows which parameters have the maximum effect on the output variable which is the surface roughness. From the chart it can be seen that the combination of RPM and Tool offset has the maximum effect on the surface roughness, followed by the polishing tool feed rate, RPM, Offset. A confidence interval of 95% was used to analyze the effect of the parameters on the surface roughness.

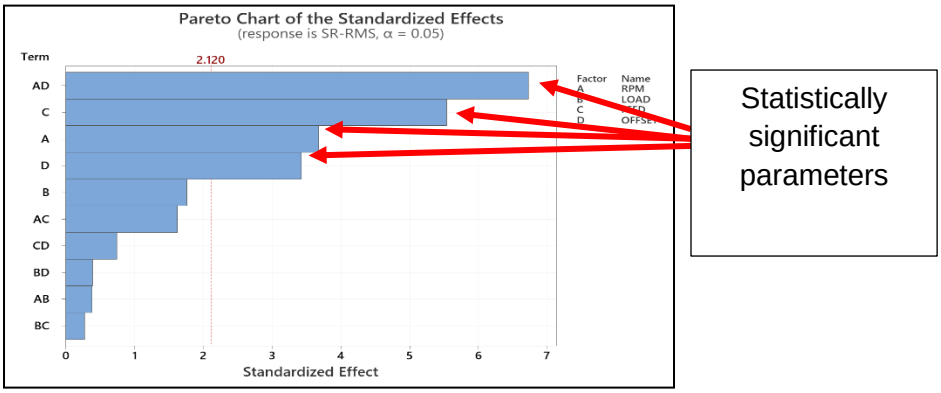

Figure 1-66: Image depicting the Pareto chart for the original model.

Next a regression analysis was performed to model the relation between the input parameters and the output variables. The input parameters are the independent variables and the output parameter which is Surface roughness is the dependent variable. The equation was coded for ease – where:

RPM – A
Load – B
Feed – C
Offset – D

SR-RMS (nm) =
4.0 + 0.000906*A - 1.269*B + 0.01780*C + 100.8*C – 0.000001*A*C – 0.00879*A*D

The above equation was obtained by carrying out a regression analysis of the measured result, and it explains the current measured data with an 86.32% accuracy and is able to predict with an accuracy of 72.78%. This accuracy is basically the R^2 value and R^2 $(pred)$ values, respectively.

R-sq	R-sq(adj)	R-sq(pred)
86.32%	82.22%	72.78%

Table 1- 6: Table depicting the R^2 for the reduced model.

The initial R^2 value of the model was 87% and R^2 (pred) was 61.86%, this was due to the fact that there was a presence of factors which were statistically insignificant, hence the model had to be reduced by removing these insignificant terms leading to a reduced model with better prediction accuracy.

To validate the prediction ability of the regression equation an experiment was conducted at a given parameter level, with the theoretical surface roughness was calculated using the regression equation mentioned above, the actual surface roughness was measured, and the error between the predicted and the actual was calculated.

RPM	LOAD	FEED	OFFSET	SR-RMS (Predicted)	SR-RMS (Measured)	ERROR PERCENT
10000	1	100	0.1	13.96 nm	10.78 nm	22%

Figure 1-67: Data depicting the validation experiment results.

From Figure 1-67 above it can be seen that the regression equation predicted the surface roughness value to be 13.96 nm, while the measured value was found out to be 10.78 nm, which is an error percent in the predictability of 22%, which is to be expected as the R^2 (pred) for the statistical model was at 72.78, meaning that model can predict the surface roughness with an accuracy of 72.78%.

Next the response surface model was used to identify the optimal parameter range to carry out the polishing process for the current data set. The workpiece had an initial surface roughness value of 25 nm, and all the experiments were performed using single polishing passes. In the measured result the lowest roughness obtained was 10.46 nm for a single polishing pass. The response optimization process yielded the optimal setting to perform the experiments, which were 10000 RPM, 1.5N normal load, 50mm/min feed rate, 0.01mm feed rate, which gave us a desirability of 0.9 on a scale of 0-1 to obtain the best surface finish.

Now coming over to the multi variable effect on the surface, contour graphs were used to understand how the change in one or more response affects the surface roughness. The contour graphs were generated by varying the two factors, keeping the third factor constant and their corresponding response was studied. These contour graphs also allowed to obtain the optimum operating region for the polishing process. The contour graphs are depicted below in Figure 1-68 to 1-72.

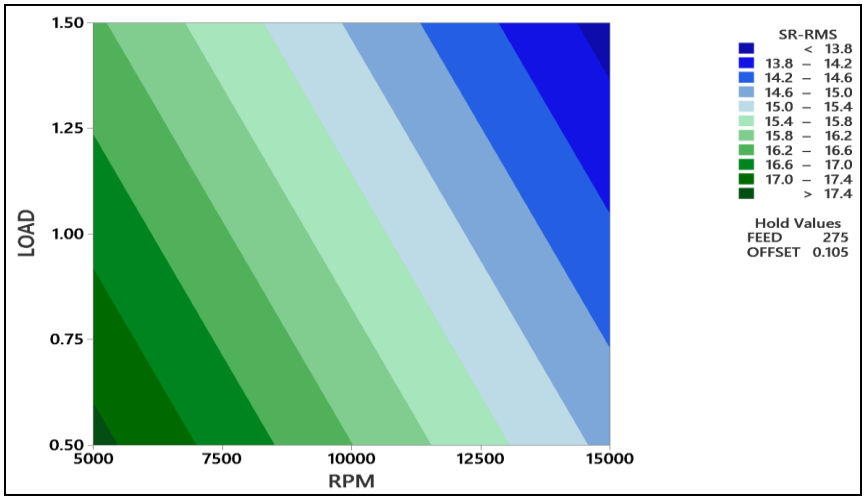

Figure 1-68: Contour plot of surface roughness variation with normal load and RPM

Figure 1-68 shows the variation of the surface roughness variation at feed rate of 275 mm/min and a 0.105 mm tool offset distance. The blue contours in the graph shows the best surface finish region or the optimal region for varying the normal load and the polishing tool RPM, the green region is the region where the finish obtained was not good. From the graph it can be observed that the best finish is obtained at high polishing tool RPM's and high normal loads, this could be because of the fact that at higher polishing RPM, a given point on the polishing tool would come in contact with the workpiece surface more often, leading to an increased polishing action and hence a better surface finish. A higher polishing RPM would also denote a larger film thickness for the polishing fluid thereby allowing more abrasive grains to enter the polishing zone and increasing the polishing action. A higher load enables us to get better surface finish because as the normal load applied increases the contact pressure goes up, as the contact pressure rises, a higher material removal rate is attained in accordance with the Preston's equation which leads to an increase in the polishing action, leading to better surface finishes.

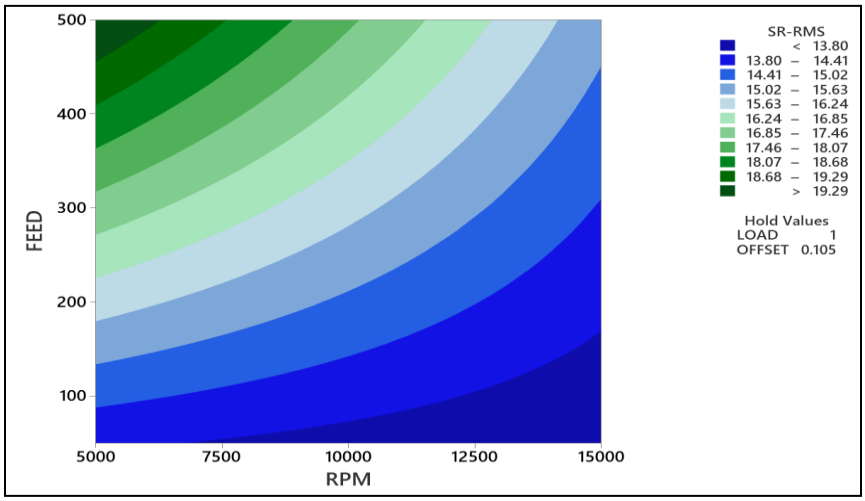

Figure 1-69: Contour plot of surface roughness variation with feed rate and RPM

Figure 1-69 shows the variation of the surface roughness variation at normal load of 1N and a 0.105 mm tool offset distance. The blue contours in the graph shows the best surface finish region or the optimal region for varying the feed rate and the polishing tool RPM, the green region is the region where the finish obtained was not good. From the graph it can be observed that the best finish is obtained at high polishing tool RPM's and low feed rates, this is because of the fact that at lower feed rates the time the polishing tool spends at a given points is higher, leading to the removal of more material and hence leading to better surface finishes. This explanation is in line with Preston's equation for polishing material removal.

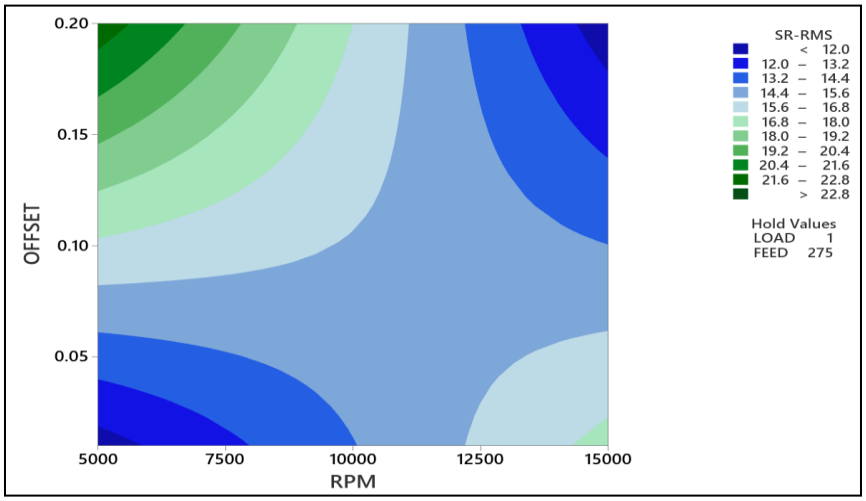

Figure 1-70: Contour plot of surface roughness variation with toolpath offset and RPM

Figure 1-70 shows the variation of the surface roughness variation at normal load of 1N and a 275 mm/min feed rate. The blue contours in the graph shows the best surface finish region or the optimal region for varying the polishing tool offset distance and the polishing tool RPM, the green region is the region where the finish obtained was not good. From the graph it can be observed that the best finish is obtained at high polishing tool RPM's and high polishing tool offset distances, and at low polishing tool RPM's and low polishing tool offset distances. This is because of the fact that a low offset distance would mean that the polishing tool would overlap its previous passes much closely, leading to the presence of regions where the polishing action occurs multiple times, thereby giving a better surface finish. Hence the best way to achieve a good surface finish would be to combine a high polishing tool RPM with a smaller overlap, or a low polishing tool RPM with a larger overlap or offset.

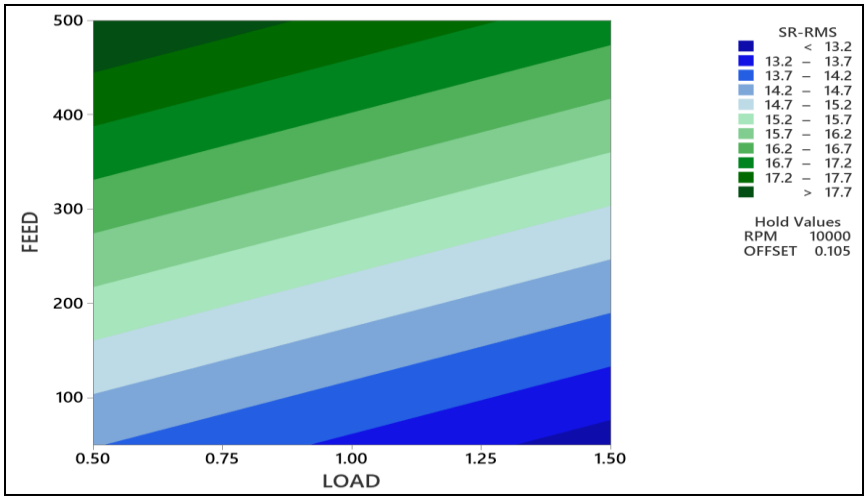

Figure 1-71: Contour plot of surface roughness variation with feed rate and normal load

Figure 1-71 shows the variation of the surface roughness variation at normal load of 10000 rpm and a 0.105 mm tool offset distance. From the graph it can be observed that the best finish is obtained at high normal loads and low feed rates, this is because at this combination the tool would have the highest contact pressure in the contact zone due to the higher normal load, leading to a higher material removal rate and a low feed would allow the tool to dwell at specific points on the surface for a longer duration of time leading to again a higher material removal rate and hence an improved surface finish due to more polishing action.

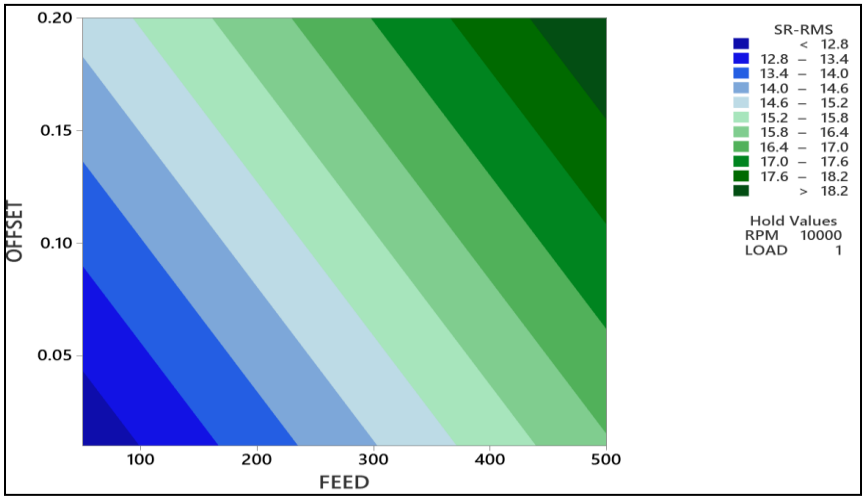

Figure 1-72: Contour plot of surface roughness variation with offset and feed rate

Figure 1-72 shows the variation of the surface roughness variation at 10,000 RPM and a 1N normal load. From the graph it can be observed that the best finish is obtained at low feed rates and low offset distances, this is because at this combination the tool would spend an increased amount of time per unit point on the workpiece surface owing to the low feed rate and a low offset

distance would allow a higher overlap between adjacent polishing passes, both these actors combined would lead to higher polishing action and a better surface finish.

1.7 CONCLUSION

1. The experimental results reported in this thesis provided an understanding of the process of sub-aperture polishing of polymers using a soft rubber tool.

2. Theoretical models were used to predict the terms involved in the polishing process - contact patch width, contact pressures. It was found that the contact pressure profile follows a Gaussian distribution across the contact patch. The contact patch and the contact pressure variation with the normal load and tool material properties was also studied for both Polycarbonate and Polymethylmethacrylate. Finite element simulation was carried out to compare the theoretical formulation of the Hertzian contact and the effect the hyper elasticity property (which is the special property of elastomers like Silicone rubber. The contact pressures and the contact width were predicted and compared with the theoretical profiles.

3. Fluid film thickness was analyzed using Dowson's equations and the effect of RPM and normal load on the fluid film thickness was studied and reported.

4. Experiments were carried out to observe the effect of the presence of the abrasive fluid in the contact zone and how it affects the material removal rates and the shape of the polished profile produced. It was found that in the absence of polishing fluid in the contact zone created deeper polished profiles, owing to a larger material removal rate as the tool would directly make contact with the surface. It was also seen that the lack of a fluid medium in the contact zone led to generation of a large amount of heat, which in turn lead to the presence of beads of molten polymer.

5. Tool influence experiments were carried out to measure the material removal rates and the shape of the profile that the polishing tool generates when it is allowed to dwell on the workpiece surface. The effect of varying the normal load and the abrasive grain size on the tool influence function was also studied. It was observed that as the normal load increased, the tool leaves behind deeper and much wider profiles with a poorer surface finish (a surface with high RMS values). The effect of using a new polishing ball vs using an old worn ball on the profiles generated was also studied.

6. Surface roughness experiments were carried out to characterize the input parameters and their effect on the resulting surface roughness of the workpiece. Singular experiments were carried out to analyze the effect of varying one variable on the surface roughness. Single variable experiments were carried out by changing input variables like RPM, Normal load, Feed rate,

Polishing tool offset, Abrasive concentration, Abrasive grain size, and Number of polishing passes. These studies were carried out on both Polycarbonate and Polymethylmethacrylate surfaces, two types of surfaces were polished – diamond turned surfaces and as manufactured smooth surfaces.

8. Experiments were also performed to analyze the shape of grooves produced by the polishing tool. This was important because in order to create any type of shape or form, one needs to know how the polishing tool reacts with the surface. Multiple experiments were performed to polish grooves onto the workpiece surface at 25% and 50% toolpath overlap. This experiment provided the data on how the tool polishes the surface in terms of how much material is being removed by the polishing tool in unit time, 't', and the surface finish of the polished surface inside the groove. A study was also carried out which compared the different angles of tool feed motion on the workpiece surface – with the feed motions being parallel, perpendicular, and at an angle of 45 degrees with the polishing tool rotation direction.

9. A statistical response surface study was done to measure the response of varying multiple parameters on the surface roughness, and the interactions of these parameters with the surface roughness. A regression analysis was done to relate the RMS surface roughness with the RPM, Load, Offset and Feed rate. This model was able to explain the variation in the RMS surface roughness with an accuracy of 86% and was able to predict the theoretical surface roughness value with an accuracy of 72%. The response surface model was also used to determine the optimum parameter values to carry out the polishing process which are mentioned in Table 1-7 (One point to note is that number of polishing passes is very subjective, it will depend upon how rough the initial surface was to begin with which will decide the number of polishing passes) .

Polishing Parameter	**Optimum Setting**
Polishing Tool RPM	10000
Feed Rate (mm/min)	50
Offset distance (mm)	0.01
Normal load (N)	1.5
Abrasive Grain Size (nm)	10

Table 1- 7: Optimal settings to achieve the best surface finish.

As a rule of thumb, it is advised to use the following settings as shown in Table 1-8 to get improved results in the case of sub-aperture polishing of polymers. (As manufactured surface were sourced commercially and were cell casted blocks of PC and PMMA).

	For a diamond turned surface	For an as manufactured surface
Polishing Tool RPM	High (<15000)	Low
Feed Rate (mm/min)	Low	High
Offset distance (mm)	Low	High
Normal load (N)	High	Low
Abrasive Grain Size (nm)	Low	Low
Abrasive Concentration (%)	High	High

Table 1- 8: Suggested parameter level to obtain good polishing action.

REFERENCES

[1] V. Doushkina and E. Fleming, “Optical and mechanical design advantages using polymer optics,” *Adv. Optomech.*, vol. 7424, no. September 2009, p. 74240Q, 2009.

[2] T. E. of E. Britannica, “Lens,” *Encyclopedia Britannica*. Encylopaedia Britannica, Inc., 2019.

[3] S. Powell and D. Fisher, “Polymer optics gain increased precison,” *Laser Focus World*, vol. 43, no. 6, pp. 111–117, 2007.

[4] L. Zhang, H. Y. Tam, C. M. Yuan, Y. P. Chen, Z. D. Zhou, and L. Zheng, “On the removal of material along a polishing path by fixed abrasives,” *Proc. Inst. Mech. Eng. Part B J. Eng. Manuf.*, vol. 216, no. 9, pp. 1217–1225, 2002.

[5] Mitutoyo, “General Social Survey , 1972-2010 [Cumulative File],” *Mitutoyo Am. Corp.*, vol. 1, no. 2229, pp. 1–8, 2010.

[6] S. Mishra, R. Singh, and A. Ghosh, “A study of material removal response of various glasses in computer controlled sub-aperture polishing,” *Int. Conf. Opt. Photonics 2015*, vol. 9654, no. June 2015, p. 96540O, 2015.

[7] M. Kanaoka, H. Takino, K. Nomura, H. Mimura, K. Yamauchi, and Y. Mori, “FACTORS AFFECTING CHANGES IN REMOVAL RATE OF ELASTIC EMISSION MACHINING Nikon Corporation Department of Precision Science and Technology Research Center for Ultra-Precision Science and Technology,” pp. 3–6.

[8] U. Ali, K. J. B. A. Karim, and N. A. Buang, “A Review of the Properties and Applications of Poly (Methyl Methacrylate) (PMMA),” *Polym. Rev.*, vol. 55, no. 4, pp. 678–705, 2015.

[9] G. Palm, R. B. Dupaix, and J. Castro, “Large strain mechanical behavior of poly (methyl methacrylate) (PMMA) near the glass transition temperature,” *J. Eng. Mater. Technol. Trans. ASME*, vol. 128, no. 4, pp. 559–563, 2006.

[10] T. E. of E. Britannica, “Polycarbonate,” *Encyclopedia Britannica*. Encylopaedia Britannica, Inc., 2017.

[11] T. P. Elastomers, “10 Elastomers and Rubbers,” 2017.

[12] A. Roswell, F. Xi, and G. Liu, “Modelling and analysis of contact stress for automated polishing,” *Int. J. Mach. Tools Manuf.*, vol. 46, no. 3–4, pp. 424–435, 2006.

[13] Y. T. Su, S. Y. Wang, P. Y. Chao, Y. D. Hwang, and J. S. Hsiau, “Investigation of elastic emission machining process: lubrication effects,” *Precis. Eng.*, vol. 17, no. 3, pp. 164–172, 1995.

[14] R. G. (Richard G. Budynas, J. K. Nisbett, and J. E. Shigley, *Shigley’s mechanical engineering design*. New York: New York : McGraw-Hill, [2011], 2011.

[15] E. Dintwa, E. Tijskens, and H. Ramon, “On the accuracy of the Hertz model to describe the normal contact of soft elastic spheres,” *Granul. Matter*, vol. 10, no. 3, pp. 209–221, 2007.

[16] A. C. Fischer-Cripps, “The Hertzian contact surface,” *J. Mater. Sci.*, vol. 34, no. 1, pp. 129–137, 1999.

[17] B. J. Hamrock and D. Dowson, “Elastohydrodynamic Lubrication of Elliptical Contacts for Materials of Low Elastic Modulus.,” *Am. Soc. Mech. Eng.*, vol. 100, no. 78-Lub-1, 1978.

[18] Y. Mori, K. Yamauchi, and K. Endo, “Elastic emission machining,” *Precis. Eng.*, vol. 9, no. 3, pp. 123–128, 1987.

[19] J. C.J. Bart, E. Gucciardi, and S. Cavallaro, “Properties of Lubricants,” no. 2013, Elsevier Science & Technology, 2013, pp. 10–23.

[20] L. Hu, J. Zhan, and D. Zheng, “Study on the influence of the rotational speed of polishing disk on material removal in aspheric surface compliant polishing,” *Adv. Mech. Eng.*, vol. 7, no. 3, pp. 1–8, 2015.

[21] J. Luo and D. A. Dornfeld, “Effects of abrasive size distribution in chemical mechanical planarization: Modeling and verification,” *IEEE Trans. Semicond. Manuf.*, vol. 16, no. 3, pp. 469–476, 2003.

[22] M. Bielmann, U. Mahajan, and R. K. Singh, “Effect of particle size during tungsten chemical

mechanical polishing," *Mater. Res. Soc. Symp. - Proc.*, 1999.
[23] Y. Xie and B. Bhushan, "Effects of particle size, polishing pad and contact pressure in free abrasive polishing Yongsong," vol. 200, pp. 281–295, 1996.
[24] H. Lei and J. Luo, "CMP of hard disk substrate using a colloidal SiO2 slurry: Preliminary experimental investigation," *Wear*, 2004.
[25] D. Tamboli, G. Banerjee, and M. Waddell, "Novel interpretations of CMP removal rate dependencies on slurry particle size and concentration," *Electrochem. Solid-State Lett.*, 2004.
[26] J. Seo and U. Paik, "Preparation and characterization of slurry for chemical mechanical planarization (CMP)," in *Advances in Chemical Mechanical Planarization*, Hanyang University, Seoul, South Korea: Elsevier Ltd, 2016, pp. 274–298.
[27] R. Pan, B. Zhong, Z. Wang, S. Ji, D. Chen, and J. Fan, "Influencing mechanism of the key parameters during bonnet polishing process," *Int. J. Adv. Manuf. Technol.*, vol. 94, no. 1–4, pp. 643–653, 2018.
[28] H. yuen Tam and H. Cheng, "An investigation of the effects of the tool path on the removal of material in polishing," *J. Mater. Process. Technol.*, vol. 210, no. 5, pp. 807–818, 2010.
[29] Y. Sun, D. Feng, and D. Guo, "An adaptive uniform toolpath generation method for the automatic polishing of complex surfaces with adjustable density," *Int. J. Adv. Manuf. Technol.*, vol. 80, no. 9–12, pp. 1673–1683, 2015.
[30] H. Y. Tam, H. Cheng, and Z. Dong, "Peano-like paths for subaperture polishing of optical aspherical surfaces," *Appl. Opt.*, vol. 52, no. 15, pp. 3624–3636, 2013.
[31] D. D. Walker and C. Dunn, "Pseudo-random tool paths for CNC sub-aperture polishing and other applications," *Opt. InfoBase Conf. Pap.*, vol. 16, no. 23, pp. 18942–18949, 2008.
[32] Y. Mizugaki, M. Sakamoto, and T. Sata, "Fractal Path Generation for a Metal-Mold Polishing Robot System and Its Evaluation by the Operability," *CIRP Ann. - Manuf. Technol.*, vol. 41, no. 1, pp. 531–534, 1992.
[33] A. Singh, H. Garg, P. Kumar, and A. K. Lall, "Analysis and optimization of parameters in optical polishing of large diameter BK7 flat components," *Mater. Manuf. Process.*, 2017.
[34] M. J. Cumbo, D. Fairhurst, S. D. Jacobs, and B. E. Puchebner, "Slurry particle size evolution during the polishing of optical glass," *Appl. Opt.*, 1995.
[35] X. J. Wu, X. Tong, H. Sun, H. Jia, and L. Zhang, "Parameter Optimization of Polishing M300 Mold Steel with an Elastic Abrasive," *Math. Probl. Eng.*, 2018.
[36] X. Tong *et al.*, "Mechanism and parameter optimization in grinding and polishing of M300 steel by an elastic abrasive," *Materials (Basel).*, vol. 12, no. 3, 2019.
[37] T. B. and Q. Yuminami, "Baikalox Alumina Polishing Suspensions."

2 SUB APERTURE POLISHING Optimization

Jacob Guymon
Graduate Student
Tyler Young
Graduate Student
Dr. Mark Pankow
Director of the PEC
Assistant Professor
Mechanical and Aerospace Engineering

Elastic emission machining (EEM) is a high-accuracy sub-nanometer polishing process that is useful for removing unwanted material and refining surface finish. While many prior studies have examined aspects of EEM and tested its polishing ability, few have gone in depth on how different paths impact the surface finish or how those effects relate to a wide range of EEM polishing parameters. This study investigates the effects of the tool path determine the optimal parameters achieve a desired finish without compromising the portions of the surface that are already within the specified margin. This work couples tool pathing with a study on how different combinations of parameters such as lubrication viscosity, applied force, and rotation speed can affect surface finish. EEM of polycarbonate is investigated in this study using a silicone ball and alumina slurry. The resulting surface is imaged using an optical interferometer to measure the surface finish. The applied load is found to have a direct impact on the machining process and final surface roughness.

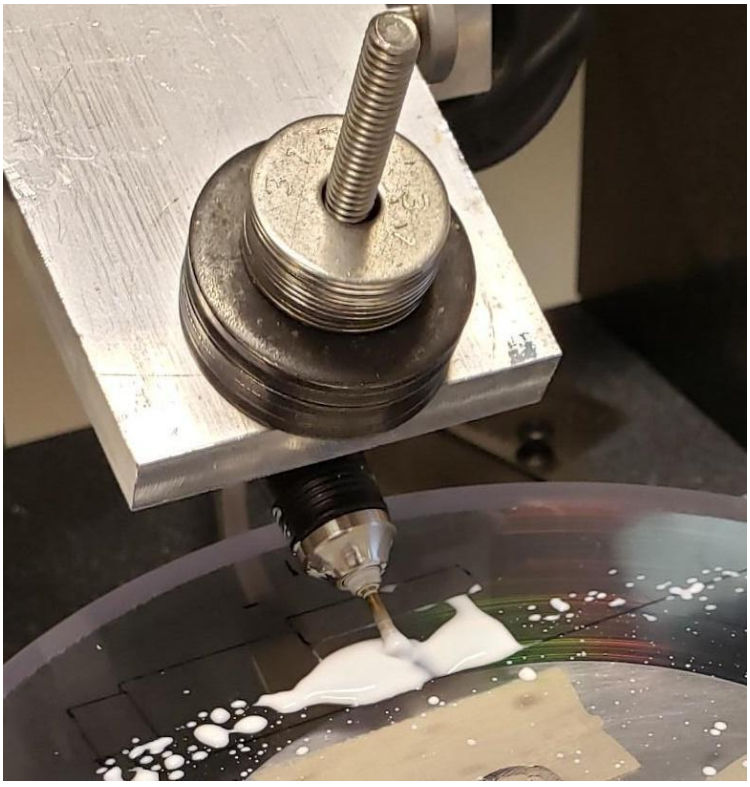

2.1 INTRODUCTION

Elastic Emission Machining (EEM) process uses a lubrication film or slurry in conjunction with a rotating elastic sphere to polish a given surface. EEM allows for material removal at the atomic level for ultra-precision machining. Surface atoms are picked up by the particles in the slurry, and do not inflict traditional abrasion defects on the surface as a result. However, the film thickness between the sphere and the surface must be maintained in order to ensure that no damage to the surface is inflicted [1]. Many studies have been conducted in the past to characterize the removal properties of EEM and its effect on various materials. For example, a study was conducted on Zerodur to see the impact that EEM would have on a material with a low coefficient of thermal expansion [2]. In this study, it was found that removal rate is negatively related to tool rotation speed and positively related to total load [2]. When considering surface finishes on the order of nanometers, accurate depictions of removal rate and appropriate tool pathing are necessary to produce the desired result. EEM using a spherical tool tends to create grooves along the toolpath. Some of these toolpath grooves are the desired surface figure while others are undesirable results of uncontrolled or unaccounted motion. Common toolpaths include raster patterns, spirals, and pseudo random toolpaths. Common undesired features can be categorized as deep sub-contact patch grooves and entrance/exit effects. EEM processes are often polished and measured several times. The repeatability problem must be addressed in order to fix near perfect surfaces without damaging them and creating a reliable system that can consistently yield desired surface finish.

2.2 DETAILS OF THE PROJECT

In the previous chapter, initial steps were taken to build and test for optimal parameters that can produce the best surface finish. This chapter will continue to build on the project by attempting to consistently produce a sub-nanometer surface finish free of defects commonly seen in EEM. The experimental setup is similar to that of Chapter 1, but includes advancements made to the tool and work surface fixtures for refined accuracy. In this work, the EEM process is studied for polishing polycarbonate by varying a number of machining parameters and investigating their impact on the surface quality. The polishing setup is modified in order to improve accuracy and be easily transferable to industrial applications.

2.2.1 Sub-contact Patch Grooves

Tool path strategy was discussed in the previous chapter as one method for mitigation of defects and improving the surface finish of EEM. Two overarching challenges exist in EEM: sub-contact patch grooves and entrance/exit features. The EEM process using a spherical tool often results in grooves that are perpendicular to the tool axis of rotation. The sub-contact patch grooves can vary depending on the toolpath direction in reference to the axis of rotation. Grooves are different

and more severe for perpendicular toolpaths (path is perpendicular to the axis of rotation), vs parallel toolpath. An example of sub-contact patch grooves can be seen formed in Figure 1 where distinct tool path lines are formed. These grooves create peaks independent of the starting surface due to material removal at the point of contact and lack of polishing at the ridges between tool passes.

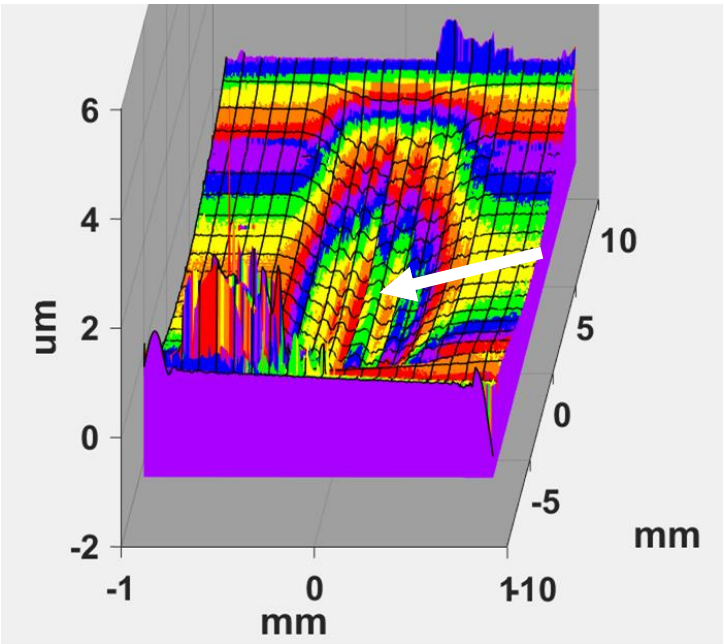

Figure 1. A polished groove where the toolpath was perpendicular to the axis of rotation. Arrow highlights deep grooves unique to perpendicular toolpaths.

2.2.2 **Repeatability of Measurements and Polishing**

One difficulty of polishing and measuring the polished surface is the ability to easily move the sample between the polishing machine and the measuring machine with a useful degree of accuracy and precision. In order to do so, a method must be devised so that the part can be moved between the machine used for imaging and the other used to polish the surface. This project proposes a part fixture that will allow the polished piece to be repeatedly placed, removed and replaced on both the polishing machine and the measuring machine (Zygo NewView 5000 Optical Interferometer) with limited movement from its intended position. Testing has also been completed to measure the accuracy of the process and quantify variations in measurements.

2.2.3 **Entrance and Exit Features**

Another defect commonly associated with EEM is the formation of valleys at the entrance and exit path of the tool. EEM material removal rate is distinctly tied to the dwell time of the tool at any given point. Extra dwell time not accounted for creates features that are unplanned and undesired. The locations where the tool enters and exits its polishing path are subject to unplanned dwell time as the stage remains static in the x-y plane and moves vertically away from the surface of the part. The result is that relatively deep holes are created at the entrance and exit points. Dwell time is also dependent on the acceleration and deceleration of the machine. (i.e. dwell time can be different in the center of the path from the ends) This project proposes unique toolpath, control, and machine configuration solutions that smooth these unwanted dwell time related features. See Figure 2 for an example of the entrance and exit features.

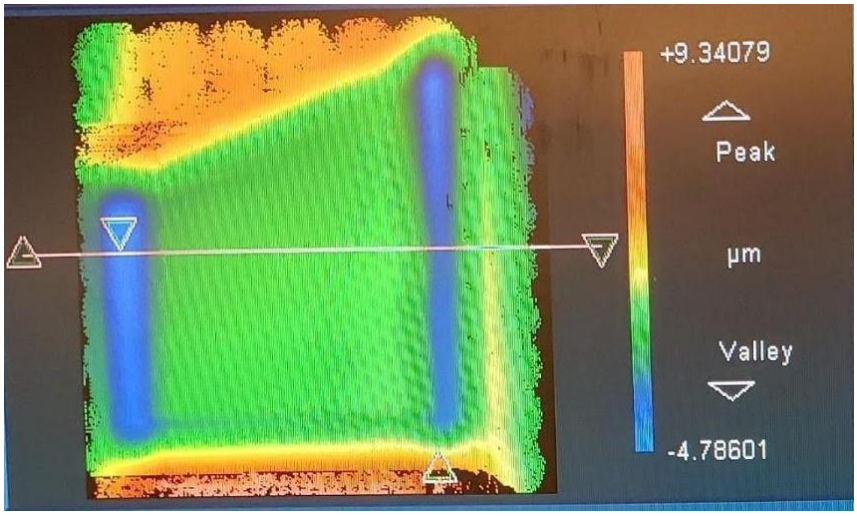

Figure 2. EEM polished surface with distinct entrance (right) and exit (left) grooves.

2.3 EXPERIMENTAL SETUP AND METHODS

Polycarbonate and acrylic plastic workpieces are fixed to the XY table of a 3 axis stage and polished with a rubber ball tool driven by a dental drill. The stage has a powerful customizable ACS controller. The XY table has 150 mm of travel in each direction. The dental drill is set at a 30 degree angle from the polishing surface. The dental drill is fixed to the Z axis (100 mm travel) of the stage and uses a seamless silicon ball with a .125 inch diameter. The dental drill can run from 1k to 40k rpm in 1k rpm increments. The drill uses feedback control to maintain rpm even under load although this tool is not capable of high torque. The work pieces are pre-turned on the Nanoform diamond turning machine to a 10-30 nm RMS surface finish. The polishing process is accomplished by pulling the rotating silicon ball through a slurry of aluminum oxide polishing compound. The polishing compound used is made of alumina particles with a 0.05 µm diameter. The workpiece is rinsed with water and then cleaned in the ultrasonic. Compressed air is used to dry the sample prior to surface roughness measurements. The sample is placed on a Zygo NewView 5000 scanning white light interferometer for surface measurement. The NewView software, Metropro, is used to take surface point data and can be exported to MATLAB for

additional analysis. A 50x objective with zoom set to 1.3x was used for all specimens. The RMS and PV values were calculated over the full field of view and averaged using four randomly selected areas. The spike removal feature was enabled. Figure 2 above is a polished measurement from Metropro.

2.3.2 Experimental Setup for Location and Repeatability of Measurements

The pallets and base plates we prepared by pre machining a center and offset hole in a .25 thick plate. The pallet pieces and stage base were fastened to a lathe with a locating pin in the center and a machine screw in the offset hole. The outer diameter was turned on the lathe. The base pieces were placed on a CNC fixture with the locating pin in the center. The magnet holes were machined, and the part was flipped to machine the locating grooves. This process was repeated for the pallets, but with machine screw holes and locating cones, respectively.

Magnets were glued into the base pieces under the locating grooves. Precision 440C bearing balls were epoxied into the cones on the pallets. The assembled pallets were re- faced with locating on the bearing balls for parallelism. Pallets were vibro-engraved with a separate number each for organization.

The Plastic work pieces for polishing were centered and epoxied to the top of the pallets. The assembled workpiece and pallet have the following naming convention. “PC_1” for polycarbonate workpiece number 1. Acrylic pieces are named “A_1”, etc. The polish tests are numbered 1,2,3.. Each test is distinguished by the workpiece and test number. Ex: “PC_2_53”.

2.3.3 Experimental Setup for Entrance and Exit Features

The baseline comparison for entrance and exit defects will be a linear z movement. Each line test will be 10 mm long. The tests will include radius, elliptical, diagonal, and interrupted straight line approaches. Tool RPM and load (z height) will be constant for all tests. 10k RPM and .5N will be used.

For each test the actual Z height will be recorded out of the controller. This will quantify the overshoot and therefore the load variation over the tool path. Load cell data will be recorded for each test and the z height and load cell data can be correlated.

Tests will be measured and analyzed on the Zygo NewView for comparison. The tests will be measured with a stitching function that will allow a measurement of the entire toolpath. The XYZ positional and load data will be analyzed vs time and vs NewView surface plot to correlate a map of tool location and load to material removal, and surface finish.

2.3.4 **Experimental Setup for sub-contact patch grooves**

Several toolpath varieties will be tested in comparison to each other. Each of these will be compared to a standard straight line tool path. Each of the tool path tests will be 10 mm long. The straight line equivalent feed rate will be calculated in order to control for dwell time. Each tool path will run with an equivalent straight line feedrate. Each tool path test will run with several loads, .5N and 1N. Each tool path test will be run with 5k and 10k tool RPM.

Each tool path test will be measured on a Zygo NewView optical profiler. Each test will be measured with 10x and 50x lenses. This will provide a surface form and finish comparison for each toolpath. The measurements will be taken at the midway point on the toolpath. This will keep the entrance and exit form defects out of the tool path measurements.

2.4 **EXPERIMENTAL RESULTS**

2.4.1 **Repeatability of Measurements and Polishing Plan**

The repeatability and measurement challenges of the system are addressed by designing and building a precise pallet system to allow removal and replacement of parts on the polishing stage and on the Zygo NewView 5000. The pallets form a kinematic coupling system that constrains 6 degrees of freedom. Kinematic coupling systems eliminate the rocking and sliding issues common in statically indeterminate systems. The system used for this project consists of a bottom fixture with grooves set at 120° from each other. Behind the grooves are glued neodymium magnets. The top pallet has three cones machined 120 degrees apart. These cones will have a tight tolerance 440C stainless steel bearing ball epoxied in each. The top pallet bearing balls sit in the grooves of the bottom fixture. The magnets in the bottom fixture provide a hold down force to keep the pallet on the fixture. See Figure 3 below for details on the kinematic coupling system.

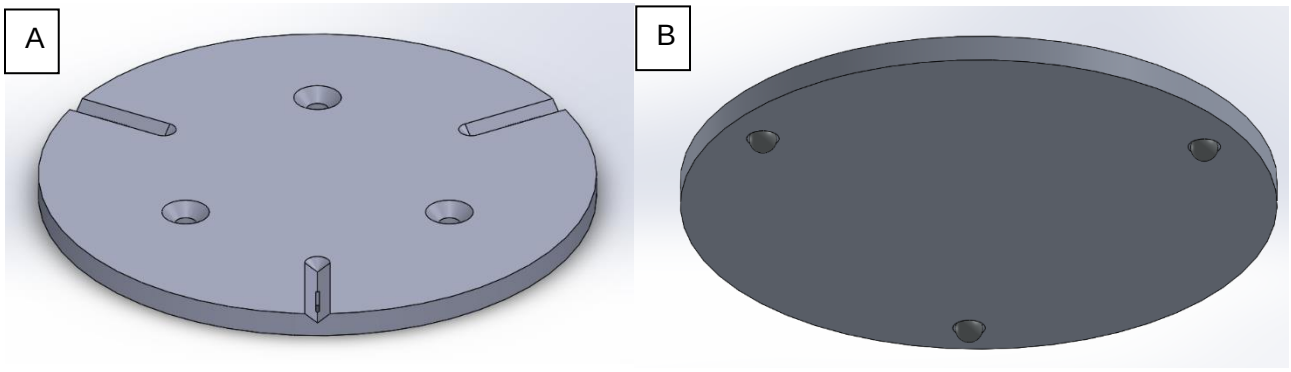

Figure 3. Kinematic coupling system. A: Bottom fixture for XY stage. (Bottom fixture for NewView is not pictured but has the same 3 grooves). The plate for the stage (pictured) matches the hole pattern on the b-axis. The plate for inspection (not pictured) will match the NewView stage hole

pattern. B: Top Pallet fixed to the bottom of each part to be polished. Pallets will be numbered for organization.

In order to determine the effectiveness of the kinematic coupling system, multiple images of the surface were taken on the NewView and repeatability was measured. A MATLAB code was developed to analyze the surface and compare the data to existing measurements from the NewView. These codes can remove outlier data, measure surface characteristics, and compare measurements. The code can import the data in Cartesian or polar coordinates. Figure 4 shows sample output from this plotting code. The code is used to measure the repeatability of the pallet system and the noise floor of the NewView by comparing similar measurements and determining the offset between the results.

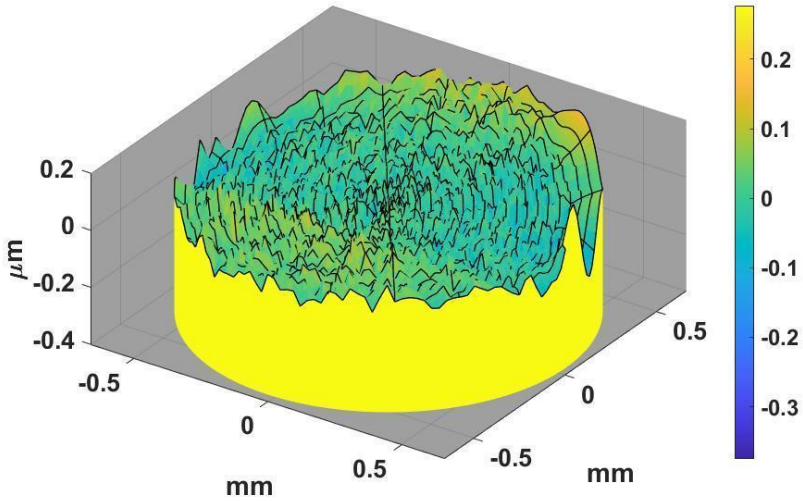

Figure 4. Polar Data Based Plotting Results for a Line Polishing Test. The results from this method closely match the form and color scheme of the output shown in the NewView.

The Cartesian import method is simpler to index and manipulate than the polar method. To analyze and measure the noise floor a single spot on an unpolished surface is measured several times over a span of time without moving the workpiece on the NewView. The measurements are subtracted from each other to calculate the noise floor. It was found that the noise floor of the NewView is around 2 nm. See Figure 5 and Figure 6 for noise floor results.

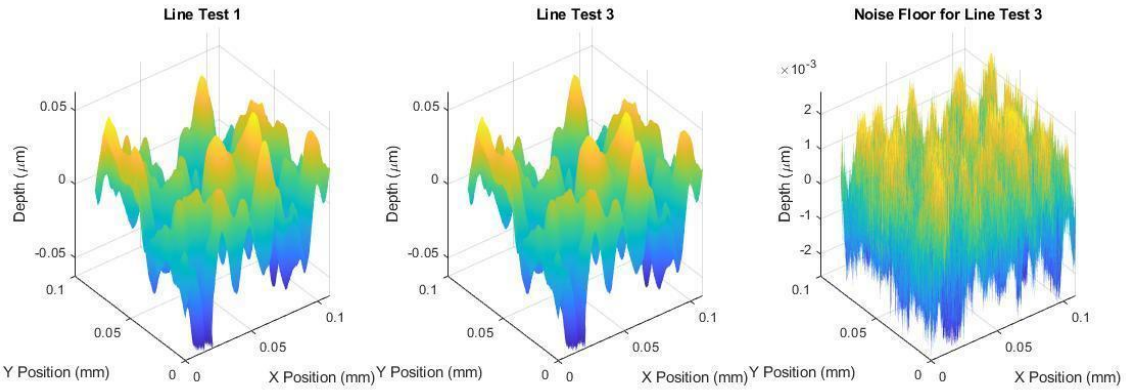

Figure 5. Noise Floor Measurements. The noise floor (Right) is a subtraction of the two measurements taken of the same point (Left). The code was tested by subtracting one measurement from itself. This resulted in a zero matrix. The calculated noise floor is ~2 nm.

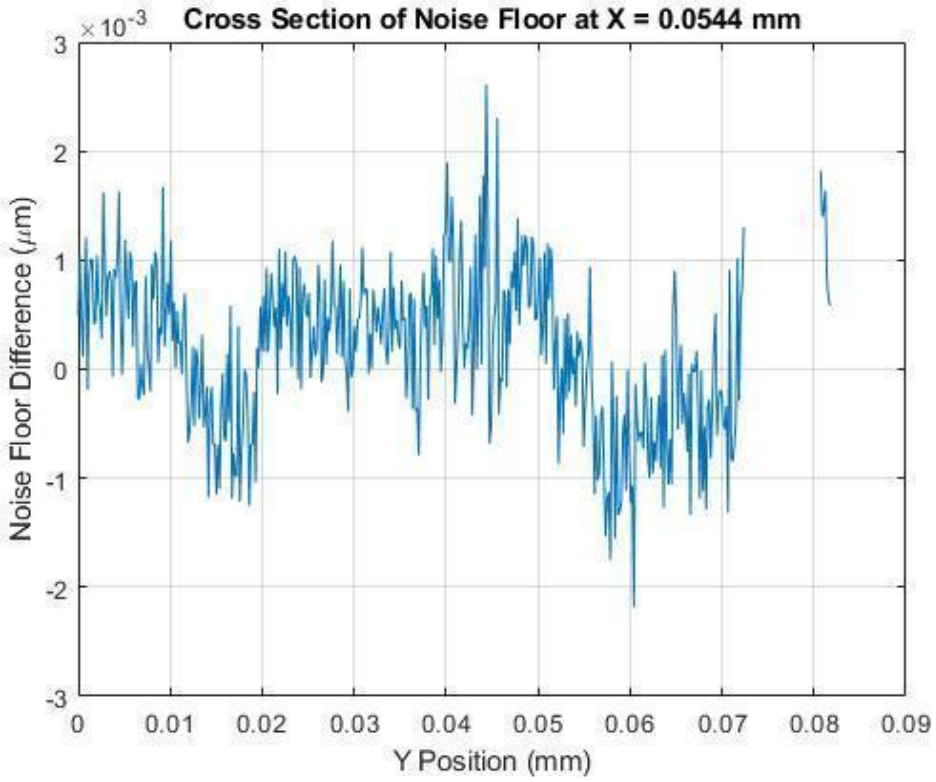

Figure 6. Noise Floor Measurement Cross Section. The noise floor measurement was sectioned at several x values and observed. Noise floor data points were within ~± 1nm.

For repeatability tests the measurements were taken in the same manner as the noise floor tests, but the workpiece was removed and reattached repeatedly to gather data on the consistency of the kinematic coupling setup. The code took this data and compared each sequential measurement to the initial reference measurement for the given test. The repeatability is consistent in the Z around 5nm. The XY repeatability of the kinematic coupling system was found

to be around 2-3 µm for each axis. Sample output for this code is shown in Figure 7 and Figure 8 below.

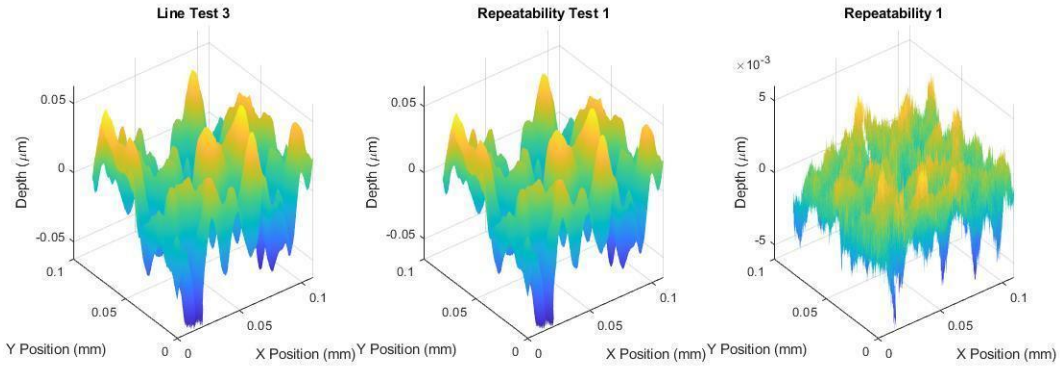

Figure 7. Repeatability Measurements. The repeatability (Right) is a subtraction of the two measurements taken of the same point(Left) after the pallet was removed and replaced again on the NewView. The measured and calculated repeatability was ~2-3um in the X and Y, and ~5 nm in the Z.

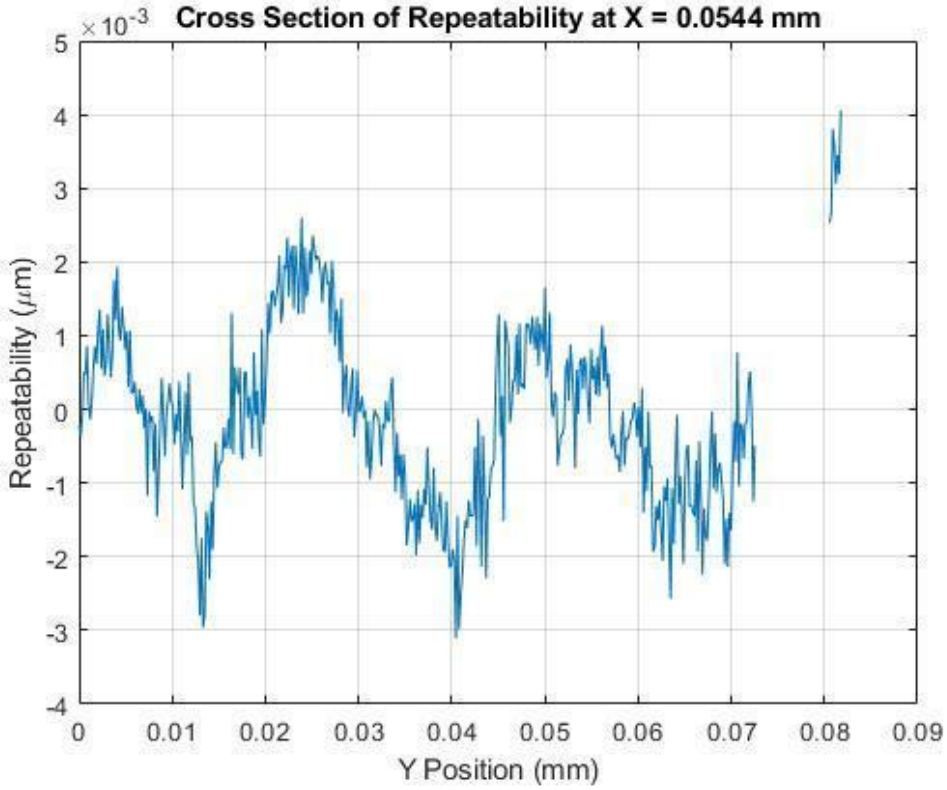

Figure 8. Repeatability Measurement Cross Section. The noise floor measurement was sectioned at several x values and observed. Repeatability data points were within ~ +2nm/-3nm.

2.4.2 **Entrance and Exit Features**

The undesirable entrance and exit features will be remedied by redesigning the polishing motor/ tool setup. The entrance and exit toolpaths will also be adjusted to eliminate these features. The XYZ stage acceleration will be studied and adjusted to optimize dwell time over the surface. The Proportional gain of the PID controller will be optimized to eliminate motion overshoot. This overshoot translates to increased load in entrance locations along the toolpath.

Preliminary results for tool path adjustments are promising. Several entrance strategies were tested and the load cell data was recorded. In comparison to the straight z motion, a simple radius entrance yielded significantly more consistent load. This strategy was effective for slower relative motion, but struggled to eliminate overshoot for faster motion. See Figure 9 below for a comparison of load profiles between straight and curved entrance paths.

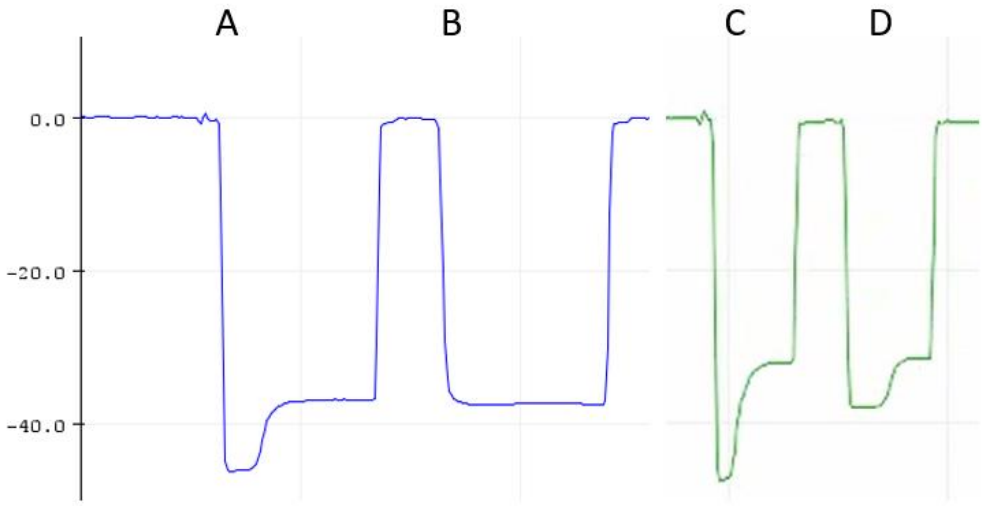

Figure 9. Load Cell Comparison for Straight and Curved Entrance Paths. The load profiles A and C are straight line Z motions. B and D are from curved paths. A and B are from relatively slow motion compared to the faster motion in C and D. B shows the curved path's ability to alleviate overshoot effects for slow motions. D shows that the curved path still had overshoot for fast motions.

The stage position was recorded for the straight line and curved entrance paths. The position data was tabulated and plotted to show the reduction in overshoot for curved entrance paths. For slow motion the overshoot was not observed on the curved toolpath. See Figure 10 below for positional data straight and curved entrance paths.

The curved paths show promise for slower motions, but the load profile will need to be more consistent for straight lines and faster motion. The Stage controller's PID gains are being explored and adjusted for better system response.

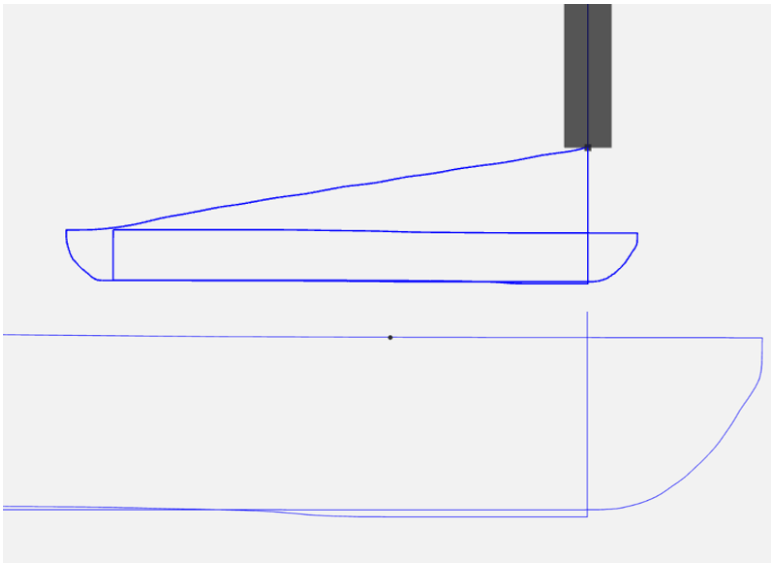

Figure 10. XZ Positional Comparison for Straight and Curved Entrance Paths. The curved entrance path did not have significant initial overshoot of steady state positional error. The straight line Z motion had both significant overshoot and steady state error was also observed.

2.4.3 **Sub-contact Patch Grooves**

Sub-contact patch groove correction experiments are underway. In order to reduce the size of the grooves, optimally eliminating them, various tool pathing options are being investigated. This experimentation will result in building unique toolpath solutions that smooth these sub-contact patch grooves.

2.5 **CONCLUSION**

Preliminary findings have been reported on building a sub aperture polishing machine that can be easily transferable to industrial applications. EEM, though well documented in finishing operations, is further explored on a small scale with corrective precision. Fixture manufactured and tested, showing necessary repeatability and accuracy. Undesirable entrance and tool features alteration is in work and show improvement from previous work by investigating different tool paths and compensations. Tool path modification and machine motion for better surface finish and figure are being demonstrated. These controller parameters and toolpath modifications will be optimized for manufacturing efficiency. Additional work to be completed in order to build an "all-in-one" measuring and polishing setup that can isolate defects and repair surfaces effectively.

REFERENCES

1. Mori, Y*, Elastic Emission Machining*. Precision Engineering, Vol 9, pp 123-128, (1987).

2. Ando, M, *Processing Efficiency of Elastic Emission Machining for Low-Thermal-Expansion Material.* Surface and Interface Analysis, Vol 40, pp 6-7, (2008).

3 MULTI-LENS ARRAY: MODELING OF THE MICROINDENTATION PROCESS TO CREATE LENS ARRAY FEATURES ON A MOLD

Sumit Gundyal
Graduate Student
Dr. Mark Pankow
Director of the PEC
Assistant Professor
Mechanical and Aerospace Engineering

ABSTRACT

This report addresses the design of multi-indenter die and development of indentation strategies to create the negative features of a microlens array on a mold. A material parameter study is performed using the commercial finite element analysis software Abaqus™ to understand the effects of different indent patterns and processes on the pile-up and the maximum force required and shape error. Al 1100 is selected as the mold material based on this study. Glassy carbon is used as the die material. Multiple Indentation strategies are explored to understand the best die shape to reduce form error.

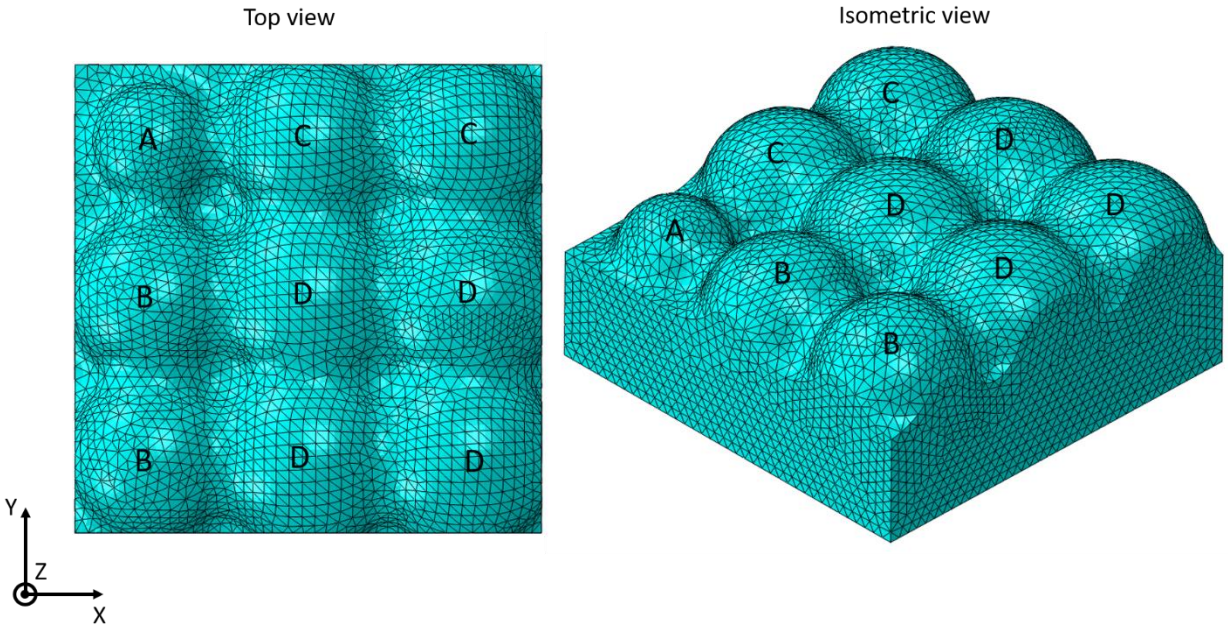

3.1 INTRODUCTION

Microlens arrays have a series of miniature lenses that are arranged in a two-dimensional grid on a supporting substrate. Individual lenses can have circular apertures with no overlap between each other and can be placed in a hexagonal or square packed arrangement. If an overlap is allowed between each of the individual lenses, square apertures and hexagonal apertures can be formed. Fill-factor (active refracting area) up to 100 % can be achieved by increasing the overlap between each individual lenses. Figure 1 (a) and Figure 1 (b) shows an example of a square packed lens arrays and hexagonally packed lens arrays [1].

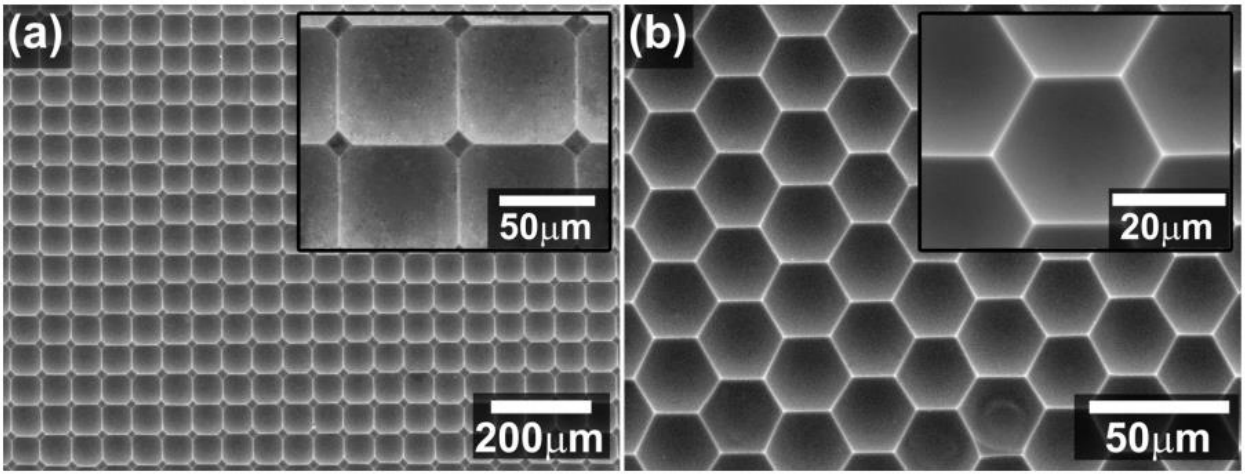

Figure 1. FE-SEM images of (a) square packed microlens arrays and (b) hexagonally packed microlens array with overlap between each individual lens [1].

Figure 2 shows the cross-section of microlens arrays and a trace of collimated light rays through a medium of lower refractive index to a point behind the lens. Depending on the application, microlens arrays can act as light collectors or beam collimators. As beam collimators, microlens arrays find applications in display screens or high power lasers by producing higher output intensity, while lowering the power consumption. Microlens arrays are used as light collectors in Charge-Coupled Device (CCD) image sensors which are used for digital imaging technologies. Microlens arrays are also used in light field technology which is used to create a virtual reality which a human eye cannot distinguish from the real world. The main motivation of this work is to devise a method to fabricate microlens arrays for the Virtual Reality (VR) headsets.

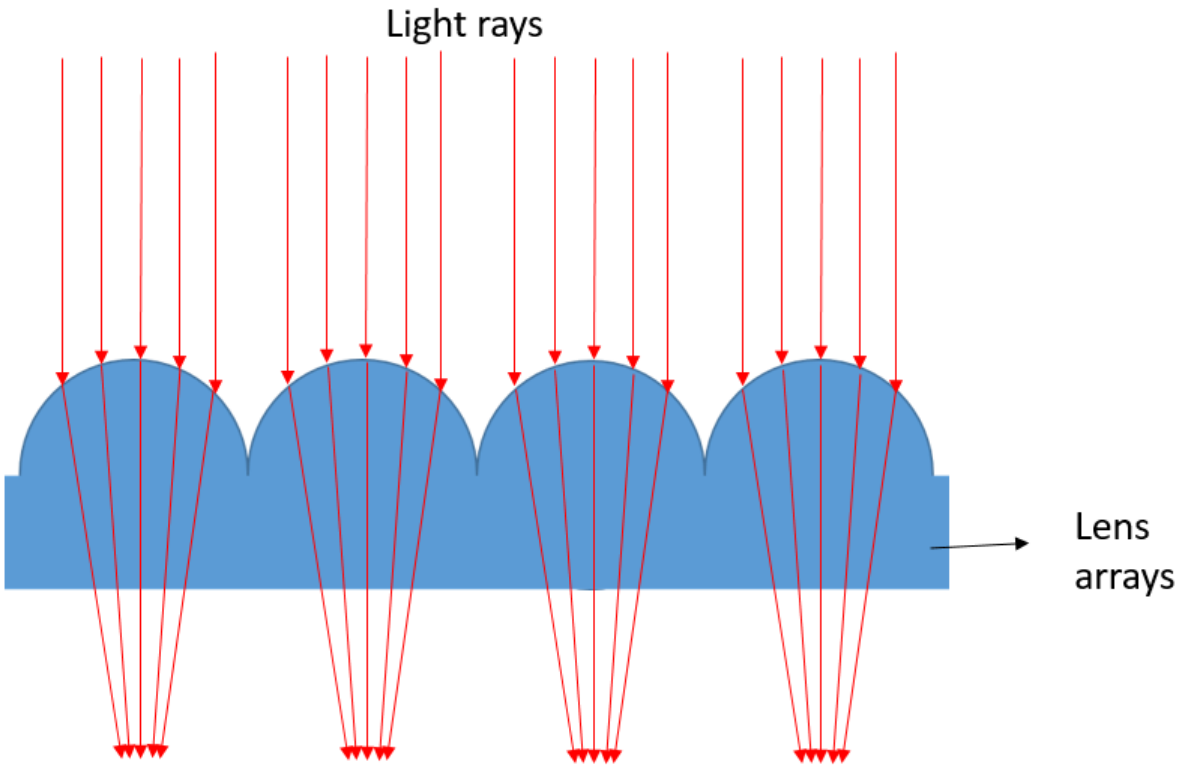

Figure 2. Trace of light rays through microlens arrays.

Two methods are used to fabricate these lens arrays: direct and indirect methods. In the direct method, surface tension is utilized in the formation of the lens surface at the liquid-air interface. The material is usually heated until it reaches a thermoplastic or liquid state. Thermal reflow method, microplastic embossing method, and microdroplet jetting method are some of the direct methods to fabricate a microlens array. Some examples of the direct method include thermal reflow, microplastic embossing, and microdroplet jetting. However, this method has its limitations. The shape of these lenses can only be minimally controlled which makes it difficult to achieve the required form accuracy of the features [2, 3, 4]. These methods are simple and cost-effective but come with a trade-off in precision.

The indirect method of microlens fabrication requires the fabrication of the mold with concave features. This mold is then used to create the final lens array using techniques such as injection molding, hot embossing or UV molding. The form accuracy of the final microlens array is directly dependent on the precision of the geometry of these concave features. Microelectromechanical system (MEMS) based technologies and ultraprecision machining are two categories in which these methods are classified. The standard MEMS methods utilize photolithography to generate patterns on the mask layer and chemical reactions to etching the curvature of microlens onto the substrate [5, 6, 7]. However, this approach requires expensive equipment and complicated procedures. Ultraprecision machining technologies utilize diamond micro-milling and single point diamond turning to fabricate microstructures and nanostructures with good uniformity in a large area [8, 9, 10]. Good surface roughness of R_a 5 nm is achieved. However, this method requires each microlens to be prepared one by one which increases the operation time and cost. An

alternative of high-speed indentation using spherical convex dies is one of the methods to create concave spherical features on the mold.

This work specifically focuses on investigating the process of fabricating a mold by indentation of convex spherical dies to create concave spherical features. Indentations at a frequency of 1 KHz are being aimed. This work, however, investigates indentations carried out quasi-statically. Figure 3 shows the required specifications of the microlens arrays. Finite element analysis is used to perform indentation simulations to understand the plastic flow of the mold material and to study the form accuracy of the indents formed. The indentation process involves many factors that affect the form accuracy of the indent. During the indentation process, the die experiences a reaction force which causes the die to compress elastically changing the actual indent depth and thus the indent shape at the end of loading. As the mold undergoes elastic-plastic deformation during indentation, the shape of the indent changes due to elastic springback. The volume of the material displaced during indentation accumulates as pile-up surrounding the indent. For a single indent this is not an issue, however, for multiple indents the pile-up will build-up to the point where it could impede the movement of the impactor and change the final shape of the indent. Also, the pile-up from one indent will change the shape of previously made indents in that area. Some researchers have attempted to solve the form errors due to the elastic deformation of the die and the elastic springback of the mold. However, the issue of compressional deformation of the surrounding indents caused due to the close-packed arrangement of the lens features is not yet studied.

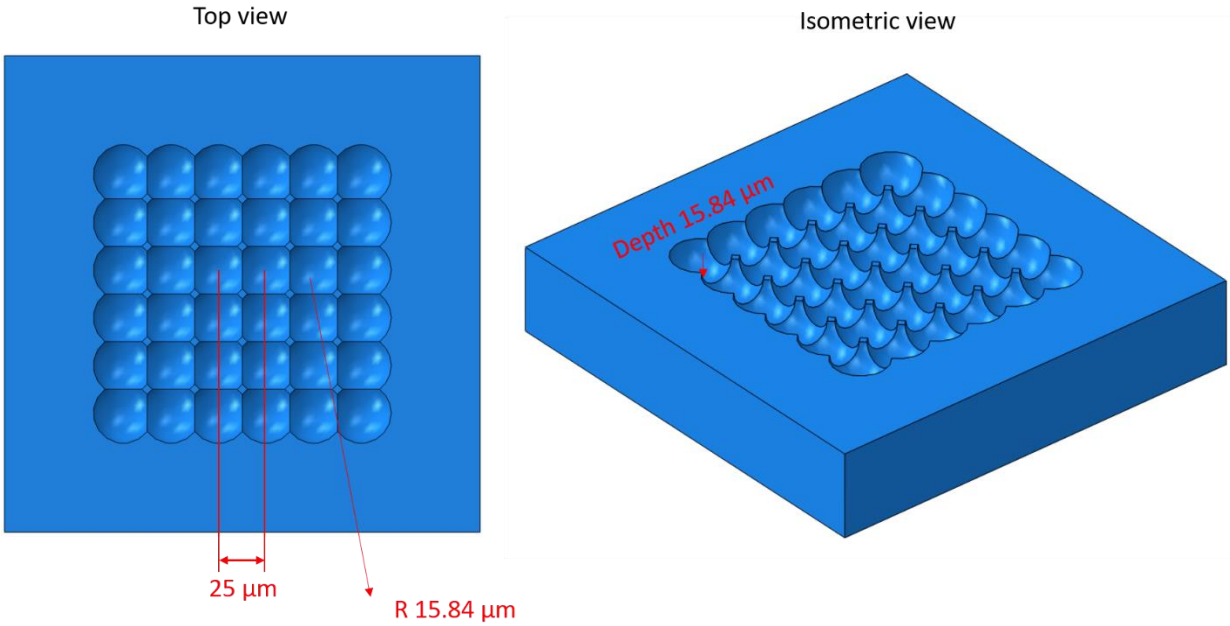

Figure 3. A 6x6 concave spherical lens features on a mold. Diameter of each feature = 15.84 µm, pitch = 25 µm, depth = 15.84 µm.

3.2 **RESEARCH BACKGROUND**

Jiwang Yan et al. [11] in his paper has proposed a way of creating concave spherical features on metal materials made of oxygen-free copper and electroless - plated nickel using piezo actuated high-speed repetitive indentation and then diamond turning the pile-ups generated around the indents. The spherical die was made of a tungsten carbide ball (tip radius = 500 μm, roundness tolerance within 0.1 μm, surface roughness is 155nmRz and 18nmRa). The authors have shown clearly in Figure 4 (a) the depth error of the indent formed after 5 indentations in the same place due to the springback of the mold material and the elastic deformation of the machine elements including the die holder and the tool post. The nominal indentation depth is 20 μm, but the actual depth achieved is 11 μm. Figure 4 (b) also shows that a form error of approximately 0.65 μm is evident by fitting a curve of the same radius to the indent profile. The effect of diamond turning to remove the material pile-ups at different depth of cuts is also discussed. It is shown that diamond turning at higher depth of cut leads to the formation of exit burrs as shown in Figure 5(a) and Figure 5(b). The pitch of the indents studied in this paper is high enough so that no interference is caused between adjacent indents. This ensures that the shape of the surrounding indents is not disturbed.

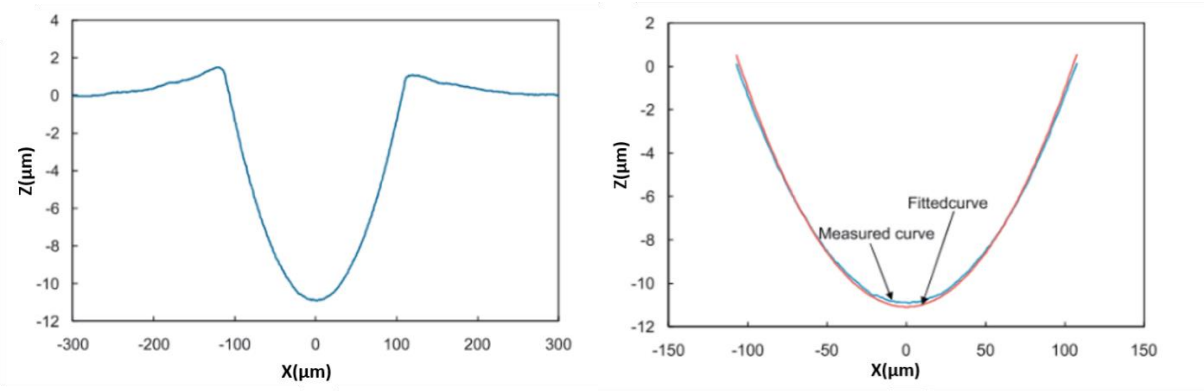

(a) (b)

Figure 4 (a) Indent profile showing depth error (b) comparison of indent profile and best fitted curve of the same radius [11].

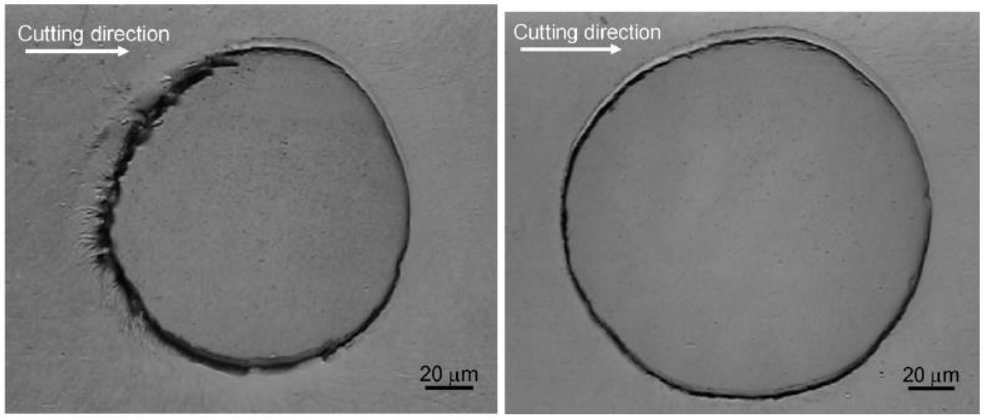

(a) (b)

Figure 5. SEM micrographs of indents after diamond turning: (a) depth of cut = 2 μm and (b) depth of cut = 1 μm [11].

Yaqun Bai et al. [12] investigated using finite element analysis technique to study both single-indentation and multi-indentation on copper to a depth of 0.1 mm using tungsten steel balls of diameter 1.0 mm. Though the die size and the depth of the indent in the study of Yaqun Bai et al. are much larger compared to the requirements for this study, it gives some important insights. Based on the author's study, factors affecting the form accuracy, such as springback at the compressed area of single indent and compressional deformation at the adjacent area of indent arrays were determined and were verified with the experimental results. A critical pitch necessary to prevent compressional deformation of adjacent indents was found by conducting a series of seven experiments involving three adjacent indents. The distance between two adjacent indents, pitch (t) was defined by a coefficient k multiplied by the indent diameter (t = kd) [12]. Figure 6 shows the contour plot of a set of seven indents using finite element analysis, each set having three indents at different pitches. Figure 7 shows matching results for a similar experiment conducted. Thus, a critical pitch for a k value of 2.36 showed no compressional deformation in the adjacent indents. These experiments and simulations were conducted by indenting a die of 1.0 mm diameter to a depth of 0.1 mm. A die compensation method was also proposed. The form error was calculated by subtracting the ideal indent profile from the actual indent profile. By compensating the form error to the die shape the maximum form error was reduced from 2.6% of the indent depth to 0.0075% of the indent depth.

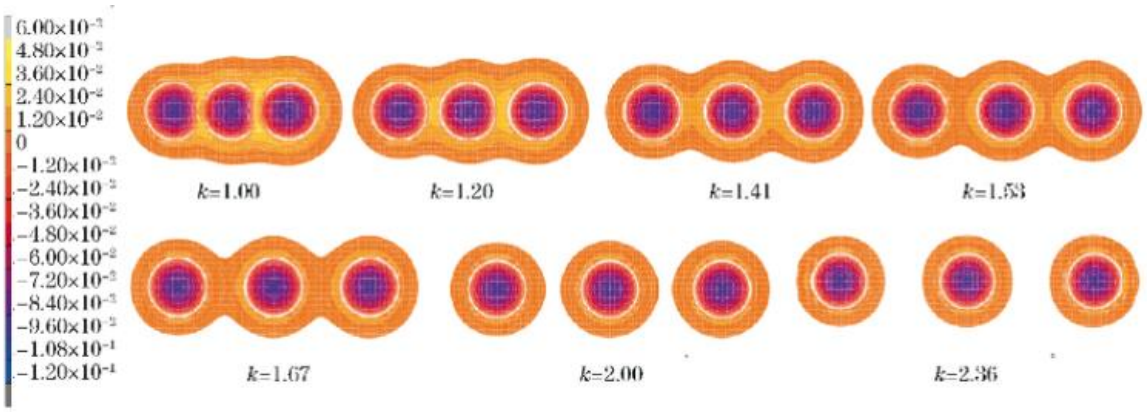

Figure 6. Contour plot of seven indents with different pitches in simulation. Coefficient k is the ratio of pitch (t) and final indent diameter (d) (k = t/d) [12].

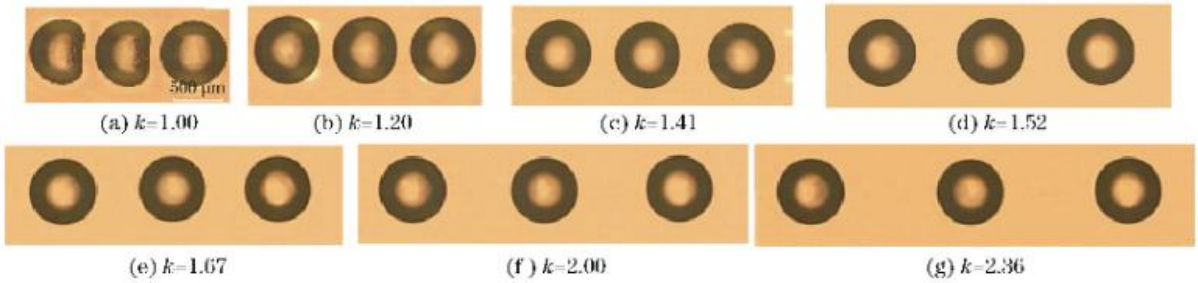

Figure 7. Contour plot of indents made at different pitches in the experiment after the pileups were removed using micro-grinding process. Coefficient k is the ratio of pitch (t) and final indent diameter (d) (k = t/d) [12].

Although, compared to the current requirements for our work, Jiwang Yan et al. [11] and Yaqun Bai et al. [12] used a die diameter around 30 times greater and an indent depth around 6 times greater, they provide important insights which is also applicable to the scale of the indents required for our work. However, the work by the above authors does not propose any method to create features which are tightly packed with a pitch less than the diameter of a single indent. To create arrays of closely packed indents, a die with a single feature will not help as it would not prevent the compressional deformation of adjacent indents. A die having multiple features which implements novel indentation strategies must be explored.

E Zdanowicz et al. [13] used a diamond die having structured nanofeatures in an area of 20 μm x 20 μm to transfer features to a mold surface. The nanocoining process was carried out on a 6 mm wide ring on a 1.25” diameter stainless steel plated with a 380 μm thick layer of electroless nickel sample at a rate of 1 kHz by using an actuating system.

To carry out finite element simulation study of the microindentation procedure it is important that the FEA models are validated against well-calibrated experimental tests. Nanoindentation test is a good calibration experiment. A. Karimzadeh et al. [14] and S.W. Moore et al. [15] had performed finite element simulations of nanoindentation on elastoplastic materials Al 1100 and Al 6061. A

Berkovich indenter is typically simplified to a theoretically equivalent 70.3^{o} conical die. They compared the results obtained from the simulation by modeling the Berkovich die as an axis-symmetric conical rigid die and as a 3D Berkovich die and found conflicting results. They also investigated the validation tests of the finite element simulations. A. Karimzadeh et al. and S.W. Moore et al. used a non-sharp conical die to conduct the simulations. A. Karimzadeh et al. found good agreement between the values of Young's modulus obtained from the nanoindentation test and the uniaxial tensile test. Good agreement was also found for the force-displacement curves. However, the force-displacement curves obtained by S.W. Moore et al. in the simulations had significantly lower loads than the experiments. Warren and Guo [16] attributes the lower loads to the machining-induced residual stresses that significantly affects the force-displacement curves. H. Lee et al. [18] showed that friction coefficient does not affect the force-displacement curves.

Electronics in today's age with their continued reduction in size demand for small size optics. Digital projectors use microlens array to focus light to generate the image to be projected. Similarly, 3D displays free of 3D glasses also use the arrays of microlens to create the desired effect. Section 2.1 Figure 1 shows the cross-sectional view of a microlens array and a ray trace of a single lens. To create such a lens array, a male die made of a hard material with around 4-9 lens features shown in Section 3.1 Figure 2 needs to be pushed rapidly into a mold specimen by an actuator to plastically deform the surface and transfer the die features on to the mold. This mold will be used in a conventional compression or injection molding machine to create the final lens array that will be like as shown in Section 1 Figure 1.

The aim of this report is to develop a validated FEA model to understand this microindentation process to fabricate the microlens array. Glassy carbon is used as the die material owing to its high compressive yield stress and ease of carrying out focused ion beam (FIB) milling process to create micron length features on it. This process involves problems: spring back of the indents; shape distortion of the surrounding indents due to plastic flow of successive indents; deformation of the die during the indentation; and pile-up of the mold material around the indents. These issues negatively affect the optical performance of the microlens array. This report attempts to study these issues in more detail and mitigate them by designing a die and developing indentation strategies.

To create around 4 million lenses quickly the indentations must be done fast. Strain rate dependency of the mold material must be accounted for to understand the effect of fast indentation. Currently, due to limitations in data acquisition from high-velocity indentation experiments, correlation of FEA models to fast indentation experiments is not addressed in this report. Although, the effect of dynamic indentation is presented.

3.3 OVERVIEW OF MULTI-INDENT PROCESS

To fabricate a mold with millions of lens features on it, the indentation process has to be done fast. An indentation rate of 1 KHz will be used to create microlens arrays (3840 x 2160 pixels, 4K resolution) which is a total of 8294400 pixels. Indenting with a die having multiple lens features on it helps to transfer the features on to the mold in a faster and efficient way. The specifications

of the desired multi-lens array mold are shown in Figure 1. The radius of the spherical lens is 15.84 µm, the pitch is 25 µm and the indent depth is 15.84 µm. A 3x3 die was designed as shown in Figure 2. As the features on this die have uniform size, this die will be referred as 3x3 die (U) in the rest of the thesis for convenience. Each hemisphere is of radius 15.84 µm with a pitch of 25 µm and a fillet radius of 5 µm at the intersection of the spheres. The edges in the desired mold have mathematically sharp edges which is not possible to be fabricated due to manufacturing limitations. For the same reason, the die is modelled with filleted edges which also aids in carrying out FEA simulations without causing any element distortion and singularity issues.

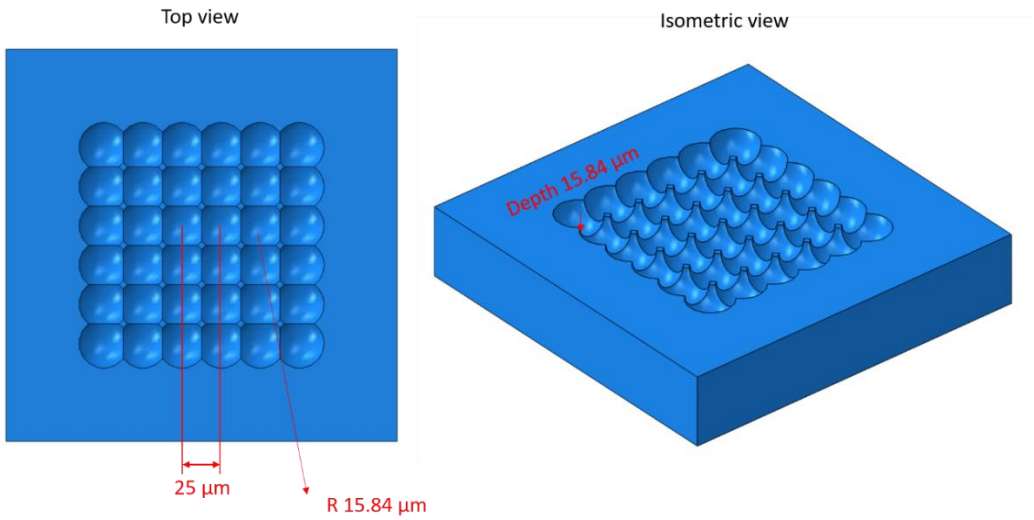

Figure 1. A 6x6 concave spherical lens features on a mold. Diameter of each feature = 15.84 µm, pitch = 25 µm, depth = 15.84 µm.

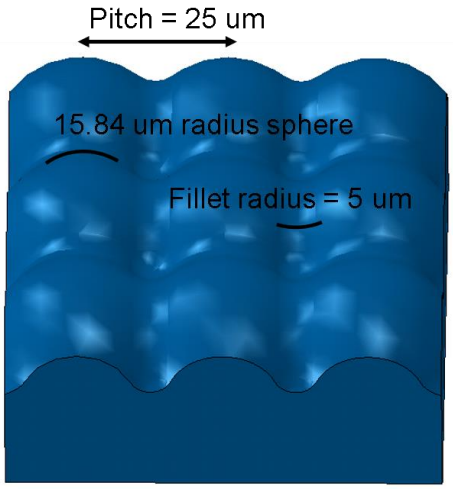

Figure 2. CAD model of the 3x3 die. Die referred as 3x3 die (U).

Terminologies to refer indents in an indent array is important to avoid any ambiguity. For this purpose, the vertical array of indents would be called ‘columns’ and the horizontal array would be called ‘rows’. Figure 3 shows a schematic of a sample lens array. Three preliminary indentation strategies as shown in Figure 4 are discussed and analyzed. In the first indentation strategy, the 3x3 die skips three columns of features for every successive indentation without any overlap of indents. This would account for a 3x6 lens arrays in two indentation steps. A total of 921,600 indentation steps would be required to create arrays for a 4K resolution display and the total time of fabrication at a rate of 1 KHz would be around 15 minutes. In the second indentation strategy, the 3x3 die skips two features for every successive indentation with one column overlap of indents. This would account for a 3x5 lens arrays in two indentation steps and a total of 2,073,600 indentation steps for a 4K resolution display would require a total time of around 34 minutes. In the third indentation strategy, the 3x3 die skips one column of features for every successive indent with a two column overlap of indents. This would account for a 3x4 lens arrays in two indentation steps. This strategy will take 8,294,400 indentation steps, the most compared to the previous two strategies which accounts for a total fabrication time of 138 minutes.

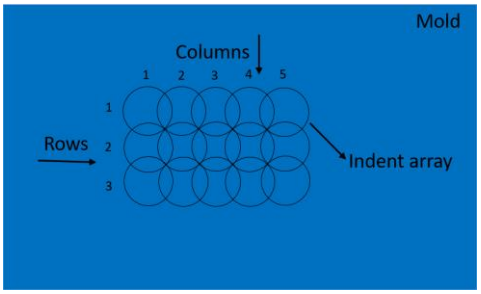

Figure 3. Plan view explaining the terminologies of column and rows to refer to indent.

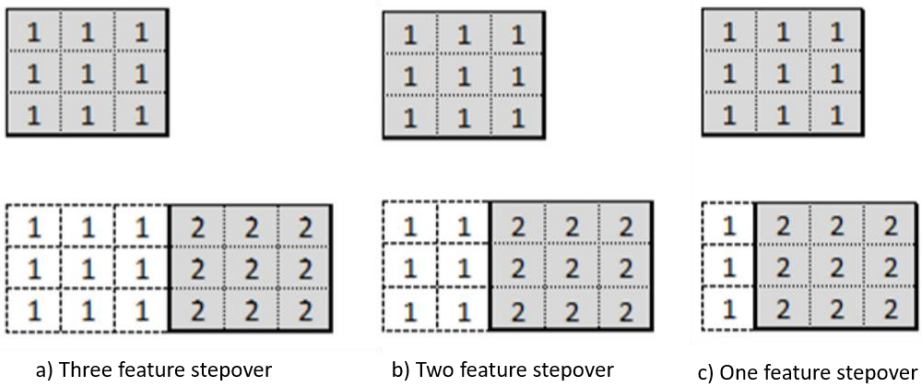

Figure 4. Preliminary indentation strategies where each square represents one lens feature. The number represents the indent order and the gray represents the current indent. 3x3 die (U) is used for the indentation.

3.3.1 Finite element model setup for the preliminary indentation strategies

Abaqus/Explicit which implements the explicit solution method to solve the model was used for this simulation as it solves contact problems with greater ease as compared to implicit procedure. Since a quasi-static process is, by definition, a long-time solution, it is often computationally expensive to simulate an event in its natural time scale. The advantage of using Abaqus/Explicit is that the event can be accelerated while keeping inertial forces very low leading to faster solution times [17].

A finite element model of the indentation procedure using a 3x3 die was developed. The die was meshed with C3D10M (10 noded tetrahedral quadratic elements) as this is the preferred element to model finite sliding surface to surface contact conditions to get accurate results. The mold specimen was meshed with C3D8R: 3D continuum 8 noded reduced integration elements. Figure 5 shows the meshed 3x3 die and mold specimen. The mesh on the mold was made finer in the central region where the indentations would be made as compared to a coarser mesh in the remaining region to save some computational time. Non-linear geometry option was used in the finite element simulation. Arbitrary Lagrangian Eulerian (ALE) adaptive mesh domains was defined for the mold specimen as it involved large deformations. The mold specimen was fixed at the bottom.

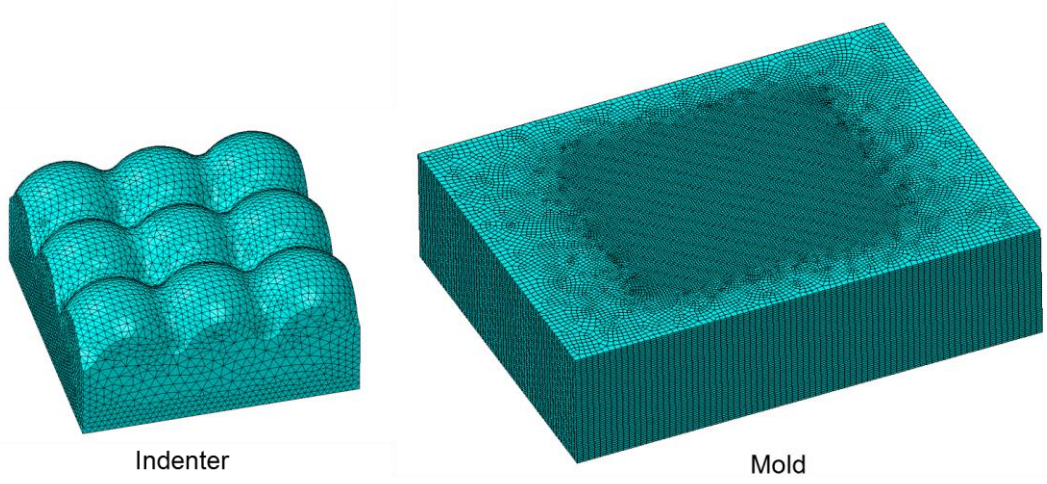

Figure 5. Mesh pattern of the 3x3 die and the mold specimen: Die meshed with C3D10M elements and Mold specimen meshed with C3D8R elements.

Surface-to-surface contact condition was used with the die as the master surface and the mold surface as the slave surface since a master surface can penetrate the slave surface. The mechanical properties of Al 1100 H14 obtained from the correlation of nanoindentation experiments and FEA modeling and are presented in Table 3-1**.** These properties were used for

the material definition of the mold. Isotropic hardening material behavior was employed to model the plasticity region of the mold material. The 3x3 die was modeled as a perfectly linear elastic material with glassy carbon properties obtained from the nanoindentation experiments in section 2.1.2. As Abaqus / Explicit solver was used for the analysis, a load step and an unload step time of 1.2 e-5 seconds was employed. Mass scaling with a factor of 1000 was used to artificially decrease the computational time needed for the simulation. The loading rate and the mass scaling value chosen were suitable enough to ensure that the kinetic energy was always below 5% of the internal energy of the whole model during the simulation, thus satisfying the conditions for the simulation to remain quasi-static. An indent depth of 8 μm was used for all the indent strategies. Penalty based friction formulation was employed as the interaction between the die surface and the mold surface in simulations with frictional contact.

Table 3-1: Aluminum alloy 1100 H14 used for FEA modeling.

	Modulus (GPa)	**Yield Stress (MPa)**	**Tangent Modulus (MPa)**
Al 1100 H14	60	120	102

3.3.2 Finite element analysis results for the preliminary indentation strategies

Figure 6 (a) shows the Z contour plot of a desired indent arrays formed with the three feature stepover method. Figure 6 (d) shows the cross section view A-A' of the desired indent plot. Figure 6 (b) shows the Z contour plot of the indents formed in the simulation with the three feature stepover method. The maximum depth achieved in the simulation was around 7.1 μm. Elastic deformation of the die and the springback experienced by the indent after unloading causes the decrease in the maximum depth achieved. The third column of indents experienced compressional deformation as shown in Figure 6 (b) which is clearly visible in the cross section view of the indents in Figure 6 (e). Figure 6 (c) shows the error plot (actual profile – desired profile) of a three feature stepover method. Areas with black color are close to zero error. The third column of indents shows significant error due to compressional deformation. The error in the remaining indents shown in the shade of red is due to the the elastic deformation of the die and the springback of the indent after unloading. These errors can be easily visualized with the cross section view of the error plot across A-A' shown in Figure 6 (f).

Similar sets of plot are shown in Figure 7 for a two feature stepover method. The compressional deformation in the case of a two feature stepover is less intense compared to that in a three feature stepover. The overlap in the third column of indents reduces the compressional deformation in the second and first column of indents. The error in the remaining indents shown

in the shade of red is due to the the elastic deformation of the die and the springback back of the indent after unloading.

Finally, Figure 8 shows a similar set of plots for a one feature stepover method. The compressional deformation in the first column of indents is considerably reduced and is not clearly visible in the simulation contour plot in Figure 8 (b) nor in the cross section across A-A' of the simulation plot in Figure 8 (e). However, the compressional deformation can be noticed in the error plot (actual profile – desired profile) in Figure 8 (c) and the cross section across A-A' of the error plot in Figure 8 (f). The compressional deformation is considerably reduced in the case of the one feature stepover method.

The one feature stepover method appears to be the most promising in terms of reducing the compressional deformation, but this method takes the most amount of fabrication time. As compared to the three feature stepover method, the maximum error in the one feature stepover method is reduced by about 75%. An indentation scheme to create a 2D array to understand the complete effect of this method on the quality of the indents will be discussed further.

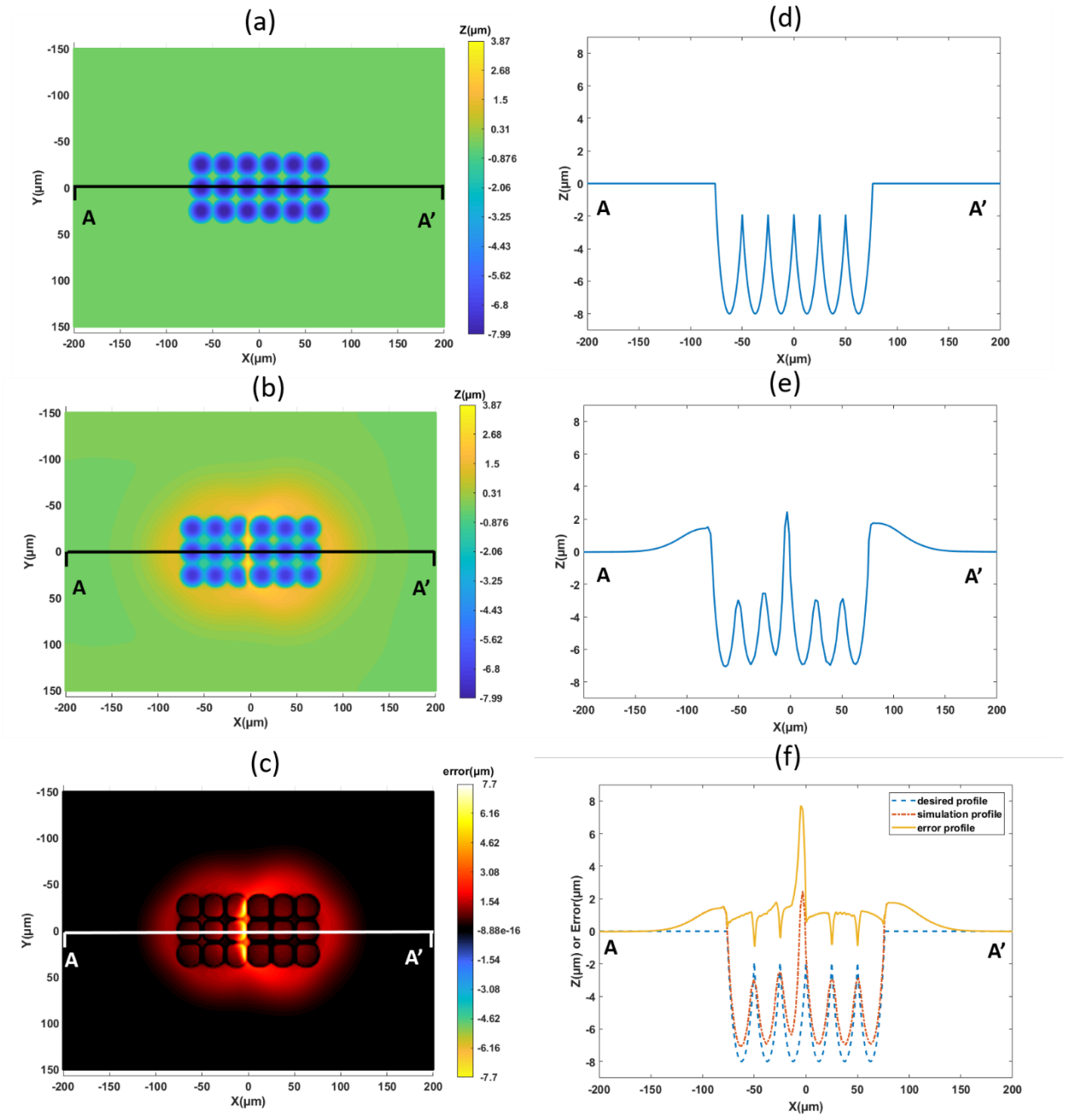

Figure 6. Three feature step over. (a) Desired contour plot. (b) Simulation contour plot. (c) Error plot (actual profile – desired profile). (d) The cross-section view across A-A' of desired plot shown in (a). (e) The cross-section view across A-A' of simulation plot shown in (b). (f) Comparison of the desired, simulation and error plot across cross-section across A-A'.

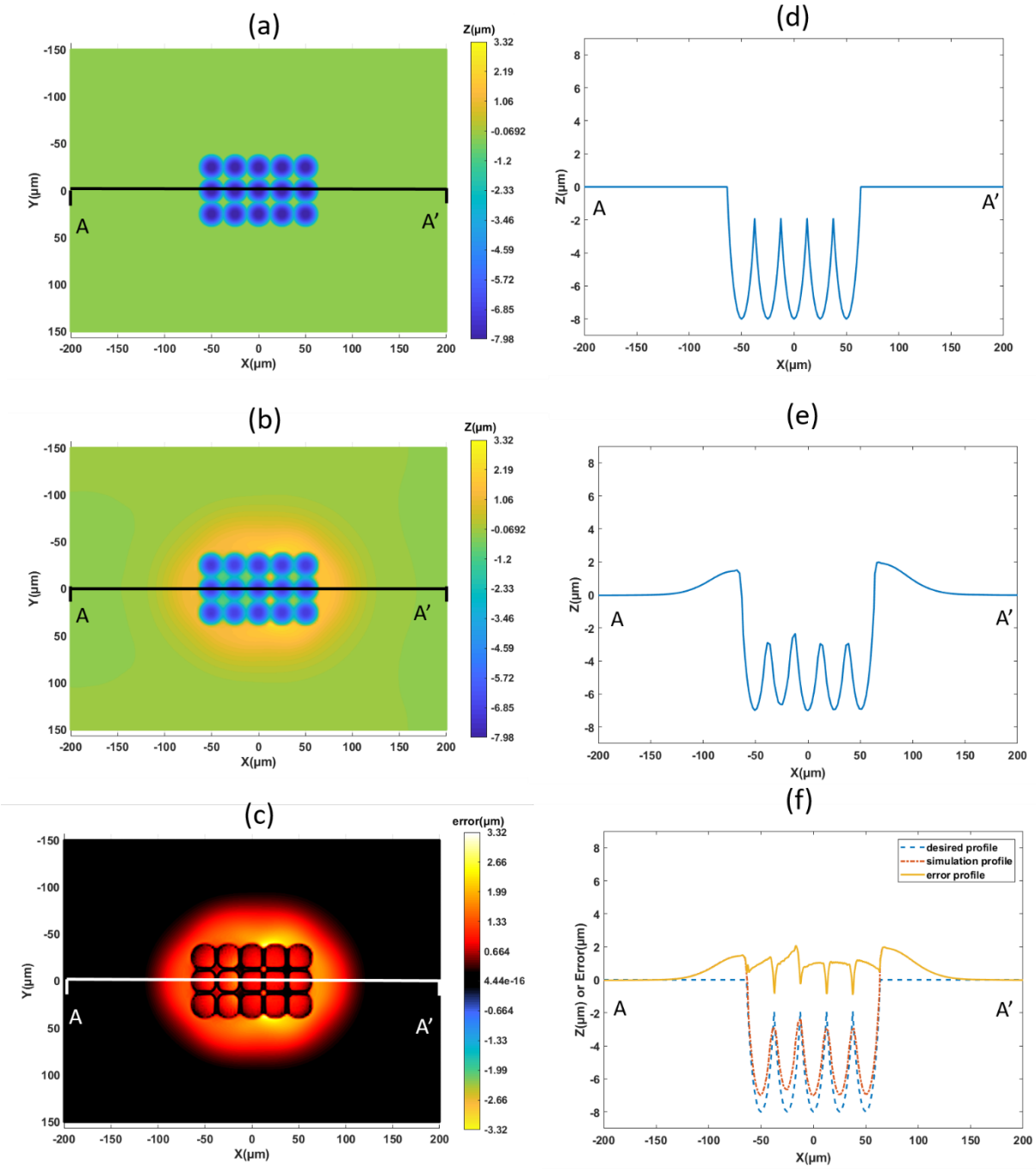

Figure 7. Two feature step over. (a) Desired contour plot. (b) Simulation contour plot. (c) Error plot (actual profile – desired profile). (d) The cross-section view across A-A' of desired plot shown in (a). (e) The cross-section view across A-A' of simulation plot shown in (b). (f) Comparison of the desired, simulation and error plot across cross-section across A-A'.

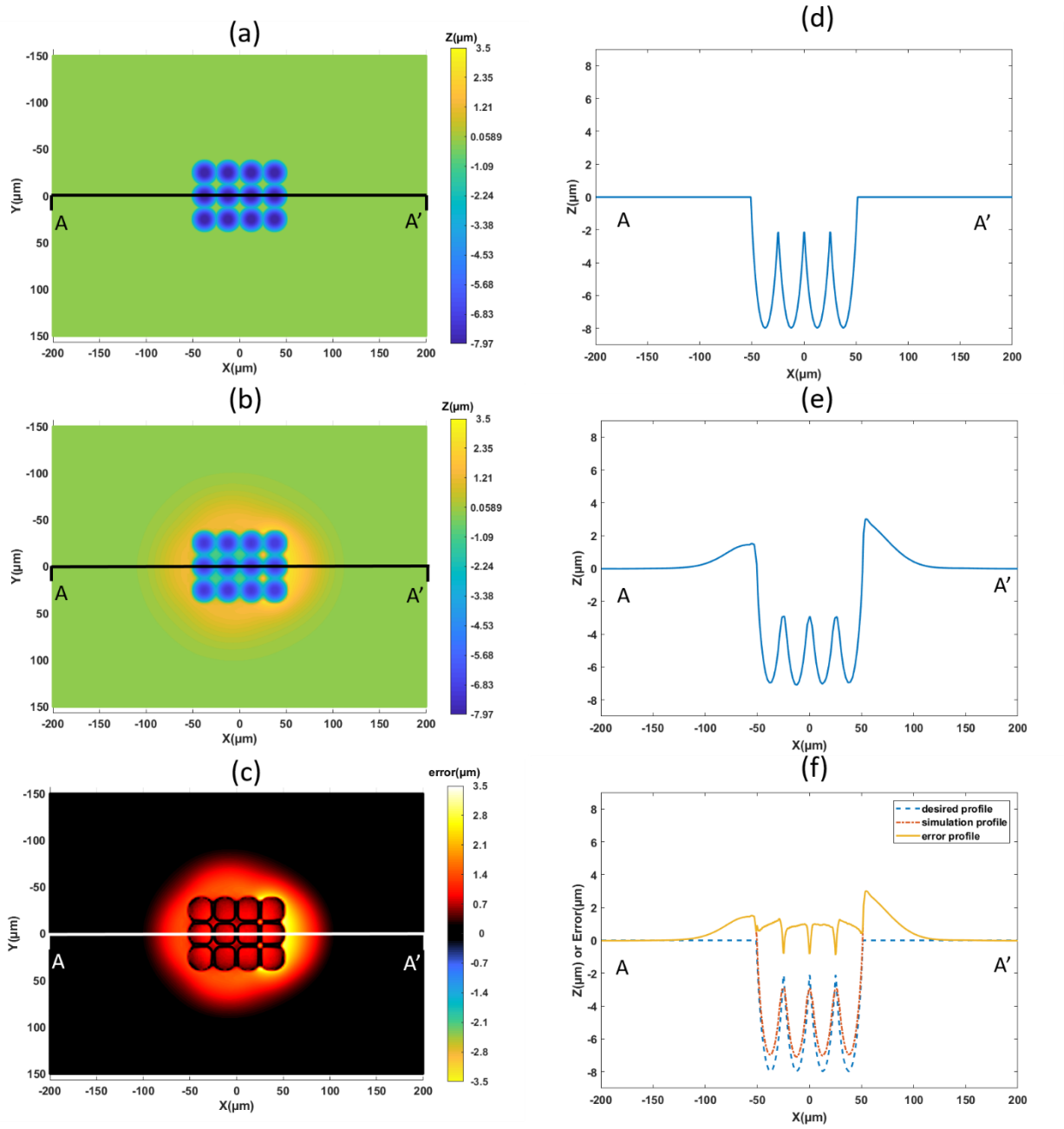

Figure 8. One feature step over. (a) Desired contour plot. (b) Simulation contour plot. (c) Error plot (actual profile – desired profile). (d) The cross-section view across A-A' of desired plot shown in (a). (e) The cross-section view across A-A' of simulation plot shown in (b). (f) Comparison of the desired, simulation and error plot across cross-section across A-A'.

To understand the cause of the compressional deformations two simulations with a 4x4 die and a 1x3 with a one feature stepover were performed. Figure 9 (a) shows the design of a 1x3 die with each feature of radius 15.84 µm and a pitch of 25 µm. Figure 9 (b) shows the indentation scheme used for the simulation with the 1x3 die. Figure 10 (a) shows the design of the 4x4 die with each feature of radius 15.84 µm and a pitch of 25 µm. Figure 10 (b) shows the indentation scheme used for the simulation with the 4x4 die.

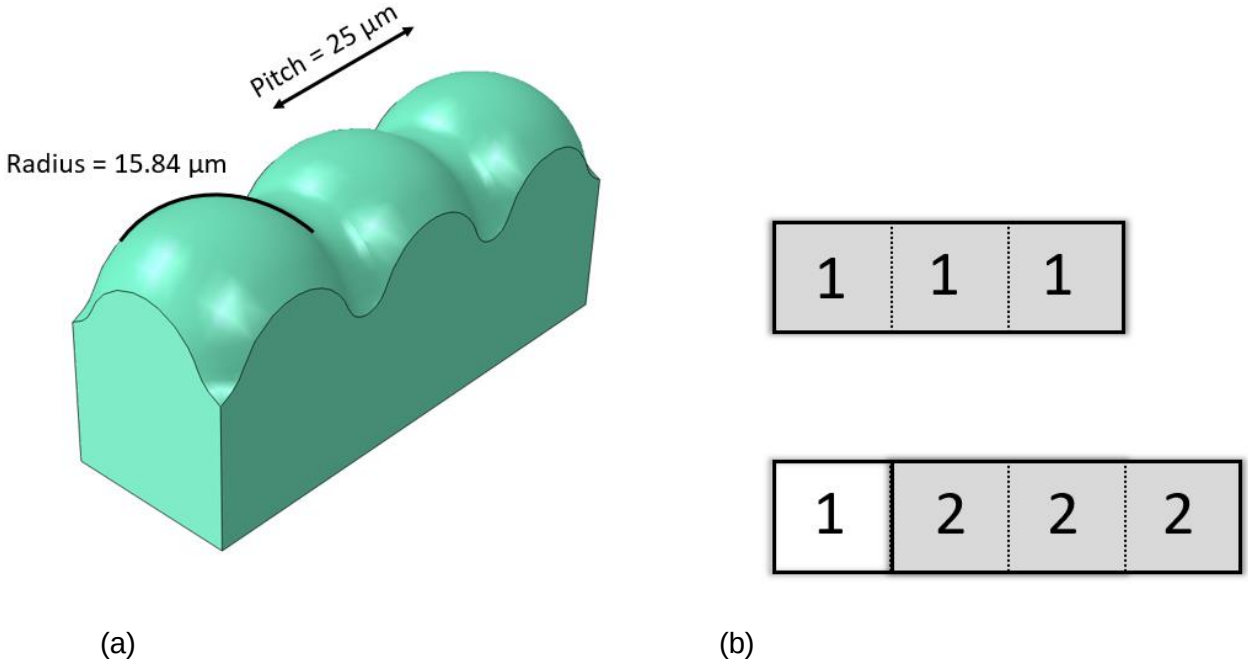

Figure 9. (a) 1x3 die with each feature of radius 15.84 µm and the center to center distance between each feature 25 µm (b) one feature stepover indentation strategy with the 1x3 die.

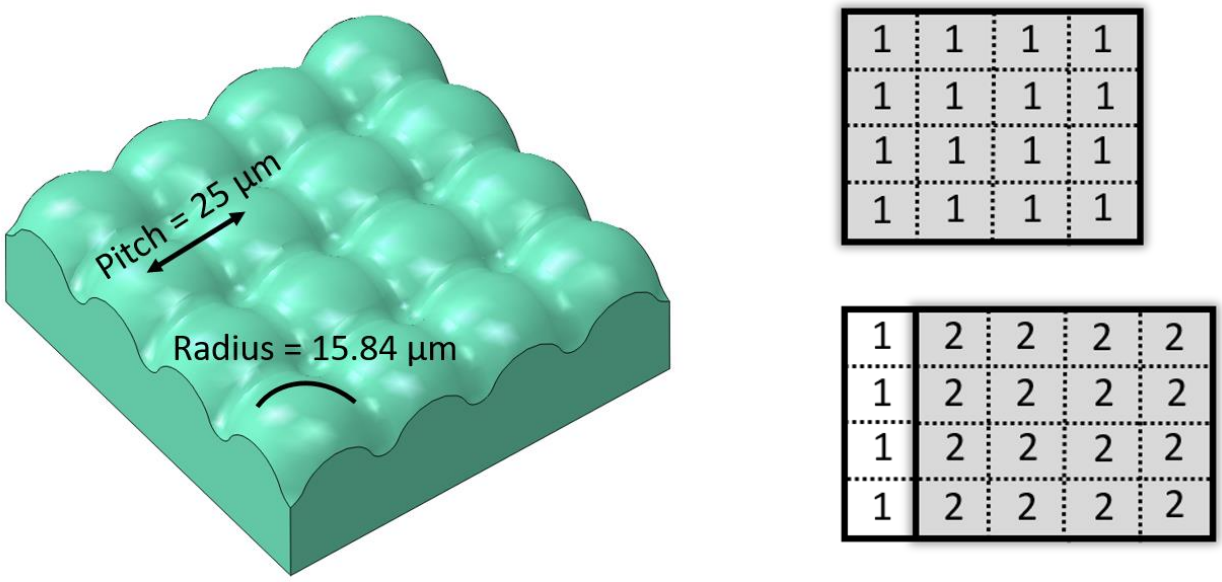

(a) (b)

Figure 10. (a) 4x4 die with each feature of radius 15.84 µm and the center to center distance between each feature 25 µm (b) one feature stepover indentation strategy with the 4x4 die.

Figure 11 and Figure 13 shows the simulation contour plot for the 1x3 die indentation and 4x4 die simulation. Figure 12 and Figure 14 shows the error contour plot of the 1x3 die indentation and 4x4 die indentation. Figure 12 shows very little compressional deformation in the first indent whereas, Figure 14 shows significant compressional deformation in the first column of indents. It can be concluded that the cause of compressional deformation is higher volume of material displaced in case of a 4x4 die indentation compared to that of a 1x3 die indentation. For a 4x4 die indentation, during, the second indentation step, four features on the right are pushing the material down. The material flows in the direction of least resistance i.e. towards the already formed indents. As the indentation progresses the overlapping features of the die restore the compressional deformation in the adjacent indents. However, as there are no die features to hold the first column of indents, compressional deformation occurs in them. This explains, the cause for compressional deformation in the 3x3 die indentation.

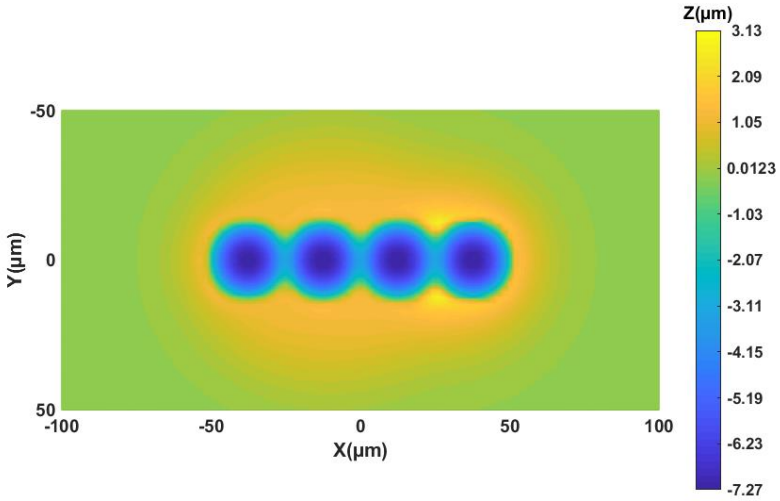

Figure 11. Simulation contour plot for a 1x3 die indentation using the indentation strategy in Figure 9 (b).

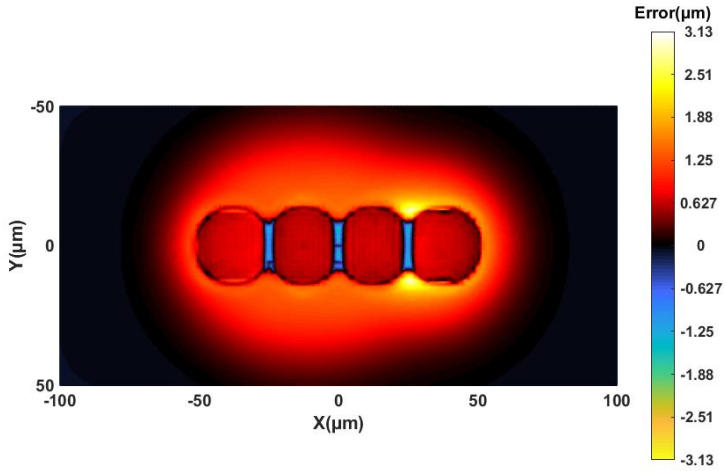

Figure 12. Error contour plot for a 1x3 die indentation using the indentation strategy in Figure 9 (b).

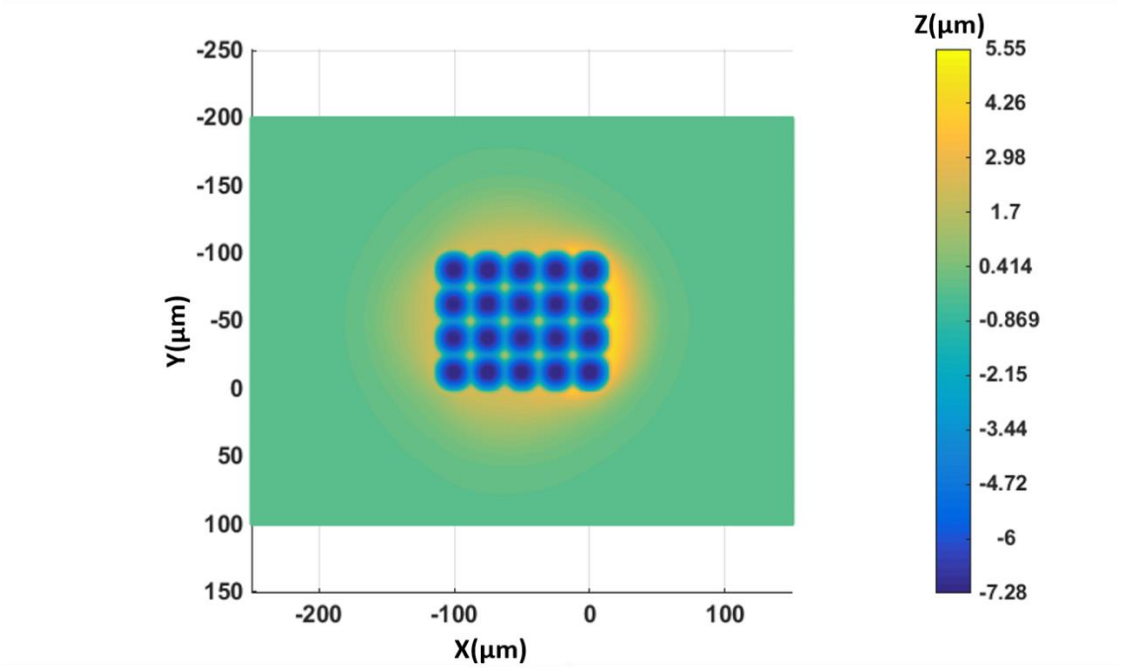

Figure 13. Simulation contour plot for a 4x4 die indentation using the indentation strategy in Figure 10 (b).

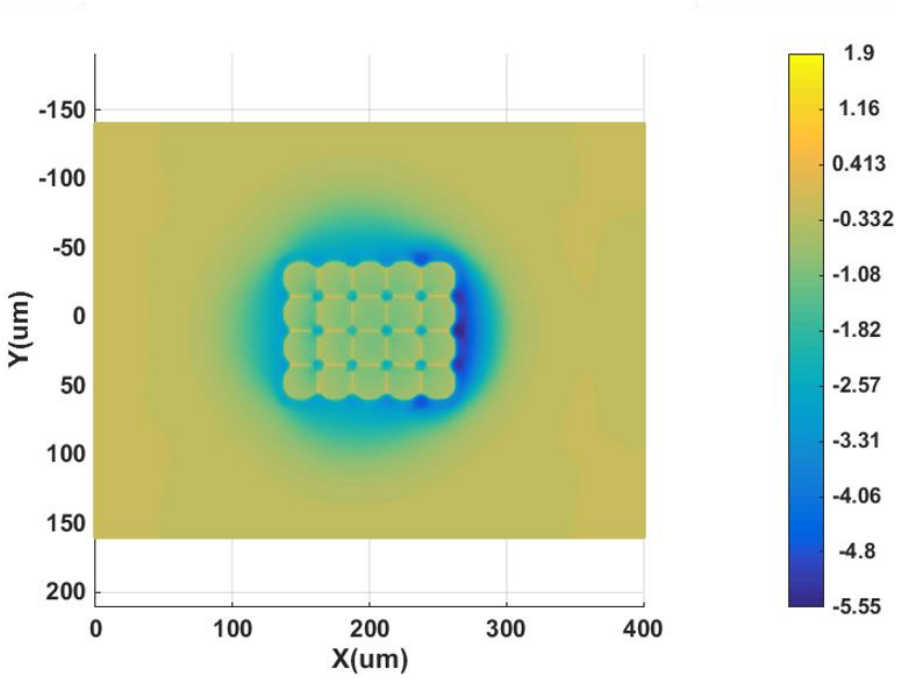

Figure 14. Error contour plot for a 1x3 die indentation using the indentation strategy in Figure 10 (b).

3.4 ADVANCED STUDY

For one feature stepover method, the compressional deformation is less severe as compared to the other two indentation strategies. To study the indents formed due to this indentation strategy the indentation scheme shown in Figure 15 was perfomed. This scheme proposes a total of sixteen indentation steps with one feature stepover every successive indentation to get 6x6 indent arrays. The red dashed box shown in the sixteenth indentation step is the indent that will be repeated and represents all the indents in the array. The simulation failed to complete beyond the 12^{th} indentation step and therefore, contour plots and various cross sections across the indent arrays were studied at indentation steps 4, 8, and 12 to get some important insights about the behaviour of material flow of the mold. The indentation steps from 13 to 16 will be conducted in the future.

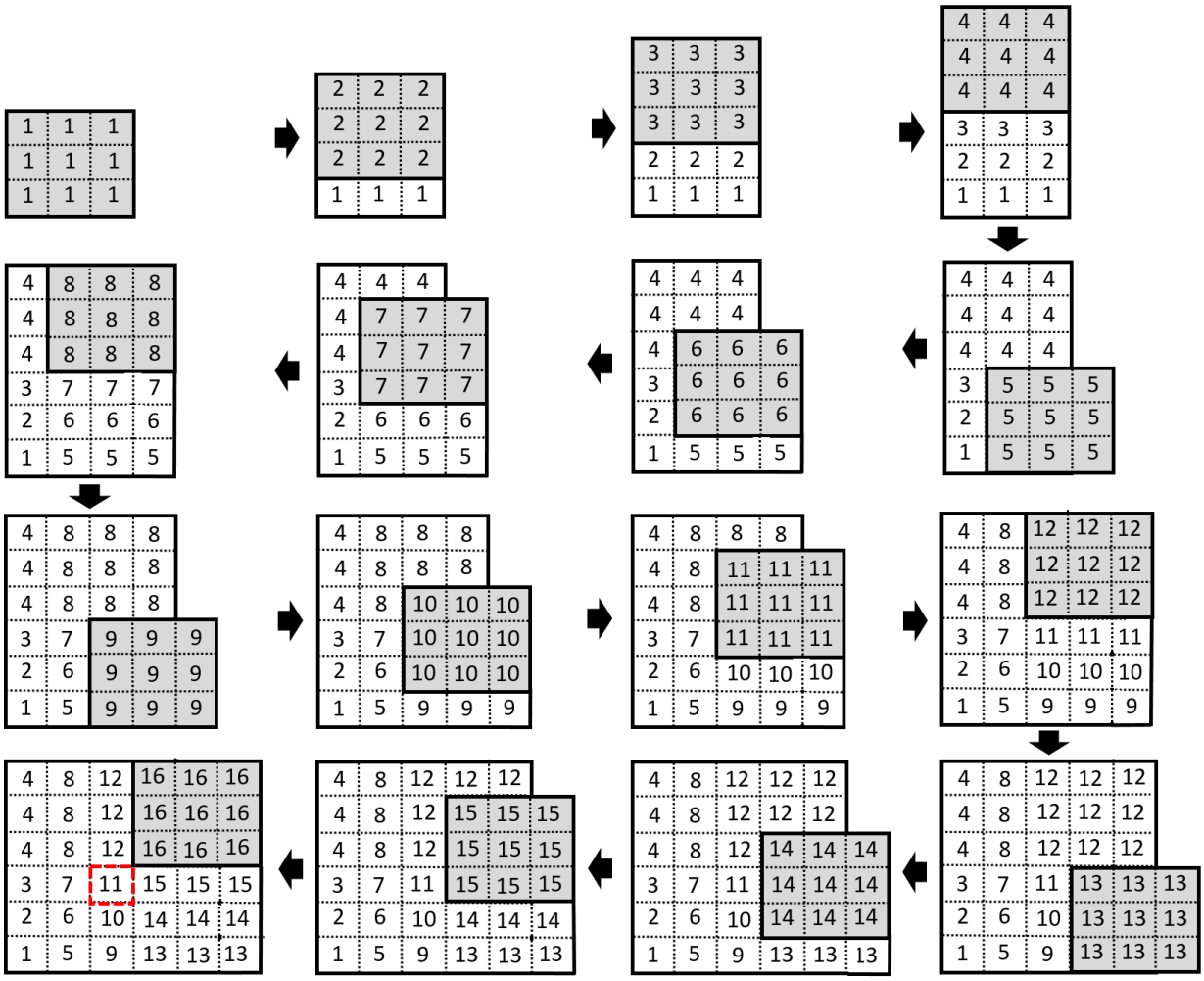

Figure 15. Indentation scheme A: Schematic of a one feature stepover indentation strategy with a total of sixteen indentations steps to form a 6x6 arrays of indents. The grey shade represents the current position of the die and the number in the cells represents the order of the indentation step. 3x3 die (U) is used for the indentation.

3.4.1 **Finite element model setup for the indentation scheme A**

The simulation was carried out by dividing the indentation scheme into individual indentation steps. Each indentation step was run as a separate simulation. The same finite element setup and mesh patterns as seen in section 3.2.1 were used for this indentation scheme. The mold instances in the any indentation step is associated with an initial state field of the mold instance from the previous indentation step. This procedure applies a deformed mesh and its associated material state from the previous indentation step to the mold instance in the current indentation step allowing the simulation to be continued after each indentation step. Abaqus/CAE imposes many restrictions and limitations when applying an initial state field which are mentioned in the section 'Transferring results between Abaqus analyses' of the Abaqus User's Manual [17]. It also provides a detailed step by step approach to carry out the import analysis. This procedure helps

in simplifying the FEA simulation by dividing the entire indentation scheme into separate individual indentation steps which helps distributing the memory required for the entire indentation scheme into 16 simulations. Also, it becomes convenient to debug any issues that arise during the simulations and make necessary changes after every indentation step.

3.4.2 **Finite element analysis results for the indentation scheme A**

Figure 2.16 shows the contour plot of the desired indent arrays for the indentation scheme A. The desired contour plot which has 6x6 indent arrays with a maximum depth of 8 μm of each indent, will be used to compare with the simulation plots at different indentation steps. An ideal desired indent array would have mathematically sharp edges at the intersection of the indents. It is not possible to fabricate a mold which has sharp edges and for the same reason the die used in the simulation has filleted edges and therefore significant errors can be expected at these intersections. These errors are not significant for the study as they are unavoidable and lie on the periphery of each lens feature far away from the central lens region of the lens aperture.

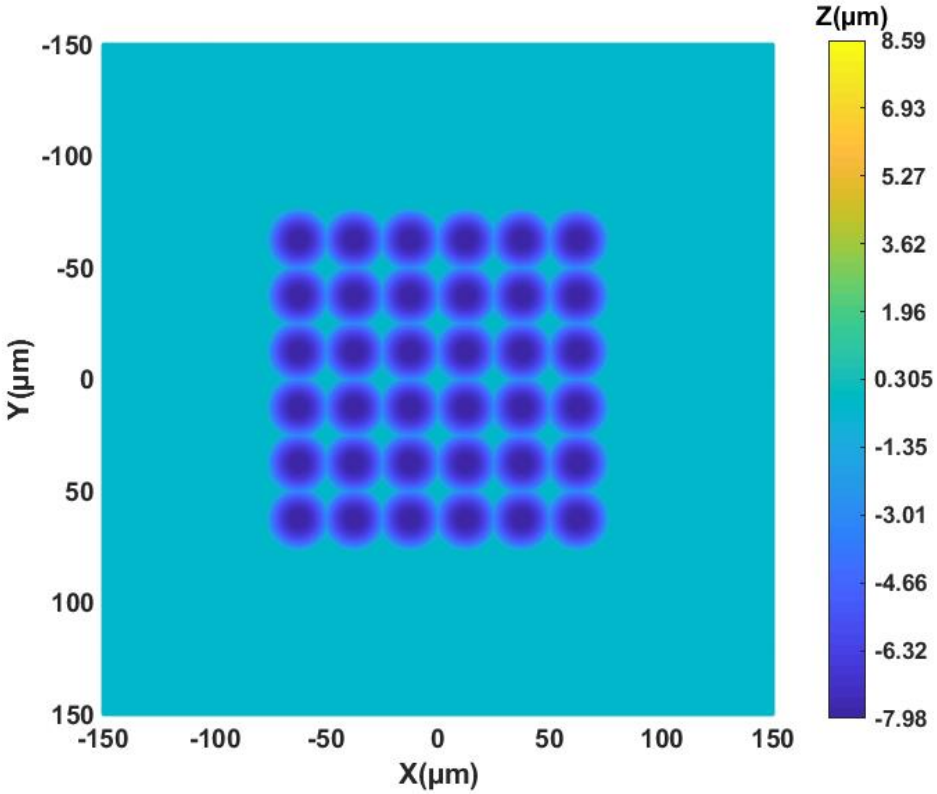

Figure 2.16. 6x6 desired indent arrays plot for the indentation scheme A.

Indentation step 4: Form error study

Figure 17 shows the contour plot of the simulation at the end of indentation step 4. Figure 18 shows error contour plot at the end of indentation step 4 along with the comparison of the desired plot, simulation plot and the error plot across different cross sections parallel to X axis. There is no compressional deformation visible along this cross section. However, there exists the error due to the the elastic deformation of the die and the springback back of the indent after unloading. Figure 19 shows error contour plot at the end of indentation step 4 along with the comparison of the desired plot, simulation plot and the error plot across different cross sections parallel to Y axis. Compressional deformation is visible across these cross sections in the first three indents and the error due to the elastic deformation of the die and the springback back of the indents after unloading of step 4 is visible in the last three indents.

Figure 20 explains the flow of material during indentation steps 1 to 4. The green dashed box represents the region of the mold where no indent cavities are present. The arrows indicate the direction of the material flow that is causing the compressional deformation during the indentation. In each of these indentation steps, three of the features on the die indent in the region of the mold where no indent cavity is present, causing the material displaced to flow in the direction of the least resistance, i.e along the positive Y direction. This leads to the formation of compressional deformation in the indents shown in the red dashed box. The compressional

deformation in these indents decreases in the direction of the arrow and are therefore visible in the cross sections parallel to the Y axis and not in the cross sections parallel to the X axis.

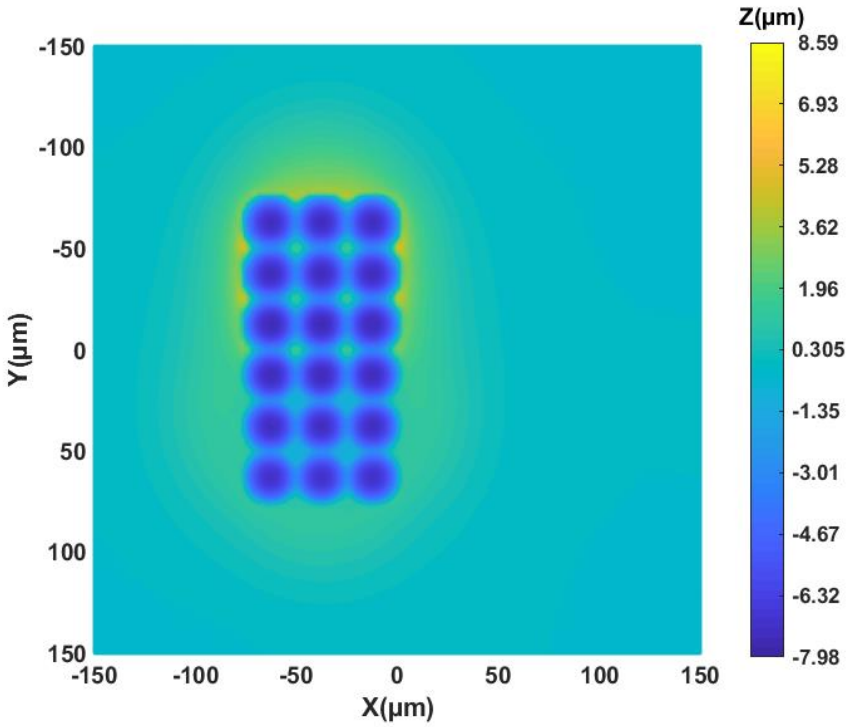

Figure 17. Simulation contour plot of the indent arrays for indentation scheme A at the end of the indentation step 4.

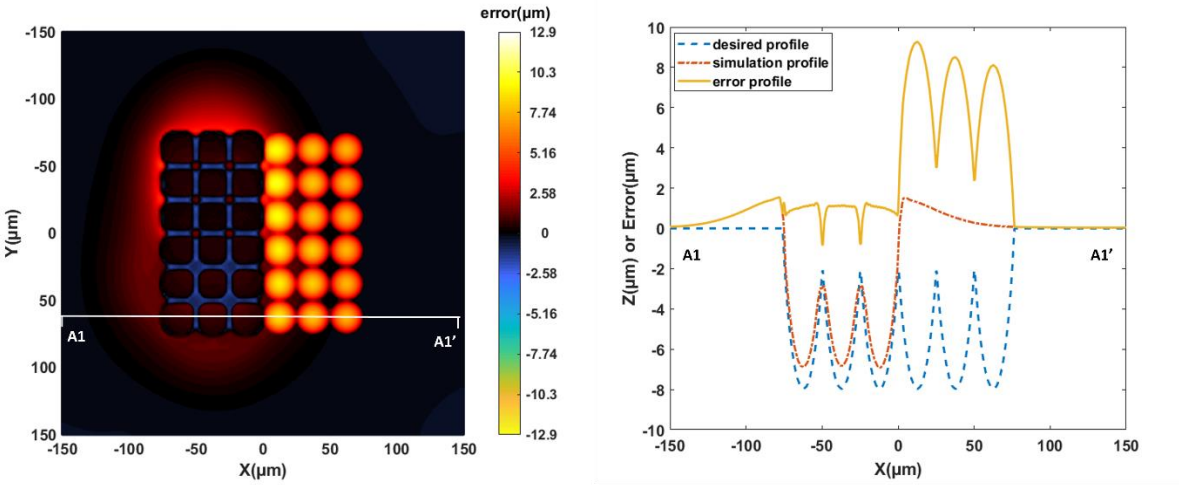

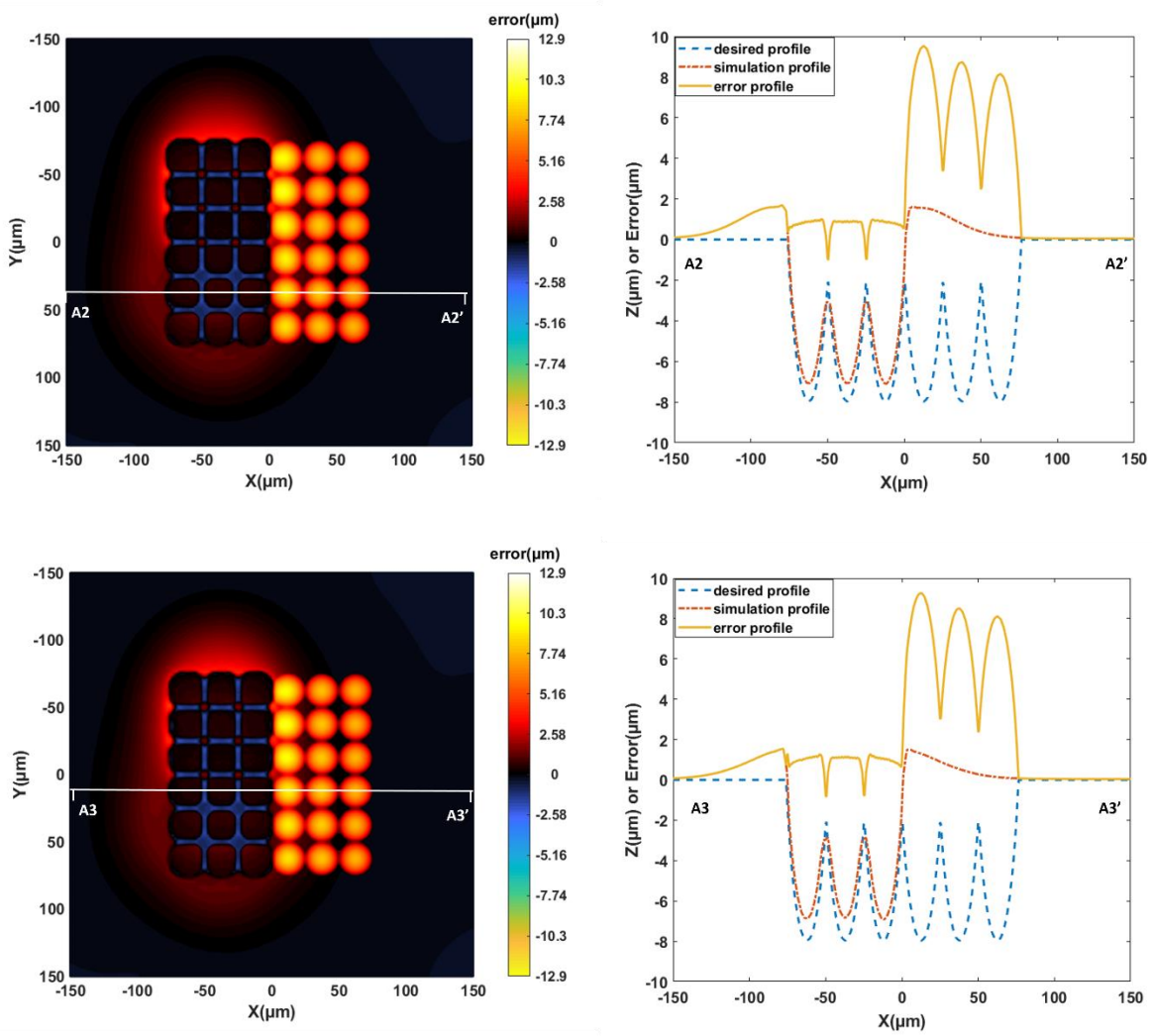

Figure 18. Error contour plot and comparison of different cross section views parallel to the X-axis using the indentation scheme A at the end of indentation step 4.

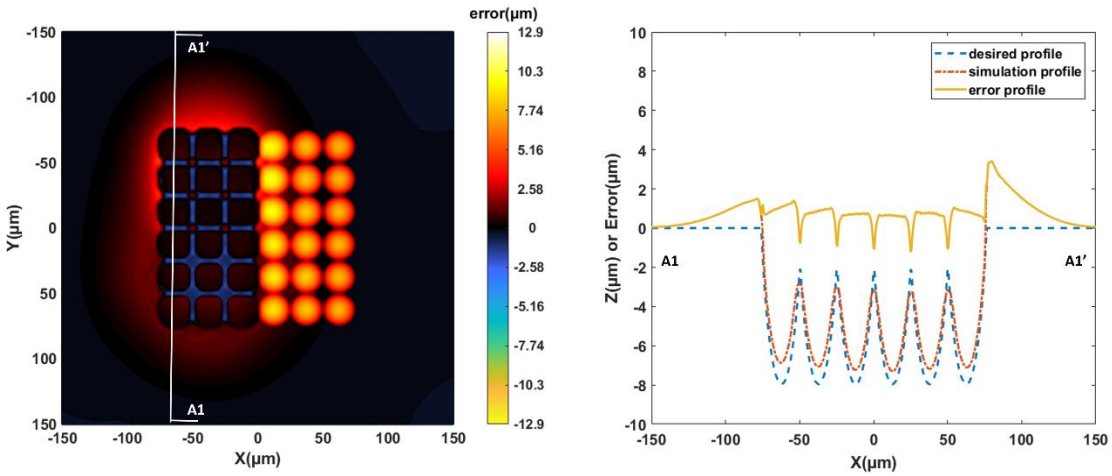

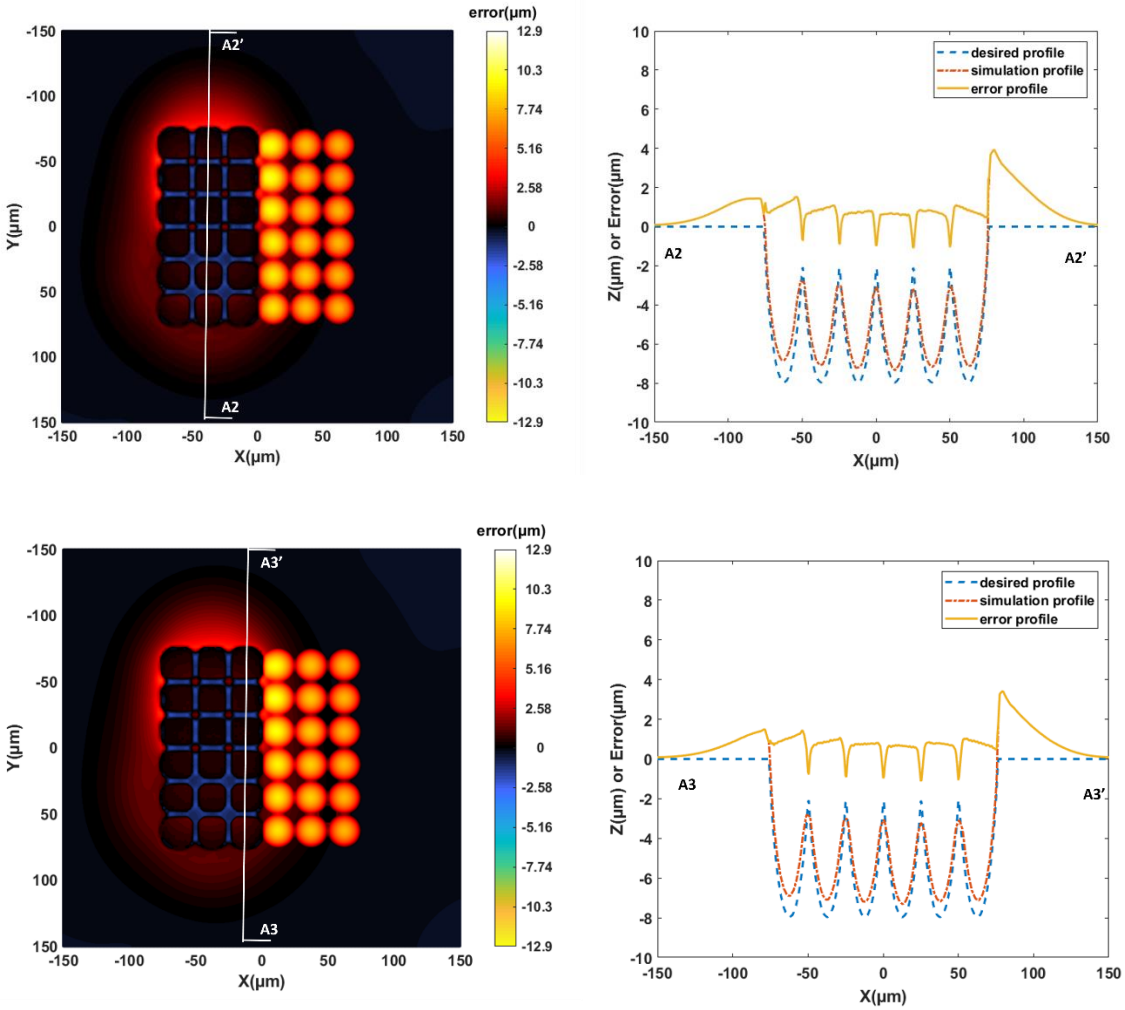

Figure 19. Error contour plot and comparison of different cross section views parallel to the Y-axis using the indentation scheme A at the end of indentation step 4.

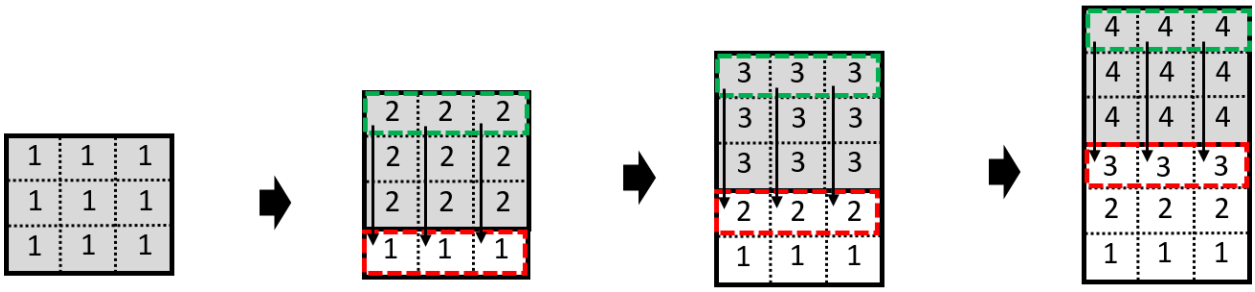

Figure 20. Schematic of the indentation steps 1 to 4 of the indentation scheme A, explaining the behavior of the material flow. Green dashed box indicates no indent cavity below it. Red dashed box indicates the compressional deformation in the indents formed due to that indentation step. Arrows indicate the direction of the material flow causing compressional deformation during indentation.

Indentation step 8: Form error study

Figure 21 shows the simulation plot of the indent arrays at the end of the indentation step 8. Figure 22 shows the error plot of the indent arrays across cross sections parallel to the X axis at the end of the indentation step 8. Compressional deformation is visible across these cross sections in the first indents. Figure 23 shows the error plot of the indent array across cross sections parallel to the Y axis. The compressional deformation present across these cross sections is less as compared to that across the cross sections parallel to the X axis.

Figure 24 explains the flow of the material during indentation steps 5 to 8. The green dashed box represents the region of the mold where no indent cavities are present. The arrows indicate the direction of the material flow during the indentation. In the indentation step 5, three of the features in the third column of the die indent in the region where no indent cavity is present, causing the material displaced to flow in the direction of the least resistance, i.e along the negative X direction. This leads to the formation of compressional deformation in the three indents of the first column shown in the red dashed box. The compressional deformation in these indents decreases in the direction of the arrow and are visible in the cross sections parallel to the X axis. The material also flows diagonally upwards causing compressional deformation to occur in the indent above. The compressional deformation in this indent decreases in the direction of the arrow. In the subsequent indentation steps 6, 7, and 8 one feature on the die pushes in the region of the mold where there is no indent cavity present shown in the green dashed box and one feature pushes in the region where compressional deformation is present in the indent as shown in the blue dashed box. As more material is displaced along the arrow in the negative X direction than in the negative Y direction, the compressional deformation along the former direction is more severe than in the later direction which can be observed by comparing the cross sectional error plots parallel to the X axis and Y axis in Figure 22 and Figure 23 respectively.

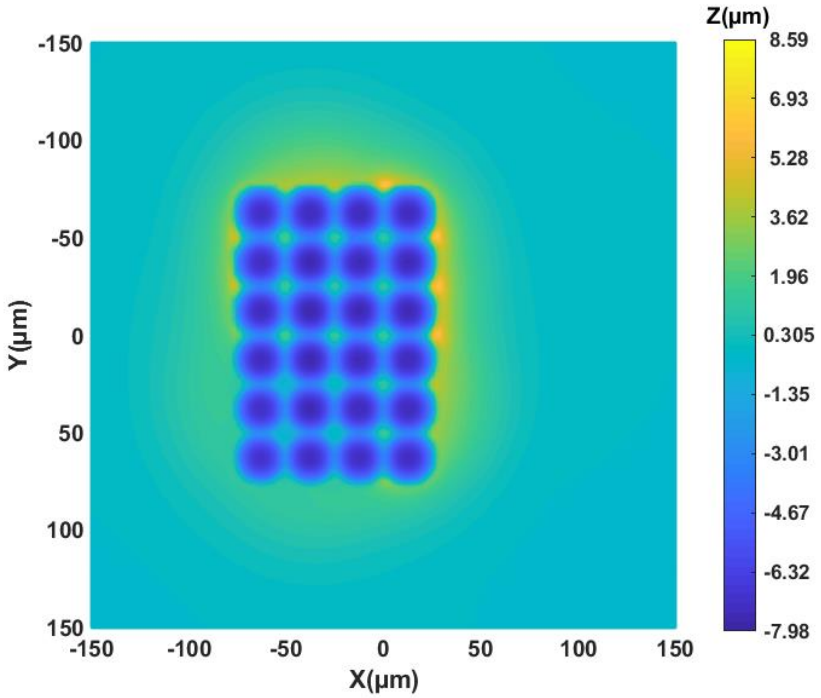

Figure 21. Simulation contour plot for indentation scheme A at the end of the indentation step 8.

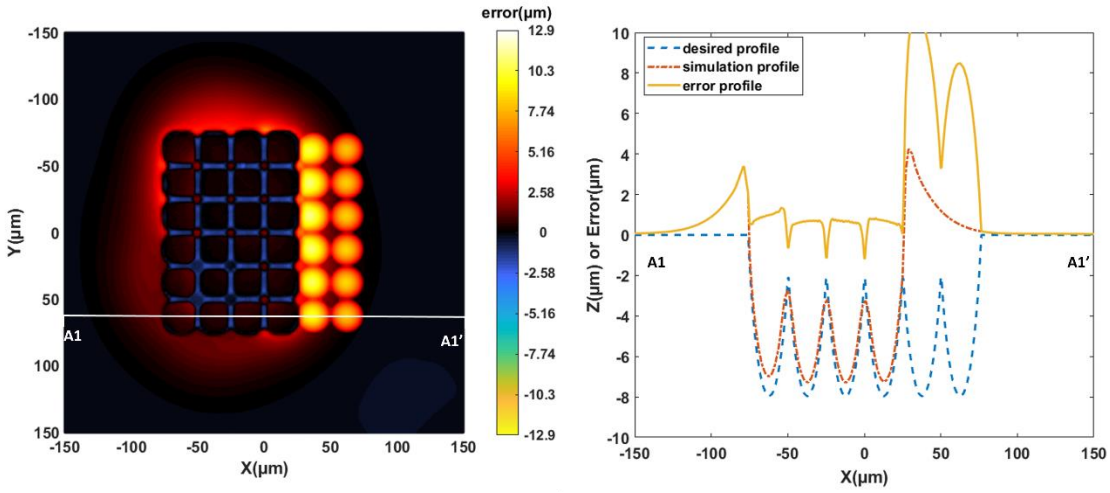

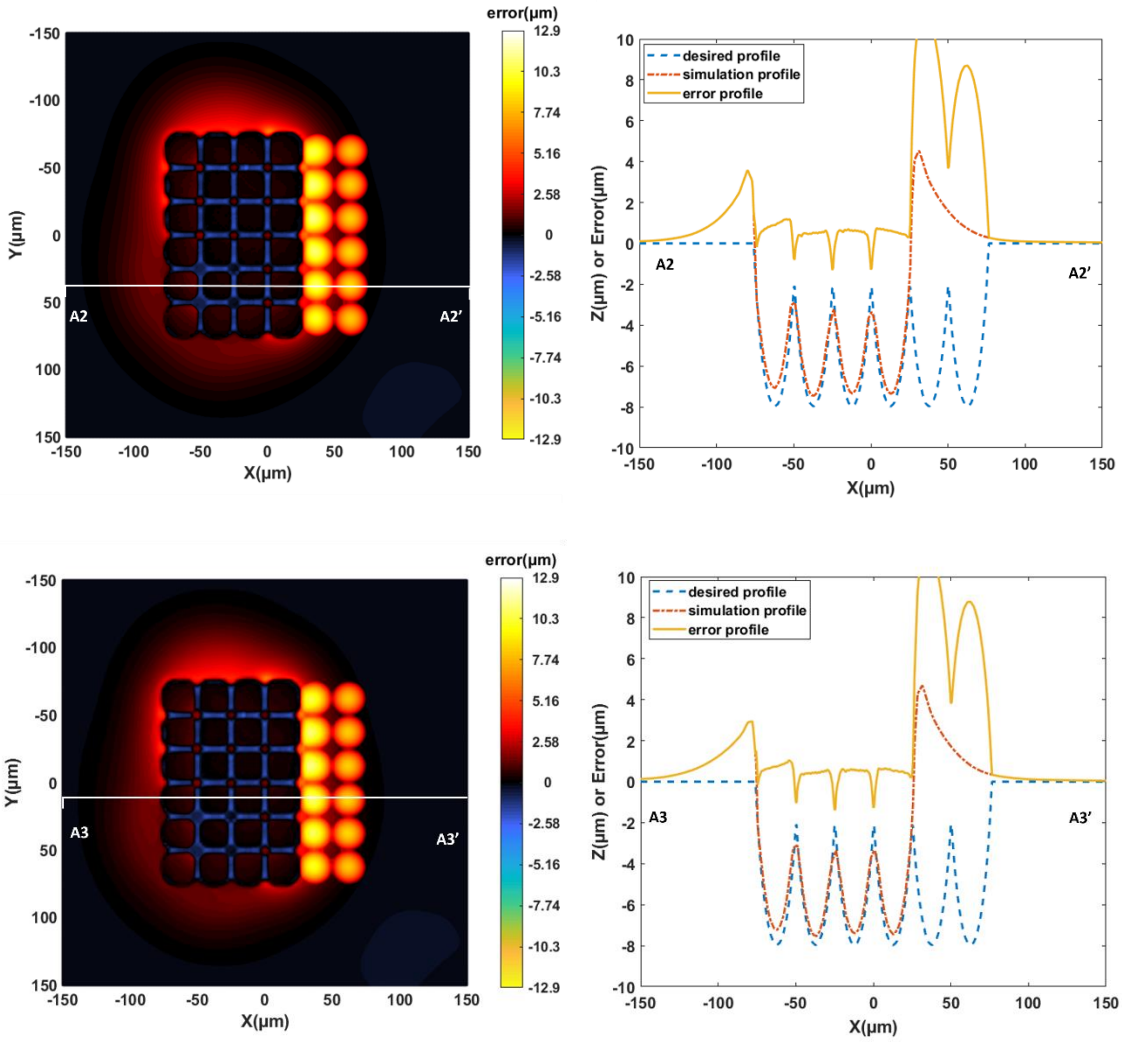

Figure 22. Error contour plot and comparison of different cross section views parallel to the X-axis using the indentation scheme A at the end of indentation step 8.

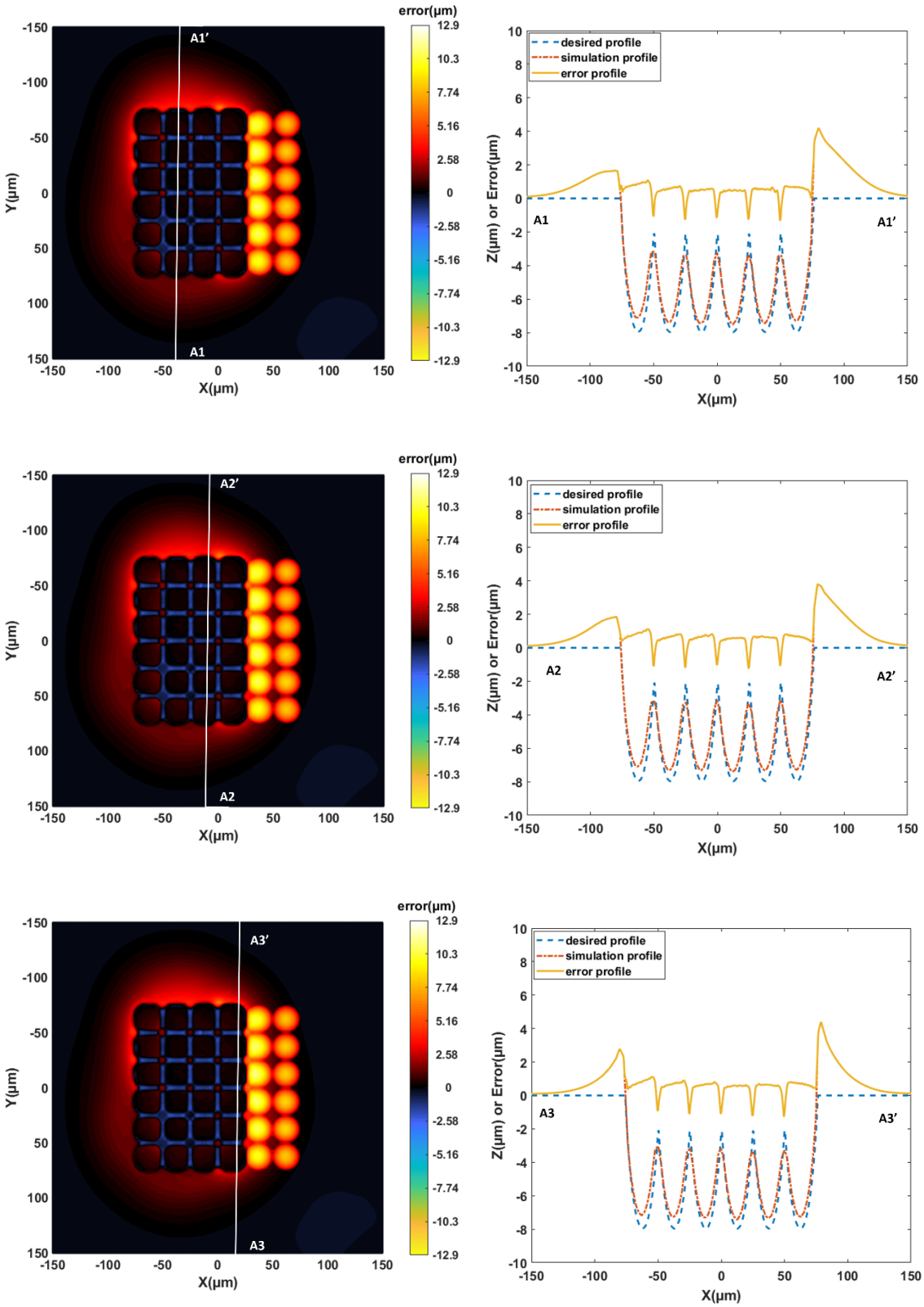

Figure 23. Error contour plot and comparison of different cross section views parallel to the Y-axis using the indentation scheme A at the end of indentation step 8.

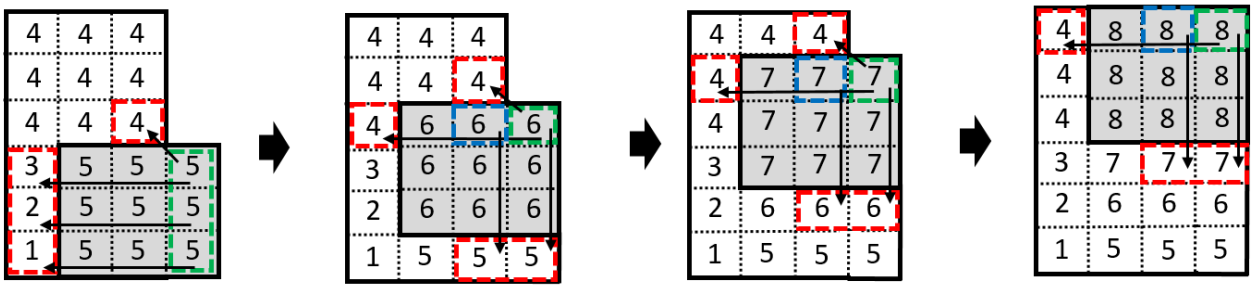

Figure 24. Schematic of the indentation steps 5 to 8 of the indentation scheme A, explaining the behavior of the material flow. Green dashed box indicates no indent cavity below it. Blue dashed box indicated the presence of compressional deformation in the indent caused in the previous indentation step. Red dashed box indicates the compressional deformation in the indents formed due to that indentation step. Arrows indicate the direction of the material flow causing compressional deformation during the indentation.

Indentation step 12: Form error study

Figure 25 shows the simulation plot of the indent arrays at the end of the indentation step 12. Figure 26 shows the error plot of the indent arrays across cross sections parallel to the X axis at the end of the indentation step 12. Compressional deformation is visible across these cross sections in the first indents. Figure 27 shows the error plot of the indent array across cross sections parallel to the Y axis. Similar, pattern of compressional deformation is evident as seen in the indentation steps 5 to 8. Figure 28 explains the material flow during indentation steps 8 to indentation steps 12. It follows the same rules as explained before for the indentation steps 5 to 8.

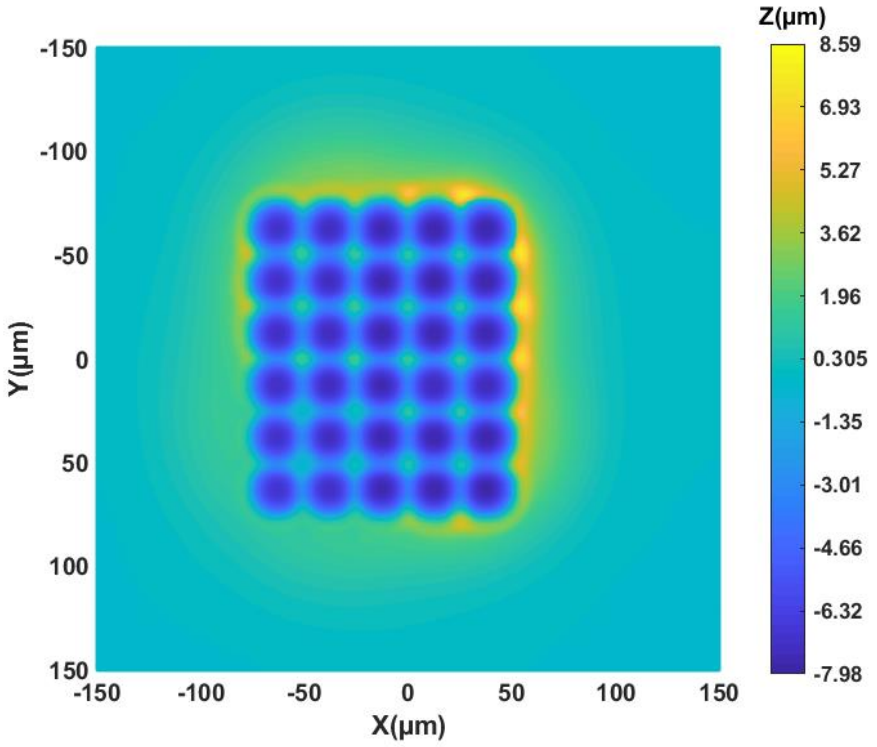

Figure 25. Simulation contour plot for indentation scheme A at the end of the indentation step 12.

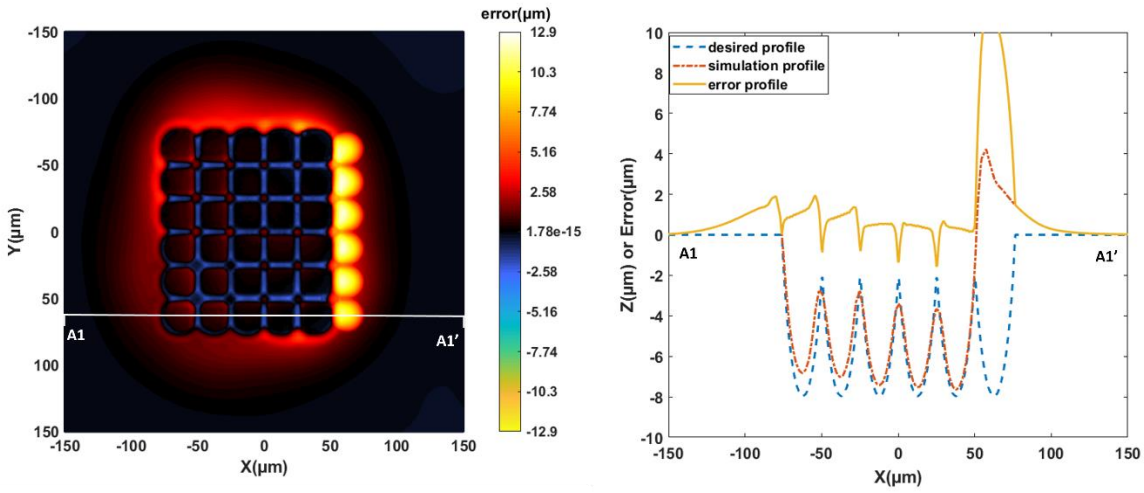

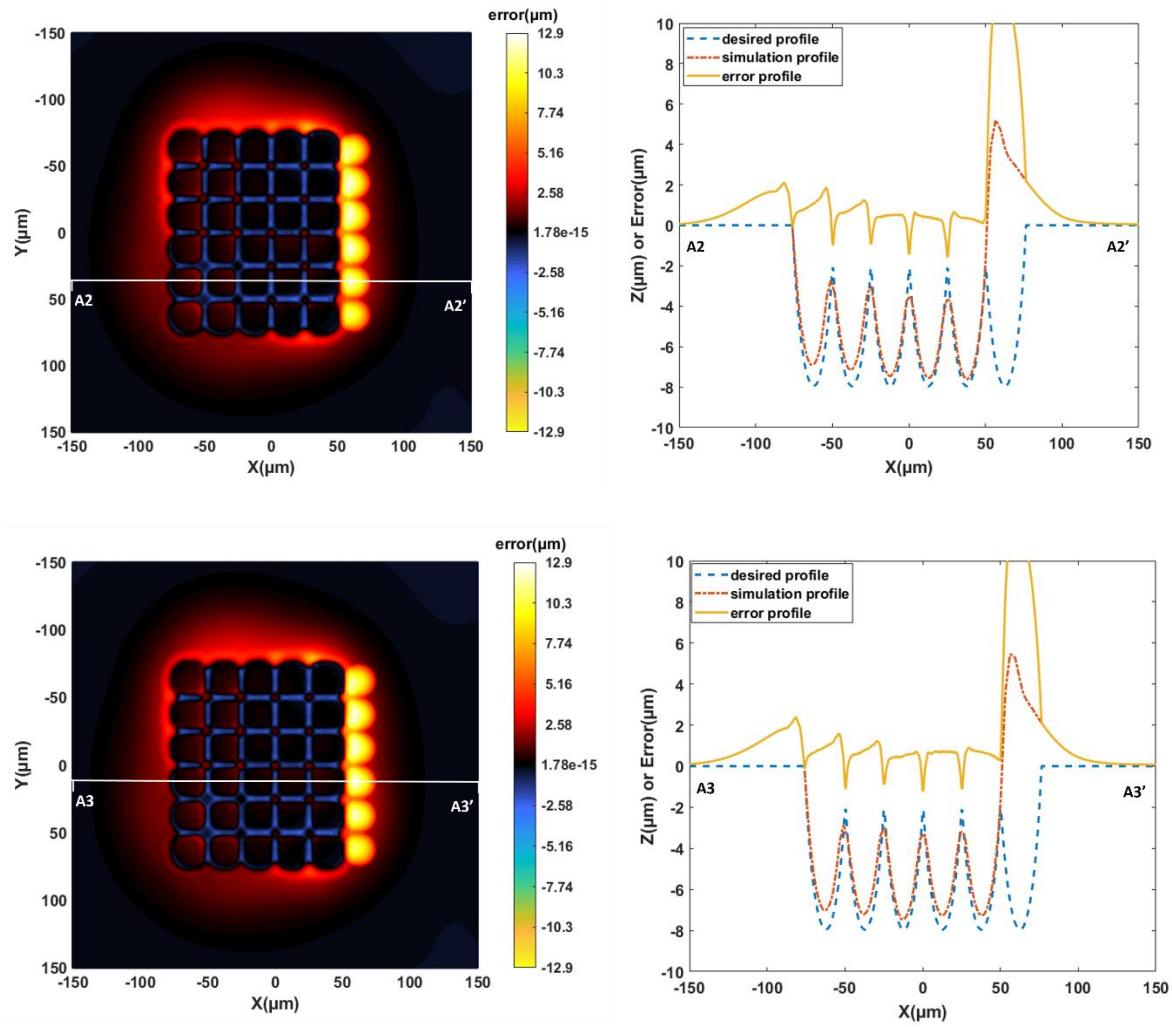

Figure 26. Error contour plot and comparison of different cross section views parallel to the X-axis using indentation scheme A at the end of indentation step 12.

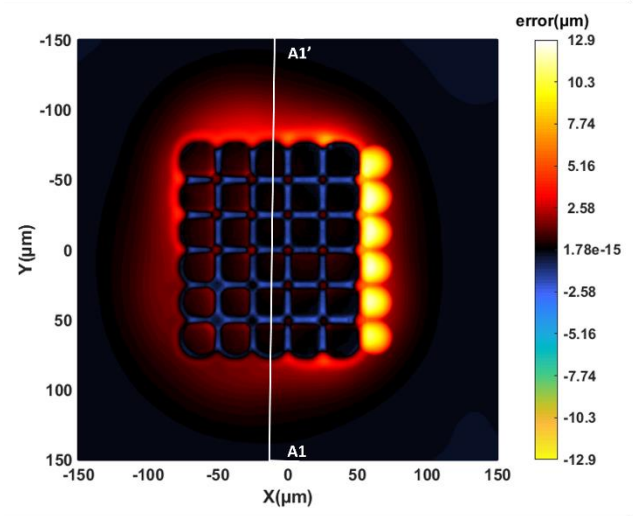

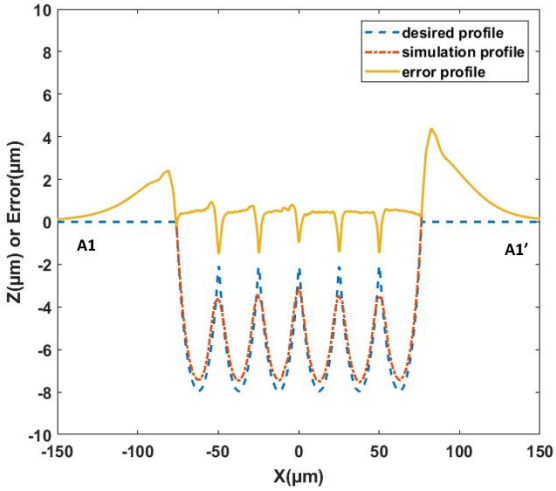

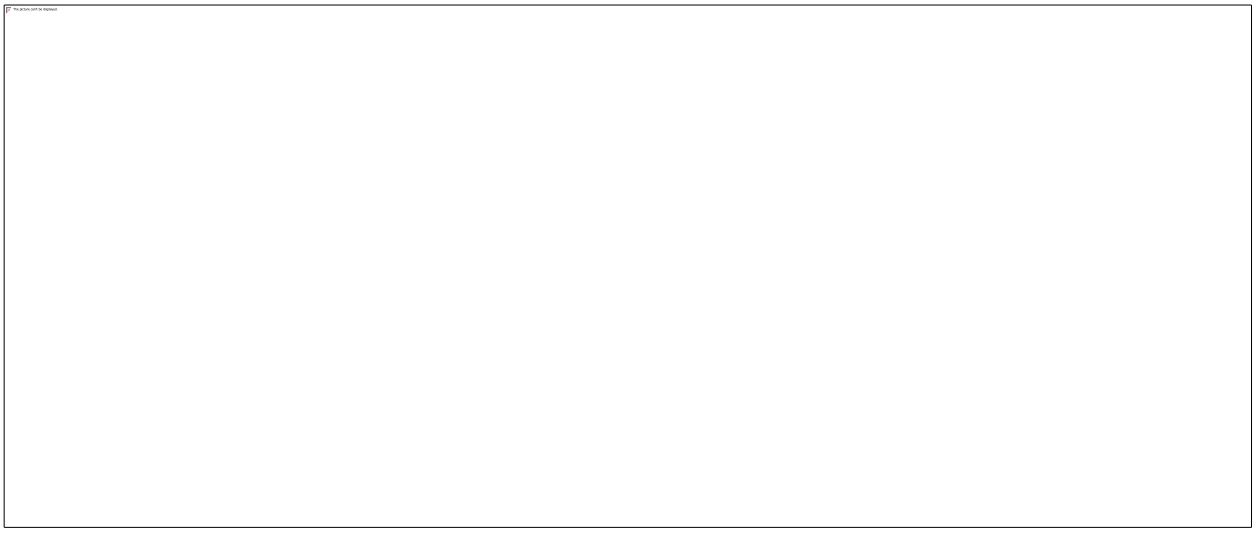

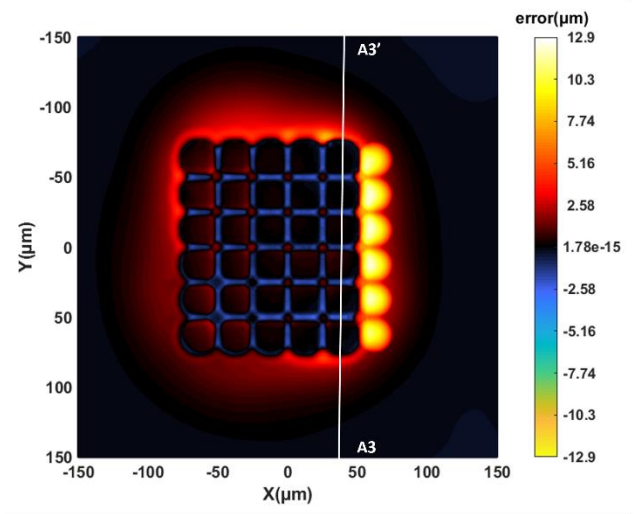

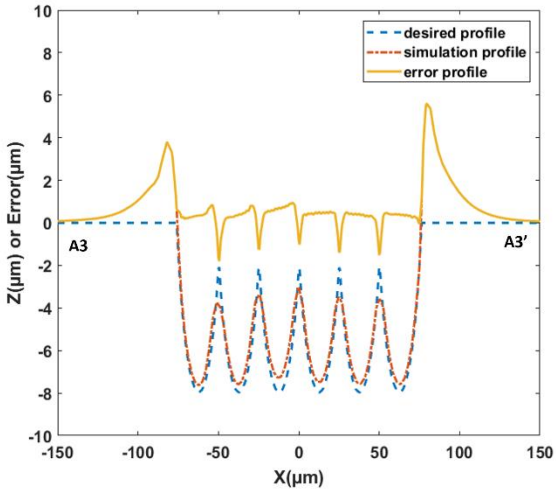

Figure 27. Error contour plot and comparison of different cross section views parallel to the Y-axis using indentation scheme A at the end of indentation step 12.

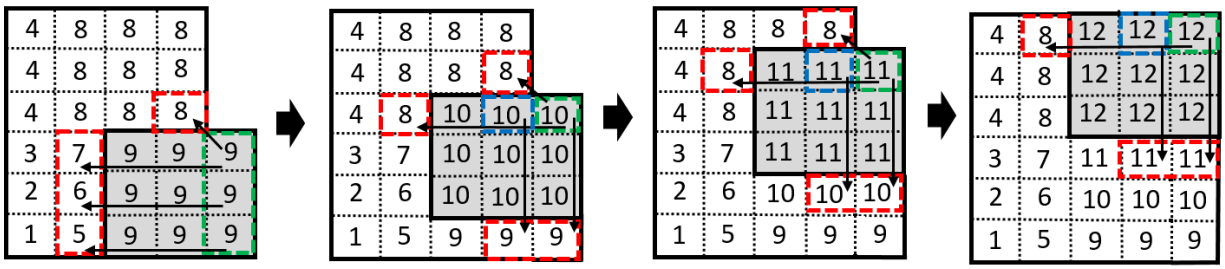

Figure 28. Schematic of the indentation steps 8 to 12 of the indentation scheme A, explaining the flow of material. Green dashed box indicates no indent cavity below it. Blue dashed box indicates the presence of compressional deformation in the indent caused in the previous indentation step. Red dashed box indicates the compressional deformation in the indents formed due to that indentation step. Arrows indicate the direction of the material flow causing compressional deformation during indentation.

The repeatability of the form error of the indents is necessary so that a die shape compensation method can be applied successfully to account for these errors. Figure 29 shows the comparison of the form errors of the indents across cross sections parallel to the X axis. The form error of the first column of indents is not considered because the compressional deformation formed in these indents are not repeated in the rest of the indents in the arrays. Figure 30 shows the comparison of the form errors of the indents across cross sections parallel to the Y axis. The form errors have good repeatability.

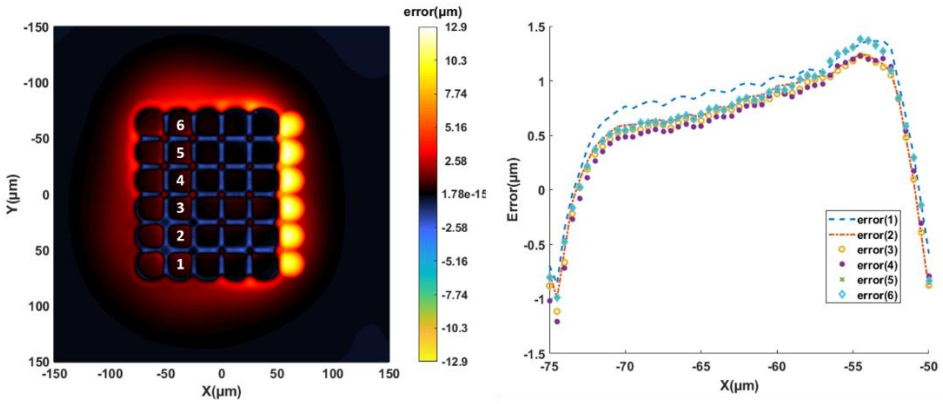

Figure 29. Comparison of the form error of indents across cross sections parallel to the X axis using the indentation scheme A.

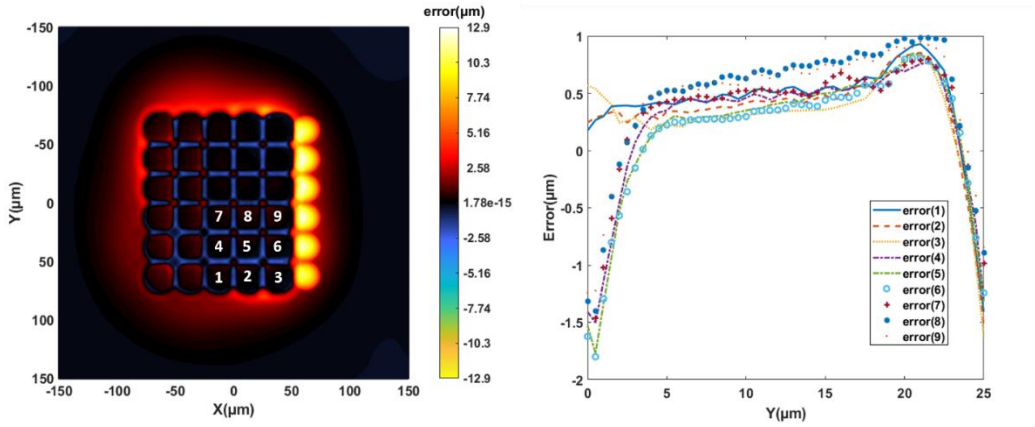

Figure 30. Comparison of the form error of indents across cross sections parallel to the Y axis using the indentation scheme A.

3.5 CONCLUSIONS

Preliminary studies which employed simple indentation strategies using multi-featured dies were explored. The three feature stepover method, had the highest “number of indents per indentation step” (9 indents per indentation step) but lead to severe compressional deformation in the indents. The two feature stepover method had lesser “number of indents per indentation step” (4 indents per indentation step) but the form accuracy of indents was better than the three feature stepover method. A modified two feature stepover scheme was explored which proposed using higher dimension dies (4x4 die or 5x5 die) to carry out the indentation procedure. This modified scheme involved two indentation stages: the first stage to create initial microlens arrays and the second stage to recover the compressional deformation in the indents. Form accuracy of indents better than the one feature stepover can be anticipated by this method. Finally, the one feature stepover method provided the best form accuracy of the indents but was the slowest of the other two indentation strategies. The maximum form error of the indents using this method was still 12 % of the maximum indent depth, which is significant in terms of the optical quality of the lens. When, the one feature stepover method was extended to create full two dimensional microlens arrays, the compressional deformation was more dominating along the X direction than the Y direction. A modified multi-featured die was proposed to carry out this indentation scheme. With this modified die, form accuracy better than all the indentation strategies can be expected.

The multi-featured progressive dies which employed the one feature stepover method experienced much worse compressional deformation in the indents as compared to the multi-featured die. The progressive dies has an advantage that it experiences less reaction forces each indentation step, thus increasing the life of the die. Future work would involve resizing the features of the progressive die with the aim to improve the form accuracy of the indents.

Once the form accuracy of the indents is improved by reducing or completely eliminating the compressional deformation of the indents, the next step would be to solve the form errors due to the elastic deformation of the die and the springback of the mold during indentation. This can be

achieved by correcting the shape of the features of the die by compensating for the errors. Table 1 shows a summary of all the advantages of the die designs and indentation strategies in terms of the indentation time required and form accuracy achieved.

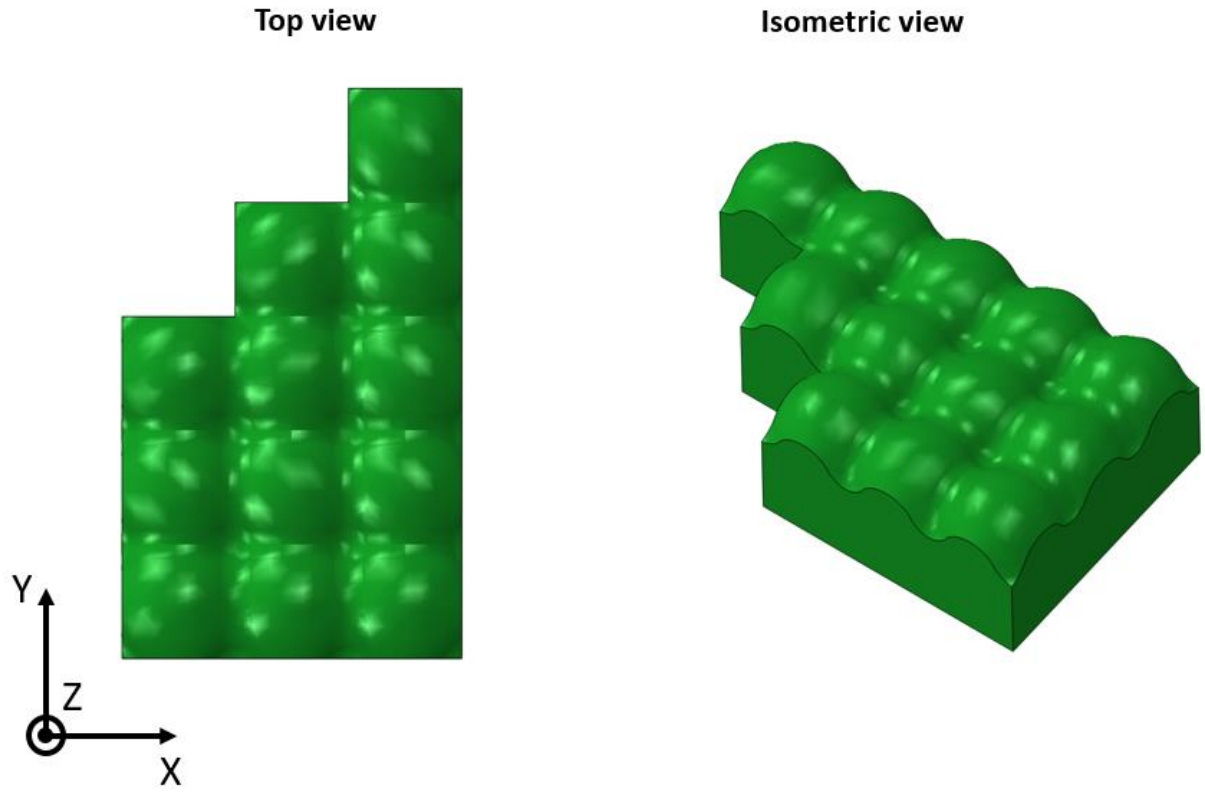

Figure 31. Design of new die with three features added to the 3x3 die (U). This modified die is referred as 3x3 die (M).

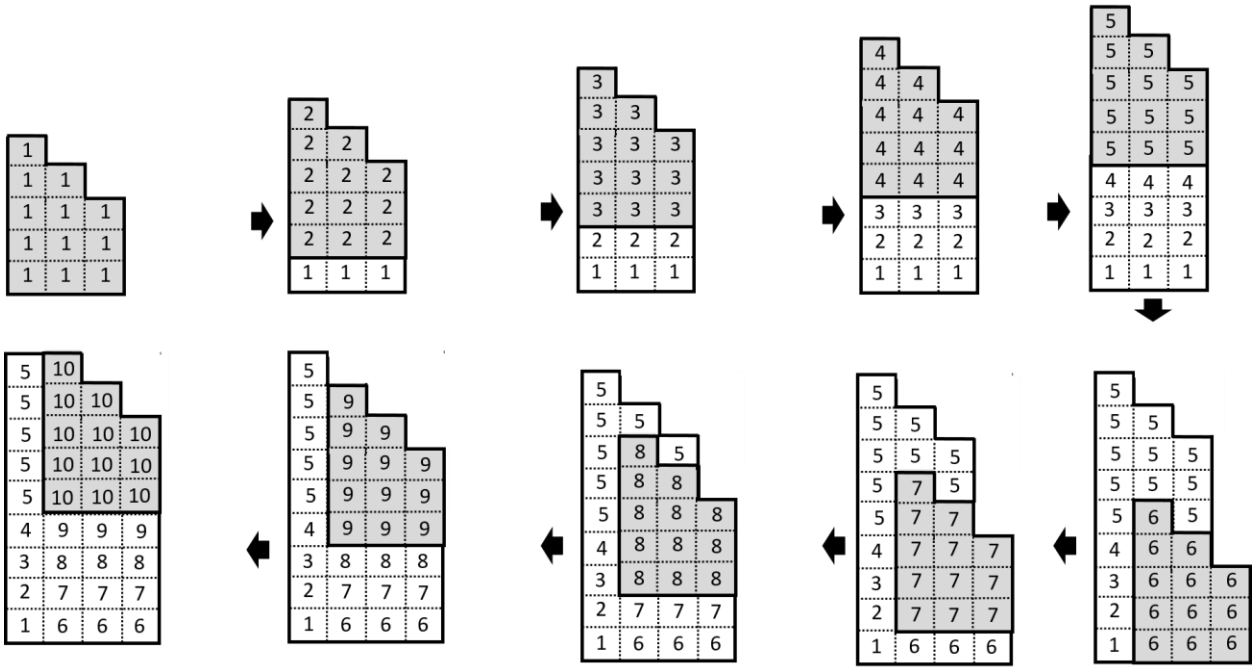

Figure 32. Indentation scheme using the 3x3 die (M).

Table 1. Summary of the die designs and indentation strategies for a 4K resolution display. Indentation frequency is 1 KHz.

	Three feature stepover	Two feature stepover	One feature stepover	One feature stepover – 3x3 die (M)	Modified two feature stepover scheme – higher dimension dies	Progressive dies - one features stepover method
Indentation steps	921,600	2,073,600	8,294,400	8,294,400	4,147,200	8,294,400
Indentation time	≈ 15 minutes	≈ 35 minutes	≈ 138 minutes	≈ 138 minutes	≈ 70 minutes	≈ 138 minutes
Form error	Worst (≈96% of max indent depth)	Better (≈ 25% of max indent depth)	Good (≈ 12 % of maximum indent depth)	Form accuracy expected to be better than all the other indentation schemes	Form accuracy expected to be better than one feature stepover method	Bad (> 31% of the maximum indent depth) Resizing of features to improve form accuracy
Number of indents per indentation steps	Nine	Four	One	One	Two	One

REFERENCES

[1] F. Chen, H. Liu and Q. Yang, "Maskless Fabrication of Concave Microlens Arrays on Silica Glasses by a Femtosecond-Laser-Enhanced Local Wet Etching Method," *Optics Express,* vol. 18, no. 19, pp. 20334-20343, 2010.

[2] R. Syms, E. Yeatman and B. V.M., "Surface Tension-Powered Self-Assembly of Microstructures - the State-of-the-Art," *Journal of Microelectromechanical Systems,* vol. 12, no. 4, pp. 387-417, 2003.

[3] H. Yang, C. Chao and M. Wei, "High Fill-Factor Microlens Array Mold Insert Fabrication using a Thermal Reflow Process," *Journal of Micromechanics and Microengineering,* vol. 14, no. 8, pp. 1197-1204, 2004.

[4] S. Moore, J. Gomez and D. Lek, "Experimental Study of Polymer Microlens Fabrication using Partial-Filling Hot Embossing Technique," *Microelectronic Engineering,* vol. 162, pp. 57-62, 2016.

[5] J. Albero, L. Nieradko and G. C., "Fabrication of Spherical Microlenses by a Combination of Isotropic Wet Etching of Silicon and Molding Techniques," *Optics Express,* vol. 17, no. 8, pp. 6283-6292, 2009.

[6] K. J.Y., N. Brauer and F. V., "Hybrid Polymer Microlens Arrays with High Numerical Apertures Fabricated using Simple Ink-Jet Printing Technique," *Optical Materials Express,* vol. 1, no. 2, p. 259, 2011.

[7] P. Nussbaum, R. Volkel and H. Herzig, "Design, Fabrication and Testing of Microlens Arrays for Sensors and Microsystems," *Pure and Applied Optics: Journa of the European Optical Society Part A,* vol. 6, no. 6, pp. 617-636, 1997.

[8] A. Yi and L. Li, "Design and Fabrication of a Microlens Array by use of a Slow Tool Servo," *Optics Letters,* vol. 30, no. 13, pp. 1707-1709, 2005.

[9] X. Zhang, F. Fang and L. Yu, "Slow Slide Servo Turning of Compound Eye Lens," *Optical Engineering,* vol. 52, no. 2, p. 023401, 2013.

[10] J. Yan, Z. Zhang and T. Kuriyagawa, "Fabricating Micro-Structured Surface by using Single-Crystalline Diamond Endmill," *The International Journal of Advanced Manufacturing Technology,* vol. 51, no. 9, pp. 957-964, 2010.

[11] J. Yan, A. Horikoshi and T. Kuriyagawa, "Manufacturing Structured Surface by Combining Microindentation and Ultraprecision Cutting," *CIRP Journal of Manufacturing Science and Technology,* vol. 5, no. 1, pp. 41-47, 2012.

[12] Y. Bai, X. Wang, T. Zhou, Z. Liang and G. Li, "Compressional Deformation in Indentation Process for Microlens Array Mold," *Journal of Beijing Institute of Technology,* no. 1, pp. 15-21, 2018.

[13] E. Zdanowicz, T. Dow and S. R.O., "Rapid Fabrication of Nanostructured Surfaces using Nanocoining," *Nanotechnology,* vol. 23, no. 41, p. 415303, 2012.

[14] A. Karimzadeh, M. Ayatollahi and M. Alizadeh, "Finite Element Simulation of Nano-Indentation Experiment on Aluminum 1100," *Computational Materials Science,* vol. 81, pp. 595-600, 2014.

[15] S. Moore, M. Manzari and Y. Shen, "Nanoindentation in Elastoplastic Materials: Insights from Numerical Simulations," *International Journal of Smart and Nano Materials,* vol. 1, no. 2, pp. 95-114, 2010.

[16] A. Warren and Y. Guo, "Machined Surface Properties Determined by Nanoindentation: Experimental and FEA Studies on the Effects of Surface Integrity and Tip Geometry," *Surface & Coatings Technology ,* vol. 201, no. 1, pp. 423-433, 2006.

[17] Anonymous, ABAQUS/Standard User's Manual, Version 6.9, Providence, RI: Simulia, 2016.

[18] D. T.A., J. Nowak and J. Kessing, "Design of Elliptically-Vibrating Ultrasonic Actuator for Nanocoining," *Precision Engieering,* vol. 45, pp. 301-310, 2016.

4 Novel Manufacturing Methods of Microscale Lens Arrays

Anthony Wong
Research Associate, Precision Engineering Consortium
Dr. Mark Pankow
Director of the PEC
Assistant Professor
Department of Mechanical and Aerospace Engineering

ABSTRACT

*In order to build off of the work outlined in the previous chapter, this work explores manufacturing a mold and die that can be used to create an optimal indent pattern for microlens arrays. This study details the steps taken to manufactur**e** a mold and die from aluminum and diamond, respectively. The Al 1100 H14 was first characterized through nanoindentation and diamond turning. Indentation grids were effectively created using a Berkovich and conical nanoindenter. The diamond die was FIB milled and analyzed using surface interferometry. The FIB dwell time for 1 nA and 0.50 nA beam currents used to create a consistent parabolic array is documented. Future testing using an iterative analysis can be used to optimize the die shape and mold indentation schemes.*

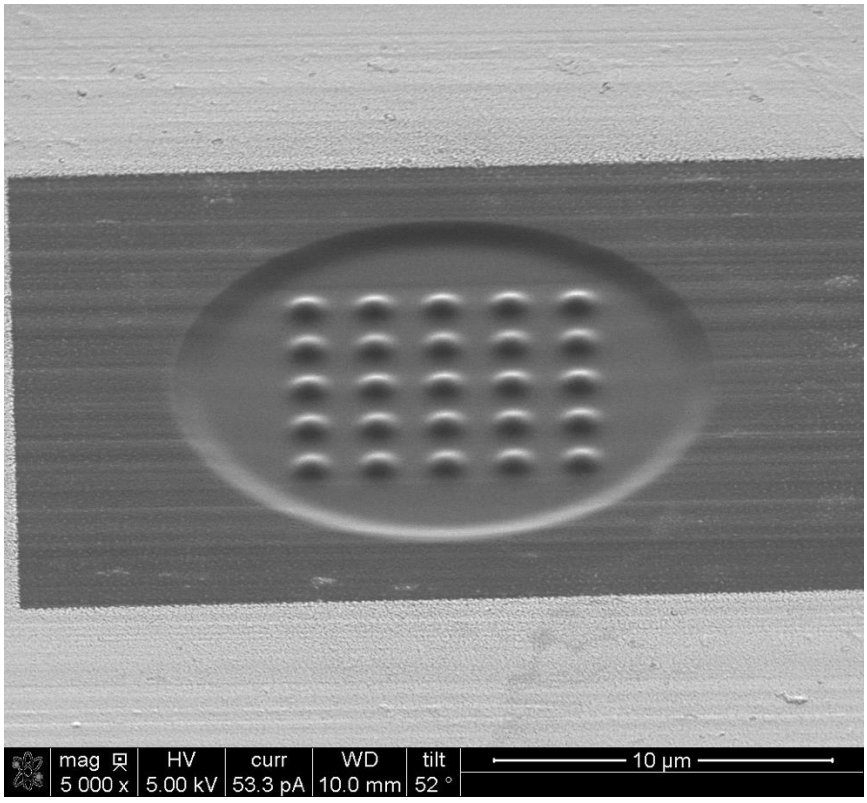

4.1 INTRODUCTION

The goal of this work is to investigate a novel manufacturing method for lens arrays using a mold and die manufactured from aluminum and diamond, respectively. For proof of concept the target geometry changed a few times over the course of the project. Initially, the target geometry was hemispherical features 3 µm apart, but not close packed. Thus, the radius must be less than 1.5 µm for the features not to be close packed. The top of Figure 1 shows a plan view of the array, while the bottom portion shows the cross section of what a single concave feature would look like. Later the feature spacing was changed to 2 µm.

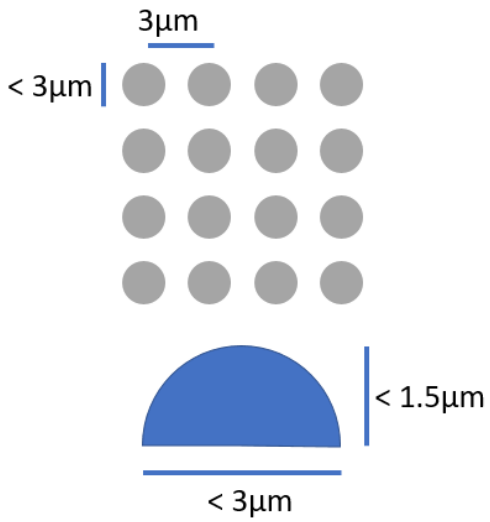

Figure 4-1: Microlens Array Diagram

Ultimately, it was decided to target a paraboloid (conic constant of -1) with a radius of curvature of 1 µm over a Ø1.5 µm aperture. Figure 2 shows a surface plot of a single feature. The maximum height is .281 µm. The maximum angle of the surface is 36.9° as shown in the cross section in Figure 3. This angle corresponds to the angle at which a degradation of the surface finish has been reported in diamond [1]. Figure 5 shows a 3 x 3 grid of the features with a 2 µm pitch.

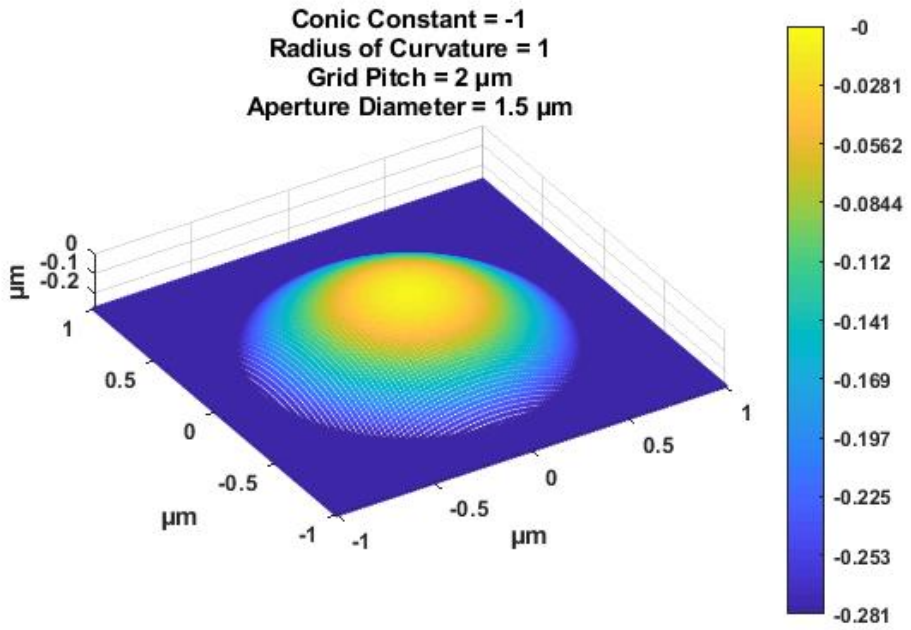

Figure 4-2. Surface plot of the proposed die geometry

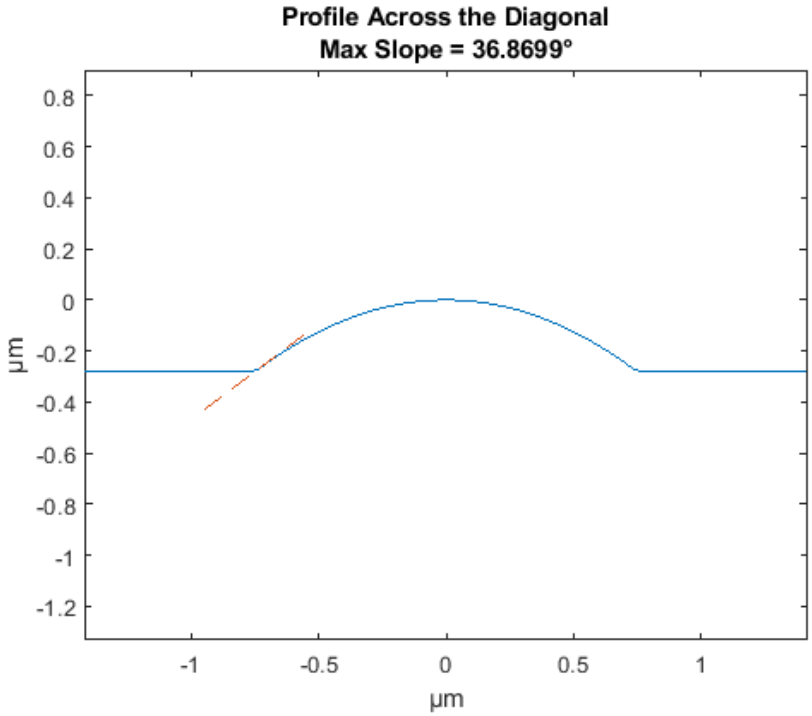

Figure 4-3. Cross section of the proposed die geometry (maximum slope shown with the dashed line)

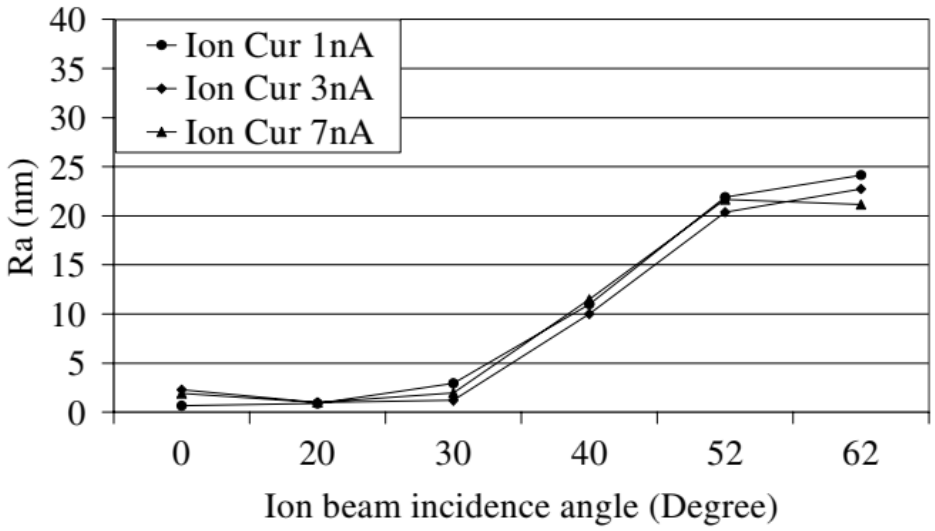

Figure 4-4. Surface roughness dependence on angle of incidence in diamond [1]

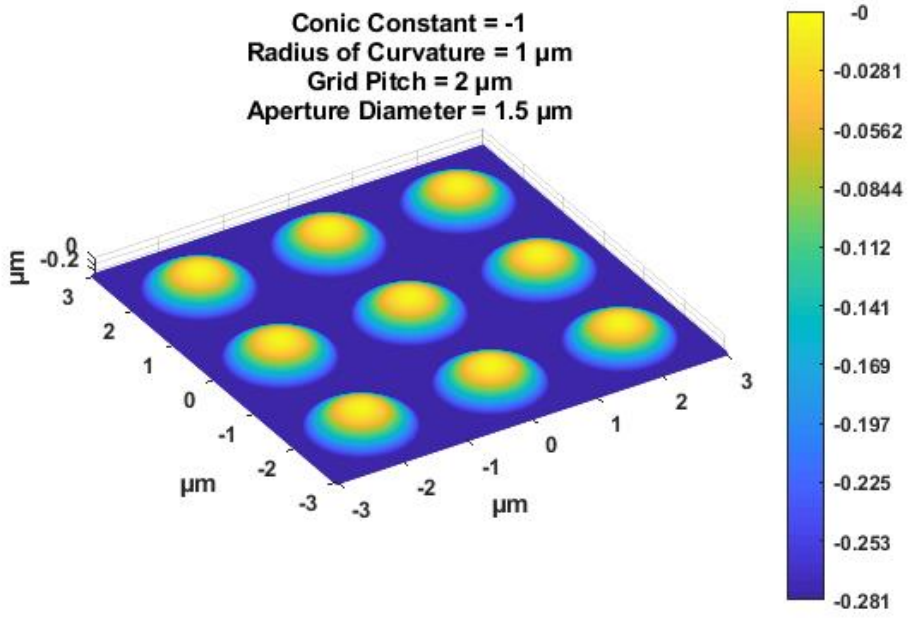

Figure 4-5. Surface plot of die geometry on a 2 µm grid

For a single feature, 0.9 μm^3 needs to be removed assuming the apex of the feature is level with the original virgin surface of the material.

4.2 NANOINDENTATION

As described in the proposal, one of the first tasks in the project is to use the Bruker Hysitron TI980 at the AIF to conduct single indent experiments on the correct length scale and characterize the indentation process as a means of creating an array. The AIF has a conical indenter tip with a 90° cone angle and 1 µm radius available for general use. A drawing of the nominal dimensions of this tip is shown in Figure 6. This tip should yield indentations of the correct length scale.

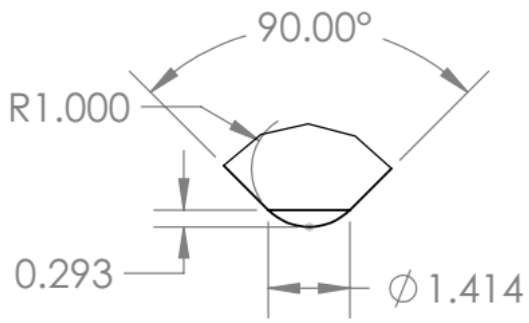

Figure 4-6: Nanoindenter tip geometry (tangents shown for clarity)

4.2.1 **Diamond Turning 1100 Aluminum for Surface Finish**

1100 Al was characterized with experimental data in previous work with Sumit Gundyal. In Sumit's nanoindentation experiments and analysis, the need for high quality surfaces was identified. Previously, surface finish on the order of 15-20 nm RMS was used for the larger scale indentation tests (~R15 µm hemispheres). However, better surface finish is needed for the much shallower nanoindentation experiments. Particularly challenging are streaks caused by chip striking. A Ø19 x 6.35 mm 1100 Al sample was mounted to a large aluminum disc with double-sided tape off of the spindle axis. The large disc was vacuumed to the chuck of the Nanoform. Experiments were conducted with various cutting fluids and feeds to determine parameters to achieve the best finish. The experiments were conducted with a 521 µm radius diamond tool (serial number 21256). For all experiments the spindle speed was 1000 rpm. Chips were managed with shop vac crevice tool setup near the cutting zone or a 1/8" tube spraying compressed air at the tool. The idea of the shop air spray is that the compressed air will blow the chips away from the part and prevent chip striking. Figure 30 shows the setup with the compressed air on the left.

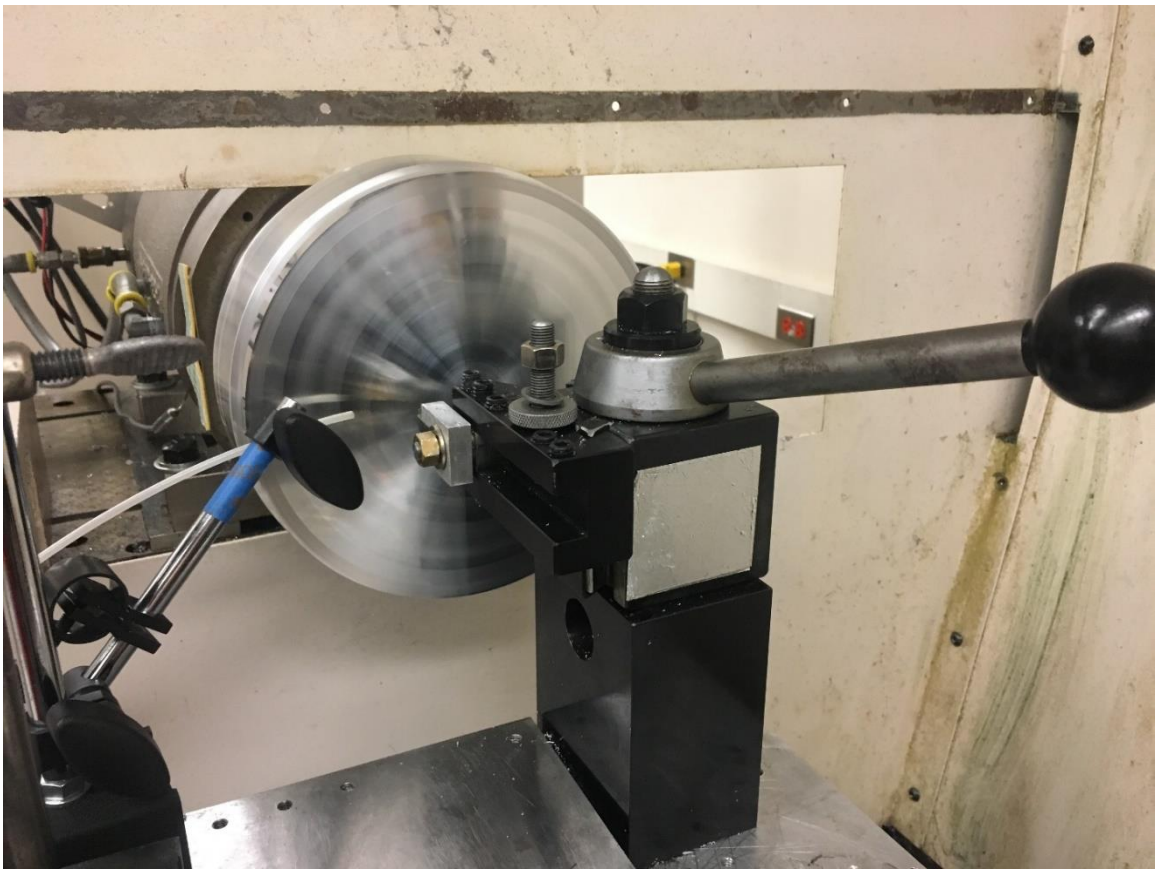

Figure 4-7: Diamond Turning Setup. Note the tube on the left side of the tool post.

Table 1 shows the results of the experiments. The vacuum is not controlling the chips adequately. With the compressed air both a 5 µm/rev and 1 µm/rev crossfeed yielded similar average RMS surface finish. However, the slower crossfeed led to a more consistent finish and lighter streaks from chip damage. The undamaged surface did not show cutting marks. An example of the surface cut with a 1 µm/rev crossfeed is shown in Figure 31. The compressed air will influence the form of the part, but these parameters should be adequate for an indentation sample.

Table 4-1: 1100 Al Cutting Experiment

Feed (µm/rev)	Depth of Cut (µm)	Cutting Fluid	Chip Management	RMS Finish (nm)
5	21.5	Continuous Tap Magic Aqueous Drip	Vacuum	~ 20
1	20	Wiped with Tap Magic Aqueous before cutting	Vacuum	Visibly bad
1	20	Sprayed with WD-40 before cutting	Vacuum	>20, Visibly bad

5	20	Wiped with Tap Magic Aqueous before cutting	Compressed Air	9, Noticeable streaks
1	20	Wiped with Tap Magic Aqueous before cutting	Compressed Air	10, more consistent, smaller and fewer streaks

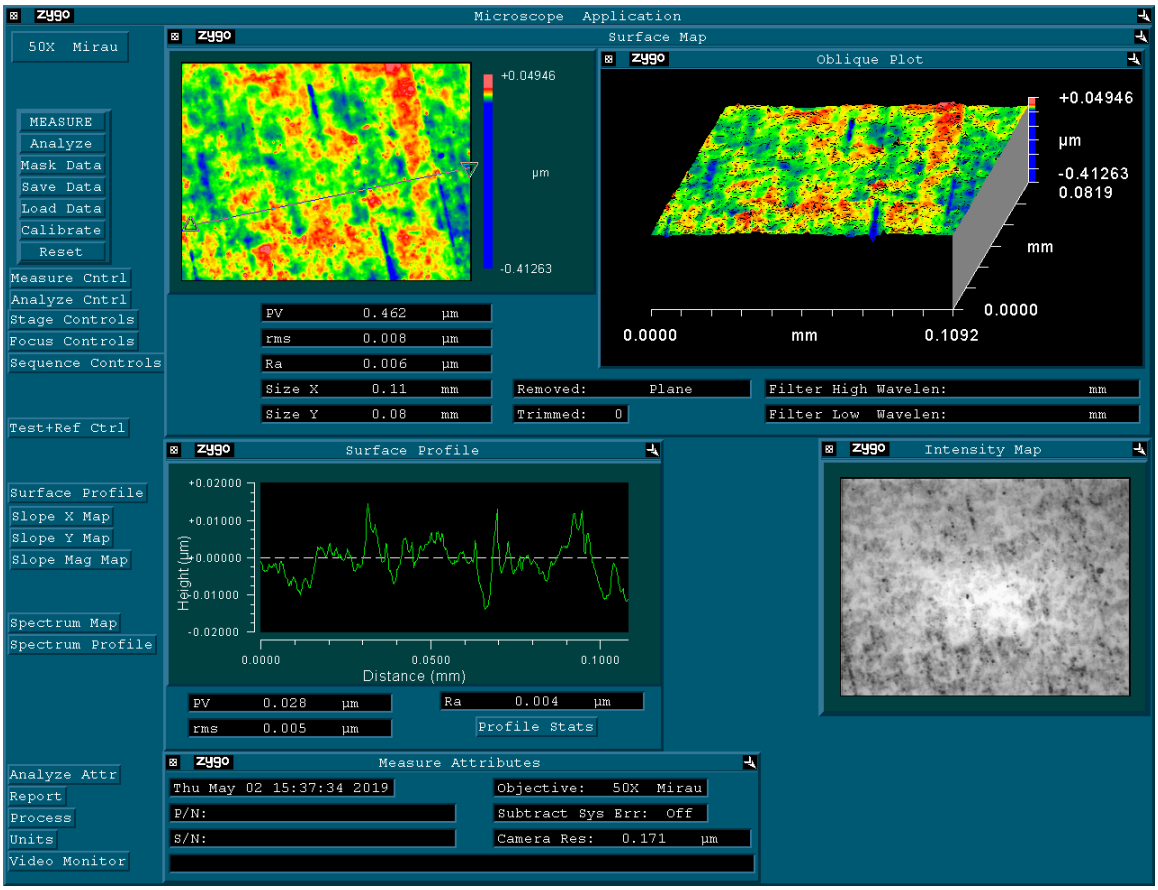

Figure 4-8: Diamond Turned 1100 Al with a 1 µm/rev crossfeed

The piece of 1100 Al used for nanoindentation was diamond turned. A surface finish of 9 nm RMS, as averaged over 7 locations, was achieved. The piece was turned on the Nanoform with a diamond tool with radius 521 µm (SN 21256). The spindle speed was set to 1000 RPM, with a cross feed of 1 µm/rev and depth of cut of 20 µm. The cut was lubricated with Tap Magic Aqueous which was wiped onto the part before commencing the CNC program. A continuous stream of compressed air was blown on the tool tip to remove chips from the cutting zone. Figure 7 shows an example measurement of the surface from the New View 5000 scanning white light interferometer.

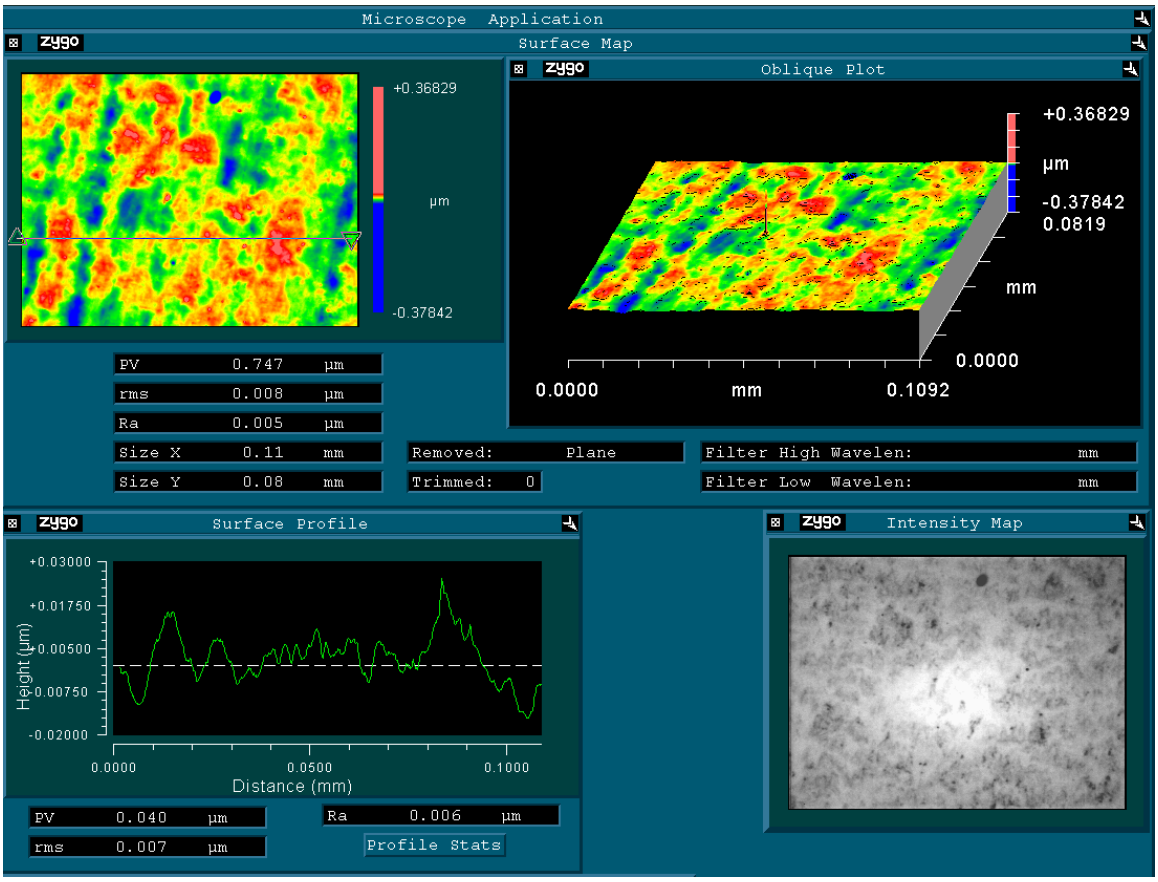

Figure 4-9. New View measurement of the diamond turned 1100 Al surface

This diamond turned surface was nanoindented with the conical and Berkovich tips. Figure 6 shows the nominal geometry of the conical indenter tip. The depth of the spherical portion of the tip is 293 nm.

A series of indents with the conical tip were conducted with forces of 1, 1.5 and 2 mN. The indentation profile had a 10 s load and unload time. Figure 8 shows the measured load profile for the first three indents. Each indentation force was replicated 5 times. The indents were placed 20 µm apart in a grid pattern. Figure 9 shows a picture of the indented area. The conical indents are the faint 3x5 grid labeled “Conical Indent.”

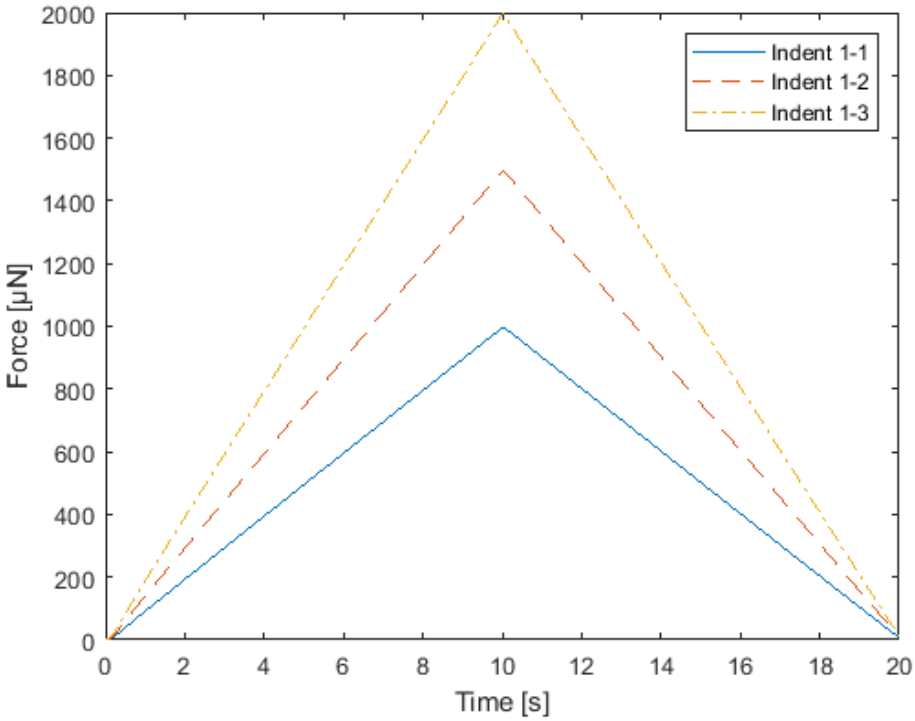

Figure 4-10. Load-time curve for the conical indents in 1100 Al

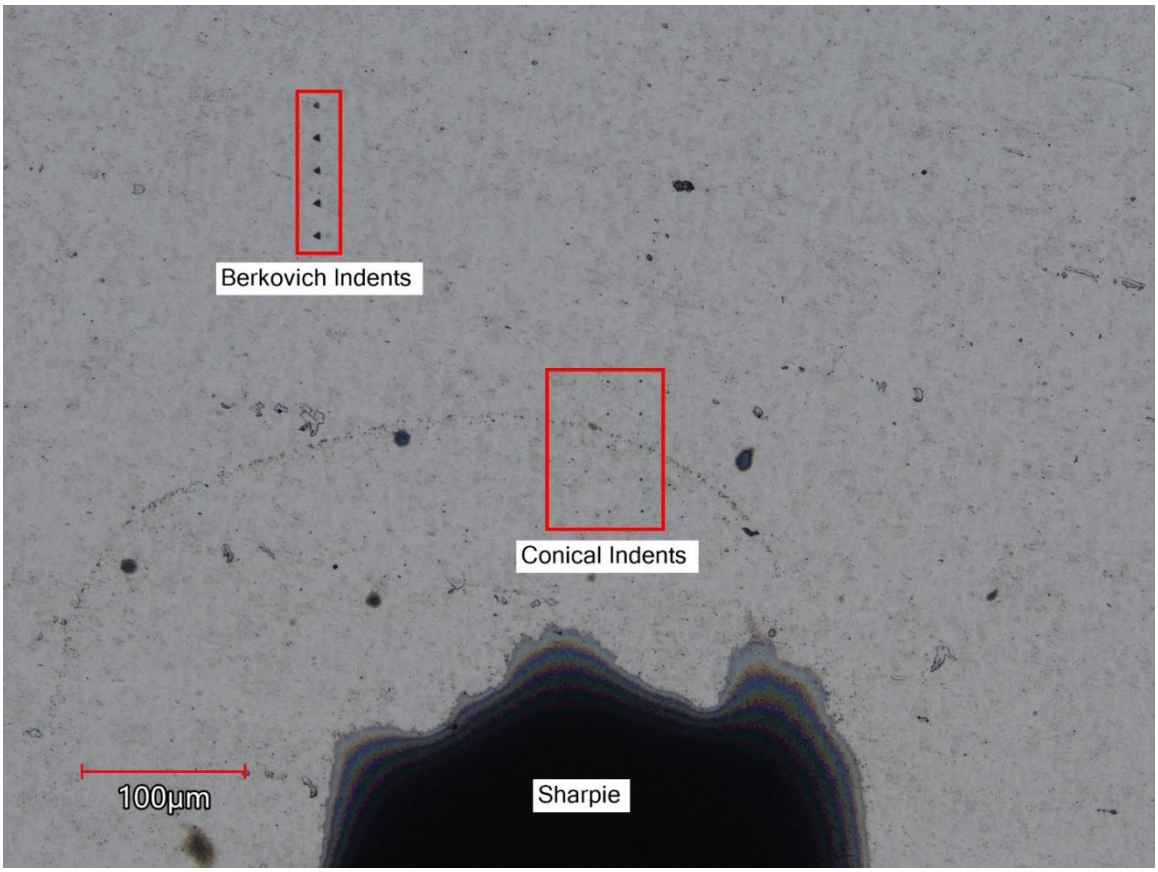

Figure 4-11. Overview 1100AL indents

The load displacement curves for the indents were captured during the indentation process. Figure 10, Figure 11, and Figure 12 show the load displacement curves for each maximum load with the replicates. These three figures all use a common axis range. For some reason the lower load indents have more variability. The cause for this variability is unknown at this time.
From the plots, a maximum load of 1.5 mN appears to yield depths that are close to 293 nm but does not exceed that depth value. 1.5 mN should be the target force for indents that seek to leave depression from only the spherical face of the indenter.

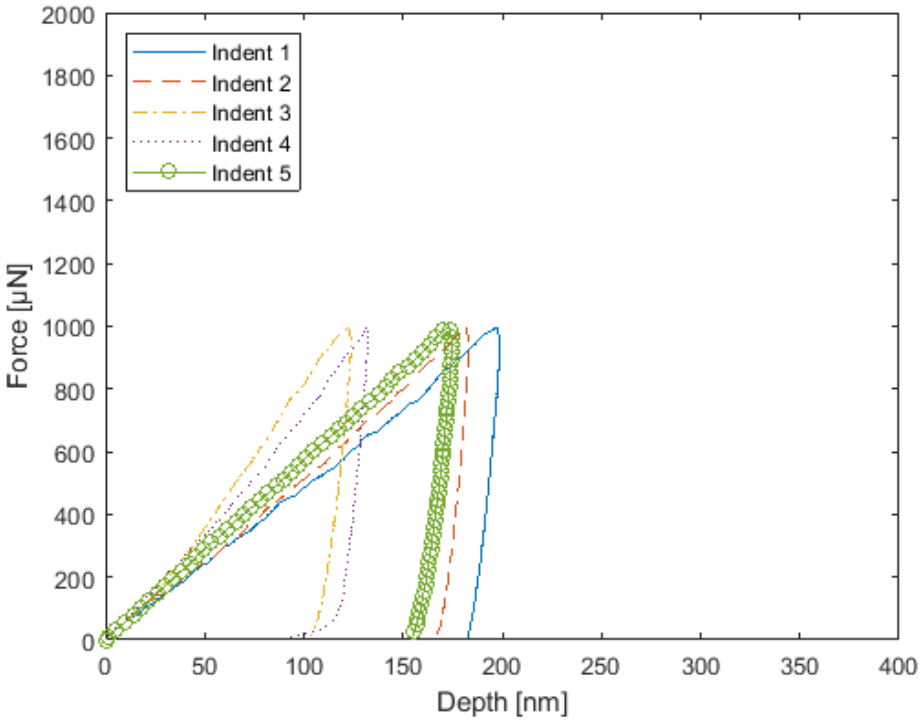

Figure 4-12. Load-displacement data for 1 mN conical indents in 1100 Al

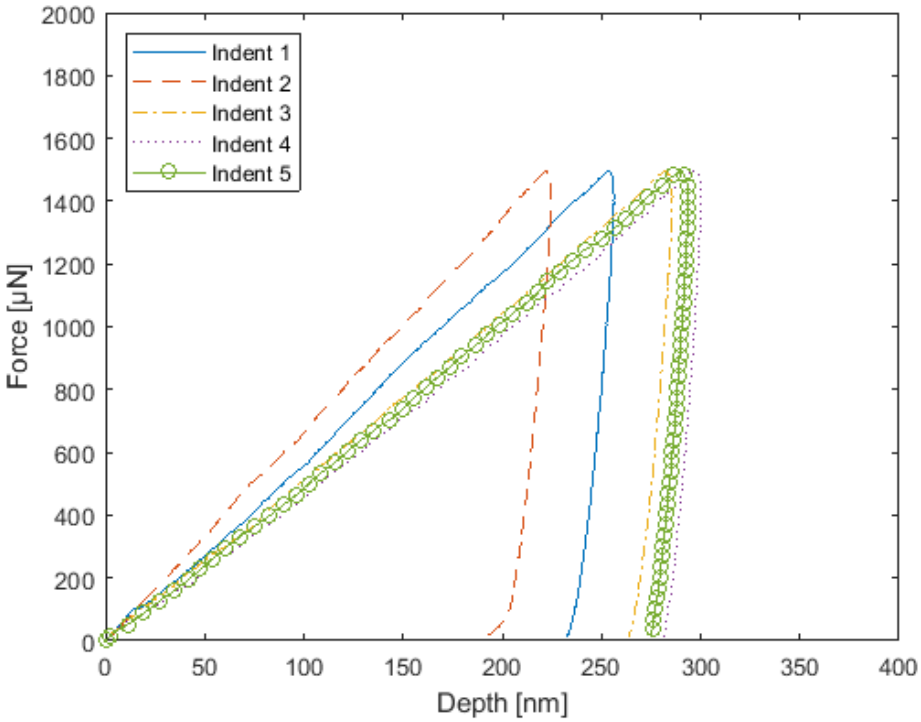

Figure 4-13. Load-displacement data for 1.5 mN conical indents in 1100 Al

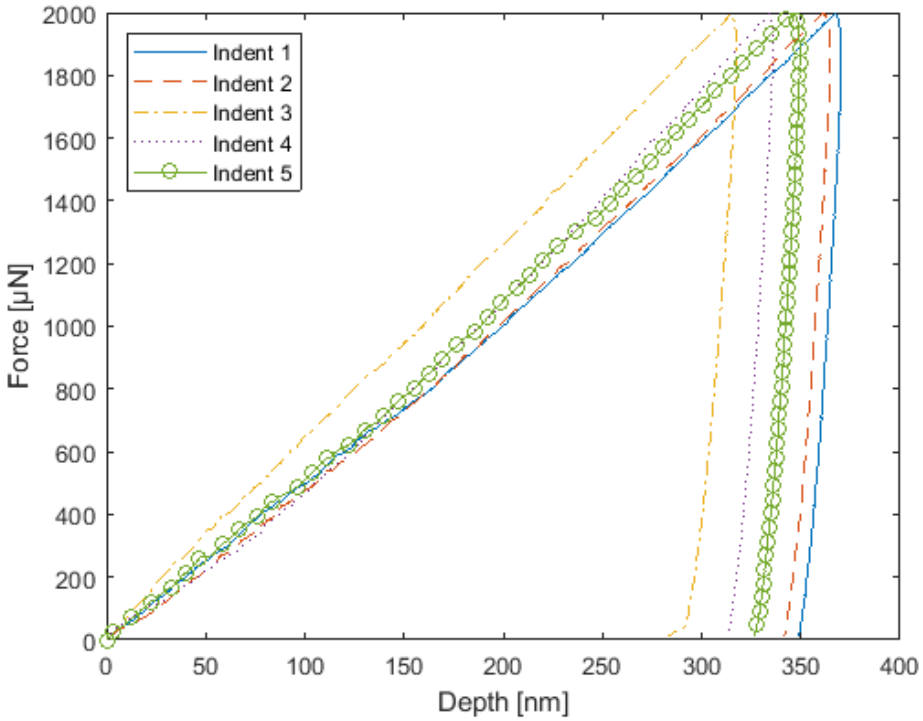

Figure 4-14. Load-displacement data for 2 mN conical indents in 1100 Al

Berkovich indents were repeated for this aluminum sample. The load profile is shown in Figure 13. The maximum load was 10 mN with a 30s load and unload time. These are parameters which were used in previous indentation experiments. The indent was replicated 5 times and spaced 20 μm apart. An image of the indents are shown in Figure 9 in the region labeled “Berkovich Indents.” The load-displacement curves for the five indents are shown in Figure 14. Indent 5 appears to have some issue. These indents were supposed to be compared to previous Berkovich indents in 1100 Al in Sumit Gundyal’s thesis, but that analysis never happened.

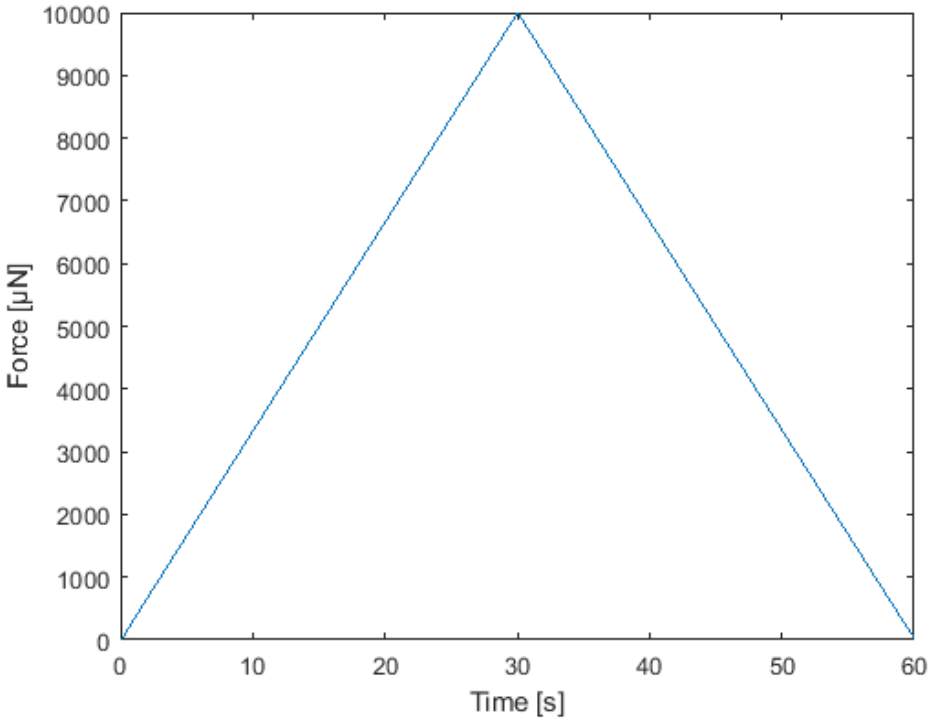

Figure 4-15. Load profile for Berkovich indents in 1100 Al

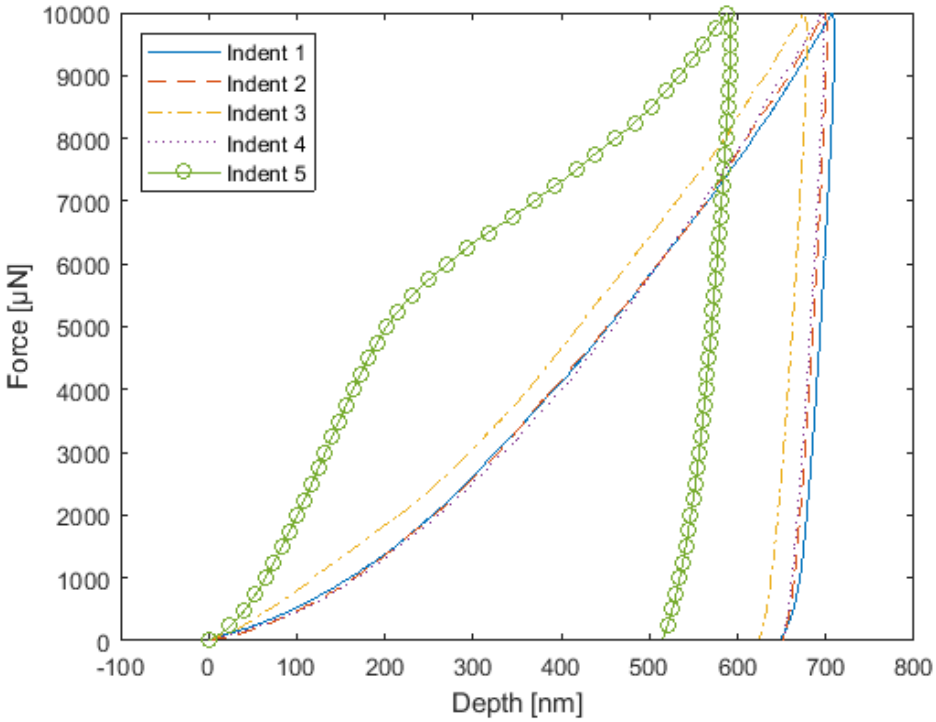

Figure 4-16. Load-displacement curves for Berkovich indents in 1100 Al

A 10 x 10 array of indents spaced 2 µm apart were created on the Nanoindenter to make it easier to find the array with metrology instruments. Figure 15 shows a low magnification (120x) image of the array of indents. Even at this low magnification the 10 x 10 array is visible. A 2 µm spacing was used because by that time the target maximum spacing had been reduced from 3 µm to 2 µm.

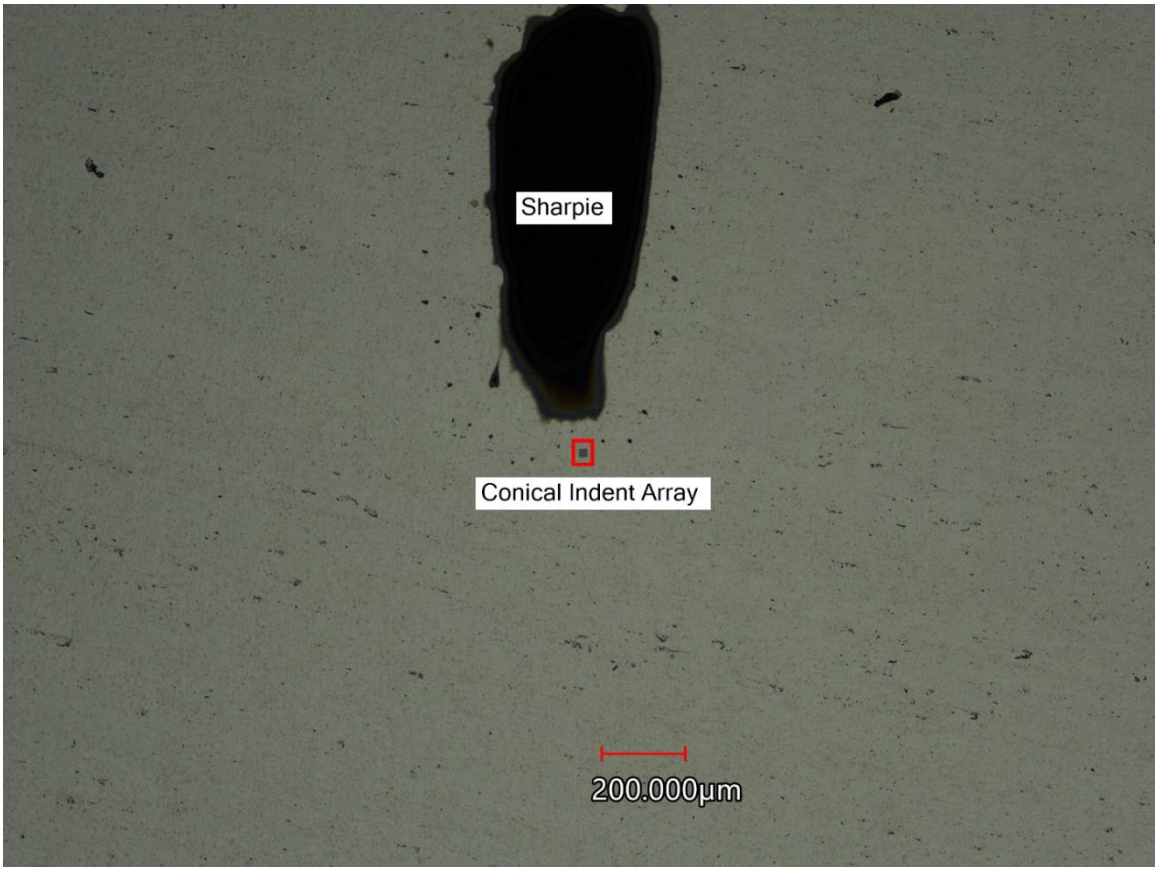

Figure 4-17. 10 x 10 array of indents in 1100 Al (120x magnification)

The load profile was chosen to be a 10 second load and unload time with no hold time, similar to previous experiments. However, the load profile was not setup correctly, and a load and unload time of 3.75 s was used for the experiment. This difference in load time is not thought to be a significant difference. 1.5 mN was used as the max force. A load of 1.5 mN will yield an indent that will replicate only the spherical surface of the conical tip and not penetrate deep enough to indent with the conical face. Figure 16 shows the load profile of the first indent in the array. Due to the incorrect load and unload time, the total time of the indent is 7.5 s instead of 20 s.

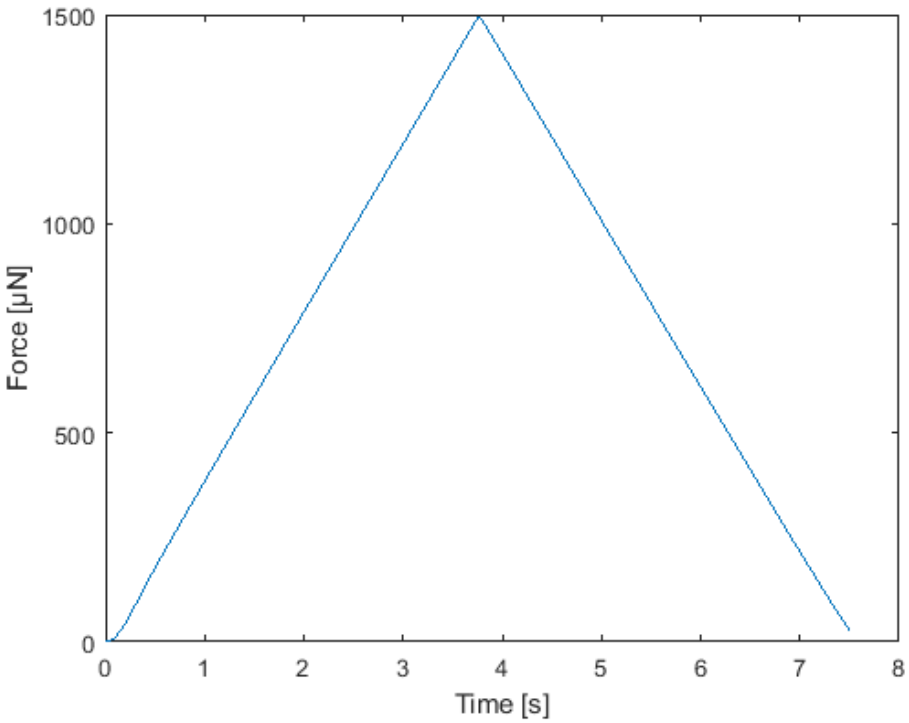

Figure 4-18. Load profile of the first indent in the 10 x 10 array

The indents were conducted in a raster pattern, and the order is shown in Figure 17. As seen in the figure, the first indent occurred in the lower left corner. A horizontal row was indented from left to right. Then the pattern was repeated after traversing 2 µm in the vertical direction, and so forth. As can be seen from the images, there is some variability in the size of the indents. This phenomenon is also seen in the load data. Figure 18 shows the load displacement curves for the first ten indents. Notice that indent 1 is much shallower, and accordingly indent 1 in Figure 17 also appears smaller. The reason for the variability is not known at this time. It could be caused by material inhomogeneity causing differing hardness within the sample. Alternatively, it could be caused by dirt or debris on the tip or the sample surface changing the contact.

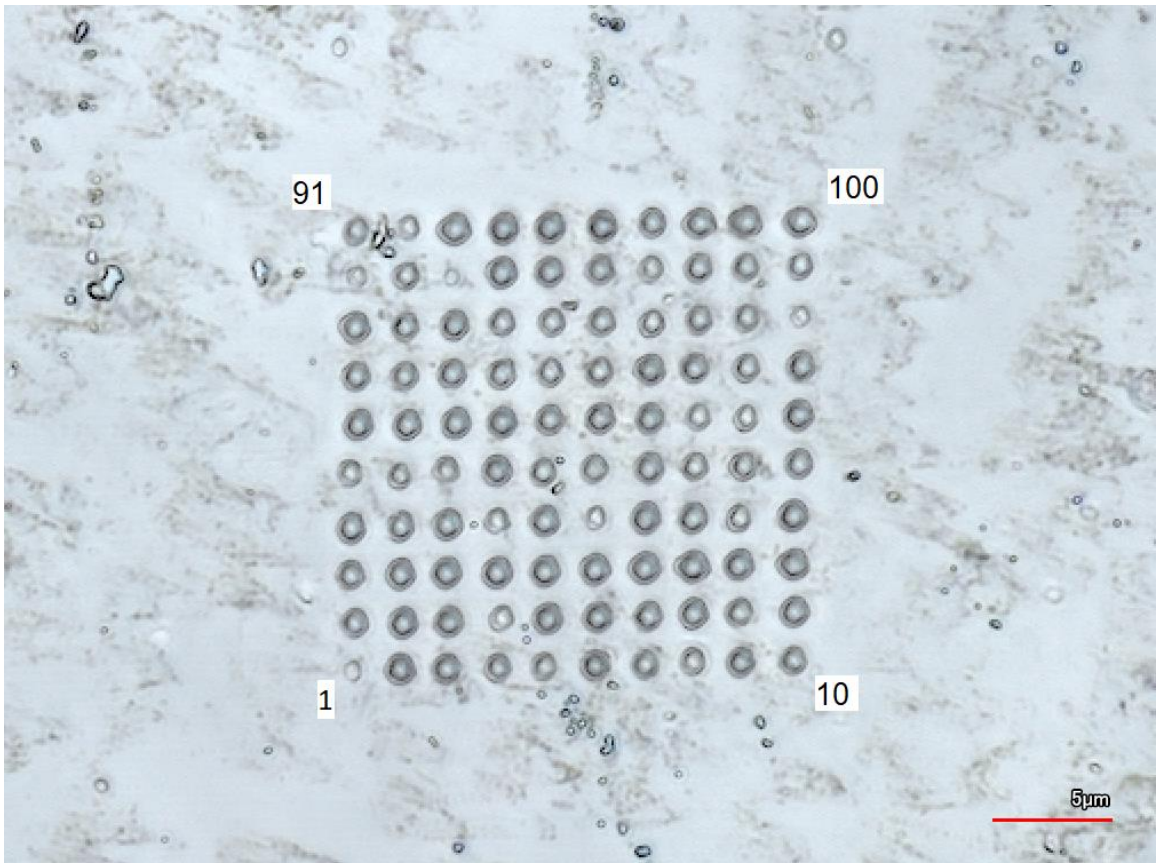

Figure 4-19. 10x10 Array of indents in 1100 Al (numbers indicate the sequence of the corner indents)

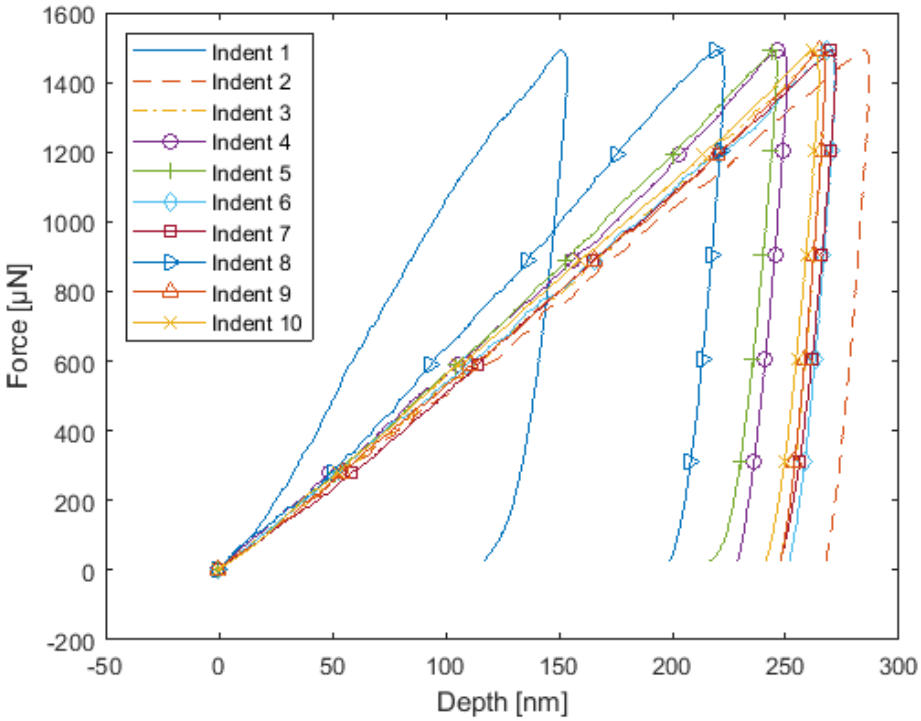

Figure 4-20. Load-displacement curves for the first ten indents in 1100 Al

For comparison, Figure 19 shows the load displacement curves for indents 21-30. As might be expected the first indent for the row is slightly different as it does not have a preexisting neighbor to its left. Otherwise, the indents all going to the same depth within 25 nm. Figure 17 also shows that the third row of indents look uniform. The load-displacement curves for the subsequent row is shown in Figure 20. The curves for indents 34, 36 and 39 look very different from the rest, and accordingly, the indents look shallower in Figure 17.

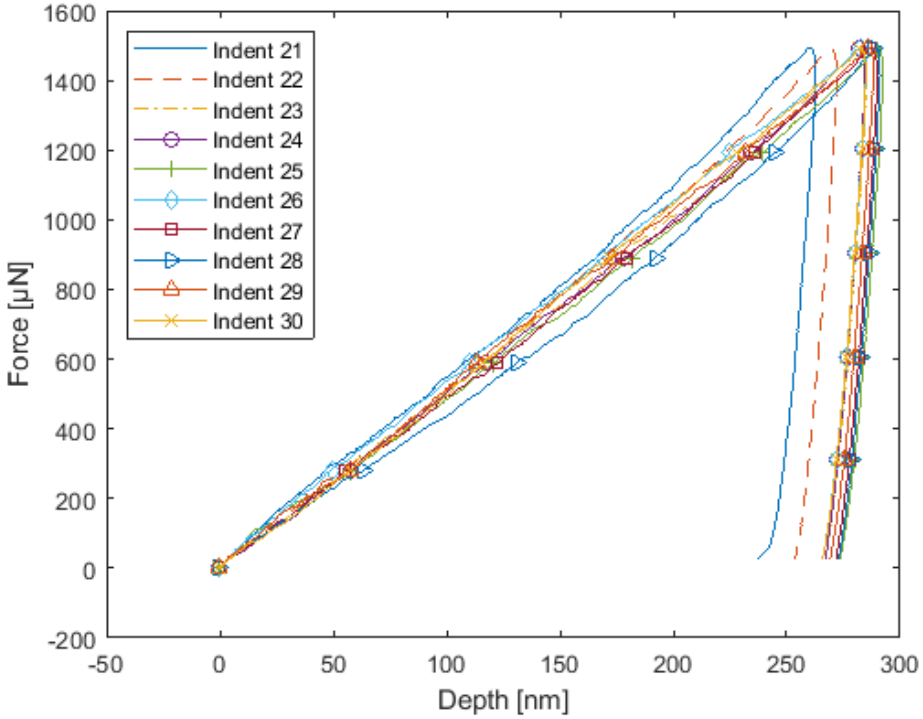

Figure 4-21. Load-displacement curves for indents 21-30 in 1100 Al

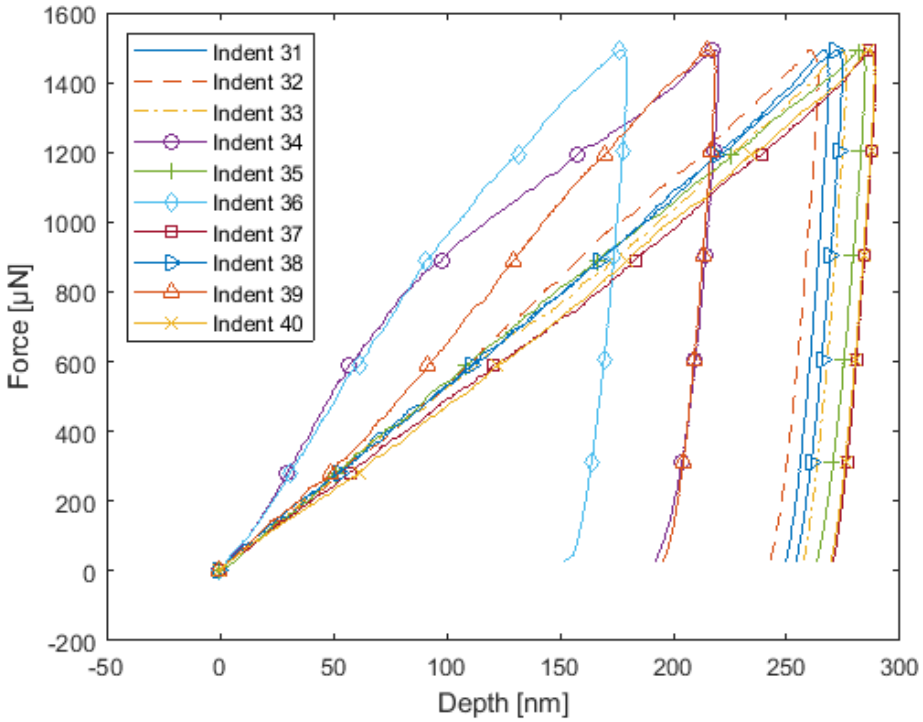

Figure 4-22. Load-displacement curves for indents 31-40 in 1100 Al

The array was imaged with the SEM and two representative images are shown in Figure 21 and Figure 22. These images, like the microscope images, confirm the non-uniformity of the indents. The non-uniformity was also quantitatively measured in the force-displacement data which showed varying depth for the same maximum load. The SEM images do not show any obvious issues with the sample preparation such as irregularities in the surface. The non-uniformity in the indents may be caused by material inhomogeneity.

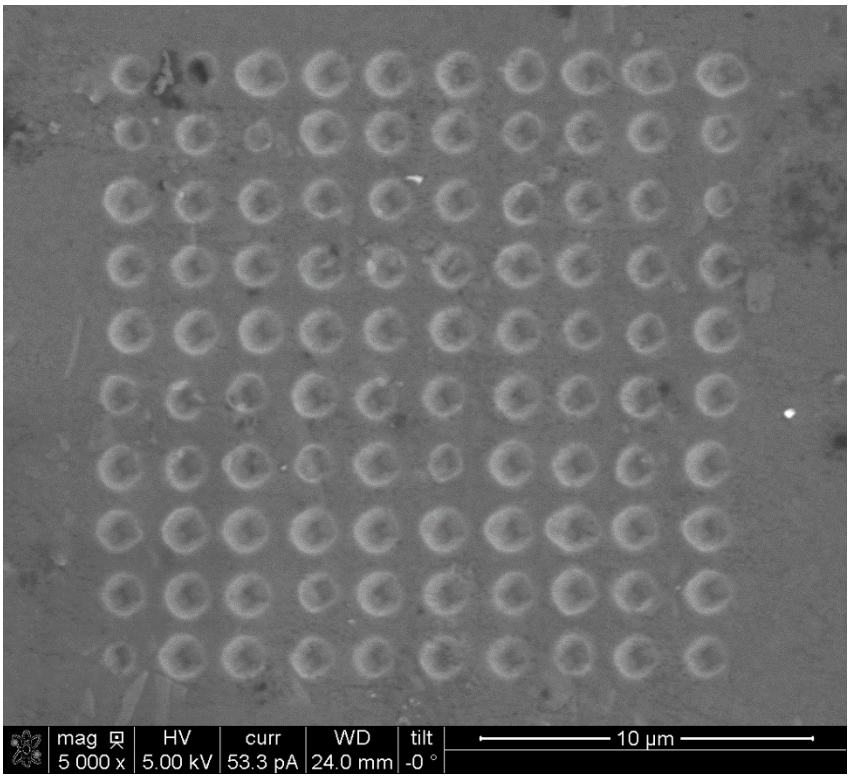

Figure 4-23. 10 x 10 array of indents in 1100 Al

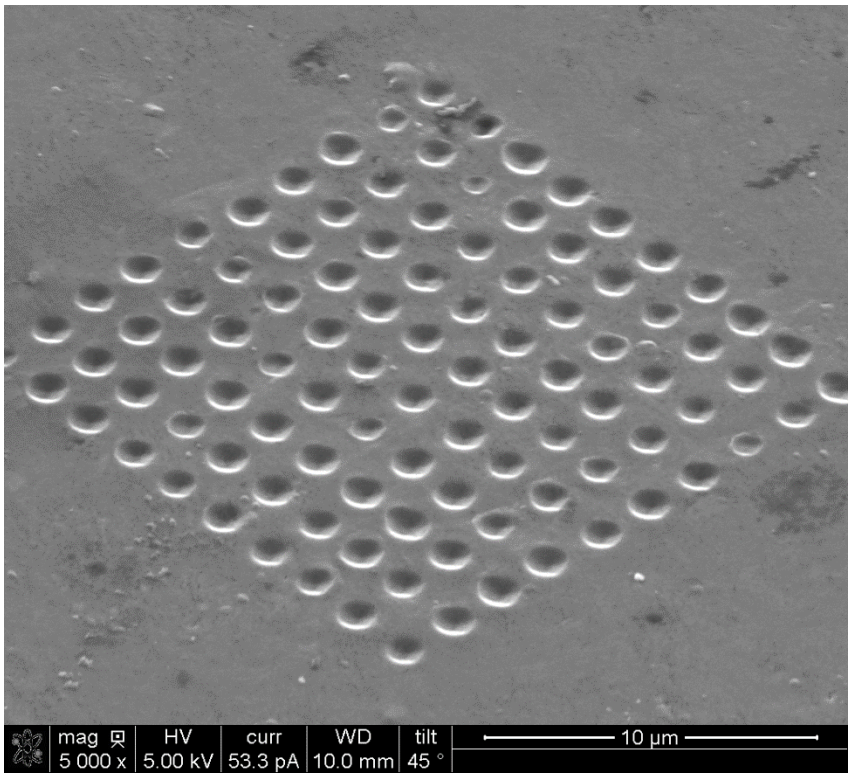

Figure 4-24. Another view of the 10 x 10 array of indents in 1100 Al

One issue that arose when imaging the aluminum sample was charging. Charging appears as sample drift when an unwanted electromagnetic field distorts the path of the electrons. Typically, this occurs in non-conductive samples as the electron beam begins to impart a negative charge on the sample over time. However, charging is not expected in a properly grounded aluminum sample. After consulting Roberto Garcia, this might have been caused by the magnetic stainless steel specimen disc used in the nanoindenter. These discs are held in the nanoindenter with a magnetic preload, which may be imparting a small amount of residual magnetism to the stainless steel. Roberto Garcia suggested degaussing the samples next time. The AIF has a machine to degauss samples.

4.3 METROLOGY

Indents were measured with the New View 5000 scanning white light interferometer (SWLI) at the highest magnification possible. The results are shown in Figure 23 and Figure 24. As can be seen in the figures, the New View cannot get data in the sloped portion of the indents. A few data points appear at the bottom of the indent, but not enough to characterize the indentation.

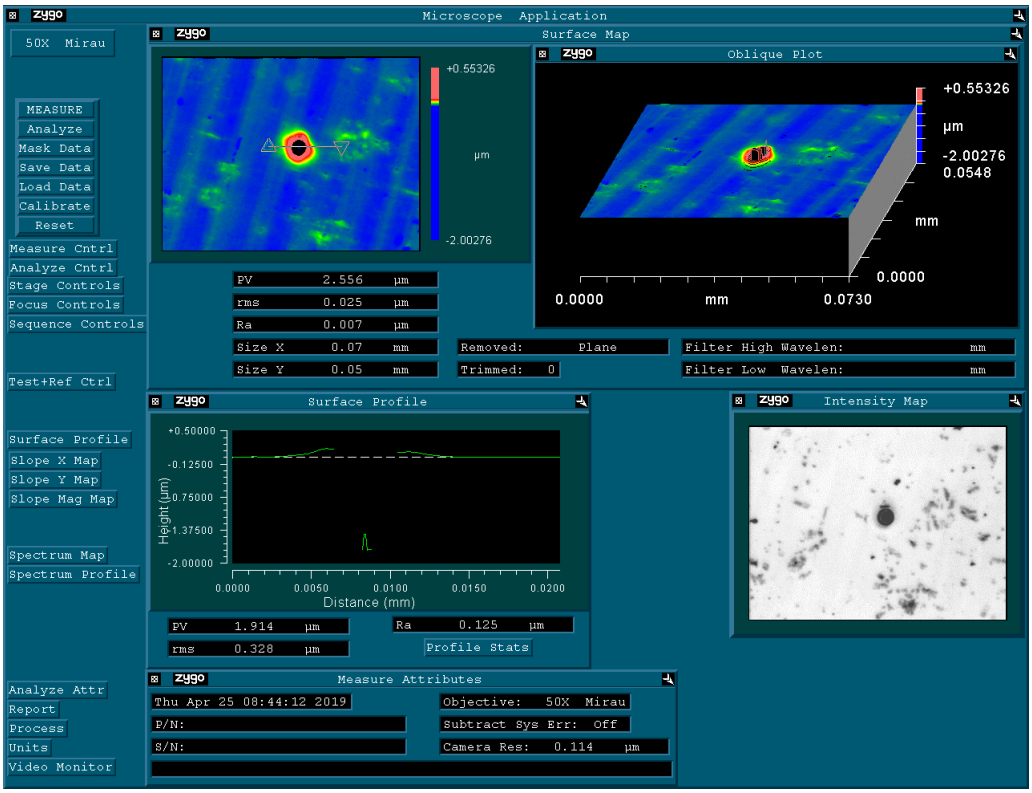

Figure 4-25: New View measurement of the single indent

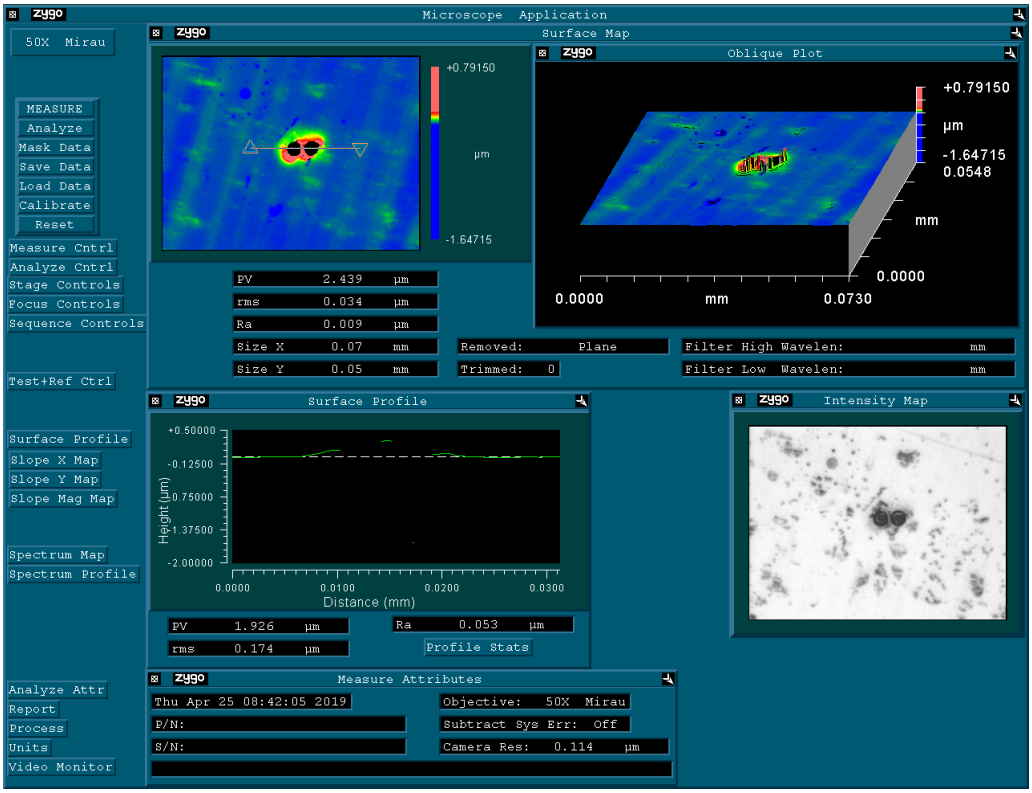

Figure 4-26: New View measurement of two indents

The indents were also measured in the Keyence laser confocal microscope at the highest magnification. Figure 25 and Figure 26 show a cross section from the laser confocal microscope measurements. As can been seen from the figures, the laser confocal measurements can capture data across the entire indent. However, the laser confocal is limited to 0.08 µm/pixel. As seen in Figure 6, the tip geometry has a spherical aperture of 1.4 µm. This means that there will be about 17 pixels across the spherical portion of the indentation. Figure 27 shows a profile of the spherical portion of the single indent. About 17 points can be counted across the radius, and the profile does not look smooth due to the low resolution.

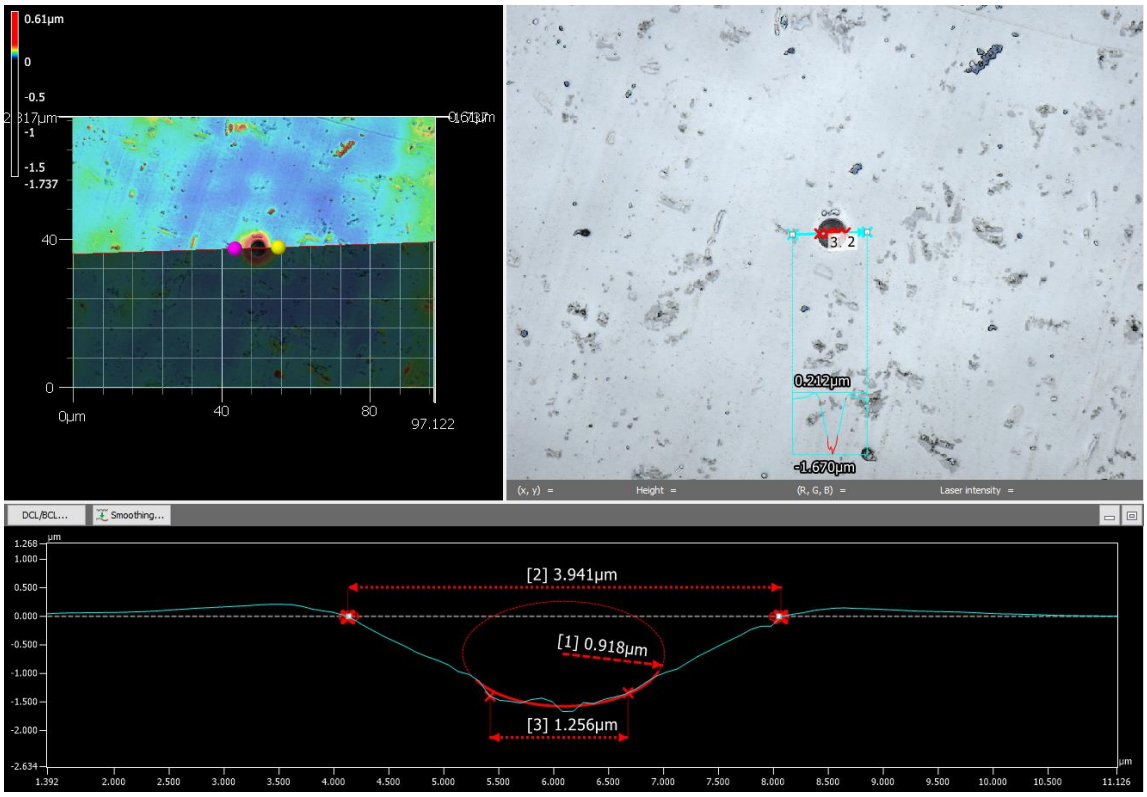

Figure 4-27: Laser confocal microscope measurement of the single indent

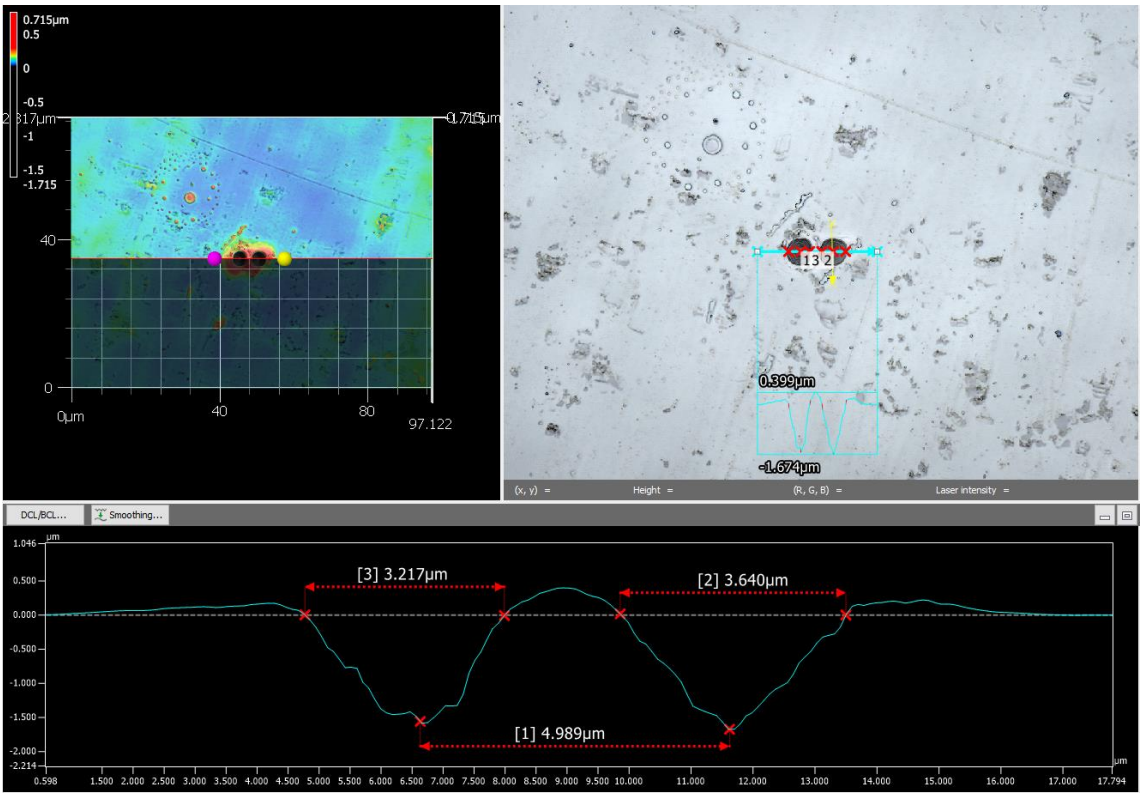

Figure 4-28: Laser confocal microscope measurement of two indents

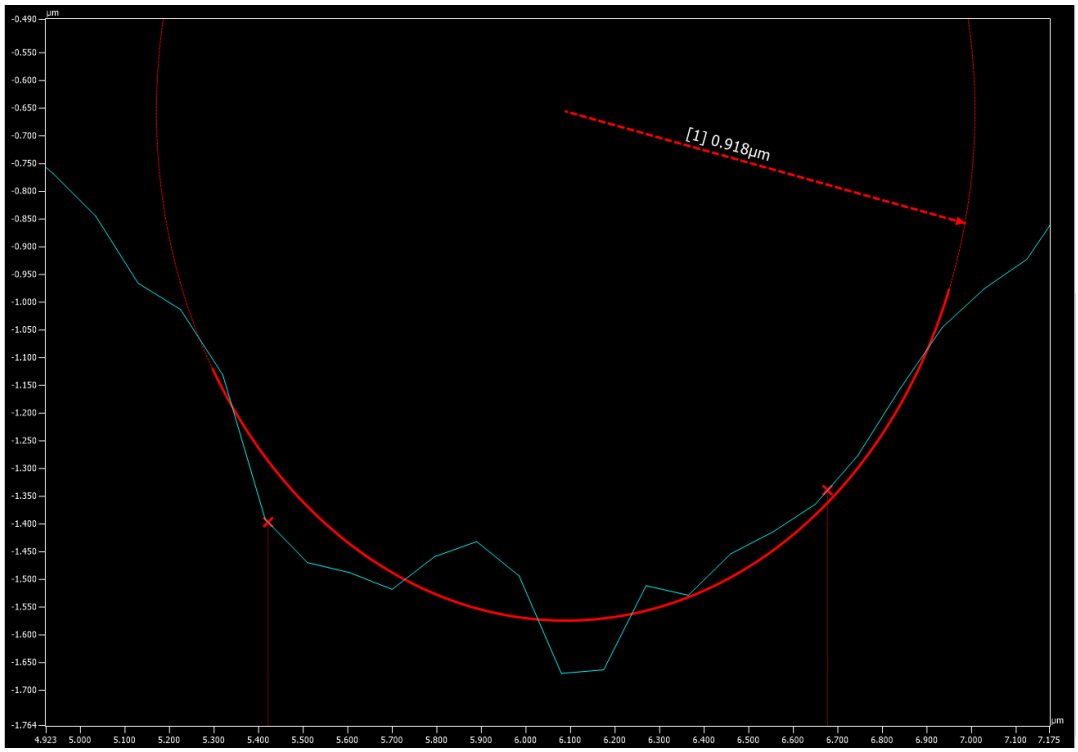

Figure 4-29: Close up of the trough of the single indent

The AFM has an optical microscope for finding features of interest, but it is not very high magnification, which made it difficult to find the small indents. Indents should be done in arrays to make them easier to find. Figure 28 shows a topographical map of the AFM data after it was imported into Matlab. Due to the pixels not being square (128 x 256 pixels covering a 10 x 10 µm area), it has some issues with sectioning in the Slicer Matlab tool. However, the AFM software was able to provide a section of the indent shown in Figure 29. The AFM appears to be the only instrument capable of providing sufficient resolution to measure the form if an indent.

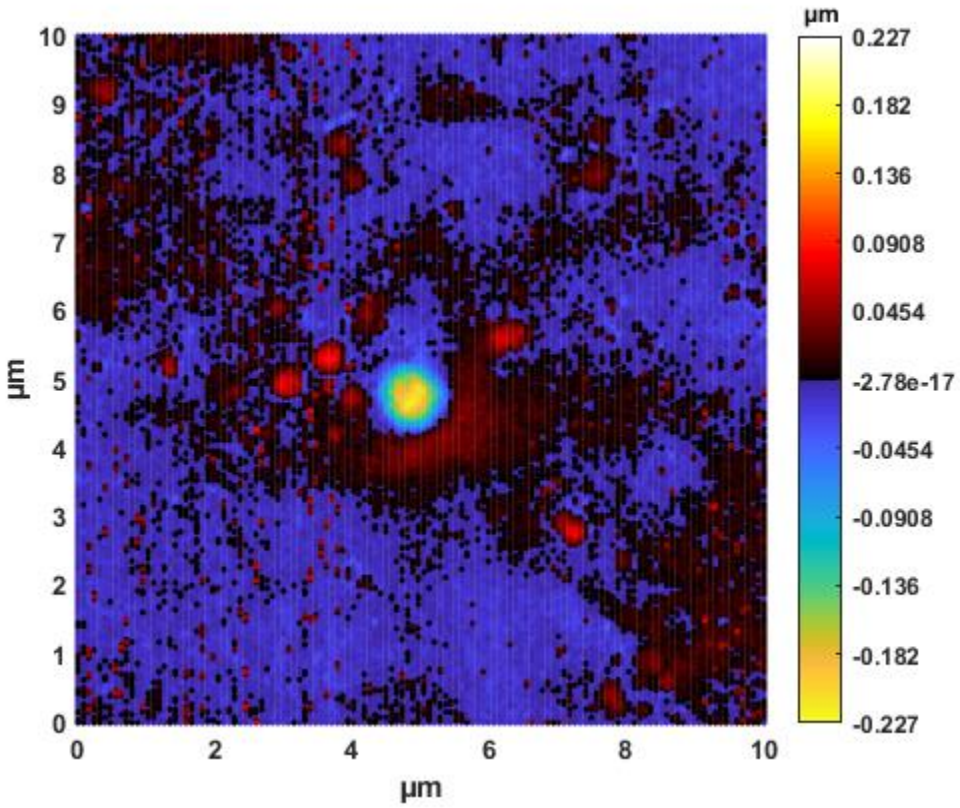

Figure 4-30. AFM measurement of an indent in 1100Al

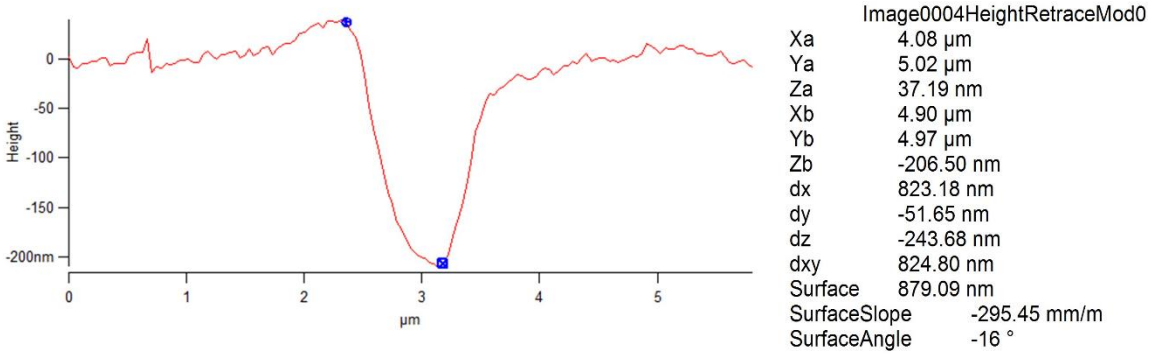

Figure 4-31. Section of the AFM data

4.4 FIB CHARACTERIZATION

Next, an investigation of machining the die into diamond using FIB milling was completed. First a sample A nominally 1 x 1 x 5 mm diamond post was purchased from Chardon tool. Though the specifications say it was to be polished on both ends, only one end is polished. The diamond sample was super glued to a 90° SEM mount, and the super glue bond was bridged with conductive tape. Then the surface was sputter coated with Au-Pd. Finally, a dab of cutting oil was placed in the corner of the diamond. Figure 32 shows the prepared diamond sample with the SEM pin mount. Figure 33 shows an SEM image of the diamond sample. Note the oil contamination in the upper right corner of the sample. The right side of the image is the conductive tape.

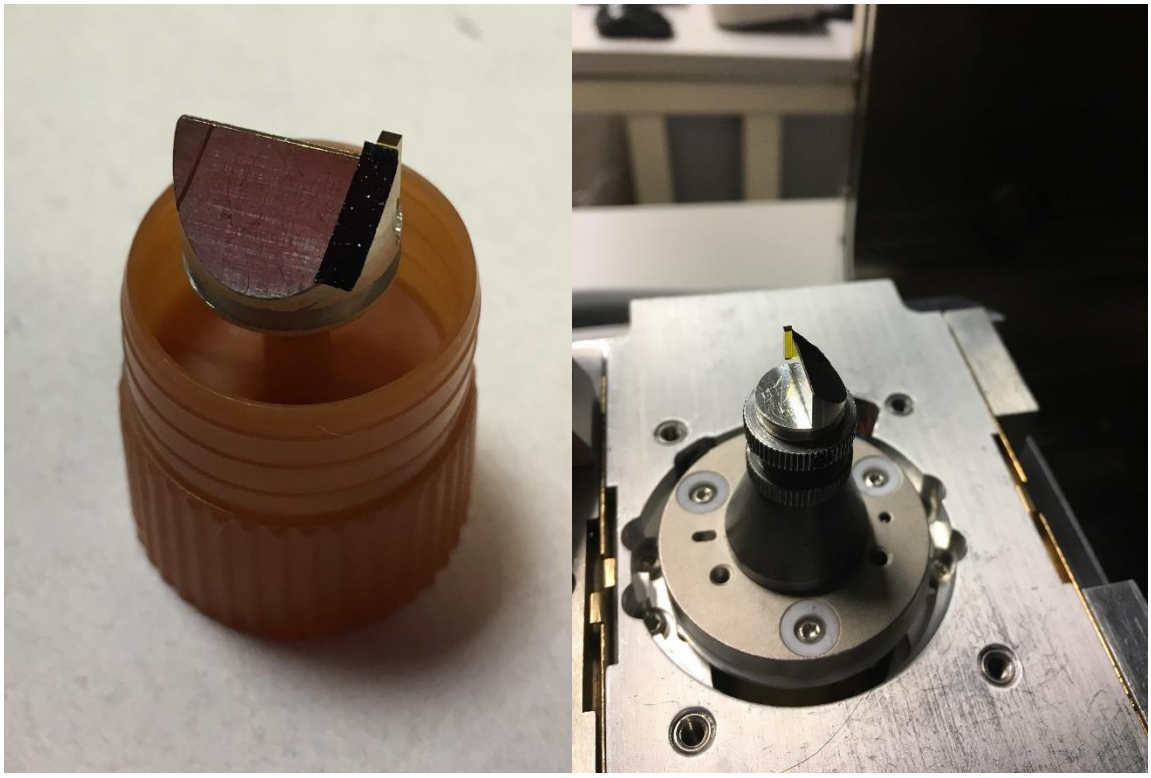

Figure 4-32. Prepared diamond sample

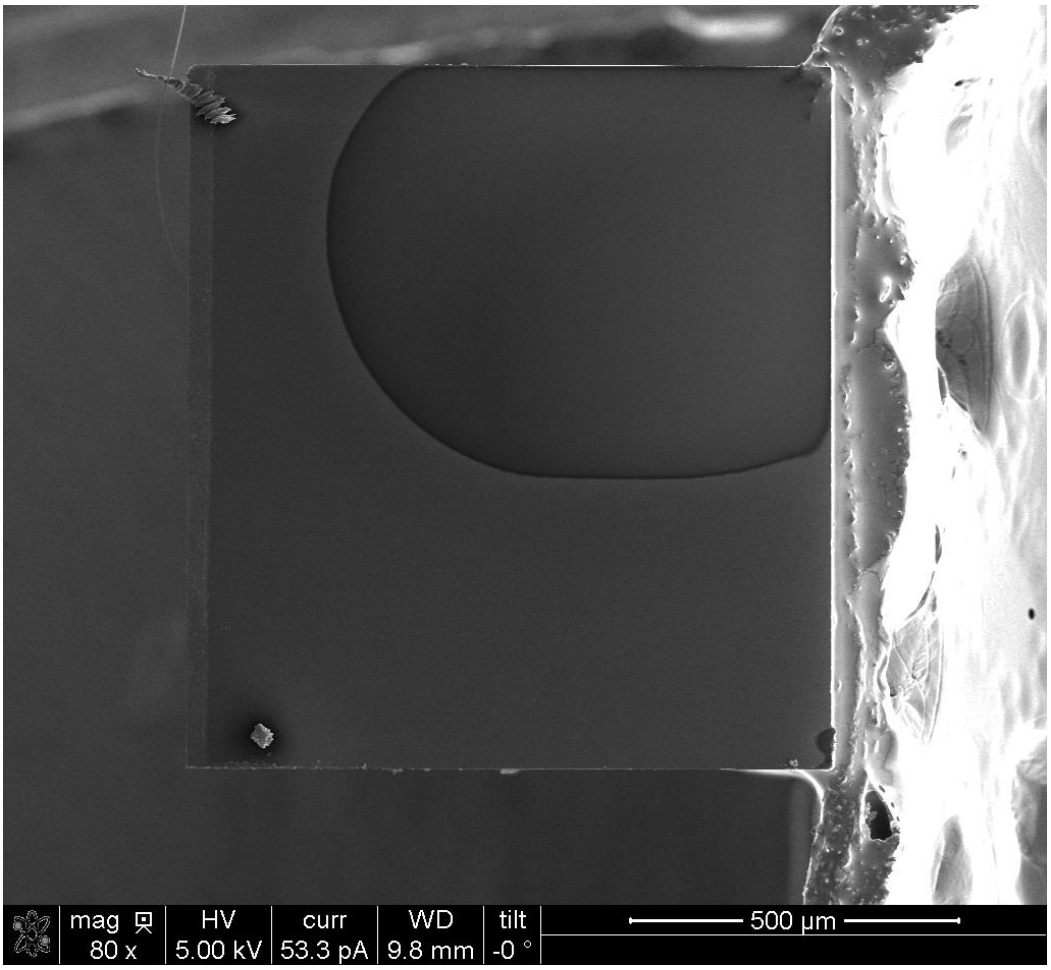

Figure 4-33. SEM image of the prepared diamond sample

A basic cutting test looking at the material removal rate was conducted. Based on previous results reported in the 2018 PEC annual report, the ion beams with currents above 5 nA were determined to not be axisymmetric. These initial cutting tests were conducted with 5 nA and 3 nA beams. According to Table 2 from the manual for the FIB, these currents have a nominal beam diameter of 85 nm and 66 nm respectively. Based on previous work, bitmap patterns work best when the overlap is about the same as the beam diameter. For this cutting test, bitmap patterns were created for a 10 µm square. For the 5 nA beam, a 100 nm overlap was used. For the 3 nA beam a 50 nm overlap was used. Other test parameters are summarized in Table 3.

Table 4-2. Ion beam currents and corresponding beam diameters from the FIB manual (Table 5-4).

Beam current [pA]	Beam Diameter [nm]	Usage
1.5	7	Very high resolution, High aspect ration holes, Pt via filling
10	13	Quick imaging, Fast Pt via filling
30	17	Navigation imaging, Milling submicron holes, Final milling on cross sections
50	19	
100	24	Milling micron-sized holes, Intermediate / final milling on cross sections, Short Pt strap deposition
300	31	Milling micron-sized holes, Intermediate milling on cross sections, Medium Pt strap deposition
500	35	
1 000	44	Initial milling for small cross sections, Long Pt strap deposition
3 000	66	Initial milling for medium cross sections, Longer Pt strap deposition
5 000	85	
7 000	102	Initial milling for medium-large cross sections, Pt probe pad deposition (40 µm × 40 µm)
15 000	182	
30 000	260	Initial milling for large cross sections, Pt bond pad deposition (50 µm × 50 µm)
50 000	300	
65 000	400	

Table 4-3. Other Parameters used for the 3 and 5 nA beam material removal rate test

Parameter	**5 nA**	**3 nA**
Magnification	8000x	
Dwell Time	100 µs	
Passes	1000	250
Total Time	16:40	
Bitmap File Name	bmp_Square_100nm.bmp	bmp_Square_50nm.bmp

It should be noted that after the sample was tilted in the stage to conduct the FIB milling operation that the oil contamination dripped down the sample due to gravity. Figure 34 shows an image taken by the laser confocal microscope of the diamond sample after all the FIB milling was completed. The spot of oil is now much larger after the part had been tilted 52°.

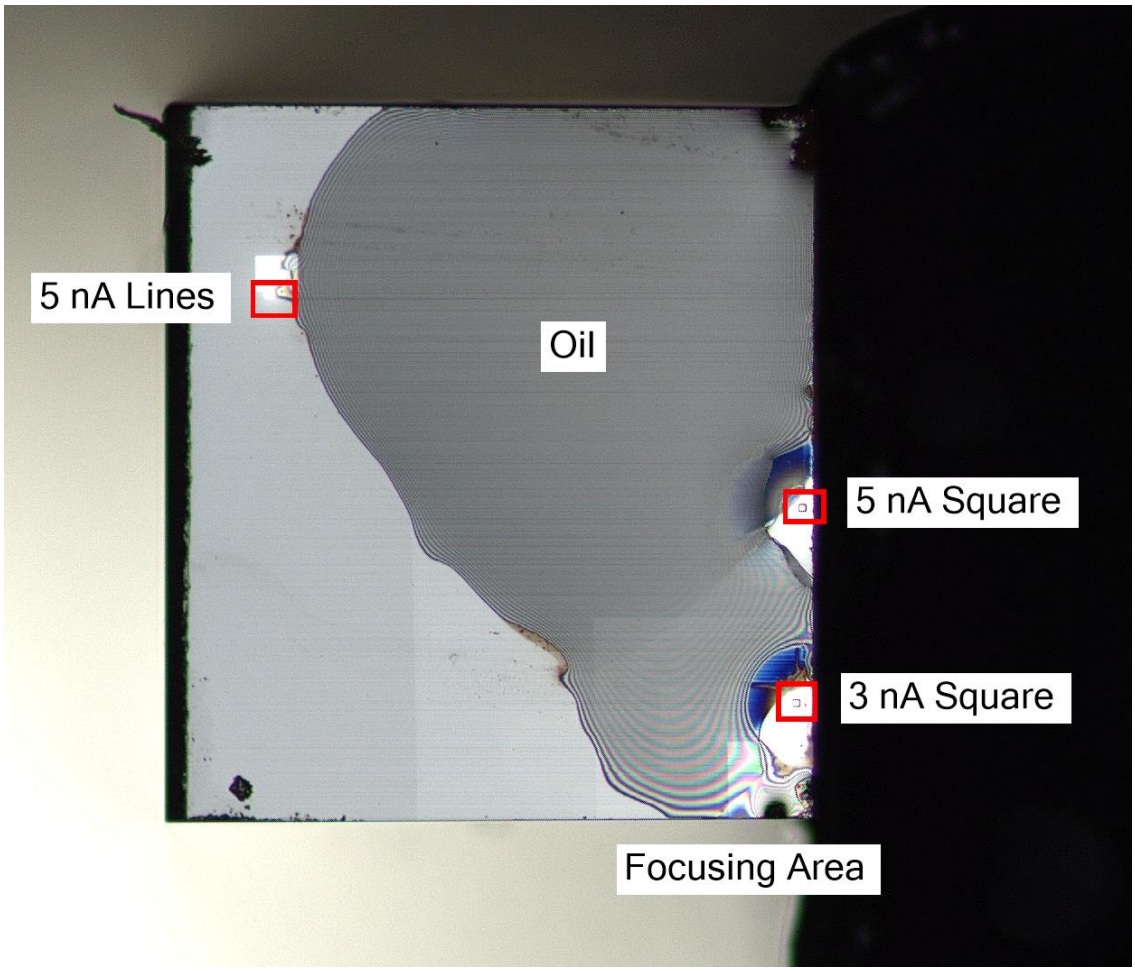

Figure 4-34 . Diamond sample after FIB milling

FIB cutting experiments with the 0.5 nA and 1.0 nA beams were conducted later. The oil and sputtered Au-Pd layer from the previous experiments were removed by wiping the diamond tip with an acetone soaked nonwoven lab tissue. The sample was very difficult to clean. While the sample looked fairly clean in the optical microscope, it was revealed to still have a significant amount of debris when it was examined in the SEM. In the future, the diamond should be completely removed from the SEM pin mount and ultrasonicated in acetone to clean it. It is simply very difficult to effectively clean such a large area by wiping it. The sample was then prepared again with conductive tape to bridge the adhesive joint, and a layer of Au-Pd was sputtered onto the top surface.

Similar experiments were conducted for these lower current beams. For both currents a 10 x 10 µm square was milled with a 50 nm overlap. According to the manual, the 0.5 nA beam has a nominal beam diameter of 35 nm, and the 1 nA beam has a diameter of 44 nm, so a 50 nm overlap is about right for the beam size.

Table 4-4. Parameters used for the 0.5 and 1 nA beam material remove rate test

Parameter	**0.5 nA**	**1 nA**
Magnification	8000x	
Dwell Time	100 µs	
Passes	500	
Total Time	33:20	
Bitmap File Name	bmp_Square_50nm.bmp	

Figure 35 and Figure 36 show the results of the FIB milling operation. The 1 nA beam was able to mill a noticeably deeper square in the same amount of time compared to the 0.5 nA beam. Also prior to milling the squares, the entire viewing area was exposed to the ion beam to remove the conductive Au-Pd layer that was sputtered onto the surface.

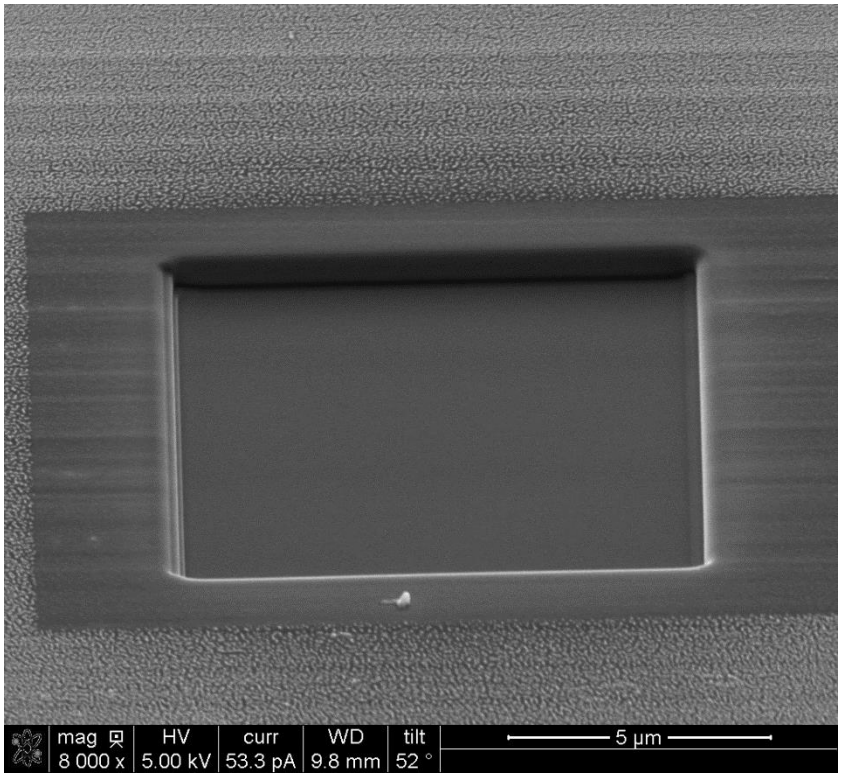

Figure 4-35. 10 x 10 µm square FIB milled into diamond with a 0.5 nA beam

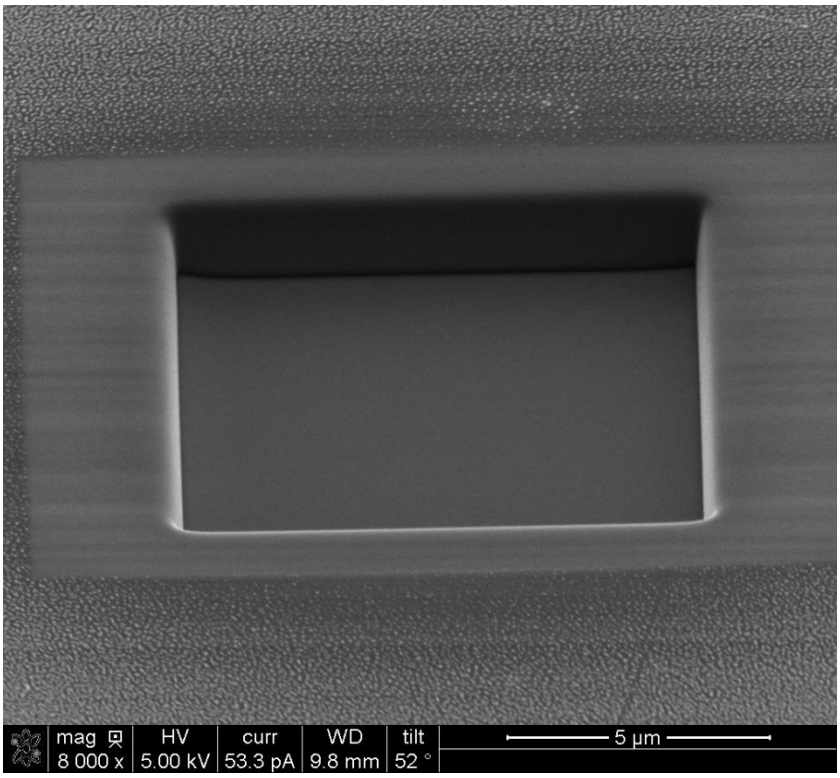

Figure 4-36. 10 x 10 µm square FIB milled into diamond with a 1 nA beam

Finally, FIB milling experiments were conducted on diamond with a 0.3 and 0.5 nA beams. A 0.5 nA beam was used to mill a 10 x 10 µm square to calculate the material removal rate (MRR) and took 33 minutes. After being measured, the square was less than 1 µm deep. For the investigation of the 0.3 nA beam, a smaller square was milled to make the cutting time lower. A bitmap for a 5 x 5 µm square was made with Matlab. This new square pattern has a 25 nm overlap and pixel size of 25 nm. The parameters for the test are shown in Table 5. The test was also repeated for the 0.5 nA beam to confirm that it is comparable to the other MRR experiments.

Table 4-5. Parameter for square test in diamond

Current	**0.3 nA**	**0.5 nA**
Magnification	15,000x	
Dwell Time	100 µs	
Passes	100	
Total Time	26:40	
Bitmap File Name	bmp_Square_25nm.bmp	

All the squares were measured with the Keyence laser confocal. The measured volumes were divided by the total FIB milling time to yield a material removal rate (MRR). Table 6 shows the results for the material removal rate study. The results from the 5 x 5 µm squares are shown highlighted in gray. The 10 x 10 µm and 5 x 5 µm square patterns yield similar results with the 0.5 nA beam. Figure 37 shows the results as a scatter plot along with a linear trend line. The linear

fit describes the relationship between current and material removal rate well with a coefficient of determination of 0.9978. This linear relationship makes sense given that the current is essentially a measure of the Gallium ion flow rate. The sputtering yield (atoms removed per incident Ga ion) is considered to be constant for a fixed angle of incidence assuming no redeposition. Thus, the slope of the linear fit could be converted to sputtering yield if the atomic density of diamond were known.

Table 4-6. Result of the diamond material removal rate (MRR) study

Beam Current [nA]	Volume Removed [μm^3]	Time [s]	MRR [$\mu m^3/s$]
5	413.695	1000	0.41
3	261.151	1000	0.26
1	187.529	2000	0.09
0.5	78.752	2000	0.04
0.5	59.088	1600	0.04
0.3	31.887	1600	0.02

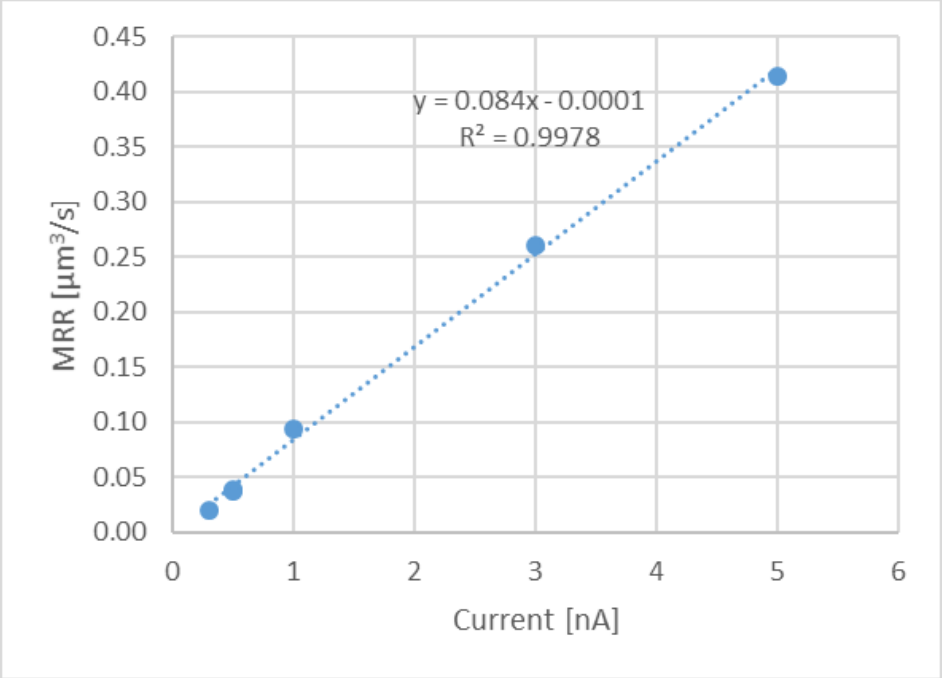

Figure 4-37. Plot of the results of the diamond material removal rate study

Single-pixel-wide line tests were conducted with the 5nA beam. The parameters for the line test are shown in Table 7. A contamination line was then deposited across the lines and processed in Matlab to create a profile of the line. Figure 38 shows an example of one of the lines with the contamination line.

Table 4-7. Parameters for the 5nA line test

	Line 1	Line 2
Magnification	10,000x	
Dwell Time	100 µs	
Passes	250	500
Total Time	627.1 ms	1 s

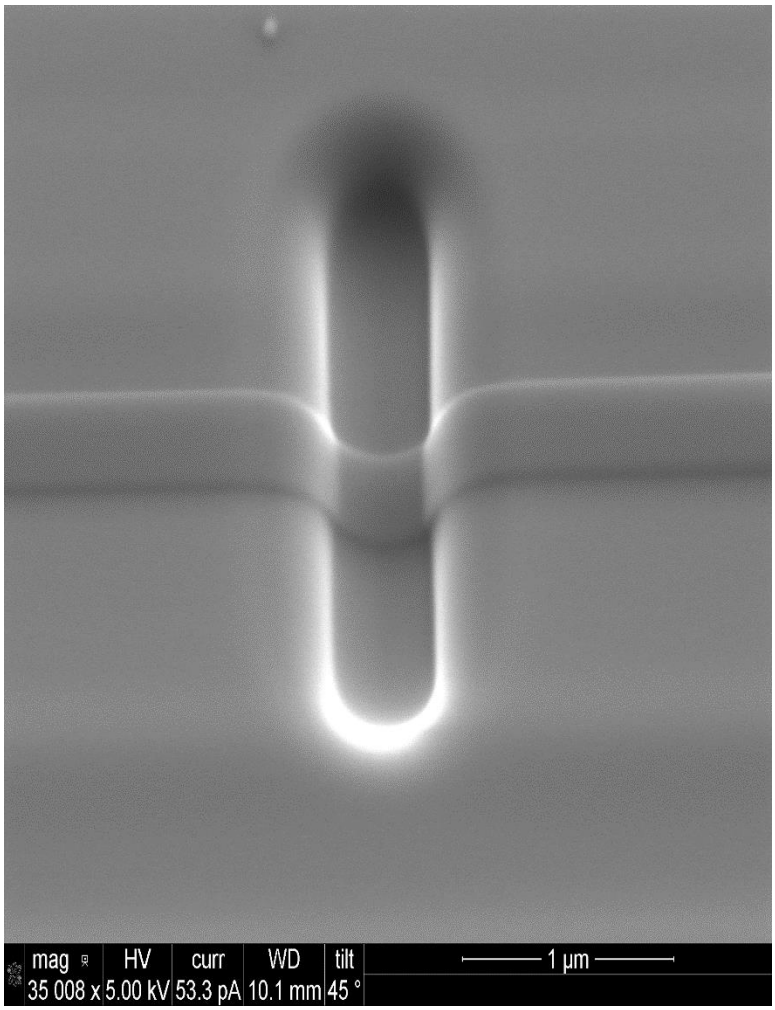

Figure 4-38. 5nA line after 500 passes with EBID line

Figure 39 and Figure 40 shows the profiles of the two lines along with a fitted Gaussian curve. The Gaussian curve has the following equation.

$$y = a1 \cdot e^{-\left(\frac{x-b1}{c1}\right)^2}$$

The c1 coefficient corresponds to the half width at 36.7% amplitude. The c1 for the 250 pass line was 0.27 µm, and 0.32 µm for the 500 pass line. This agrees with previous measurements for the 5 nA beam of about 0.3 µm. It should also be noted that if the profile of the line were axisymmetric,

as in the beam dwelled in a spot instead of a line, the shape would be roughly the negative of desired lens shape. To make a positive version of the desired lens shape, a smaller beam will need to be used.

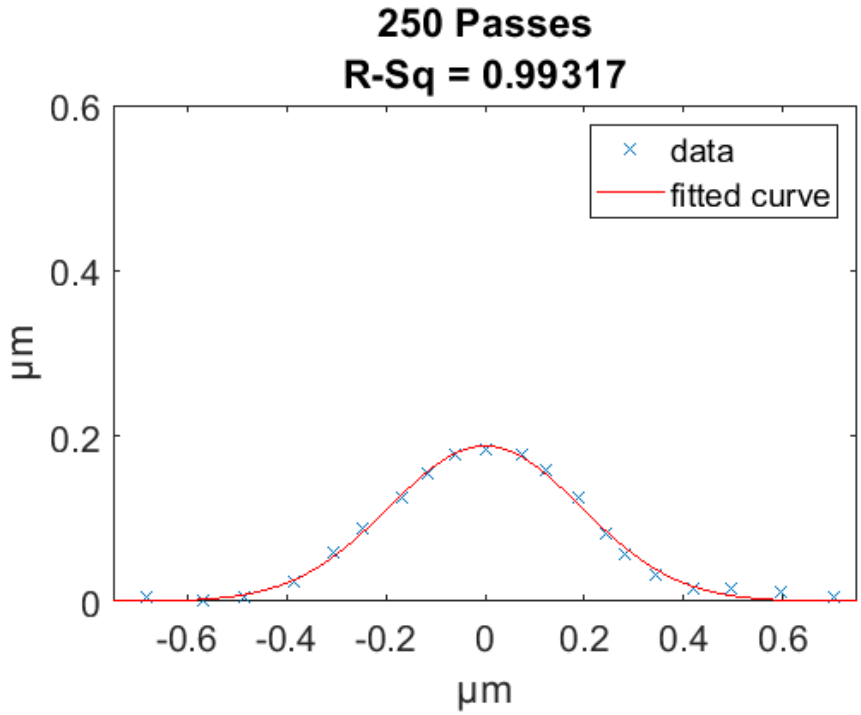

Figure 4-39. Profile of 5 nA line after 250 passes

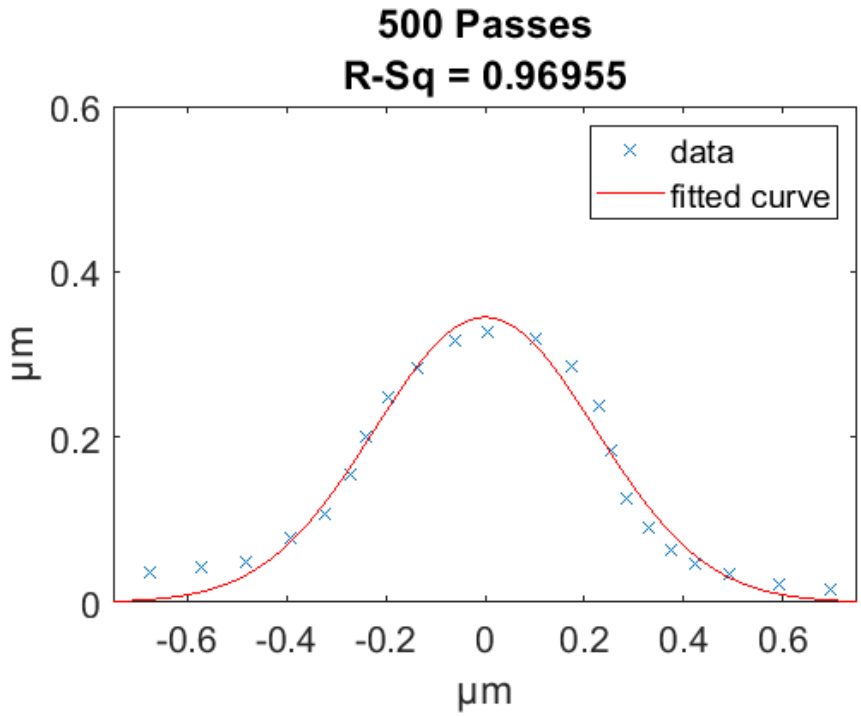

Figure 4-40. Profile of 5 nA line after 500 passes

4.5 FIB SURFACE GENERATION

A bitmap was generated for a 5 x 5 array of convex features spaced 2 µm apart. A 5 x 5 array was chosen to try to make the features large enough to find later with the AFM. This bitmap has a 40 nm overlap and 20 nm pixels. The minimum dwell at the peak of the bumps is 0. The dwell time distribution was arbitrarily chosen to be elliptical. The purpose of the experiment was to confirm that a field of convex features could successfully be made at this length scale in a reasonable amount of time.

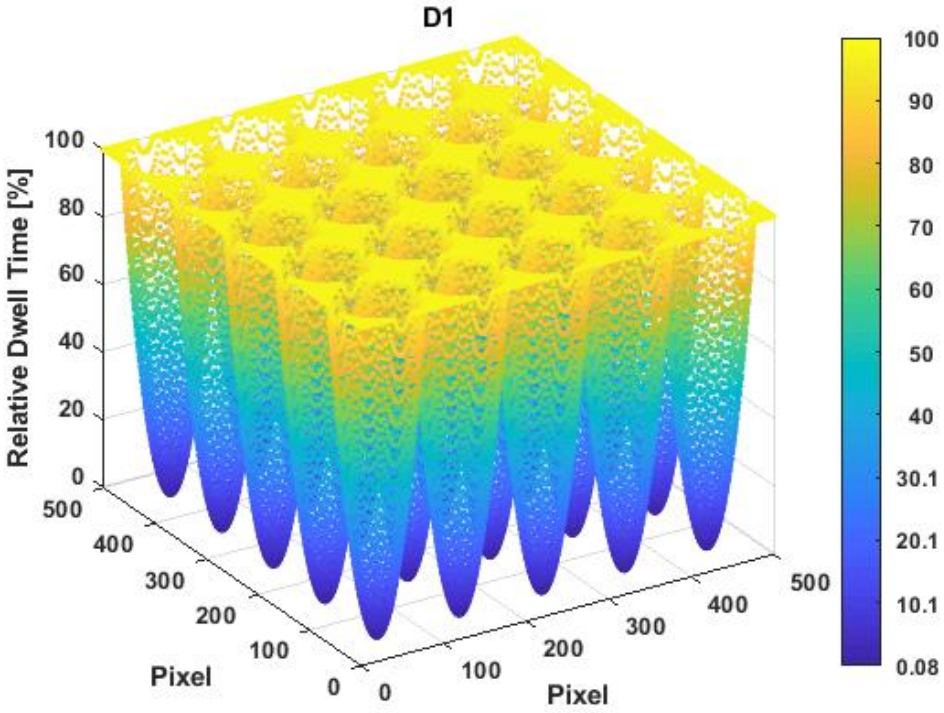

Figure 4-41. Dwell time distribution of the bitmap

The bitmap was FIB milled with a 1 nA beam. The total size of the array is 10 x 10 µm. Other parameters used for this FIB milling operation are shown in Table 8. Figure 42 and Figure 43 show the resulting surface. Like results from 25 µm pitch features in the previous project shown in Figure 44, the step or terrace errors are present at the base of the convex features. However, the bumps are thought to be more axisymmetric as the terraces appear around the entire base of the bump in Figure 43 whereas in the previous project the terraces only appears in the quadrants in Figure 44.

Table 4-8. Other parameters used for FIB milling the 5 x 5 array of convex features

Parameter	Value
Magnification	8000x
Dwell Time	100 µs
Passes	200
Total Time	12:50
Bitmap File Name	bmp_D1.bmp

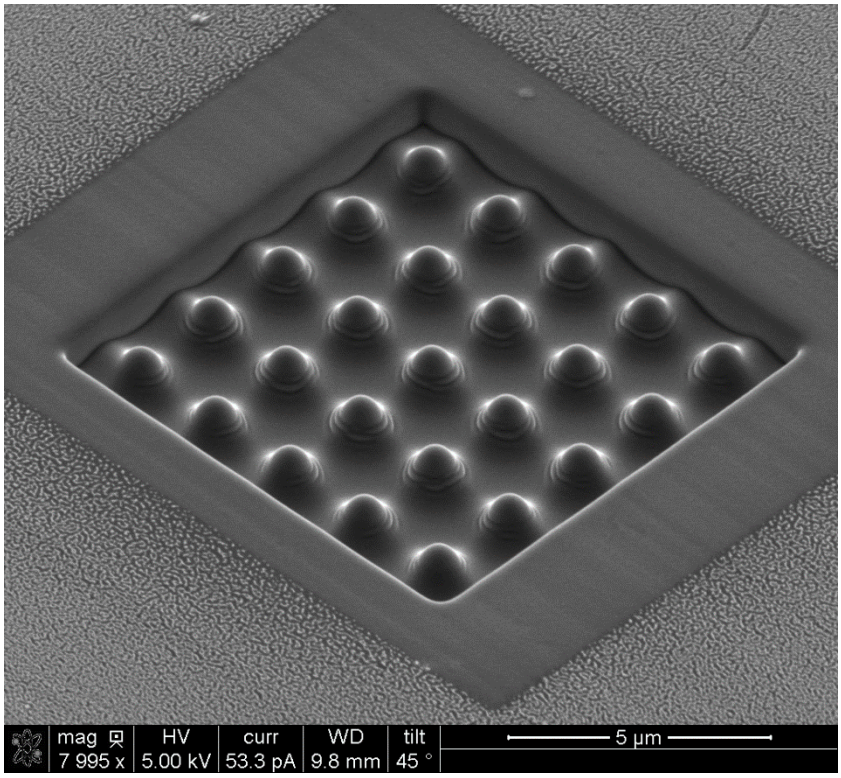

Figure 4-42. 5 x 5 Array of convex features in diamond

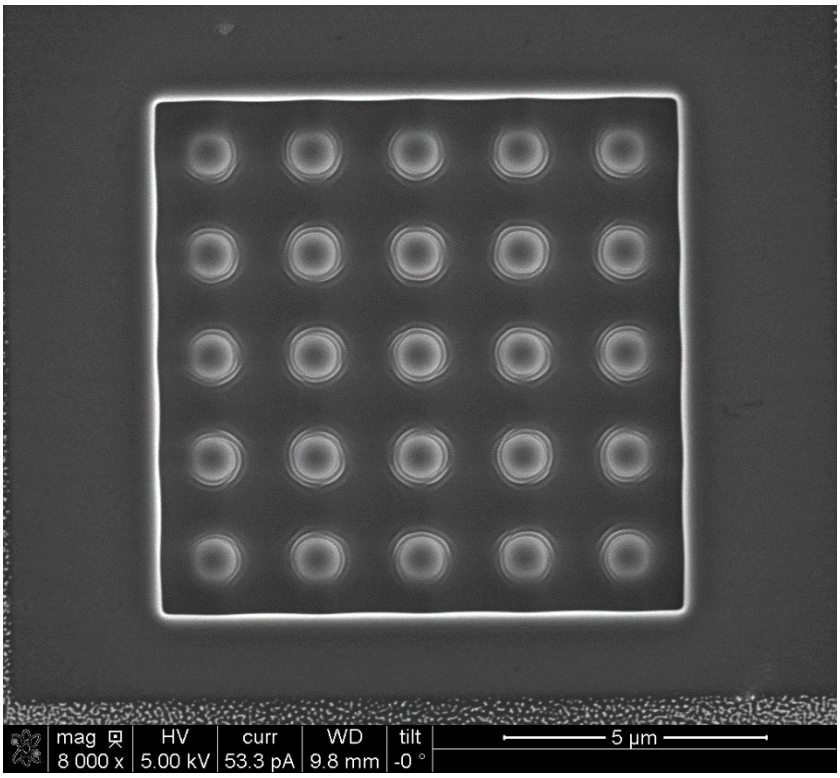

Figure 4-43. Top view of the 5 x 5 array of convex features in diamond

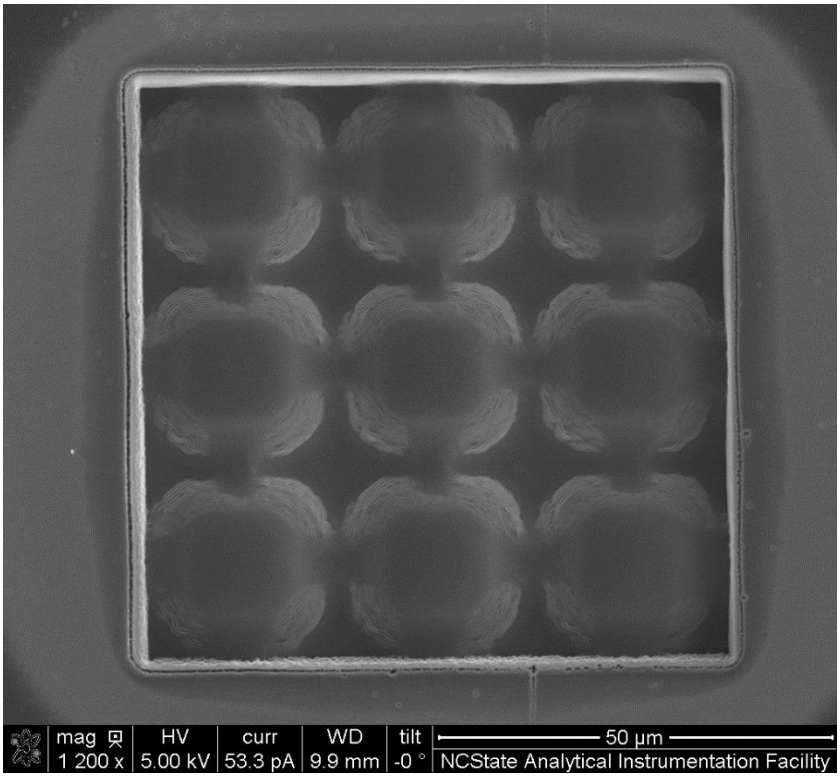

Figure 4-44. 3 x 3 array of convex features on a 25 µm pitch in glassy carbon

A 5 x 5 array of convex features was FIB milled into diamond with the 0.5 nA beam. This is a replication of the array milled with the 1 nA beam to examine the difference of milling features with the different beams. Because the 0.5 nA beam has roughly half the removal rate of the 1 nA beam, the number of passes was double. The resulting surface can be compared in Figure 45 and Figure 46. Figure 45 shows the surface made with the 0.5 nA beam while Figure 46 shows the results of the 1 nA beam. Qualitatively, the 0.5 nA surface looks smoother, but that could be a result of not producing steep enough slopes to develop the terrace morphology.

Table 4-9. Parameters used to make the 5 x 5 array in diamond

Current	**0.5 nA**	**1 nA**
Magnification	8000x	
Dwell Time	100 µs	
Passes	400	200
Total Time	23:40	12:50
Bitmap File Name	bmp_D1.bmp	

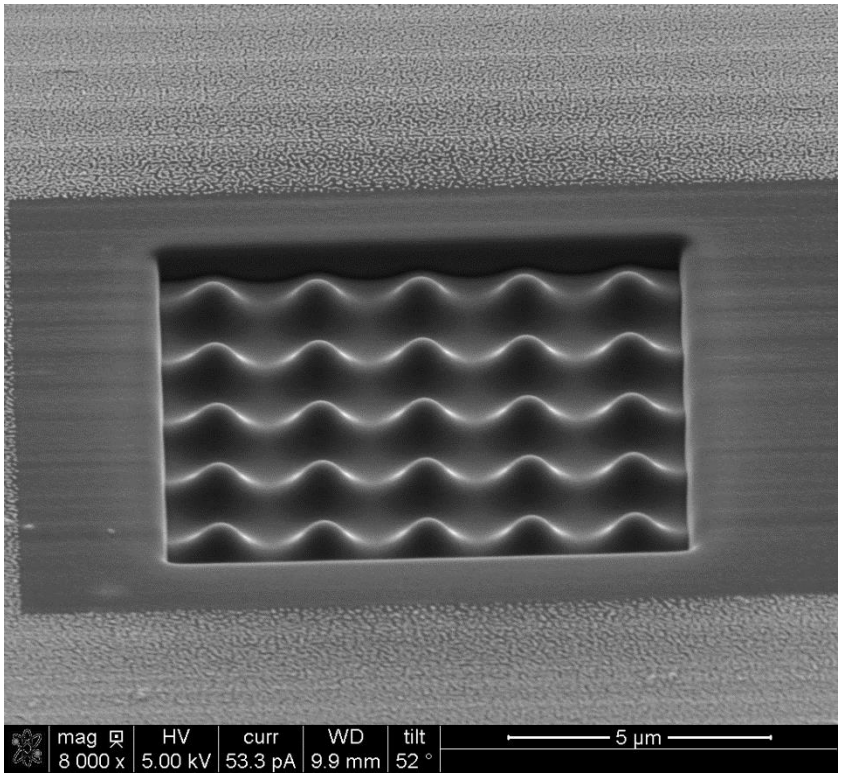

Figure 4-45. 5 x 5 array FIB milled with a 0.5 nA beam in diamond

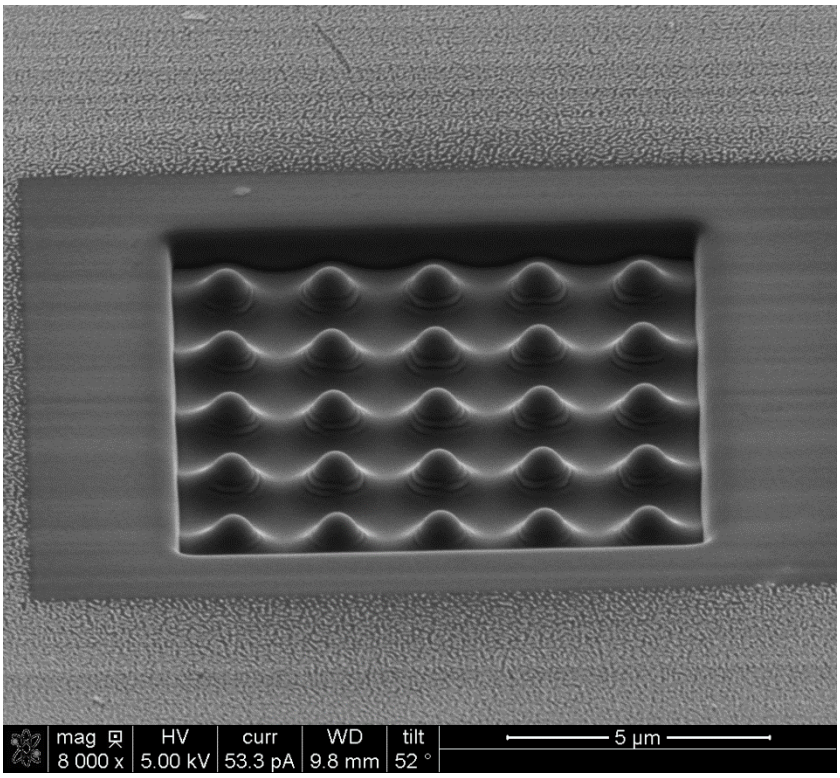

Figure 4-46. 5 x 5 array FIB milled with a 1 nA beam in diamond

The diamond surface was also measured with the AFM. The AFM measurement was conducted with 1024 lines and 1024 points per line to yield 14.7 nm pixels. The scan was conducted over a 15 x 15 µm area at an excitation frequency of 0.4 Hz. Figure 47 shows the surface of the 5 x 5 array that was FIB milled with the 0.5 nA beam. This is the raw unprocessed data. Typically, AFM measurements are post-processed to correct the AFM measurements. However, since how those corrections are calculated is not understood at this time, no post-processing was conducted. As can be seen from the AFM measurement the features appear to be longer perpendicular to the scan direction as the features do not appear to be axisymmetric. Looking at the SEM images, this does not appear to be the case in actuality. A similar effect appears in the measurement of the surface made with the 1 nA beam shown in Figure 48. This is likely an artifact of the AFM measurement.

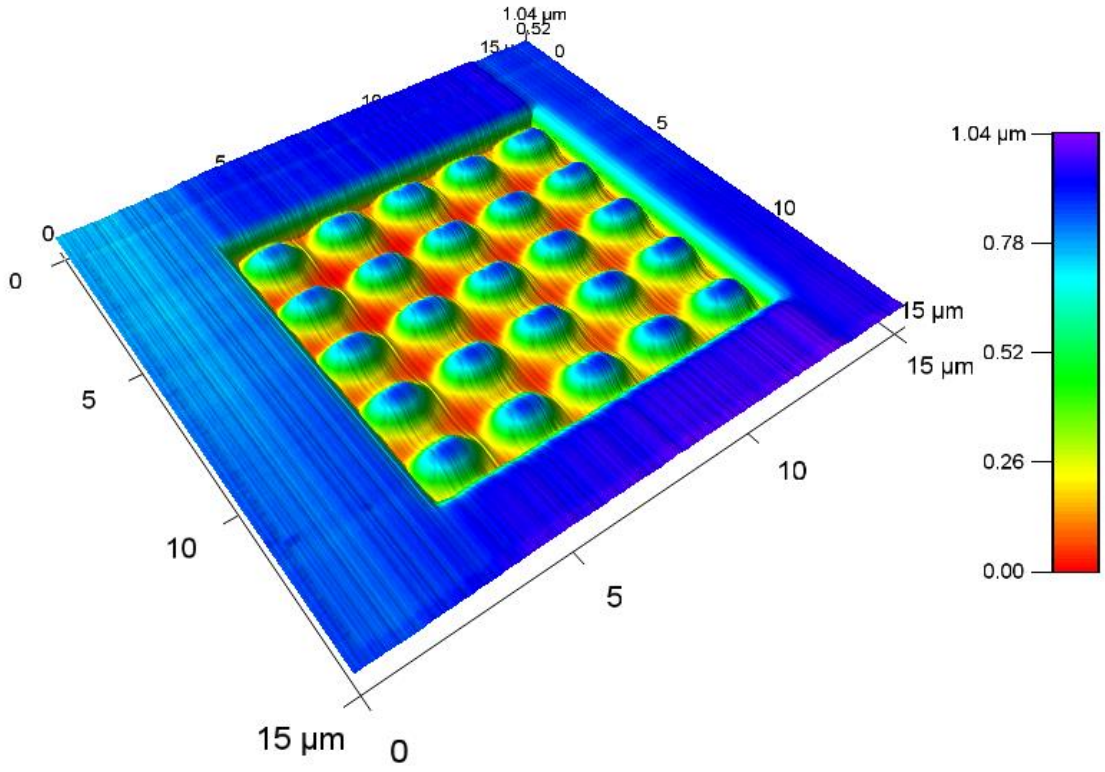

Figure 4-47. AFM measurement of the 5 x 5 array created with the 0.5 nA beam in diamond

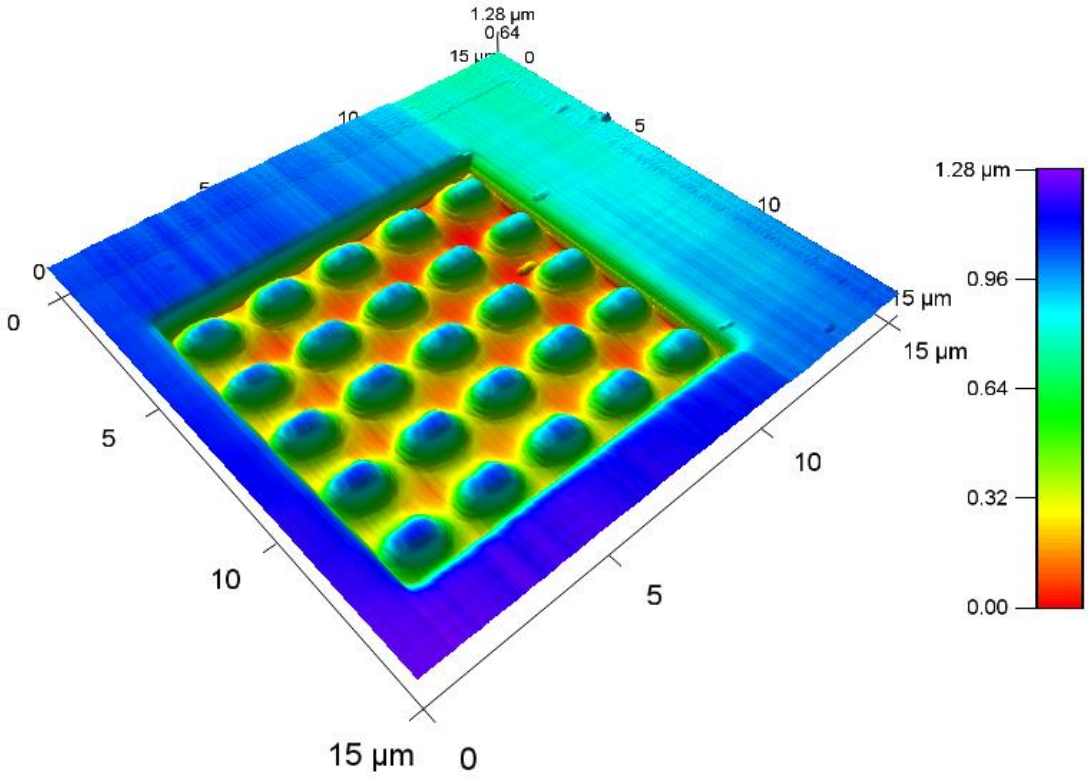

Figure 4-48. AFM measurement of the 5 x 5 array created with the 1 nA beam in diamond

Due to other priorities, the diamond sample had sat in the lab for about 6 weeks in a closed container before it could be measured again in the AFM. In the intervening time the sample was contaminated, and the sample was not able to be cleaned successfully.

The diamond sample was removed from the holder by dissolving the adhesive bonding it to the SEM pin mount with Acetone. The diamond was then ultrasonicated in Acetone. Finally, the diamond was inspected under 500x magnification in an optical microscope and wiped with a Texwipe soaked in Acetone. It was difficult to adequately clean the polished diamond as the area of interest is relatively large. As could be seen in the SEM, debris and residue were still present on the sample.

The sample was then bonded to the SEM pin mount with Gorilla brand super glue. The polished diamond surface was electrically grounded by bridging the glue joint with conductive tape, then sputter coating Au-Pd over both the diamond surface and the conductive tape.

The goal of this FIB experiment is to measure the form produced by the pattern in the FIB. The pattern was repeated 3 times to gain some understanding of the variability. Prior to FIB milling each pattern the focus and stigmation of the ion beam was adjusted. Table 10 shows the significant parameters used for the FIB pattern.

Table 4-10. Parameters used to make the 5 x 5 array in diamond

Current	1 nA
Magnification	8000x
Dwell Time	100 µs
Passes	200
Total Time	12:50
Bitmap File Name	bmp_D1.bmp

An overview of the resulting features in diamond are shown in Figure 49. The three newly FIB milled features are boxed in red. There are some FIB experiments visible outside the red box. Also note the debris and residue left on the surface from the attempts to clean the surface. Figure 50 shows a magnified SEM image of the leftmost structure in Figure 49. Note the rings at the base of the convex features which indicates the beginning of the terrace structure previously reported in literature.

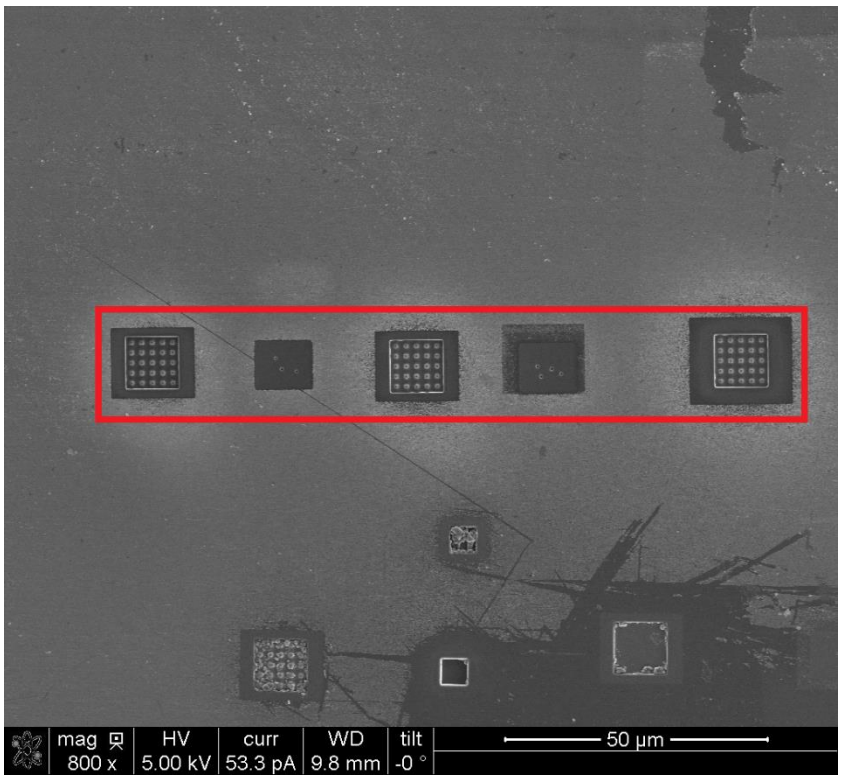

Figure 4-49. FIB milled patterns in diamond

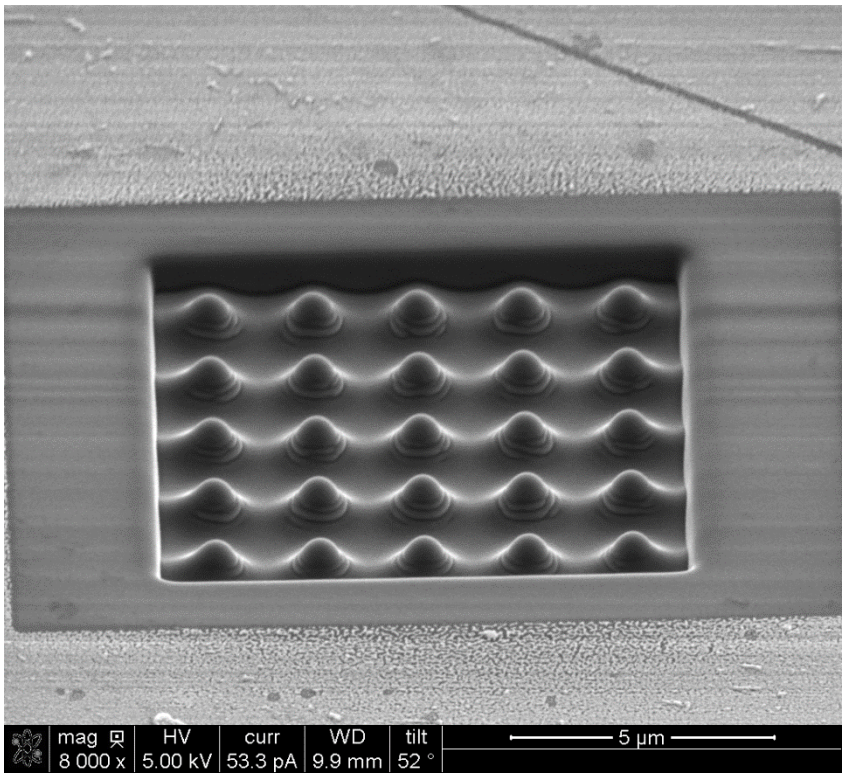

Figure 4-50. Magnified SEM image of the leftmost FIB milled structure in diamond

Figure 51 shows a cross section of the features shown in Figure 50. The features are about 850 nm tall and spaced 2 µm apart (2.8 µm across the diagonal). There appears to be an issue with the AFM measurements in the lower left quadrant of each convex feature. As can be seen in the trace of the cross section. The left side of each bump has a different slope than the right side. A cross section in another direction does not show this asymmetry in Figure 52. Each convex feature in each of the three replicates displays the same issue. This is likely an issue with the tip shape.

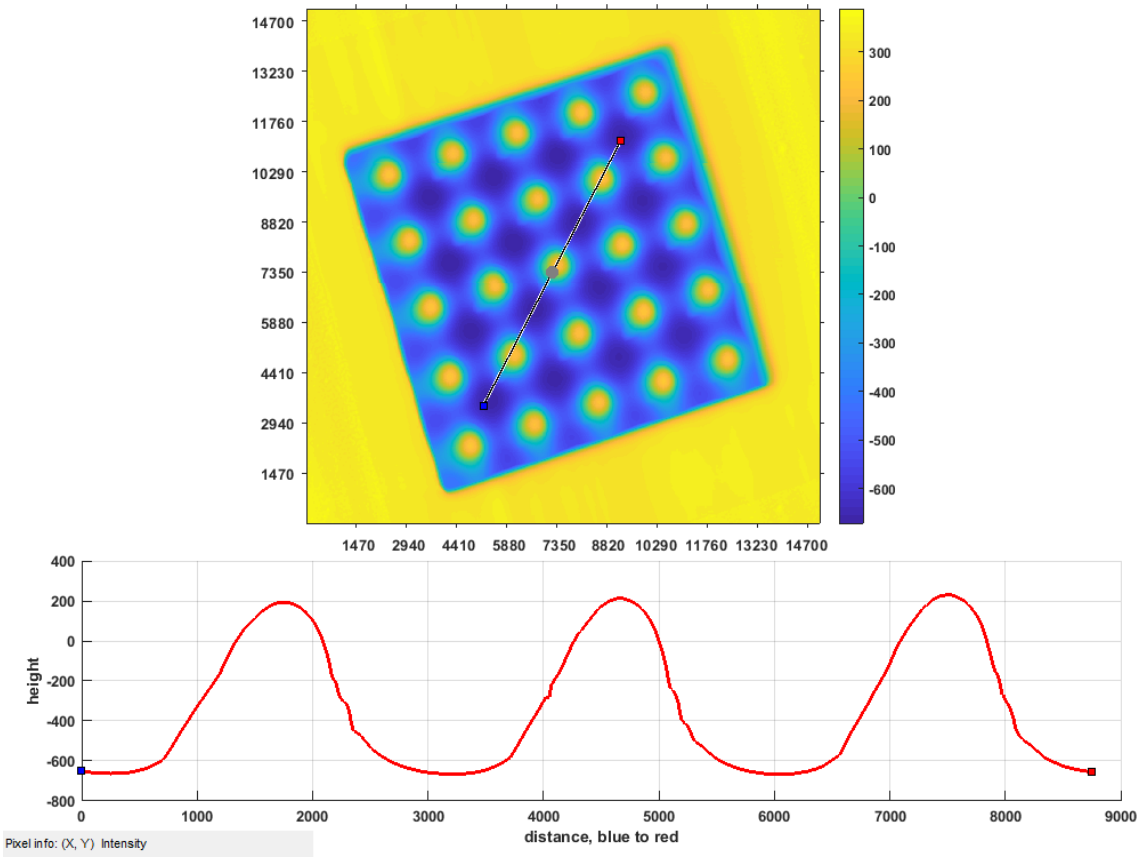

Figure 4-51. Cross section of FIB milled features in diamond (all dimensions in nm)

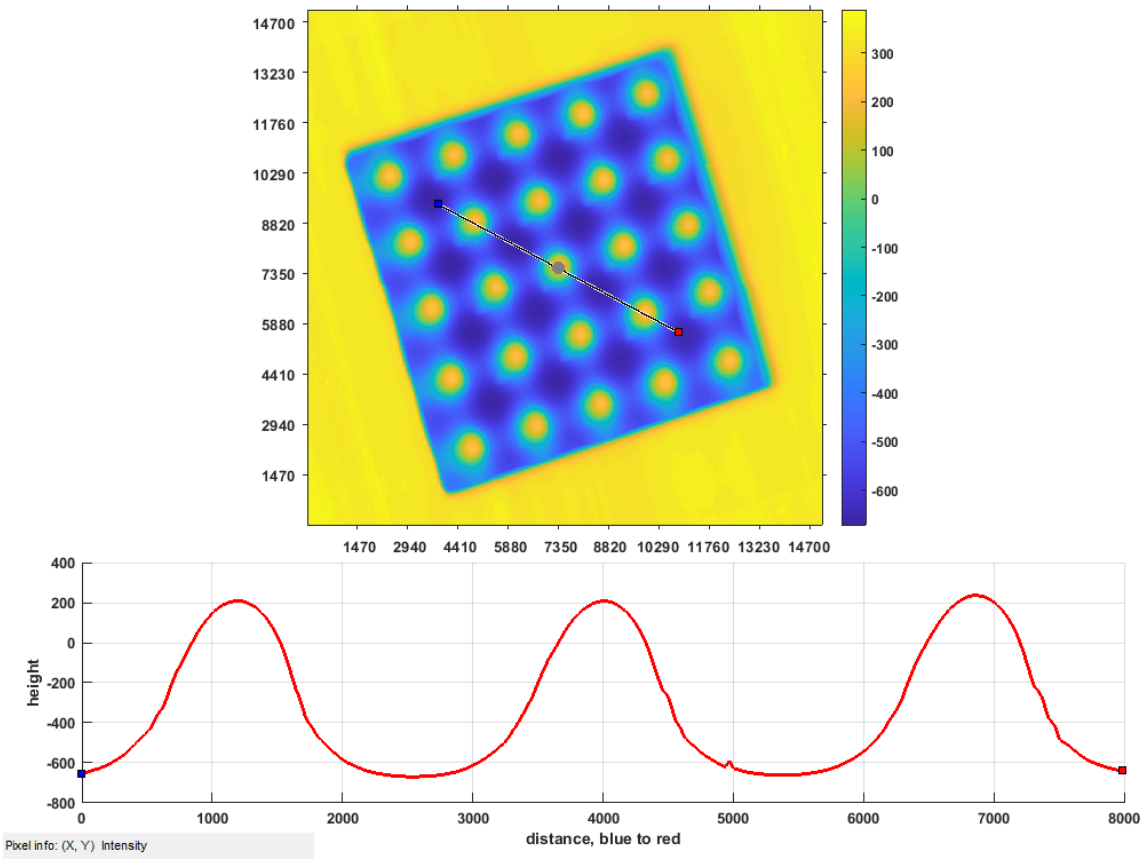

Figure 4-52. Orthogonal cross section of FIB milled features in diamond (all dimensions in nm)

For reference, the tip used for all AFM measurements thus far have been taken with a Tap300AL-G tip from budgetsensors.com. More information can be found at <https://www.budgetsensors.com/tapping-mode-afm-probe-aluminum-tap300al>. Table 11 shows the specifications for the tip from the product information. Figure 53 shows an image of one of the tips also taken from the product information web page. Given that the tip has a half angle of 30°, the highest slope that could be measured with a perfect tip is 60°.

Table 4-11. AFM tip specifications

AFM Tip

SHAPE	HEIGHT	SETBACK	RADIUS	HALF CONE ANGLE
Rotated	17 µm (15 - 19 µm)*	15 µm (10 - 20 µm)*	< 10 nm	20°-25° along cantilever axis, 25°-30° from side, 10° at the apex

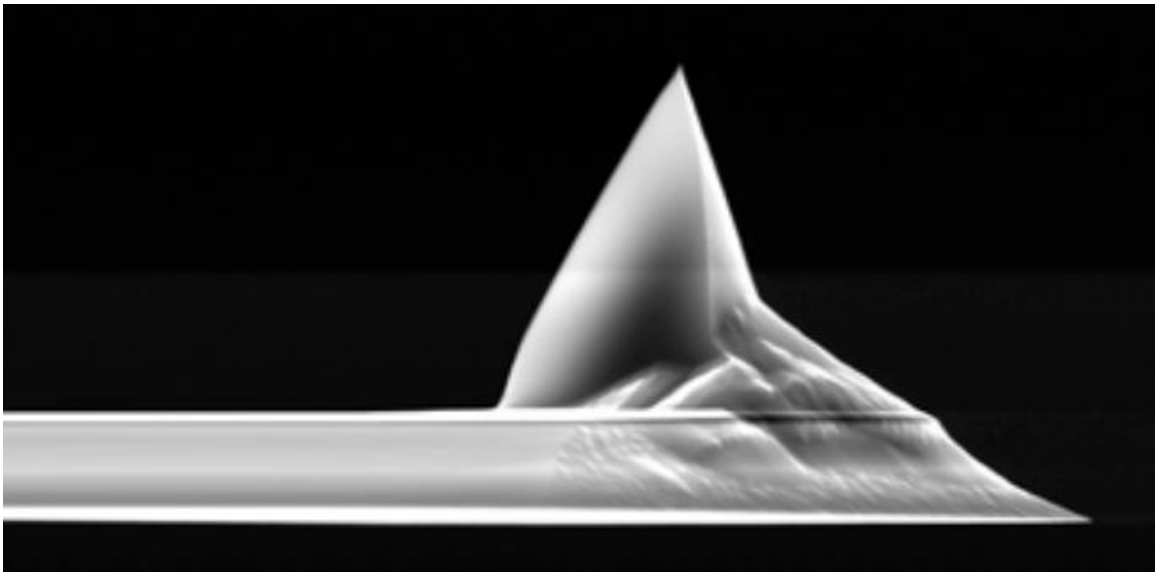

Figure 4-53. AFM tip

Before each FIB milling operation the focus and stigmation of the beam was adjusted to simulate approaching a machine for the first time and setting it up. An SEM image of the resulting surface is shown in Figure 49. The three FIB milled regions are labeled “Exp 1”, “Exp 2” and “Exp 3”, denoting the order in which the experiments were conducted.

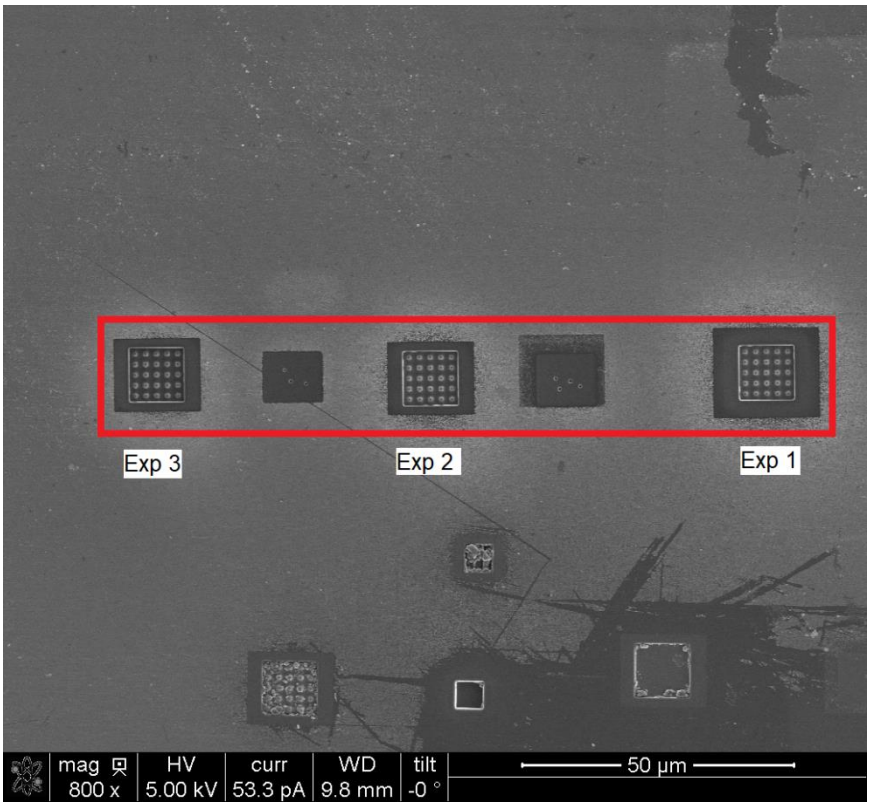

Figure 4-54. FIB milled patterns in diamond

The AFM measurements were compared in Matlab using the surfer.m script. Exp 1 was used as the reference data set for Exp 2 and Exp 3. The surfer.m tool was used to align the two data sets to reduce the RMS of the difference between them. The resulting difference plots are shown in Figure 55 and Figure 56. For both figures, the Z scale is the same. As can be seen from the plots, Exp 1 and Exp 2 are very similar to each other, with a RMS difference of .005 nm. Exp 3 is very different with an RMS difference of 64 nm. The plan view of the difference between Exp 1 and Exp 3 shown in the bottom part of Figure 56 shows that most of the error is localized in the bottom of the square array. The localization on one side indicates that this is not an alignment error. I suspect this is due to being damaged and changing shape when attempting to measure the steep dropoff at the edge of the pattern. This could be addressed by using a softer AFM tip or FIB milling a slope down to the lens features.

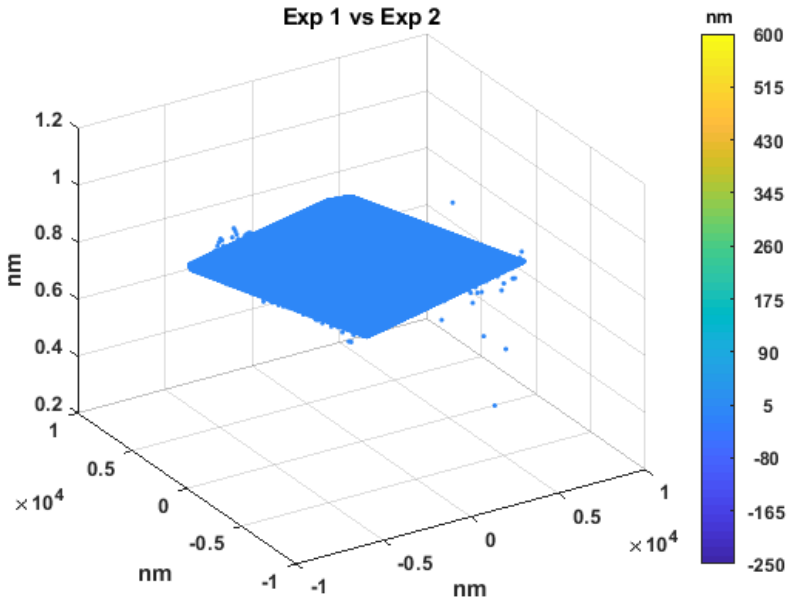

Figure 4-55. Difference plot between Exp 1 and Exp 2

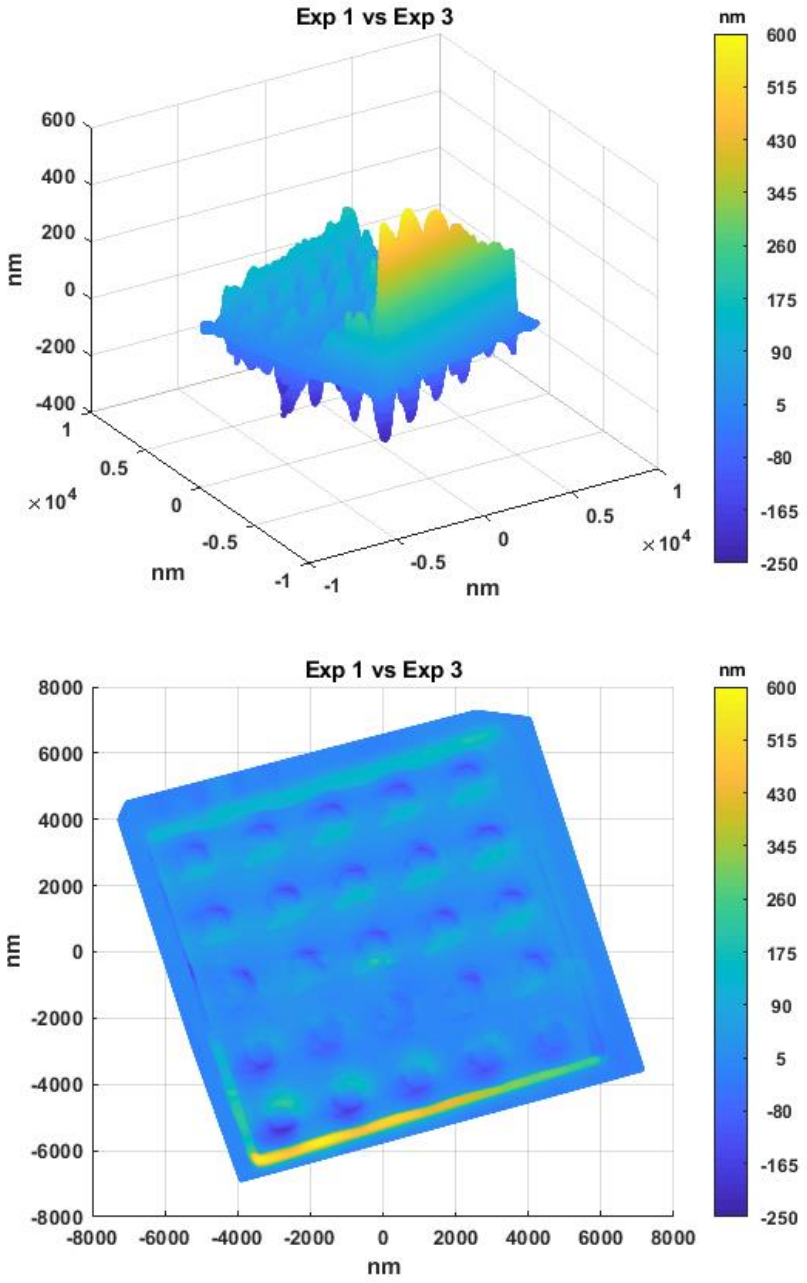

Figure 4-56. Difference plot between Exp 1 and Exp 3

A new bitmap was developed to match the new targeted paraboloid geometry. A plot of the relative dwell time is shown in Figure 57. Some of the parameters to develop this pattern are shown in Table 12.

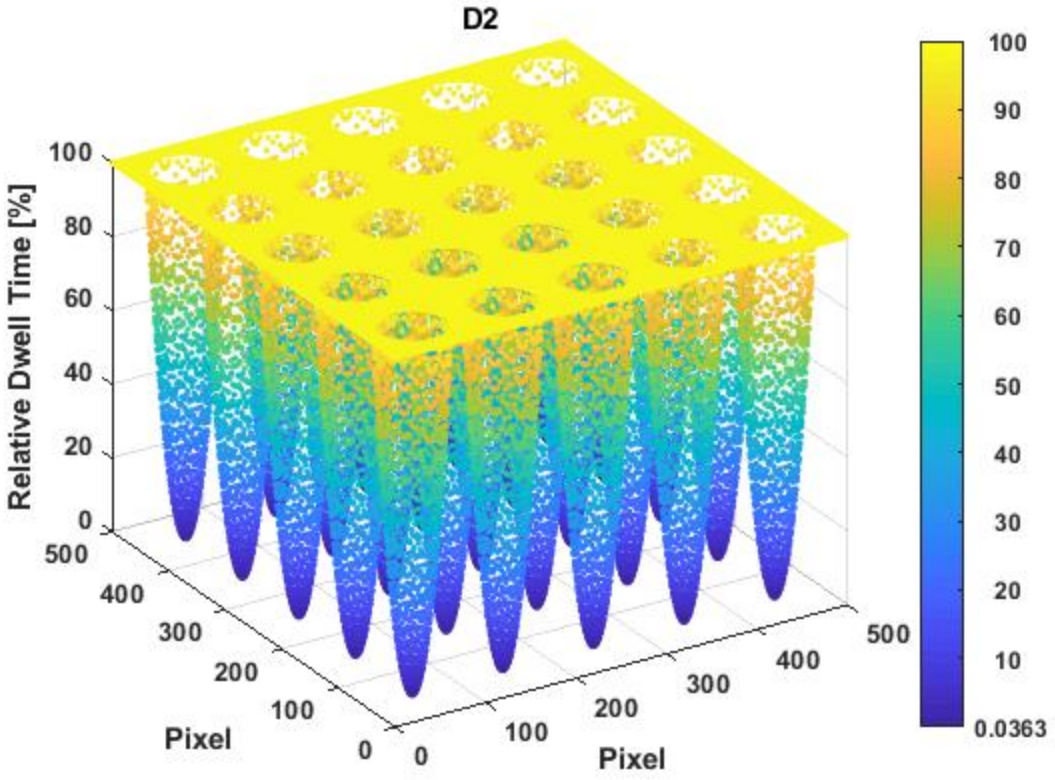

Figure 4-57. Relative dwell time plot for the new bitmap (zero values removed for clarity)

Table 4-12. Bitmap parameters

Bitmap XY Size	10 µm
Pixel Size	20 nm
Overlap	40 nm
Pixels per feature	100

This pattern was FIB milled 3 times with both 1 nA and 0.5 nA. The intention was to check the repeatability of the FIB milling process and begin developing compensation methods. Figure 58 shows an overview of these experiments. A 0.5 nA beam was used on the areas marked D2_1 through D2_3, while a 1 nA beam was used on D2_4 through D2_6. While trying to measure these features with the AFM the tips broke easily, and I was never able to measure all three replicates with a single tip. The hardness of the diamond is a problem for the durability of the silicon AFM tips.

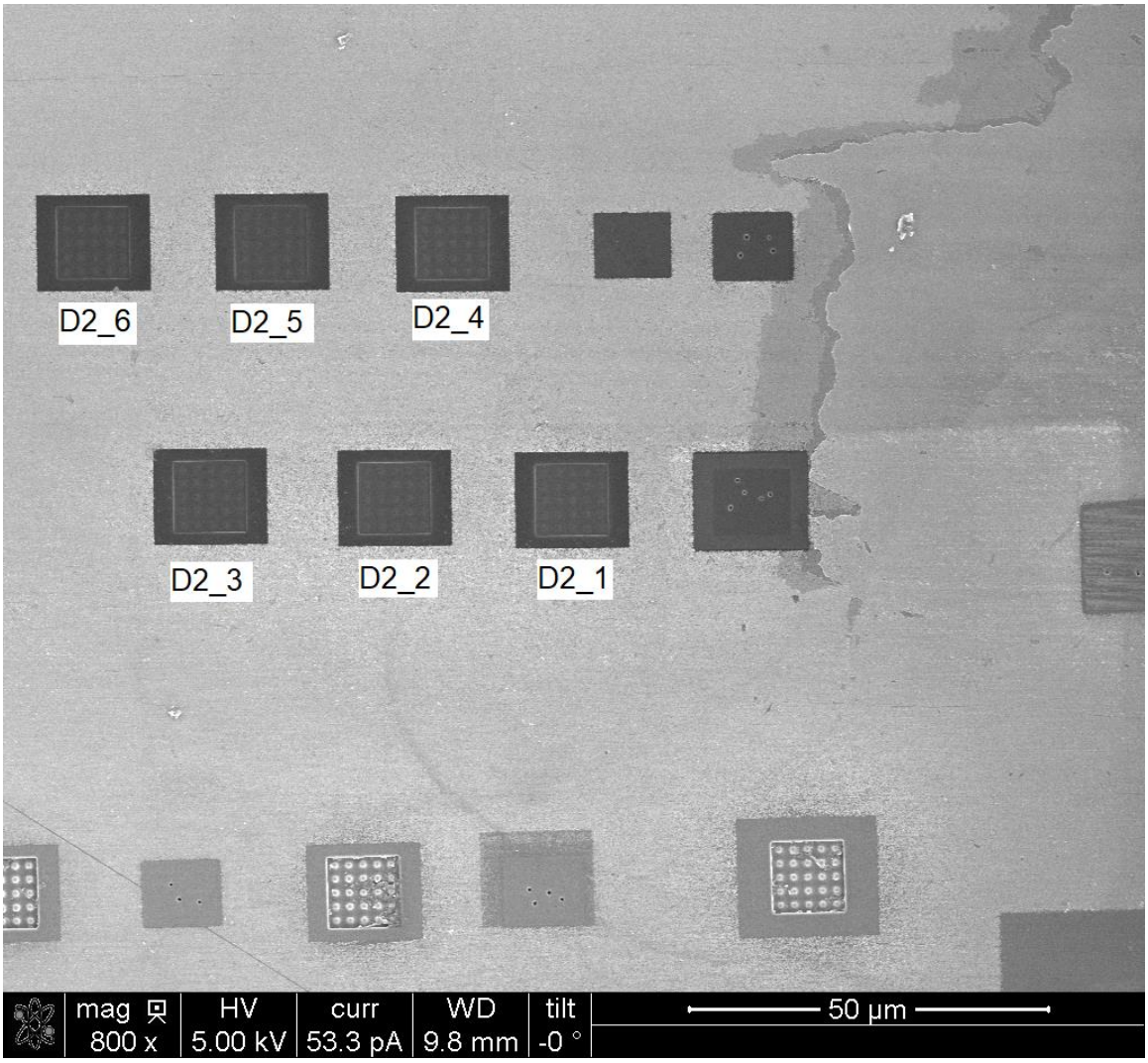

Figure 4-58. FIB milled arrays of paraboloids

To address the issue of the AFM tip damage, I added a conical sloped surface to the bitmap file. Figure 59 shows the modified bitmap. I added a Ø14.142 µm circular flat region around the paraboloids as well as a conical surface. The conical surface was targeted to have a half cone angle of about 60° to accommodate the geometry of the AFM tip.

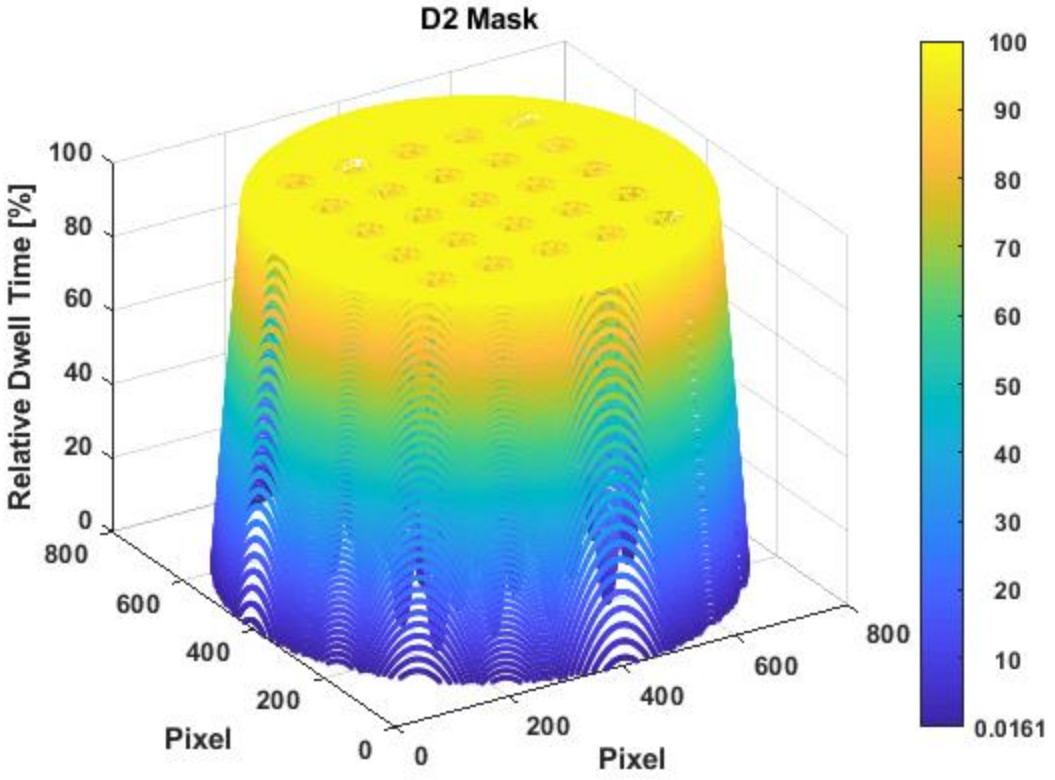

Figure 4-59. Relative dwell time plot for the new bitmap with conical depression

I FIB milled this pattern with a 1 nA beam three times. Table 13 shows some additional parameters used for this experiment. Figure 60 shows an example of the resulting surface.

Table 4-13. Parameters used to make the 5 x 5 array of paraboloids in diamond

Current	1 nA
Magnification	5000x
Dwell Time	100 µs
Passes	53
Total Time	8:40
Bitmap File Name	bmp_mask_D2.bmp

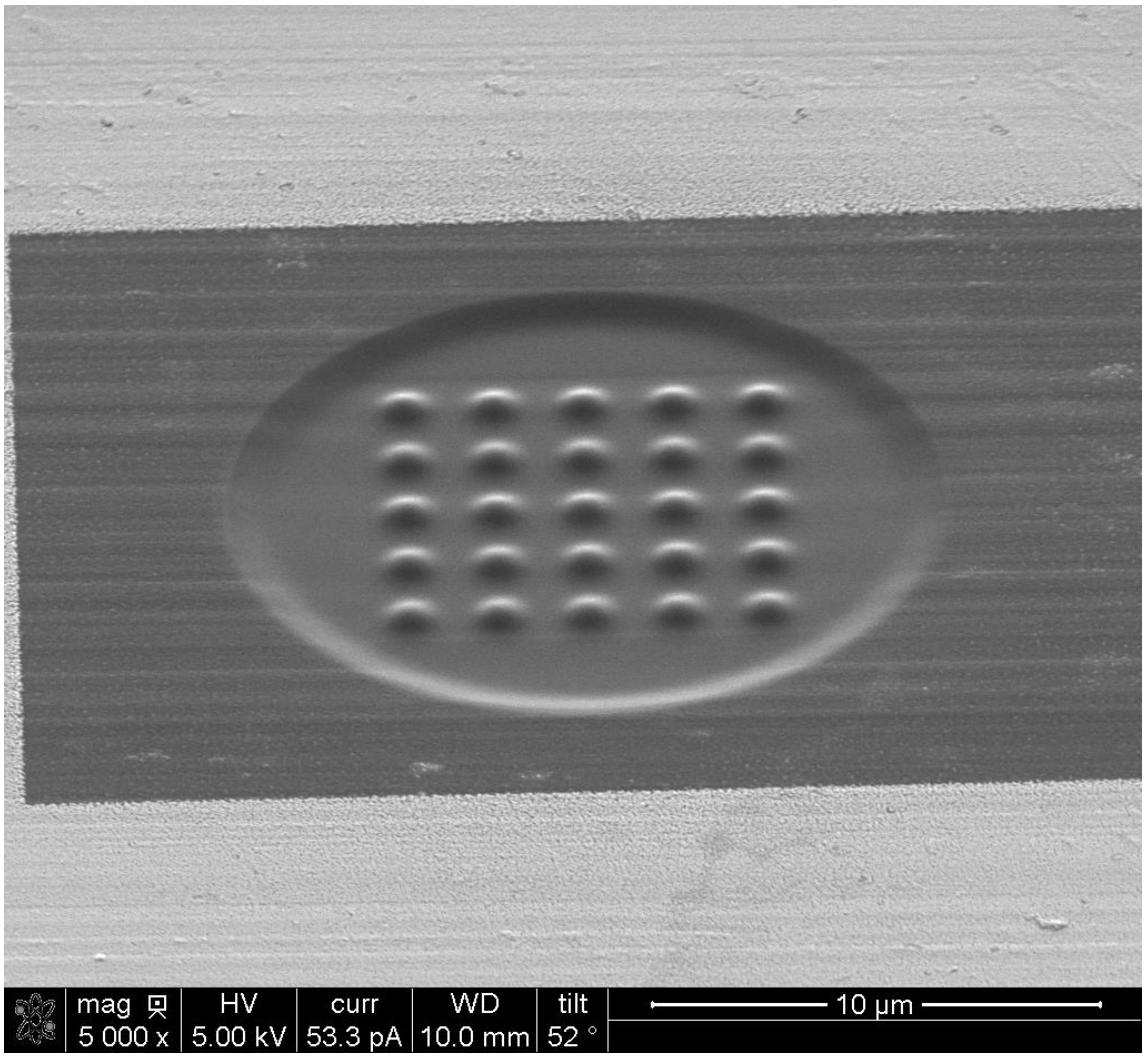

Figure 4-60. FIB milled paraboloids in diamond

Figure 61 and Figure 62 show the AFM measurements of the array of features shown in Figure 60. Figure 61 is the first measurement of the array. Figure 62 is a repeat measurement of the same surface with the same measurement setup (same AFM tip without moving the sample) after measuring the two other arrays. Figure 62 shows a ridge on the side of each convex feature at about the 6 o'clock position. This feature is not present in the first measurement in Figure 61 indicating that the AFM tip shape has likely changed. While the conical depression around the array has improved the life of the AFM tips such that there are no longer gross error after measuring one or two arrays, the tips are still getting damaged.

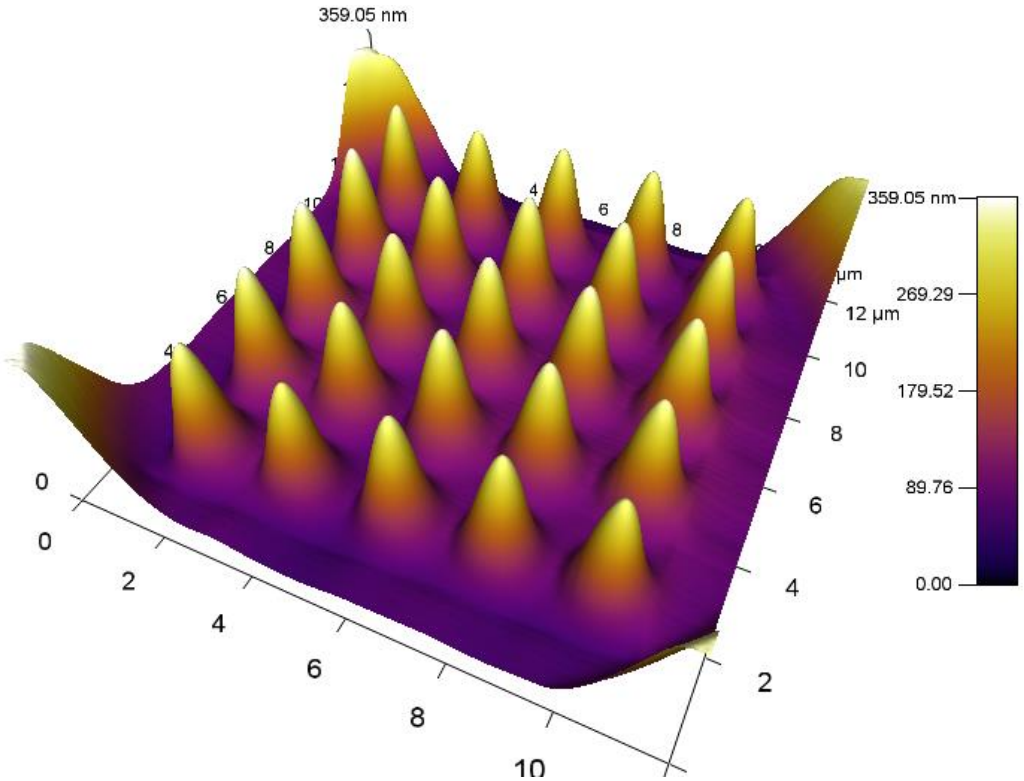

Figure 4-61. AFM measurement of FIB milled diamond

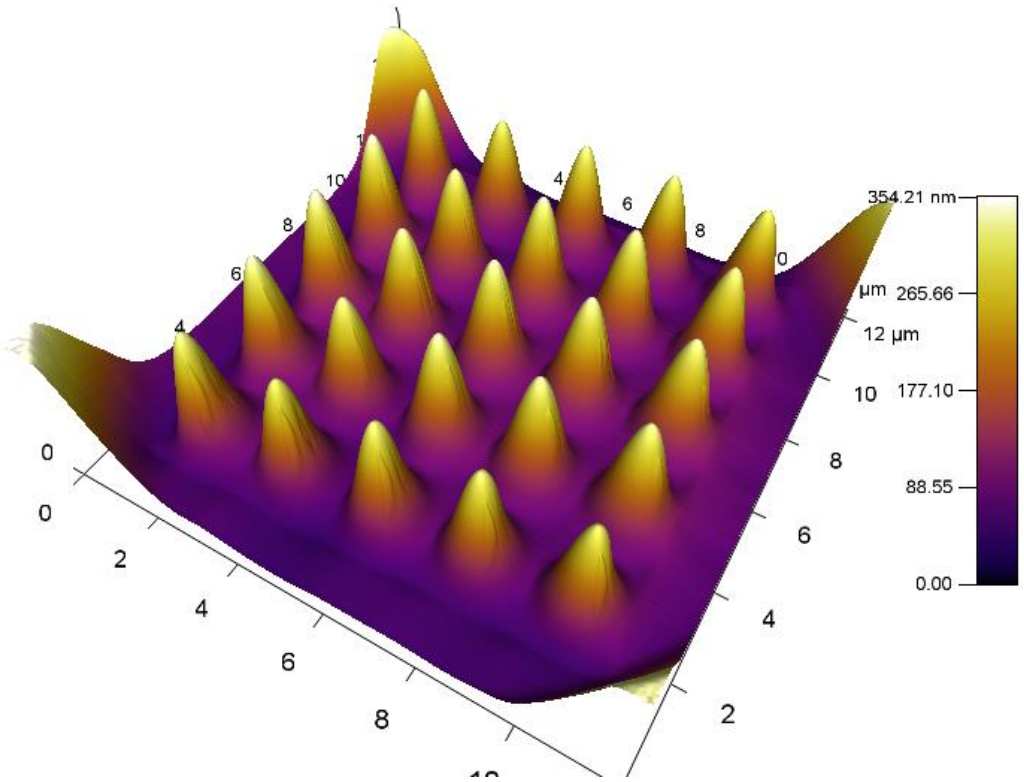

Figure 4-62. AFM measurement of the same surface after measuring two other arrays

The middle 9 lens features were extracted from the AFM measurements of each FIB milled array and compared to the desired paraboloid shape in MATLAB. Figure 63 shows an example of the error map created by this analysis. Figure 64 shows a plot of the absolute height error averaged over the 9 paraboloids.

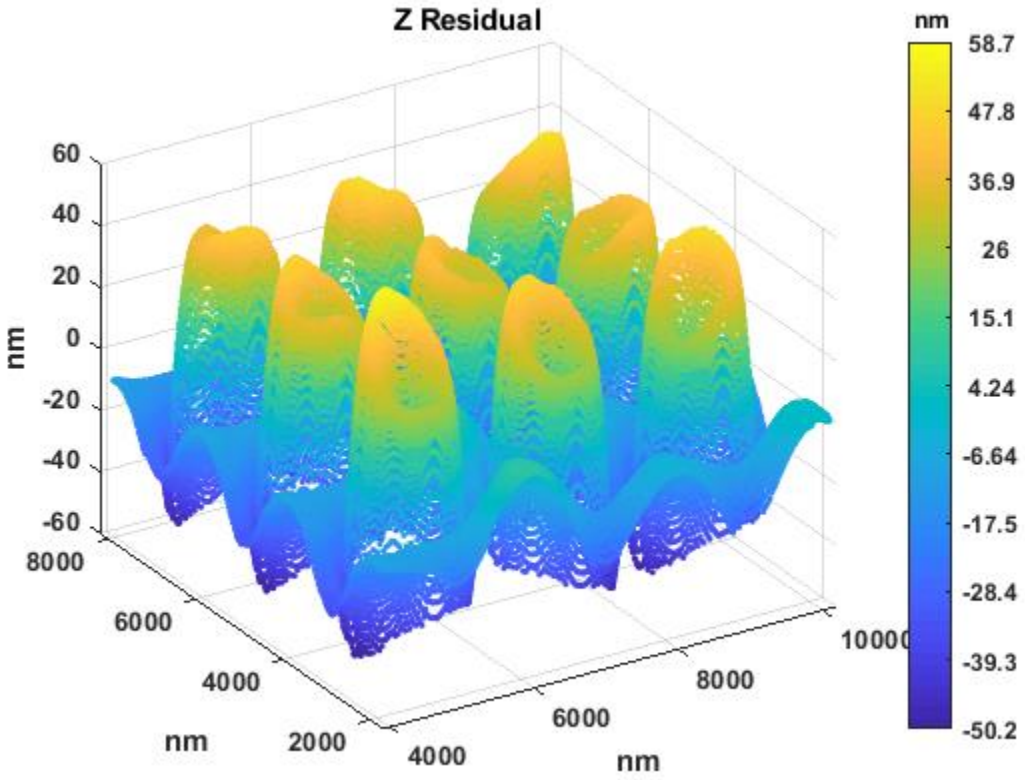

Figure 4-63. Z height error of paraboloids FIB milled in diamond

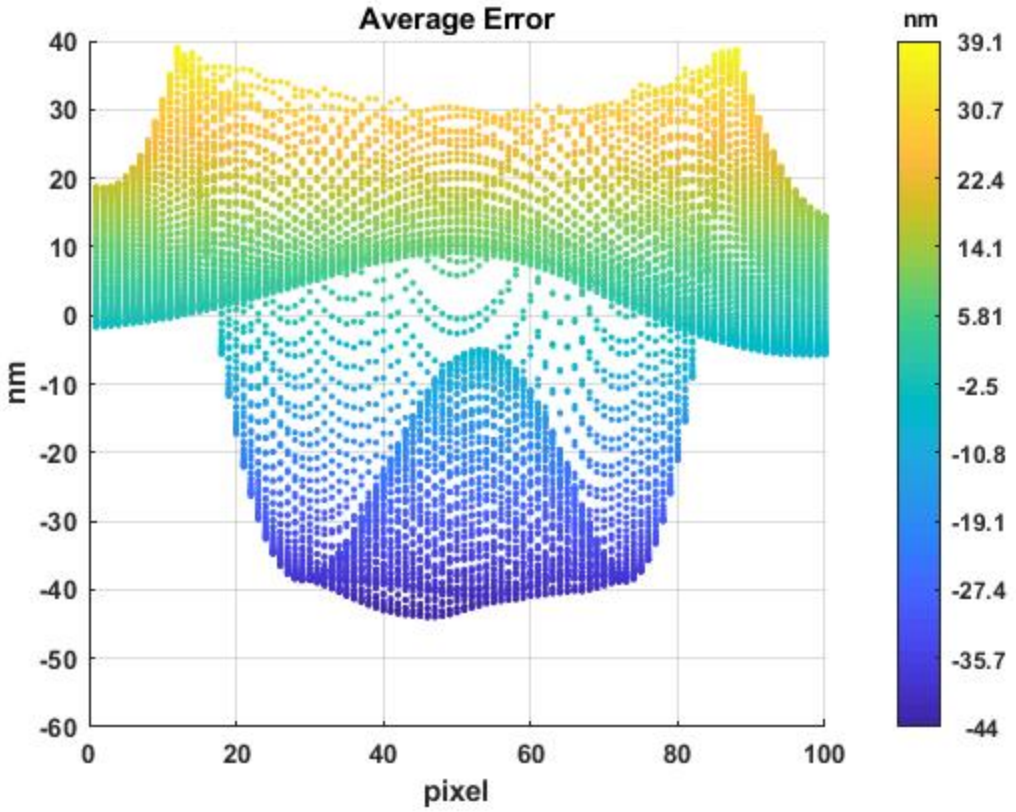

Figure 4-64. Average absolute z error of the FIB milled paraboloids

I then resampled the data into the bitmap pixel spacing and shifted the data to force the error at the center to be zero. I averaged the error over the 9 features and converted the error to a percentage of the maximum depth. Figure 65 shows a plot of this average % error map. Finally, I multiplied the original bitmap by this percentage to attempt to compensate for error in the FIB milling process. Figure 66 shows the error compensated dwell time map. The conical depression is not shown for clarity (such as in Figure 59).

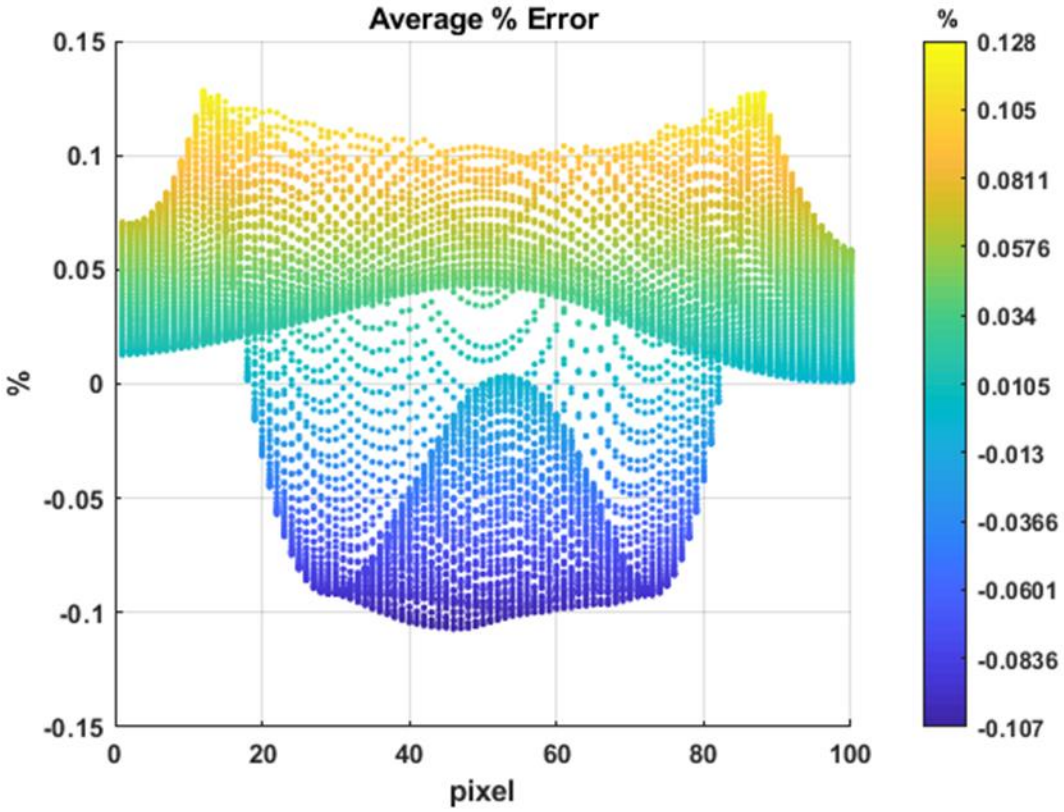

Figure 4-65. Average % error of the FIB milled paraboloids

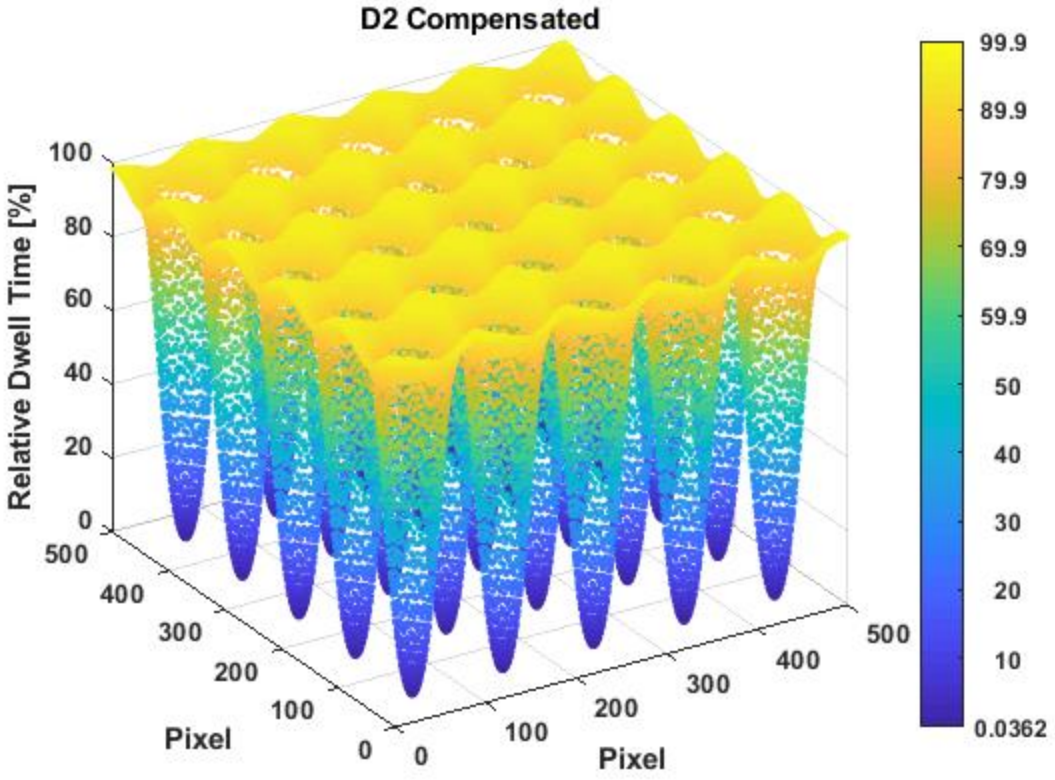

Figure 4-66. Error compensated relative dwell time map

This compensated bitmap pattern was used to FIB mill a new set of features. I used the parameters shown in Table 14. Figure 67 shows an image of the resulting surface in diamond.

Table 4-14. Parameters used to make the compensated 5 x 5 array of paraboloids in diamond

Current	1 nA
Magnification	5000x
Dwell Time	100 µs
Passes	55
Total Time	8:38
Bitmap File Name	bmp_mask_D2_comp.bmp

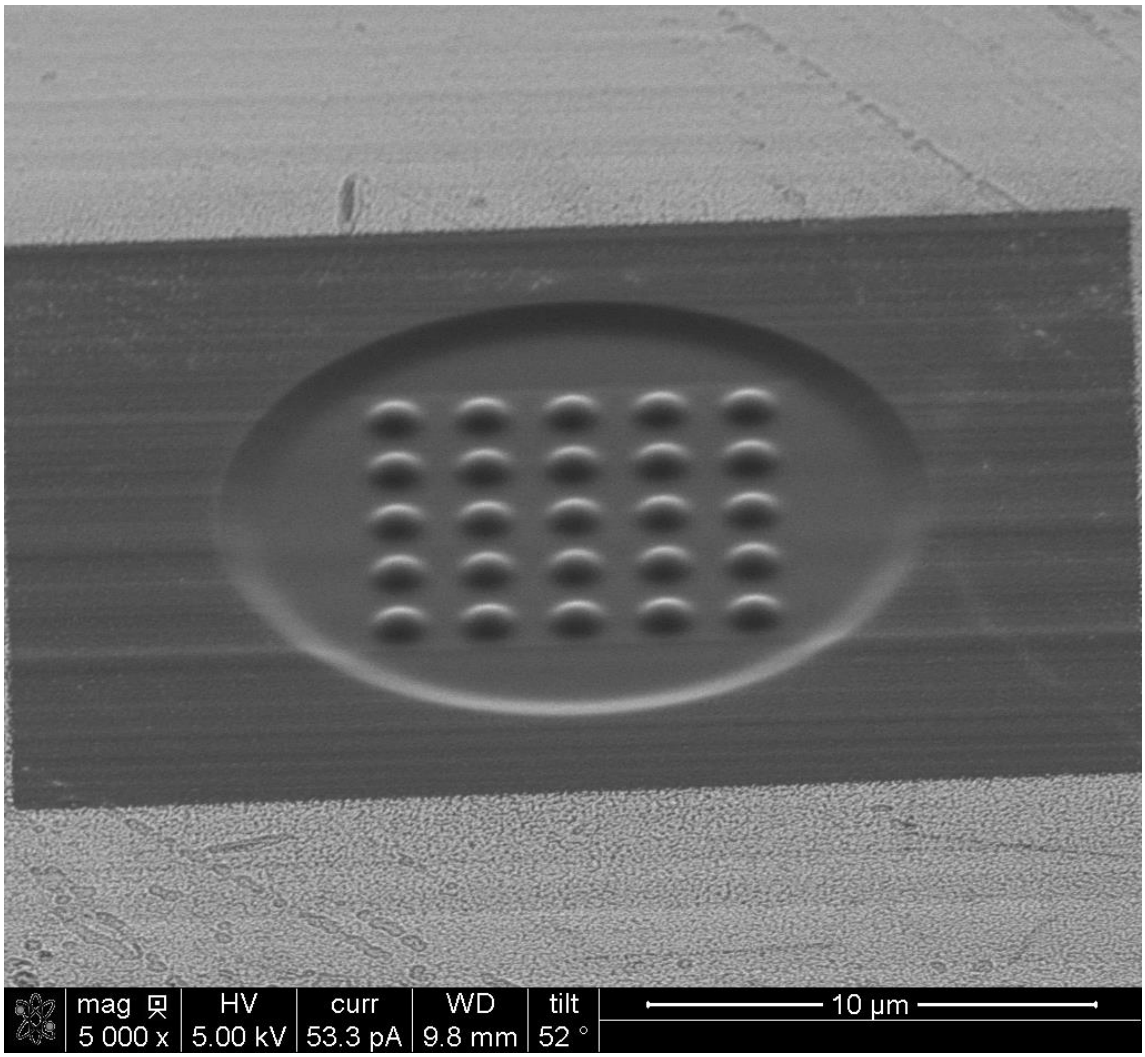

Figure 4-67. FIB milled error compensated pattern in diamond

A similar analysis was done to average the error over the 9 central paraboloid features. The resulting average absolute height error is shown in Figure 68. Compared to Figure 64 the error in the compensated surface is worse than the uncompensated. Figure 69 shows a meridian of the center paraboloid of the 5 x 5 pattern along with the desired surface after calculating the best fit transformation matrix. It appears that the error is primarily caused by not removing enough volume of material. In the future, a study of total length of FIB milling time should be conducted to see how it affects the shape fidelity.

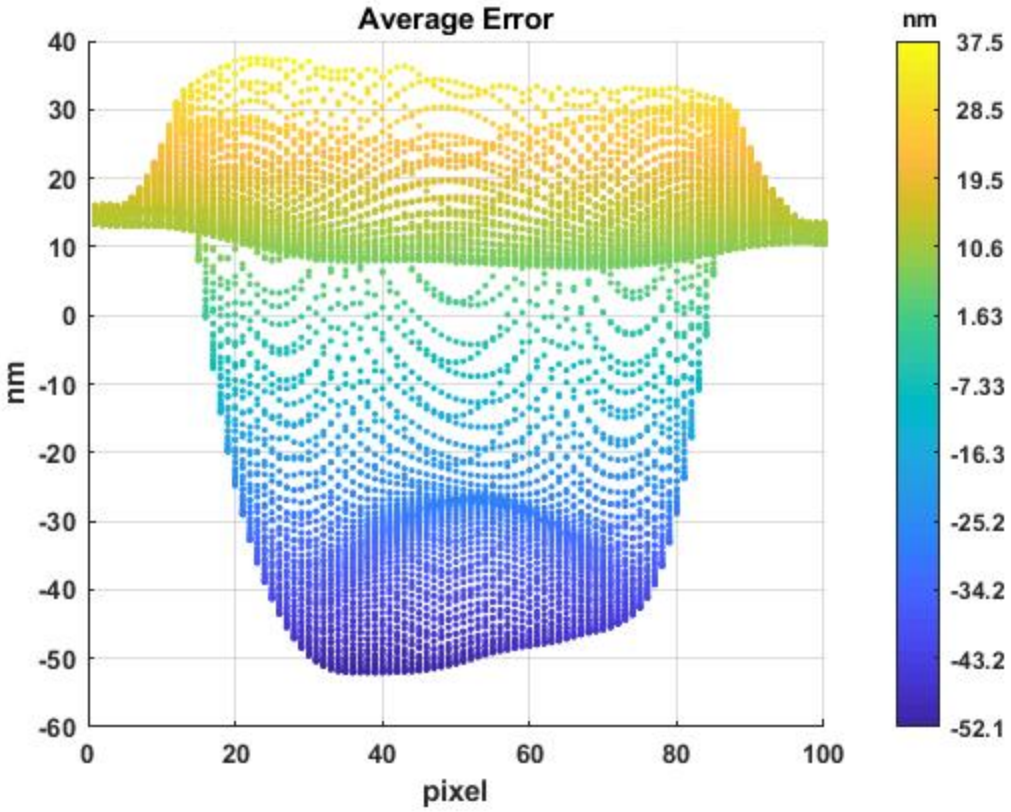

Figure 4-68. Average absolute z error of the error compensated pattern

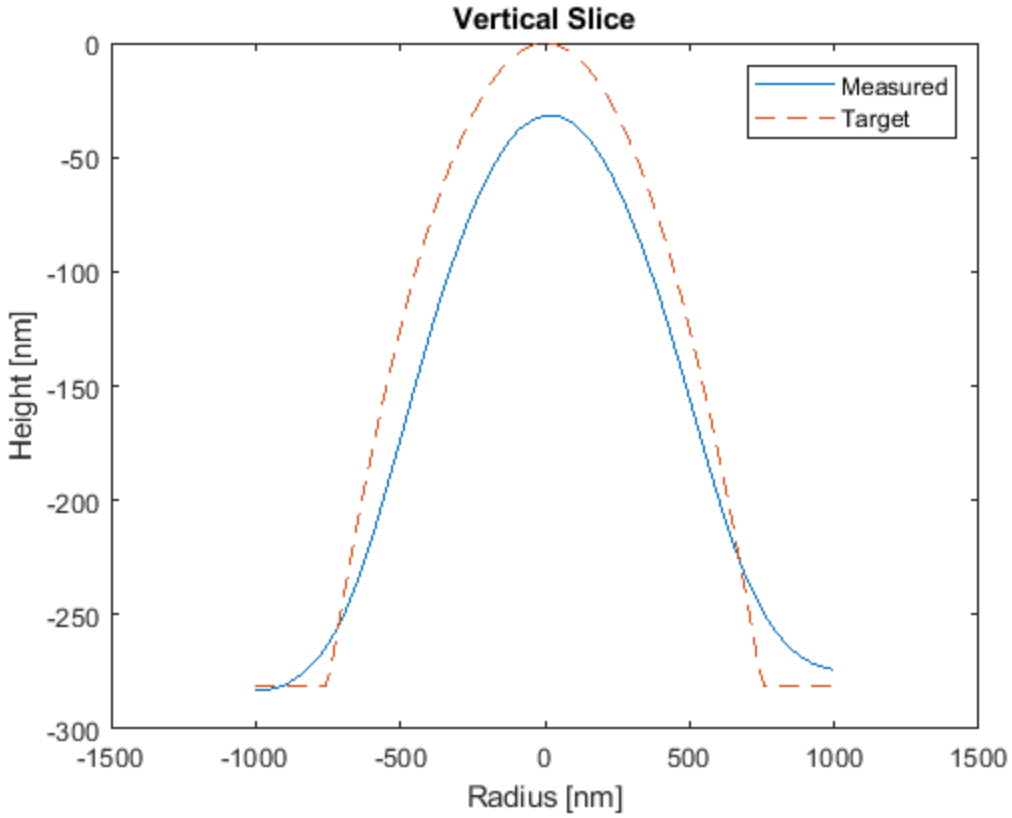

Figure 4-69. Vertical slice through the center feature of the 5 x 5 error compensated pattern

4.6 CONCLUSIONS

In this study the manufacturing of a microlens array mold and die were explored using Aluminum 1100 H14 and diamond for the mold and die respectively. Manufacturing of the array mold was explored using nanoindentation. Nanoindentation tests were completed on the Al 1100 using a Berkovich tip. The indentation method was used to create 10 x 10 arrays and characterized using the New View 500 SWLI and the Keyence laser confocal microscope in order to measure the indentation depth and form. The New View was unable to give enough data points along the slope and base of the indentations, however the Keyence microscope gives high enough resolution to analyze the cross-section of the indentations. The die was FIB milled with a 1 nA and 0.5 nA beam to explore the material removal rate and effectiveness of each beam. No dramatic differences were noticed between the two currents and a 1 nA was used for creating some of the final parabolic features. During measuring of the die grid, it was found that the AFM tip would easily damage when measuring the peak heights. In order to reduce tip damage, a conical slope was added to the surrounding of the grid. This has helped reduce damage to the AFM tip, although some artifacts still exist when taking multiple measurements.

REFERENCES

[1] X. Ding, G.C. Lim, C.K. Cheng, D.L. Butler, K.C. Shaw, K. Liu and W.S. Fong, "Fabrication of a micro-size diamond tool using a focused ion beam," Journal of Micromechanics and Microengineering, vol. 18, pp. 075017, Jul 1,. 2008.

5 REDUCING MICROLENS ARRAY INDENTATION FORM ERROR VIA TESTING AND SIMULATION

Parker Eaton
Graduate Student
Dr. Mark Pankow
Director of the PEC
Assistant Professor
Mechanical and Aerospace Engineering

ABSTRACT

This report addresses the initial methods involved in reducing the geometric form errors that occur when indenting microlens arrays. The microlens arrays are rapidly indented on a variety of metallic negative molds. A proprietary indent force and indent depth measurement technique is employed to aid in the characterization and control of the microindenting process. Insights from form error analysis and finite element simulations can then be used to make informed decisions to redefine die geometry and microindentation strategies in the pursuit of minimized geometric form error.

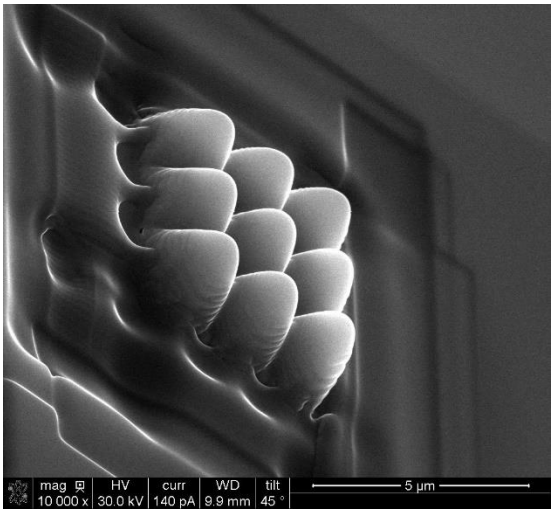

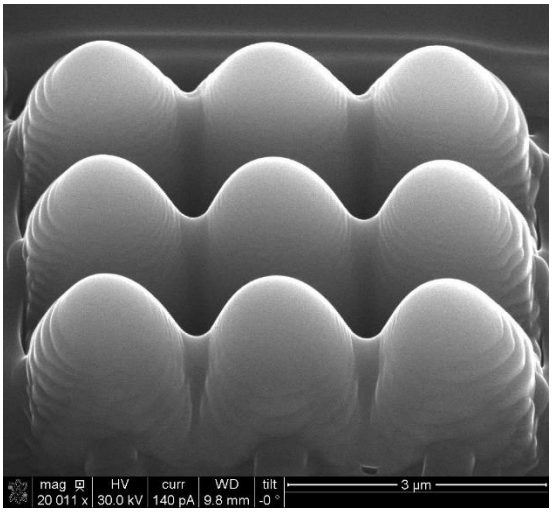

5.1 INTRODUCTION

Microlens arrays are typically composed of a grid of micrometer-scale lenses that are formed onto a substrate. The lenses may be positives or negatives of the desired lens geometry. In the context of this research, these lenses will serve as a negative mold for a final product. Traditionally, the arrays are laid out in a two-dimensional grid with lenses being aligned in two orthogonal directions. In some applications, alternative lens layouts may be used such as a hexagonal packing of lens or a stochastic layout. Figure 5.1 illustrates both an orthogonal array as well as a hexagonal array. An orthogonal lens layout will be used for the entirety of this project.

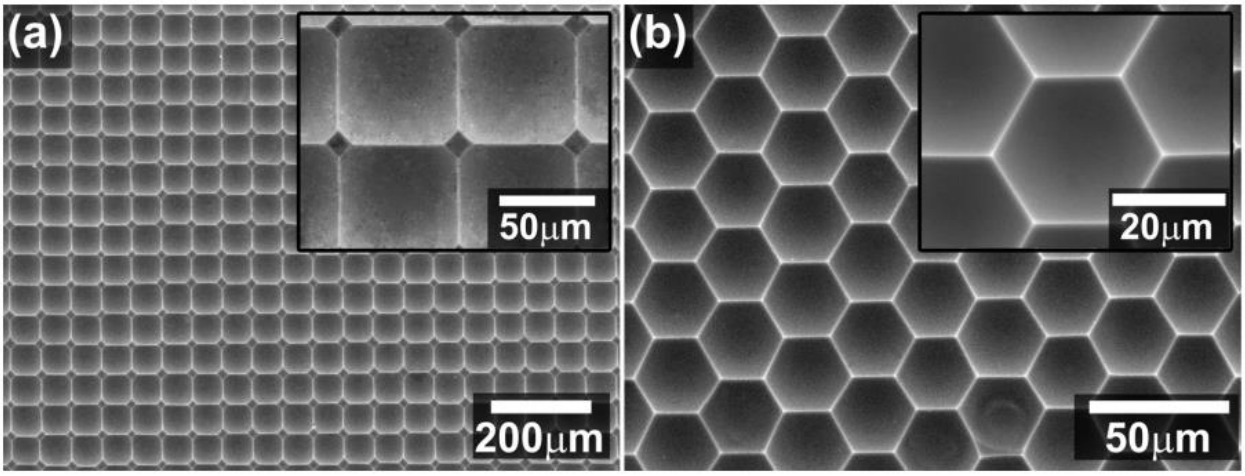

Figure 5.1. FE-SEM images of (a) orthogonal microlens arrays and (b) hexagonal microlens arrays [1].

Microlens arrays may be employed in numerous optical applications including but not limited to: LCD displays, anti-reflective coatings, photovoltaics, and virtual reality. A microlens operates under similar principles as a full-size optical lens by directing light rays to coincide on a designed focal point. Figure 5.2 illustrates the trace that the light rays follow through a convex microlens to meet at the focal point of the lens.

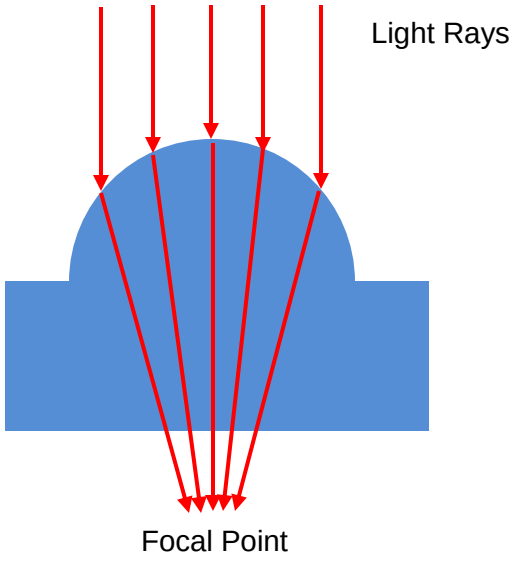

Figure 5.2. Illustration of light rays traveling through microlens.

Microlens arrays are nothing new to the worlds of industry and academia. As such, several manufacturing techniques exist. These methods can be broken down into two categories: direct and indirect. The direct method pertains to processes that involve the fabrication of convex lenses directly onto the substrate. In these methods, the lens material is typically heated to a thermoplastic or liquid state and then shaped into the desired geometry. These methods include thermal reflow, microplastic embossing, and microdroplet jetting. Alternatively, the indirect method of manufacturing involves the creation of a negative mold. A microlens array is then fabricated by injection molding, hot embossing, or UV molding. While the direct methods typically result in a better geometry than the indirect methods, the quality of the final microlens array relies heavily on the form of the negative mold.

Traditionally, microlens array molds have been manufactured via photolithography or ultra-high precision machining operations such as focused ion beam (FIB) milling. Both methods are associated with high costs and are very time-consuming if a mold of a useful scale is to be manufactured. Nanocoining, a recent technology developed at the Precision Engineering Consortium (PEC) at North Carolina State University [3], significantly reduces these costs and allows for a very short turnaround time. Nanocoining makes use of a resonant actuator to achieve a microindenting rate up to 45 kHz. A diamond die patterned with positive microlens features (Figure 5.3) impacts the mold surface at a very high frequency. Operations that could take days with traditional methods are completed in hours with nanocoining. To fully realize the benefits of this technology, the form error of the indented microlens negatives or “features” must be studied and compensated for to ensure the final microlens array behaves as designed. This report will describe the initial methods that are being used to analyze and account for form errors in indented molds.

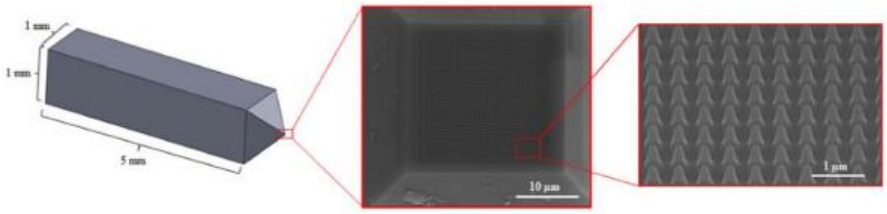

Figure 5.3. Schematic of a diamond die with parabolic features.

5.2 DATA ACQUISITION AND PHYSICAL TESTING

Up to this point, little has been completed experimentally to validate the finite element simulations. This work uses a comprehensive process that would use insights from validated simulation to drive die design and indenting strategies. The alterations to die geometry and indenting strategy can then be tested and their effectiveness analyzed for future testing. This closed-loop process will converge in a die geometry and indenting strategy that will minimize feature form error in the mold of a specified material. Through many repetitions of this design process, data will be gathered to enable faster convergence in future projects. For this goal to be realized, the simulation must first be validated for multiple mold materials and die layouts of interest. In the context of this project, the investigated mold materials will be Cu 110, electroplated Cu, and NiP (Nickel Phosphorus). To begin, a 3x3 feature die will be manufactured and used for the sake of continuity. To validate the simulation, the microlens array indenting process must be characterized in-house through accurate and reliable metrology. This is possible thanks to a proprietary force and indent depth sensing technology. In conjunction with atomic force microscopy (AFM), a detailed picture of the indenting process may be developed and used for error analysis. This section will cover the steps taken to initialize the proposed closed-loop form error minimization process pictured below in Figure 5.4.

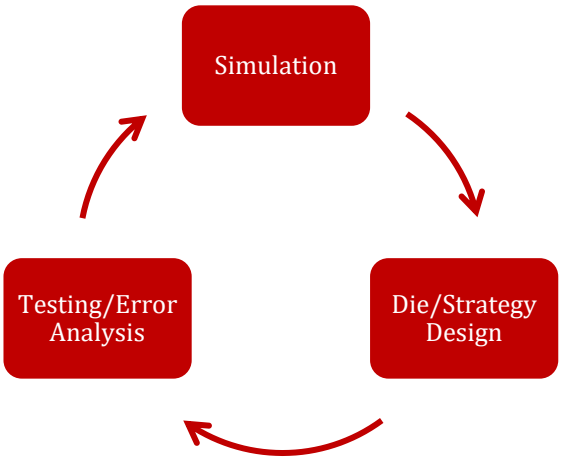

Figure 5.4. Proposed closed-loop form error minimization process.

5.2.1 **Setup and validation of metrology**

Physical testing is carried out at Raleigh-based nanofabrication startup, Smart Material Solutions, Inc. A testing stage with integrated indent force and indent depth sensing capabilities was developed and installed into an existing microindenting setup. This configuration is not capable of ultra-high frequency nanocoining operations but can indent at a frequency up to 10 Hz. Indent force vs. depth curves may be obtained using this sensor. Indent force vs. indent depth curves are very useful for characterizing the indenting process. For example, as the die indents the mold, the contact area will increase, thus increasing the required indenting force. The slope of this loading curve will vary from die to die and material to material. To validate the metrology, two experiments were conducted. The first experiment involved the recreation of a control nanoindentation experiment and comparison of the indent force vs indent depth curves of the recreation against the control. A Berkovich indenter was fabricated by Chardon Tool onto a 5mm x 1mm x 1mm single crystal diamond shank. This indenter was easily installed onto the indenting device.

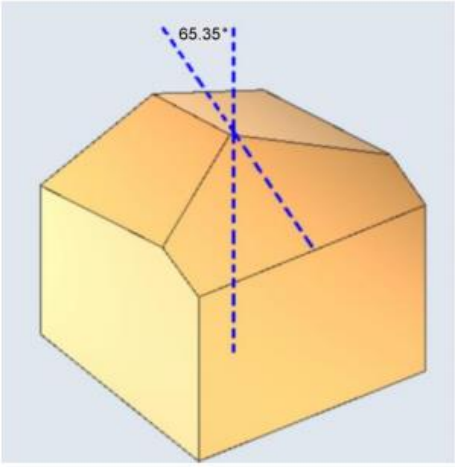

Figure 5.5. Schematic of Berkovich Indenter tip (65.35 degree half angle).

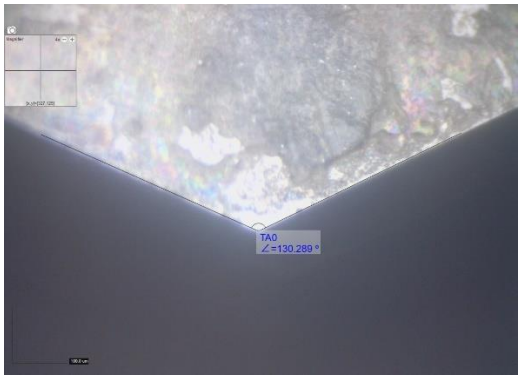

Figure 5.6. Chardon Tool Berkovich indenter (estimated 65.145 degree half angle).

Figure 5.6 demonstrates the quality of the Berkovich tip manufactured by Chardon Tool. An ideal Berkovich indenter has a half angle of 65.35 degrees whereas the provided Berkovich indenter has an estimated half angle of 65.145 degrees. This small discrepancy is acceptable given the nature of the test and the accuracy of the digital microscope measurement.

A nanoindentation experiment on a diamond-turned Cu 110 foil was carried out at the Analytical Instrumentation Facility (AIF) at North Carolina State University. The maximum load was set to be 10mN. Figure 5.7 presents the outputted indent force vs indent depth curve from one of the nanoindentation tests. The indenter reached a maximum indent depth of 467 nm before the force was held at constant for 10 seconds prior to retraction. This depth of 467 nm is the control depth for the in-house experiments. The resultant depth of the indentation can be understood to be the indent depth when the indent force becomes zero. This is the “final” indent depth after any elastic rebound during the unloading phase of the indent. In this case of the control experiment, this resultant indent depth was 434 nm. For the sake of accuracy, a force hold control feature was implemented into the control algorithm to recreate the plateau observed in the nanoindentation loading curve.

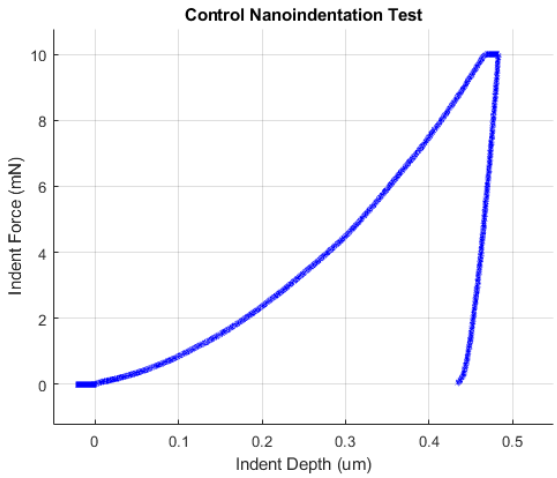

Figure 5.7. Control Berkovich Cu 110 nanoindentation curve.

Three indents were completed in a Cu 110 foil and are pictured in Figure 5.8. The loading curves obtained from these experiments are plotted against the control curve in Figure 5.9. It is important to note that both the forces and indent depths observed in the control nanoindentation experiment are at the very bottom of the range expected under typical microlens array indentation. As such, the measurements of force and indent depth are subject to a noticeable amount of noise. With this considered, the results are very promising. All three loading curves align relatively well with the control despite the loads and depths being on the mN and nm scale, respectively. A later improvement in the proprietary force and depth measurement system increased the resolution, thus reducing noise in this indent force and indent depth range.

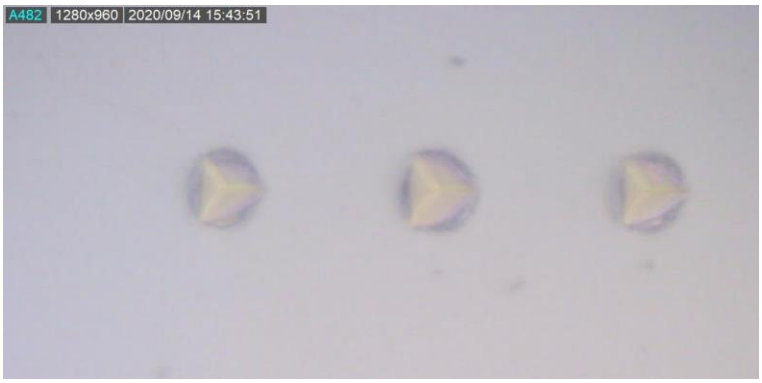

Figure 5.8. Three in-house Berkovich indents as viewed through a digital microscope.

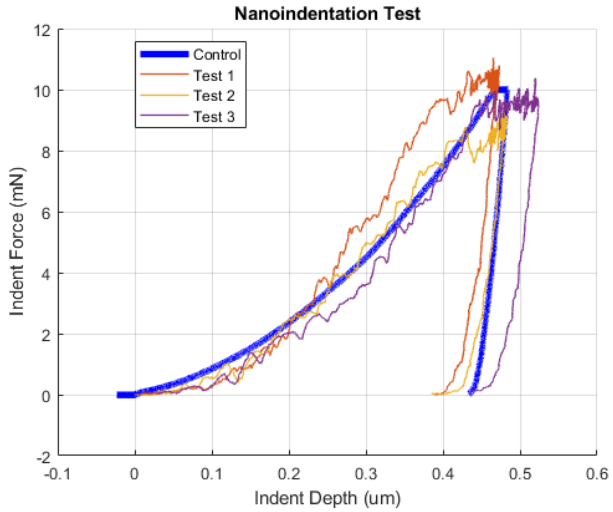

Figure 5.9. Berkovich nanoindentation loading curves.

An important metric to consider when conducting indents is the amount of normal elastic “springback”. As the die exits the mold, there is some elastic rebound or springback that occurs in the mold material. This springback can be defined as the difference between the resultant indent depth and the maximum indent depth achieved at peak force. To quantify springback, the measurement of the resultant indent depth must be accurate. The second validation experiment compares the measured resultant indent depths of in-house Berkovich indents against AFM measurements of these same indents.

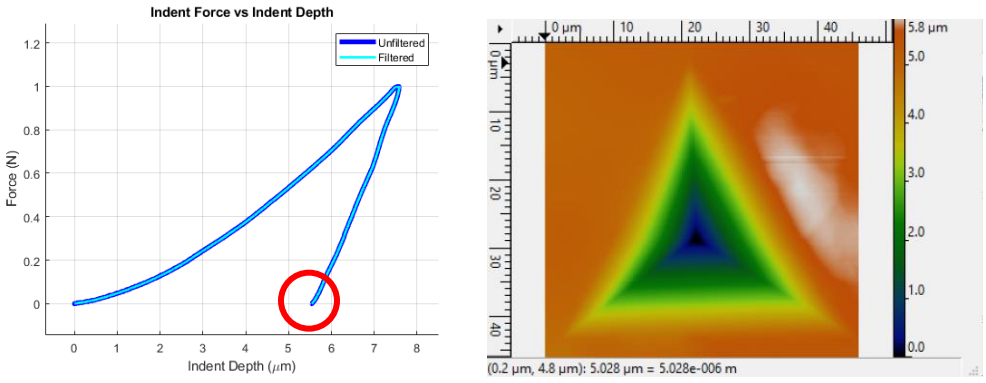

(a) (b)

Figure 5.10. Indent depth experiment measurements. (a) Indent force curve where the red circle highlights the resultant indent depth. (b) AFM image of the corresponding indent.

A total of 12 indents were completed ranging in peak force from 10mN to 1N. For the sake of time, only 8 were imaged. The resultant indent depth derived from the loading curve is the depth at which the indent force returns to zero. The indent depth derived from the AFM image data is calculated by first zeroing the height data in reference to the bottom of the indent and then probing a flat point near the edge of the indent. The reading of this probing point is understood to be the resultant indent depth. Table 1.1 highlights the results of this experiment. The results of this experiment may be visualized in Figure 5.11.

Table 1.1. Summary of resultant indent depth validation experiment

Indent #	Programmed Indent Force (mN)	Plot Resultant Depth (um)	AFM Resultant Depth (um)	Error (um)
1	10	0.463	0.518	-0.055
2	50	1.2432	1.304	-0.0608
3	100	1.8573	1.905	-0.0477
4	200	2.7038	2.641	0.0628
5	300	3.3744	3.302	0.0724
7	500	4.408	4.488	-0.08
9	700	5.0831	4.994	0.0891
11	900	5.595	5.413	0.182
			Mean Magnitude of Error (um)	**0.0812**

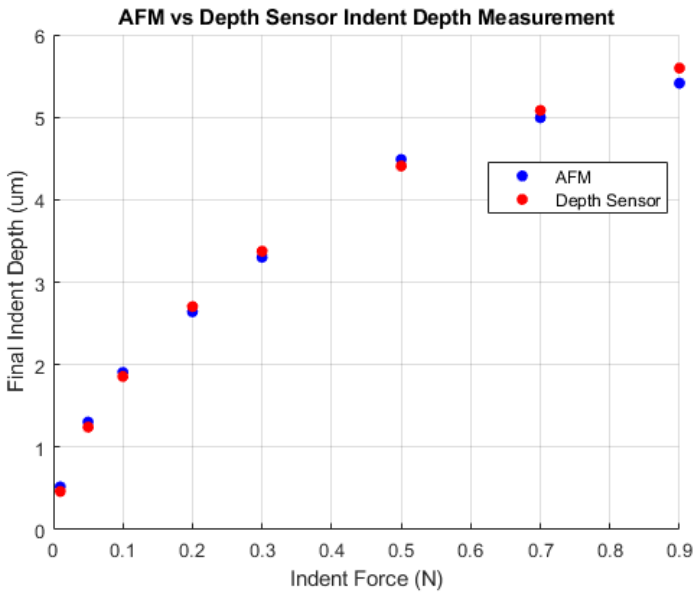

Figure 5.11. Visualization of the resultant indent depth measurements obtained from AFM and the proprietary indent depth sensor.

The results of these two experiments validate the proprietary indent force and indent depth measurement technique. Data obtained from in-house experiments can now be used to characterize and interpret the microlens array indenting process. Please note that the indent force and indent depth sensor has since been improved in function.

5.2.2 **3x3 Diamond Die**

A 3x3 feature diamond die was designed and FIB milled for the purposes of initial testing. The features' dimensions were on a similar scale to that expected of a future microlens array and are much smaller than the 2x2 die fabricated in previous research [2]. The features have a radius of curvature of 1 µm and a pitch (distance between feature vertices) of 2 µm. The die features were FIB milled onto a standard 5mm x 1mm x 1mm single crystal diamond shank. After FIB milling, SEM and AFM images were taken of the die. AFM images of the die indicate that debris was present around the central feature during the imaging (as seen in Figure 5.13). As such, the die is set to be reimaged. AFM images of the die carry a lot of value. For one, the AFM image of the die may be referenced against an AFM image of an indent. This allows for an analysis of material flow and elastic springback. Secondly, the die may be imported into a finite element solver where indents under varying conditions may be simulated, validated, and used to motivate design and process changes for that particular die.

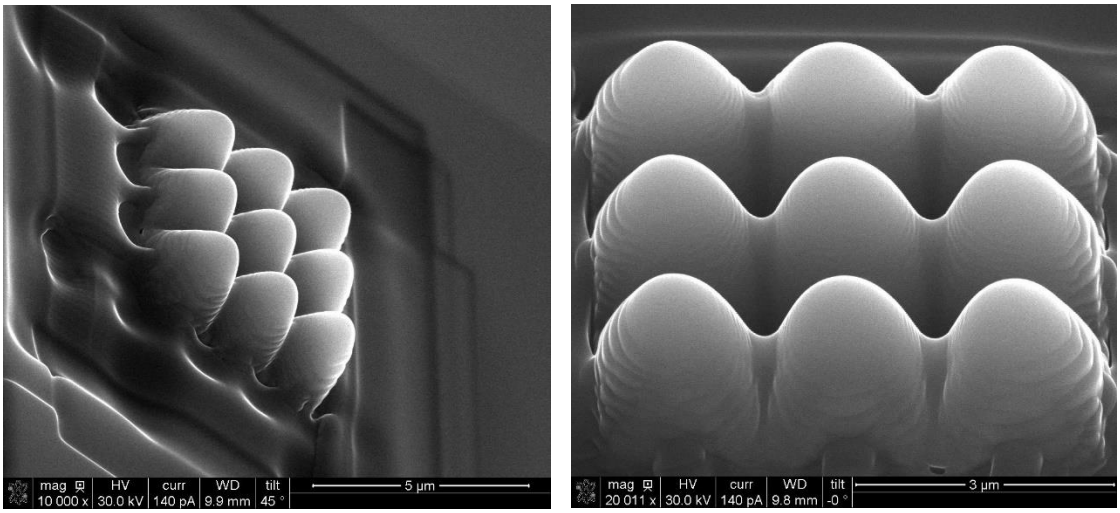

Figure 5.12. SEM images of the FIB milled diamond die.

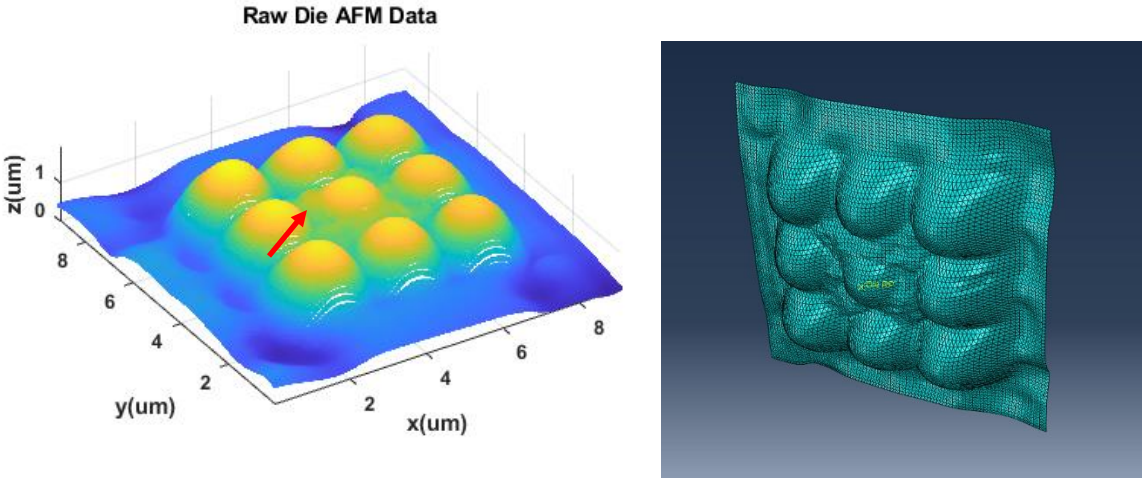

(a) (b)

Figure 5.13. (a) Raw AFM xyz data plotted in MATLAB (note debris indicated by red arrow). (b) Die AFM data imported into Abaqus™ and meshed.

5.2.3 **Indent Process Control**

Additional control has been implemented into the indent controller at Smart Material Solutions, Inc. Currently, the operator of the indenting machine may control to several indent parameters such as the indent machine axis infeed, indent depth, die tip velocity, indent strain rate, indent force, stepover between indents, and holding periods (holding time at peak indent force or indent depth). These controls give the operator the ability to study the effects of various indent

parameters on the resultant quality of the indent. For example, some mold materials may respond better to a slower indent velocity and shallower indent depth while others may react better to a high velocity indent programmed to a deeper indent depth. Indent controls may be fine-tuned to any die and material pairing through testing. In addition to controlling individual indents, entire two-dimensional arrays may be created and controlled by the same parameters. These arrays may be manufactured at a rate up to approximately 10 Hz (10 indents per second) while retaining the indent force and indent depth sensing capabilities. This enables findings from studies conducted on single indents to be applied to large scale arrays for further analysis. The wide variety of control and depth of data acquisition allows the operator of the indenting machine the ability to both replicate simulation conditions in real life and replicate real life conditions in the simulation. For the closed-loop form error minimization process to truly work, simulation must be able to match reality and vice versa.

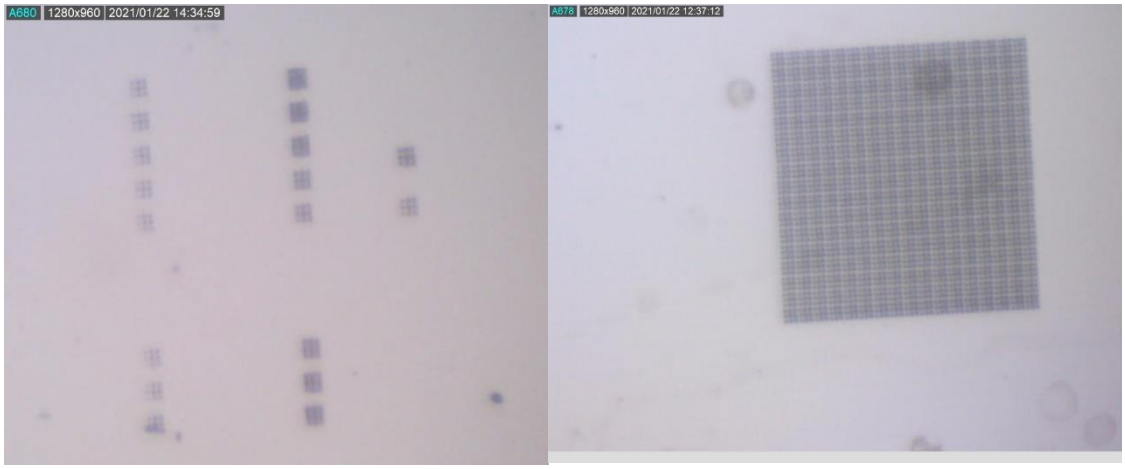

(a) (b)

Figure 5.14. Digital microscope images of indents in electroplated Copper using the 3x3 die. (a) Individual indents of varying depths. (b) 10x10 indent array.

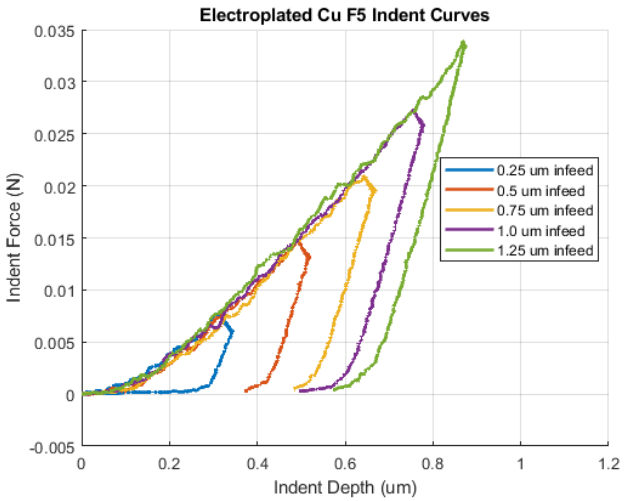

Figure 5.15. Indent loading curves from the right-hand group of five indents in Figure 5.14.a

5.3 CURRENT WORK

Several projects are currently ongoing as the closed-loop form error minimization process is now being entered. As data is collected from simulation and testing it can be used to compare and analyze die geometry and indenting process. Changes will begin to take place in the effort to converge on an indent with minimized form error. Once this is accomplished and the findings documented, the same process will begin for large scale arrays and indenting procedures. In order to accurately model the microlens array indentation process for Cu 110, electroplated Cu, and NiP metallic molds, the plasticity properties of each mold material must be obtained and implemented into the simulation. An indent form error quantification algorithm must be developed in order to compare AFM images of real indents to a reference geometry. Doing so will allow for an evaluation of the effectiveness of die geometry and/or indenting process control parameters. Additionally, mold material flow may be studied, and insight gained to drive die geometry and indent process modifications. Lastly, interesting behaviors have been observed in indent loading curves that warrant further investigation.

5.3.1 Simulation Enhancements

To properly simulate the microlens indentation process and validate the simulation for each mold material used, plasticity properties must be derived and then used in the simulation. For the case of an Abaqus™ Explicit analysis, this comes in the form of capturing the plastic region of the stress strain curve. Dao et al derives dimensionless equations that compute parameters such as the strain hardening exponent from nanoindentation loading curves [4]. These parameters are then used to reconstruct the stress strain curve. Points in the plastic region are sampled and then

imported into the simulation. Nanoindentation testing is currently underway for each of the materials used in this study. Additionally, using single crystal diamond dies allows for the simulated die to be treated as a rigid body. This allows for a decreased computational time. On average, the previously developed simulations [2] took around one day per indent to solve. With the simulations being so computationally expensive, any reduction in complexity will be well received. The ability to import the as-manufactured die geometry into the finite element model will aid in further validation of the simulation.

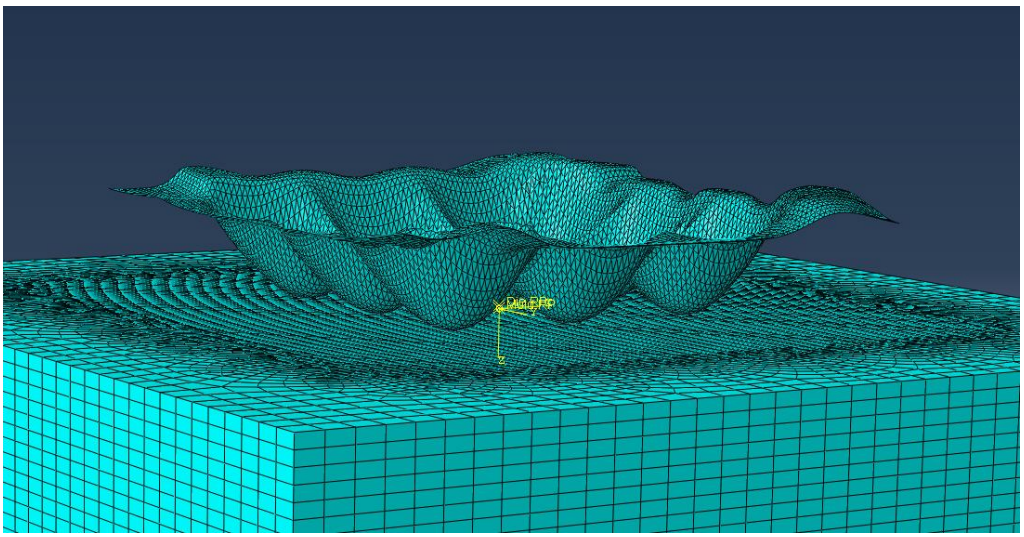

Figure 5.16. Abaqus™ FEM modeling the testing 3x3 die indenting a mold material.

5.3.2 **Form Error Quantification**

Microlens form error quantification is critical for the validation of die geometry and indentation process changes. A form error surface may be computed so that regions of large form error may be identified and compensated for. An algorithm is currently being developed to import, manipulate, and operate on AFM data of any die, indent, and target microlens array geometry. The program will automatically identify the vertices of the imported AFM images and perform iterative coordinate transformations on the coordinate points until the vertices are aligned with the global coordinate system (see Figure 5.17 and Figure 5.18). Following this, form error may be computed and analyzed via the subtraction of the aligned indent surface from the aligned die or target microlens array geometry surface. Various cross-sectional views may be taken to observe the flow of mold material within the indent (Figure 5.19). The error surface may be used to influence die geometry changes to compensate for regions of over or under-indenting. These metrics allow for the user to observe where and how indent geometry differs from the target geometry. These findings can then be used to modify die geometry to counter the observed errors. For example, the radius of the bottom of an indent might be too large while the indent itself is also too shallow in depth. This might suggest that the height of the die features be lengthened while the pitch between the features remains constant. In theory, making these modifications to die

geometry will deepen the indent and decrease the radius at the bottom of the feature. Over multiple iterations, the original geometric error may be significantly reduced. In addition, this tool will also be used to validate the finite element simulation results against physical indents in a similar manner. The AFM image of an indent may be compared to a digital recreation of it. Conveniently, all surfaces (including the form error surface) may be exported to .stl format for easy importation into CAD and FEA software.

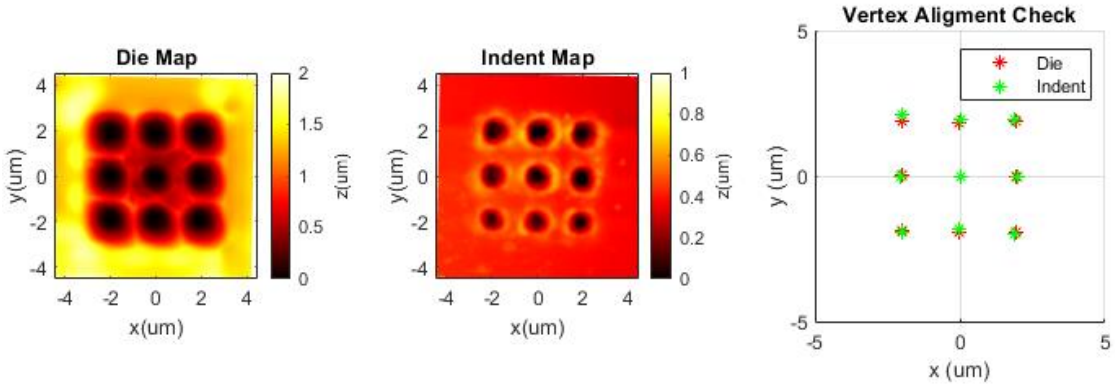

Figure 5.17. Window allowing operator monitoring of the overlay of die and indent surfaces.

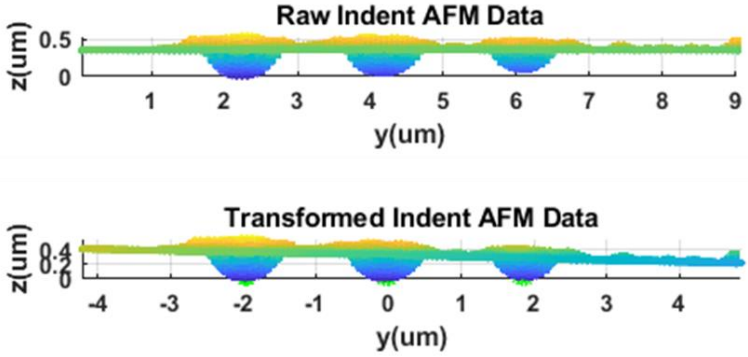

Figure 5.18. AFM data before (top) and after (bottom) iterative auto-alignment.

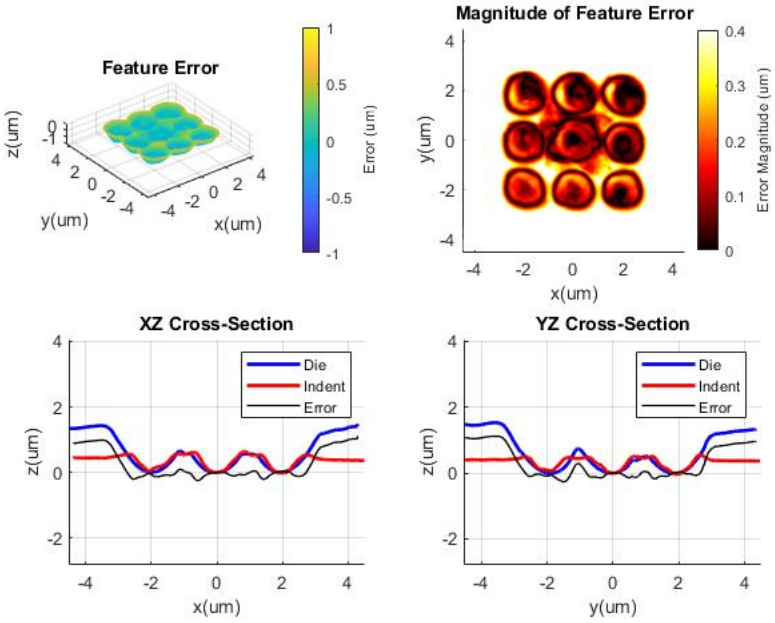

Figure 5.19. Sample output of error analysis algorithm.

5.3.3 **Indent Loading Curves**

The 3x3 die was tested under a variety of circumstances. During testing on a NiP mold, an interesting trend was observed in the loading curves. Figure 5.20 presents the loading curves obtained from this test. This experiment involved varying the indenting machine axis infeed which in turn varies the depth of the indent. Axis infeeds of 1 µm to 5 µm in steps of 1 µm were used in the experiment. Please note that “F5” is the internal name of the 3x3 die. A defined increase in the loading curve slope (indicated by the red arrow) occurs at an indent depth of approximately 1.1 µm. Let this loading curve slope be understood as the “indenting stiffness” or the indenting force required per unit indent depth. The indenting stiffness increases from approximately 0.08 N/µm to approximately 0.20 N/µm. Following this change in slope, no matter how deep the die penetrated the mold, the unloading path remained nearly identical, resulting in very similar resultant indent depths (indicated by the red circle). It is speculated that at this point, mold material has flowed fully into the valleys of the die and the contact area has increased to a nearly constant value, resulting in a larger, and approximately constant, indenting stiffness. Alternatively, the sharp increase in indenting stiffness may be due to feature-less portions of the die contacting the mold surface. To discern between the two possibilities, an experiment will be conducted to quantify the indenting stiffness of a feature-less die against a NiP mold. If this stiffness is close to 0.20 N/µm, then it can be assumed that the stiffness change is due to contact of feature-less portions of the die against the mold material. Should this stiffness be significantly greater than 0.20 N/µm, then it may be accepted that the change in indenting stiffness is due to complete filling of the valleys in the 3x3 die.

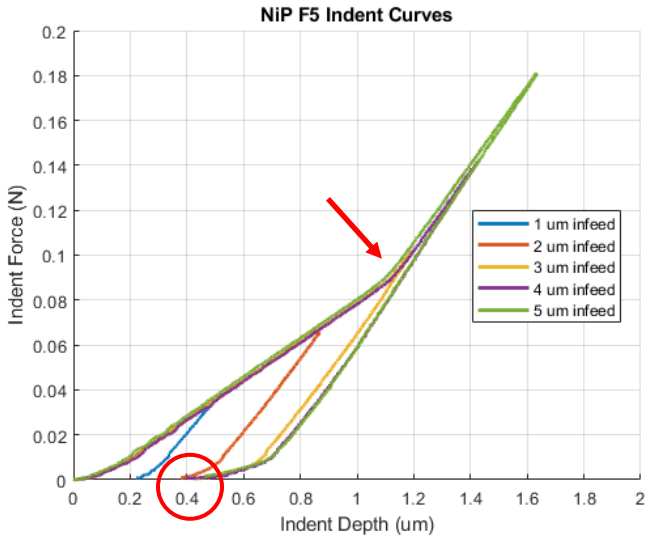

Figure 5.20. Indent loading curves of 3x3 die test on NiP Mold.

5.4 **FUTURE WORK**

Once all components of the closed-loop form error minimization process are established and vetted, many loops of simulation, testing, and design tweaking will be undergone in the effort to converge to an error-minimized die geometry and indenting process for a singular indent. The insights gained during this exercise will be used to drive a similar process to converge to an error-minimized microlens array. The data gathered can then be applied to future microlens array geometries, creating a large collection of data. This data will be used to establish a process for creating error-minimized microlens arrays in metallic molds at a frequency of approximately 10 Hz. Testing will then be conducted using the high strain rate nanocoining process in the effort to significantly reduce the manufacturing time of error-minimized microlens arrays by indenting at a frequency on the order of 45 kHz. High-speed, high-accuracy nanocoining will enable extraordinarily fast production of high quality molds for the manufacturing of microlens arrays.

REFERENCES

[1] F. Chen, H. Liu and Q. Yang, "Maskless Fabrication of Concave Microlens Arrays on Silica Glasses by a Femtosecond-Laser-Enhanced Local Wet Etching Method," *Optics Express,* vol. 18, no. 19, pp. 20334-20343, 2010.

[2] Gundyal, Sumit Anand 2019, “Modeling of the Micro-indentation Process to Create Microlens Array Features on a Mold”, MS thesis, North Carolina State University.

[3] E. Zdanowicz, T. Dow and S. R.O., "Rapid Fabrication of Nanostructured Surfaces using Nanocoining," *Nanotechnology,* vol. 23, no. 41, p. 415303, 2012.

[4] Dao, M., Chollacoop, N., Van Vliet, K., Venkatesh, T., & Suresh, S. (2001). Computational modeling of the forward and reverse problems in instrumented sharp indentation. *Acta Materialia, 49*(19), pp. 3899-3918.

6 Mechanochemical Effects on Aluminum 1100, 6061, and 7075

Abduallah Elkodsi
Undergraduate Researcher
Dr. Mark Pankow
Director of the PEC
Assistant Professor
Mechanical and Aerospace Engineering

Abstract

The Rehbinder effect can help reduce the forces required to machine certain metals. The reduced forces can improve surface finish while also avoiding flooding of hazardous commercial coolants. In this work, Sharpie™ markers were investigated as a minimum quantity lubricant to reduce cutting forces in turning certain aluminum alloys. Aluminum alloys 1100, 6061, and 7075 were turned using Sharpie™ and its individual chemical constituents in order to determine which chemical causes the highest force reduction. The cutting and thrust forces were measured for various cutting depths and speeds and compared to dry cutting conditions. Aluminum 1100 was somewhat unaffected by the lubricants due to its inherent "gumminess". Diacetone and propanol were found to reduce the cutting and thrust force compared to dry conditions for aluminum alloy 6061 and 7075. Ethanol was found to increase cutting forces while each of the lubricants had varying effects depending on the alloy.

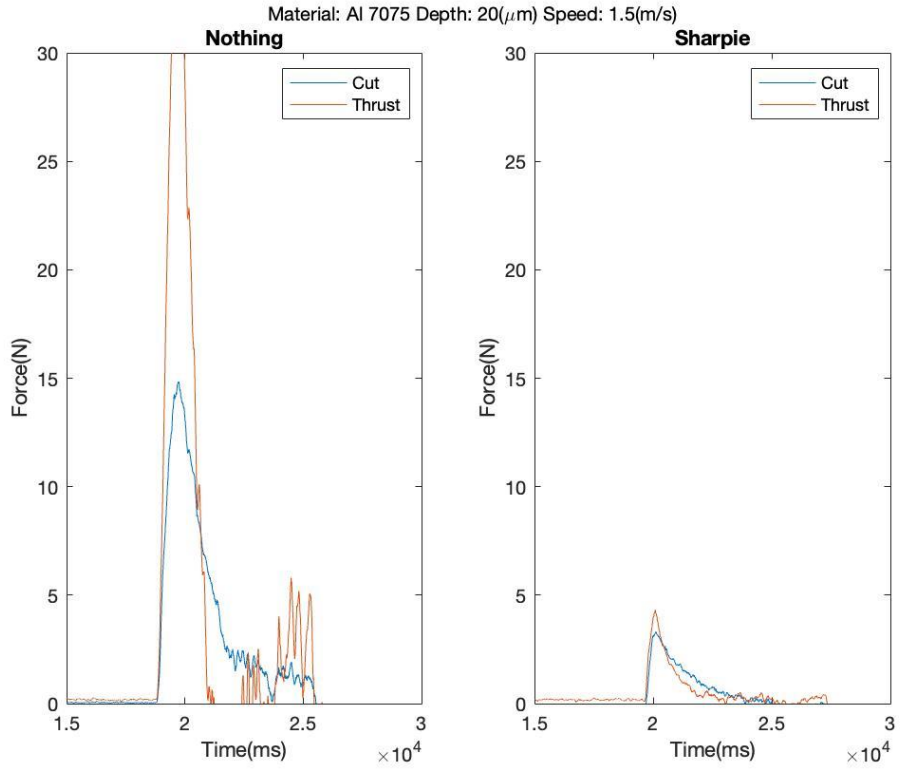

6.1 INTRODUCTION

The Rehbinder effect is a machining method discovered in the early 1990s that reduces the cutting forces of a material by creating a thin surface film [1]. Depending on the material and the surface-active media, the Rehbinder effect can reduce the cutting forces up to 50 percent [2]. The lubricants used are in such small quantities that they do not need to be regularly disposed, unlike metal working fluid lubricants (MWFL). The lubricants used range from glues, inks, alcohols and have been seen to function as surface-active (SA) chemical media [3]. Utilizing this effect, one is able to change the cutting flow mode of the work piece from a sinuous to segmented chip formation. This, in turn, is what causes the reduced cutting forces required. The use of a thin surface film also results in an enhanced surface finish and chip thickness and further improves rough surfaces with tear and cracks [3].

The Rehbinder effect is categorized into three types, depending on the lubricant selection: the first type consists of media that show strong physical adsorption to the metals, such as glue and ink; the second consists of media that show chemical affinity (specificity) for Al only, as established by their ability to react with oxide-free Al surfaces, such as isopropyl alcohol and ethanol; the last type consists of media that are not known for any significant adsorptive or other similar interactions with any of the metals, such as distilled water and diacetone alcohol [3].

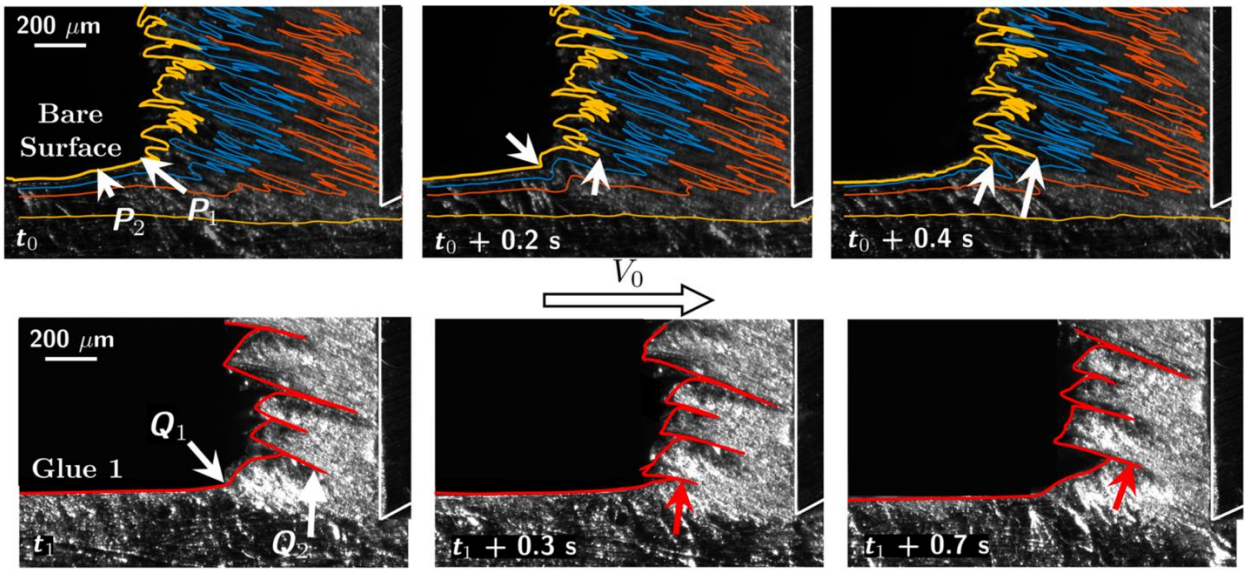

Figure 6-1: Chip formation of an annealed copper alloy (a) as a bare surface without lubricant and (b) with glue added to the surface. Chip formation can be seen occurring for the sample in (b) with the added glue surface film [4].

The effects of surface lubricants differ based on the machining technique. For instance, deep-hole drilling is very demanding due to the challenge of chip removal. The heat input onto the work piece is particularly higher in drilling than in other machining operations because the chip formation process takes place within the part and continues to remove material from the bulk,

rather than from the treated surface. Prior studies using aluminum alloys and single point diamond turning have shown SA media reduces the cutting forces [3]. It is still unexplored how these (SA) chemical media are affecting the machinability and surface roughness of aluminum alloys (1100, 6061, and 7075) when they are turned using a carbide insert compared to diamond. It has yet to be seen whether these alloys are affected by Rehbinder effect during turning operations or if it acts similarly to conventional lubricants.

In this project, commercial aluminum 6061, 1100, and 7075 alloys are subjected to parallel and perpendicular cutting forces while utilizing SA media. The lubricants chosen for this work is a sharpie marker and its individual constituents. Prior studies have shown Sharpie™ acts as an MQL and can improve cuts for soft metals such as aluminum alloys. A precision diamond turning (DT) machine was used to turn various aluminum alloys with a carbide insert tool. The experiment is conducted multiple times by varying different parameters such as cut depths and speeds. Three aluminum alloys will be tested using Sharpie™ and each of its individual chemical constituents. A load cell is used to measure the forces applied on the system, while the high-speed camera will be used to visualize the chip thickness and the flow mode type that the surface will undergo during the deformation based on the test parameters. These tests will help determine the effects of each constituent on reducing the cutting force and thrust for each aluminum alloy.

6.2 EXPERIMENTAL DETAILS AND SETUP

Aluminum alloys 1100, 6061, and 7075 were turned using a diamond turning machine (DTM) using a carbide turning insert. Commercially available Sharpie ink markers and its individual ingredients: Butanol, Propanol, Diacetone Alcohol, and 96% Ethanol, were separately tested on the aluminum alloys OD work piece. A carbide triangle turning insert without a chip breaker is used in this experiment to view the chip formation throughout the high speed camera. Each edge of the tool is used only for one specific coolant, in order to avoid any cross contamination. Aluminum 1100 is known to be much softer and more difficult to machine than 6061 and 7075, therefore the depth of cut and cutting speeds tested are slightly different. The chosen depths of cut and speeds tested are listed for each alloy in Table 1.

Table 6-1: Test Parameters

Aluminum Alloy	DOC (μm)	Speed (m/s)	Coolants
1100	20 & 50	3.5 & 5	• None • Sharpie™ • Butanol • Propanol • Diacetone Alcohol • 96% Ethanol
6061	20 & 120	1.5 & 5	
7075			

During the entire experiment, the feed rate remained constant while either the DOC or spindle speed varied. The feed rate was kept constant at 20 mm/rev. The tool's rake angle is held at zero degrees. The tested lubricants were applied to the outer diameter (OD) of the work piece. The coolants were allowed to dry and adhere to the surface for 5 minutes prior to cutting.

In order to record the parallel (cut) and perpendicular (thrust) forces during the experiment, the load cell, Kistler 9251A SN50993, is used to capture the data and transfer it to the measuring signals box, 5004 Dual mode amplifier Edition 2/81. The signals will then be transferred to the computer via the MC measurement computing (DAQ) device. The data will be analyzed and stored through MATLAB. In order to calibrate the x (cut force) and y (thrust force) direction of the load cell, a 1 lb. mass was attached to the load cell, while ensuring the system record an appropriate 4.448 N. A high-speed camera, FASTCAM SA-X2, was aimed at the side of the aluminum alloy samples OD, and the side of the tool. The high speed video was used to ensure a 0 degree rake angle and capture the chip formation and material flow during cutting. An image of the testing arrangement is shown in Figure 6-2 and highlights the work piece, tool, and load cell.

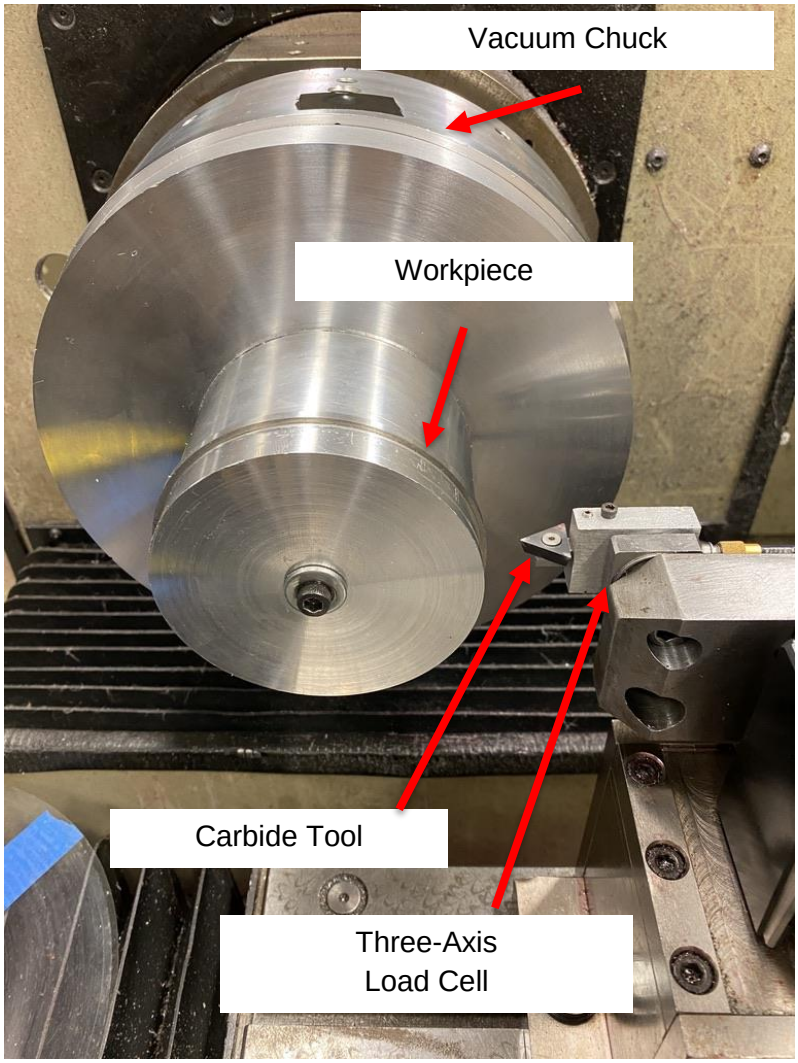

Figure 6-2: Setup for MQL testing where the aluminum alloy sample is sandwiched in the fixture and cut using carbide insert. Also highlighted are is the vacuum chuck where the fixture is attached, and the three-axis load cell used to measure force.

As the sample is cut, the RPM will increase, which also can be demonstrated by the equation RPM= $(velocity*60)/(Diameter*\pi)$. Therefore, to maintain a constant experimental behavior for all test samples, as the test sample's diameter decreases the RPM will be decreased manually to maintain a constant spindle speed. From Table 1, there will be three different types of materials, two different DOC, two different spindle speeds (SS), and six different coolants for the experiment. This leads to a total of 72 experiments being conducted. However, due to the softness of Al 1100 compared to Al 6061 and 7075, the DOC and SS were different than the other materials. In order to avoid contamination between lubricants, a 10 µm deep cut was made to level and smooth the OD surface for the next test. The cutting force data is collected and compared to determine the effects of each lubricant.

6.3 **RESULTS**

6.3.1 **Al 6061**

The cutting and thrust forces for aluminum alloy 6061 for each lubricant is plotted in Figure 6-3 at a cut speed of 1.5 m/s and 120 µm depth of cut. The force values for all of the other cutting parameters are summarized in the bar chart plotted in Figure 6-4. It was found that the added lubricants had little effect on reducing the cutting forces for all of the cutting parameters on alloy 6061. However, it can be seen that the measured force was affected by the cutting parameters as would be expected. The cutting force increases as both the speed and cutting depth increases. Ethanol seems to cause an increase in both the cut and thrust force, even more so than dry cutting conditions. This could be due to the ethanol removing residual fingerprints and oil from the surface of the aluminum, leading to a cleaner surface free of contaminants. The removed oils and contaminants would have potentially applied their own subtle MQL effect, but by removing them from the surface of the aluminum, the cutting forces are slightly higher. An interesting slope can be seen for the diacetone and propanol cuts as the force peaks and then continues to fall off as the cut continues across the surface of the part. This type of response occurs on more than one occasion for each alloy and is to be investigated further. The thrust force remains stable, while the cutting axes slopes as the tool crosses the material's surface. This sloping remains constant for alloy 7075 and may actually be due to the improved chipping action of the harder alloy.

As seen in Figure 6-4, the cutting force increases with increasing depth of cut but reduces at higher cut speeds. Ethanol consistently has some of the highest measured cutting and thrust forces for all of the different parameters. Propanol and diacetone seem to provide the lowest forces for aluminum 6061. The MQL effect was most accentuated for the higher cut depth and lower speeds due to the higher forces.

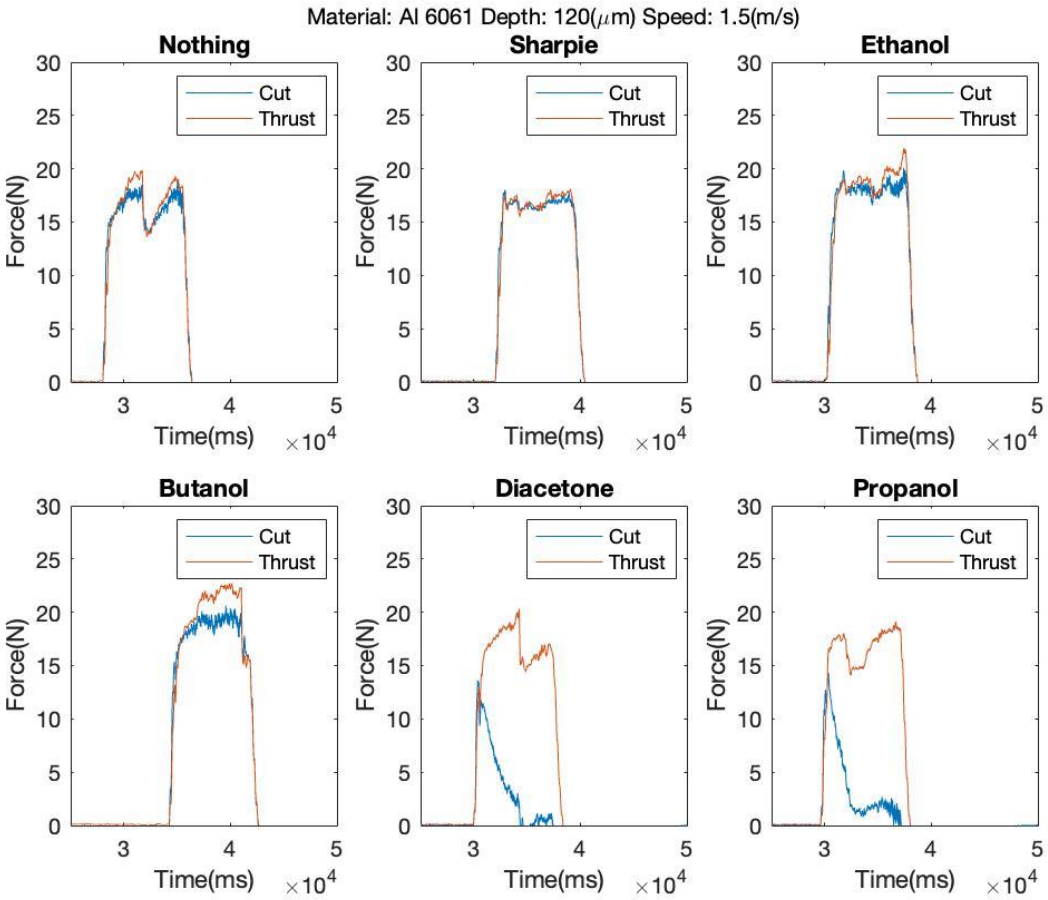

Figure 6-3: Cut and Thrust forces plotted for 6061 cut at a speed of 1.5 m/s and depth of 120µm for each lubricant type.

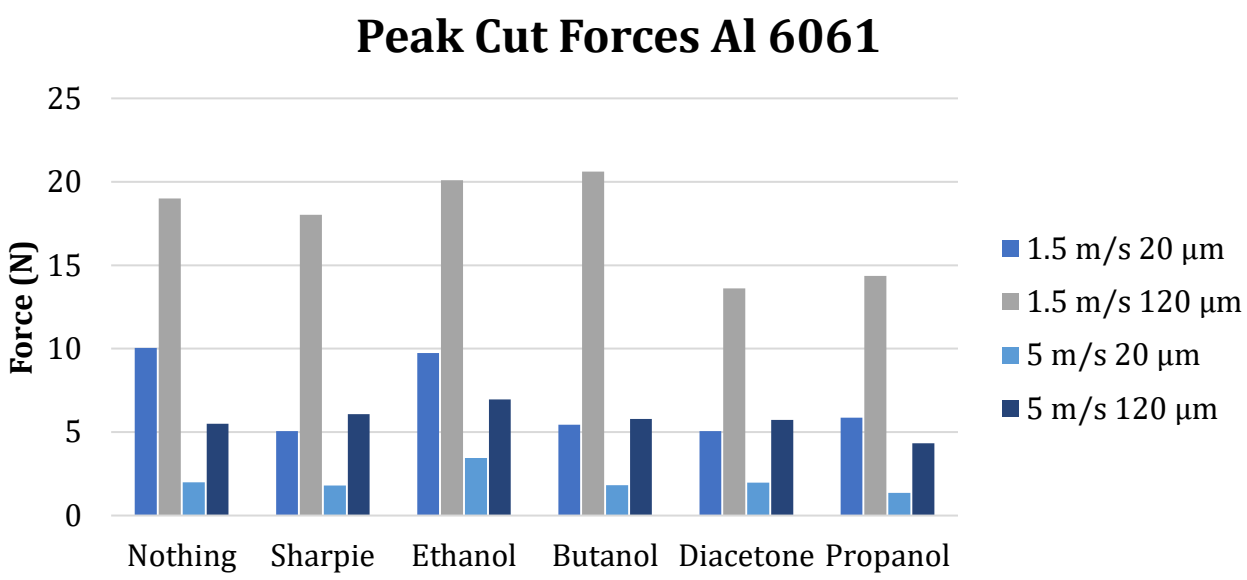

Figure 6-4: Cut forces measured for Al 6061 for all lubrications and cutting parameters.

6.3.2 **Al 7075**

The results for turning of aluminum alloy 7075 are plotted in Figure 6-5 for a cut depth of 120µm at 1.5 m/s. These are the same parameters plotted for 6061 in Figure 6-3. Aluminum alloy 7075 is harder and stronger than aluminum alloy 6061 but has similar machining characteristics [8]. *A*s can be seen from the figure, the slope of the cut is not constant across the sample, as was seen for diacetone and propanol on 6061. The force peaks at the start of the cut and continues to reduce as the cut moves across the surface. Once again, the peak force for ethanol was found to be much higher than all other surface additives. The cutting and thrust force is approximately four times higher than each of the other lubricants. It can be seen that each of the lubricants presented at 120µm depth and 1.5 m/s speed reduce the cutting force by up to 50% and reduced even further for the measured thrust (except for ethanol). There does not seem to be much to distinguish between each of the lubricants for alloy 7075.

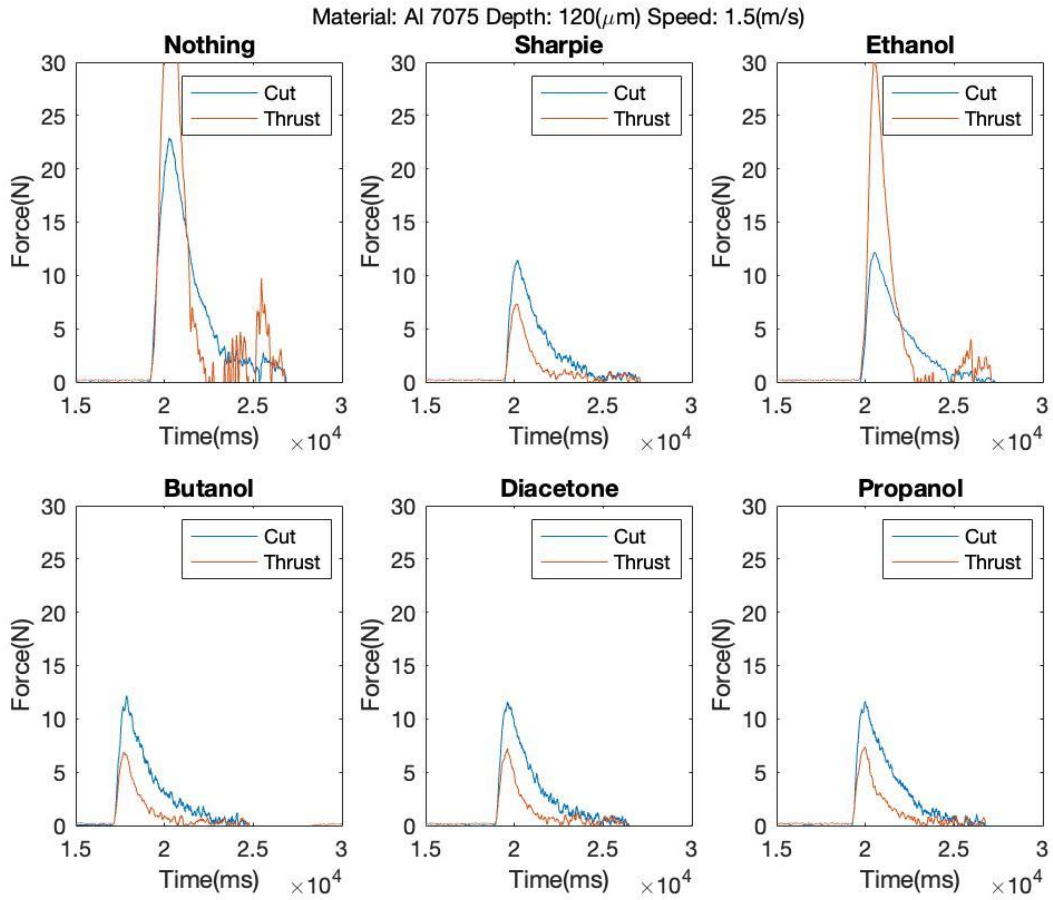

Figure 6-5: Cut and Thrust forces plotted for 7075 cut at a speed of 1.5 m/s and depth of 120µm for each lubricant type.

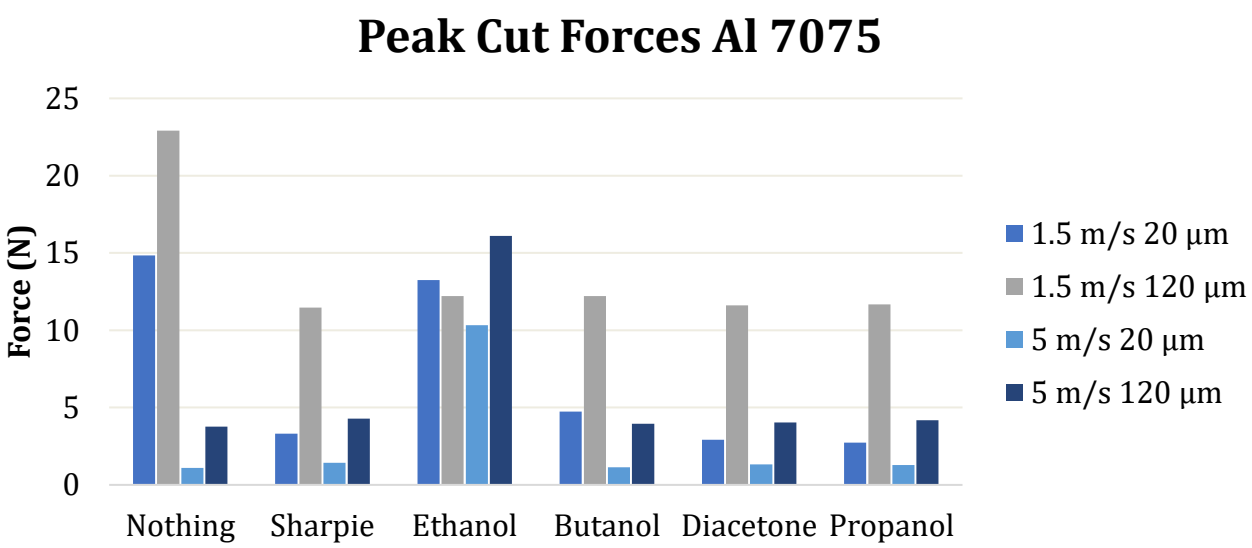

Figure 6-6: Cut forces measured for Al 7075 for all lubrications and cutting parameters.

6.3.3 **Al 1100**

Aluminum alloy 1100 is more difficult to machine when compared to 6061 and 7075. The depth of cut and speed were run at 20/50 µm at 3.5/5 m/s. The results had a much larger variation in findings due to inconsistent chip formation. The cutting and thrust force measured at a cut depth of 50 µm and speed of 5 m/s is plotted in Figure 6-7. Visual inspection of the samples shows limited chip formation and damage to the surface using the current cutting parameters. An image of the surface following cutting is shown in Figure 6-8 where material It is difficult to obtain a consistent cut force across the surface of the aluminum 1100 and the decrease in forces is not consistent with the other two alloys. The material seems to buildup and push across the surface, rather than form consistent chips using the current setup. Additional testing can incorporate the effects of rake angle and chip breaker tool inserts that may help improve the machinability of alloy 1100.

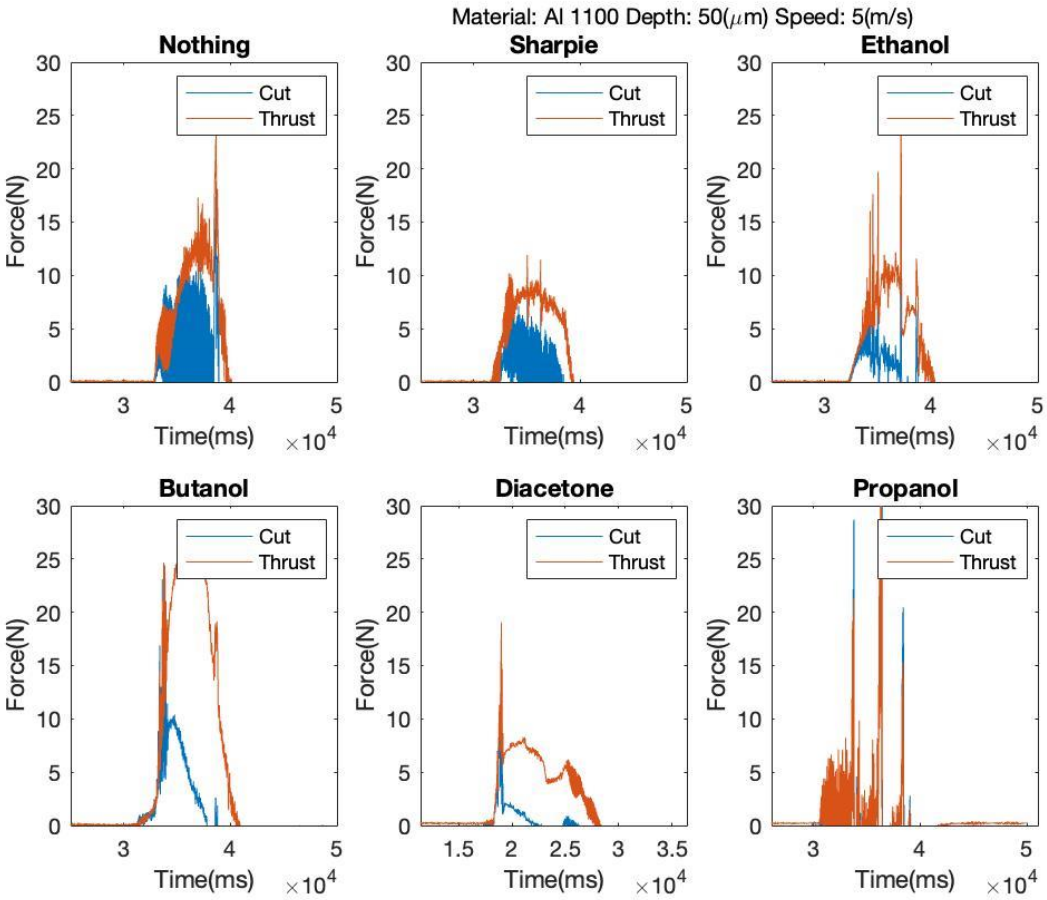

Figure 6-7: Cut and Thrust forces plotted for 1100 cut at a speed of 5 m/s and depth of 50μm for each lubricant type.

Figure 6-8: Cut edge of the aluminum alloy 1100 showing rough surface and built up material at the edge of the disc.

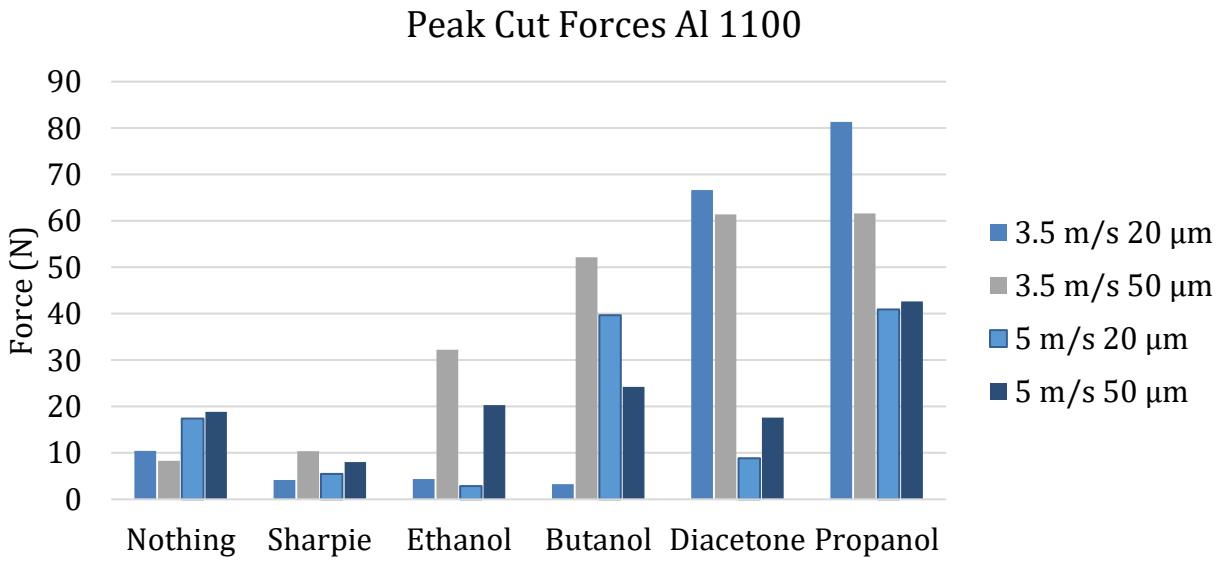

Figure 6-9: Cut forces measured for Al 1100 for all lubrications and cutting parameters.

6.3.4 **Comparing Alloys**

The forces measured for alloys 6061 and 7075 can be compared to see how each Sharpie™ constituent affects the alloys differently. The cut force values for the two alloys at a cut speed of 5 m/s and 120 µm depth are plotted in Figure 6-10. The forces are relatively similar for both alloys

except for the drastic rise measured for ethanol on alloy 7075. Generally, these two alloys preform similarly [8], as expected, and will be used in the future to test the surface roughness created by each lubricant.

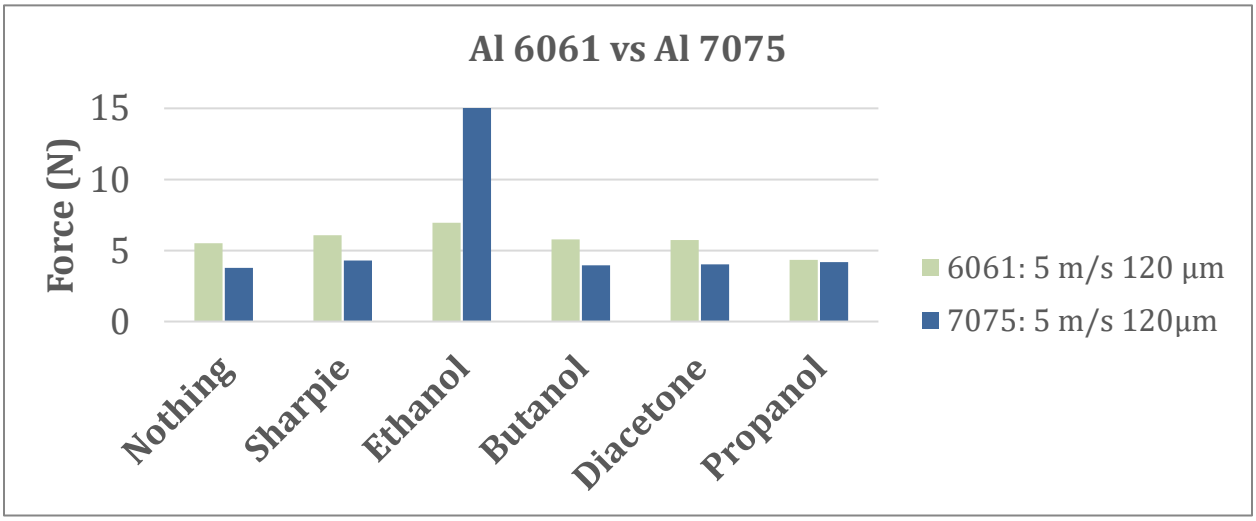

Figure 6-10: Comparison between cut forces for aluminum alloys 6061 and 7075.

6.4 FUTURE WORK

The effects of the lubricants can be further investigated using surface roughness measurements following machining. The next steps plan to use a handheld surface roughness tester to measure the OD of the discs following turning. The profilometer will allow for direct measurement of surface roughness following machining and correlate improvements to the measured tool force. Additional lubricants and application methods are expected to be explored on similar alloys.

6.5 CONCLUSION

For Al 1100:
There remained multiple difficulties in machining the aluminum 1100 alloy. The sharpie showed a slight decrease in the cutting forces while each individual constituent varied in its measured Rehbinder effect. Sharpie showed the lowest measured forces followed by ethanol and butanol for low depth of cut. Further testing is required to confirm the increased force measurements of alloy 1100 as improvements should be made to the sample setup in order to improve chipping action.

For Al 6061:
In Al 6061, sharpie ink gave the lowest forces behavior, while multiple lubricants matched the sharpie effect based on the cutting conditions. Ethanol showed very similar cutting force behavior to dry cutting for all cutting parameters. Therefore, performing a dry cut is cheaper than using ethanol as a coolant/treatment for Al 6061. At 5 m/s and (120 & 20) μm all coolants gave an

identical cutting forces behavior. This tells us at high spindle speed, none of the coolants has any effect on the cutting forces behavior. At 1.5 m/s and 120 μm, diacetone is giving the closest behavior of the sharpie effect, where it decreased the cutting forces by 60% compared to the dry cutting.

For Al 7075:

At high spindle speed, performing a dry cut is better than using Ethanol as a coolant/treatment for Al 7075. Ethanol was found to increase the cutting forces instead of decreasing it. At a (5 m/s) & (120 and 20) $\boldsymbol{\mu m}$, all coolants are giving the sharpie behavior expect for ethanol, where it increase the cutting forces instead of decreasing it. At a (1.5 m/s) & (120 $\boldsymbol{\mu m}$): Butanol, Diacetone, and Propanol give the closest behavior of Sharpie at high DOC.

REFERENCES

1. Tai BL, Dasch JM, Shih AJ. EVALUATION AND COMPARISON OF LUBRICANT PROPERTIES IN MINIMUM QUANTITY LUBRICATION MACHINING. DOI: 10.1080/10910344.2011.620910.
2. Yeung H, Viswanathan K, Compton WD, et al. Sinuous flow in metals. *Proc Natl Acad Sci U S A* 2015; 112: 9828–9832.
3. Udupa A, Viswanathan K, Davis JM, et al. A Mechanochemical Route to Cutting Highly Strain-Hardening Metals. *Tribol Lett* 2019; 67: 4.
4. Udupa A, Viswanathan K, Saei M, et al. Material-Independent Mechanochemical Effect in the Deformation of Highly-Strain-Hardening Metals. *Phys Rev Appl* 2018; 10: 14009.
5. Biermann D, Blum H, Iovkov I, et al. Modelling, Simulation and Compensation of Thermomechanically Induced Deviations in Deep-Hole Drilling with Minimum Quantity Lubrication. 2018, pp. 181–218.
6. Cui X, Zhao J, Zhou Y. Comparison of tool life and surface roughness with MQL, flood cooling, and dry cutting conditions with P20 and D2 steel Related content Tool Life Prediction for Ceramic Tools in Intermittent Turning of Hardened Steel Based on Damage Evolution Model. DOI: 10.1088/1757-899X/244/1/012006.
7. Najiha MS, Rahman MM, Kadirgama K. Machining performance of aluminum alloy 6061-T6 on surface finish using minimum quantity lubrication. *Int J Automot Mech Eng* 2015; 11: 2699–2712.
8. Khettabi R, Nouioua M, Djebara A, et al. Effect of MQL and dry processes on the particle emission and part quality during milling of aluminum alloys. *Int J Adv Manuf Technol* 2017; 92: 2593–2598.

Appendix

Table 6-2: Maximum cutting and thrust force for the 6061 aluminum alloy.

6061		Nothing	Sharpie	Ethanol	Butanol	Diacetone	Propanol
1.5 m/s, 20µm	**Cut (N)**	10.05	5.06	9.73	5.44	5.06	5.87
	Thrust (N)	11.19	5.96	11.56	8.16	7.27	9.40
1.5 m/s, 120µm	**Cut (N)**	19.00	18.03	20.09	20.62	13.62	14.36
	Thrust (N)	19.88	18.11	21.91	22.74	20.33	19.14
5 m/s, 20µm	**Cut (N)**	2.00	1.80	3.45	1.82	1.98	1.35
	Thrust (N)	2.58	2.57	5.89	2.70	2.77	2.50
5 m/s, 120µm	**Cut (N)**	5.50	6.08	6.96	5.78	5.73	4.33
	Thrust (N)	5.87	6.99	9.03	6.70	6.20	6.59

Table 6-3: Maximum cutting and thrust force for the 7075 aluminum alloy.

7075		Nothing	Sharpie	Ethanol	Butanol	Diacetone	Propanol
1.5 m/s, 20µm	**Cut (N)**	14.85	3.31	13.24	4.75	2.92	2.73
	Thrust (N)	36.66	4.31	33.21	3.12	3.15	3.42
1.5 m/s, 120µm	**Cut (N)**	22.91	11.46	12.21	12.21	11.61	11.67
	Thrust (N)	41.74	7.36	30.05	6.87	7.22	7.37
5 m/s, 20µm	**Cut (N)**	1.09	1.42	10.33	1.13	1.33	1.29
	Thrust (N)	1.84	2.27	24.28	1.61	1.93	1.91
5 m/s, 120µm	**Cut (N)**	3.77	4.29	16.11	3.96	4.03	4.19
	Thrust (N)	3.21	3.98	33.00	3.02	3.18	3.60

Table 6-4: Maximum cutting and thrust force for the 1100 aluminum alloy.

1100		Nothing	Sharpie	Ethanol	Butanol	Diacetone	Propanol
3.5 m/s, 20µm	**Cut (N)**	10.45	4.14	4.40	3.30	66.64	81.31
	Thrust (N)	11.85	8.39	7.26	4.74	59.72	63.16
3.5 m/s, 50µm	**Cut (N)**	8.29	10.35	32.24	52.16	61.42	61.64
	Thrust (N)	12.29	10.30	41.97	98.78	72.36	53.21

5 m/s, 20µm	**Cut (N)** **Thrust (N)**	17.42 16.92	5.48 8.31	2.83 5.11	39.67 44.91	8.84 8.55	40.91 31.52
5 m/s, 50µm	**Cut (N)** **Thrust (N)**	18.83 23.91	8.01 11.93	20.29 26.63	24.22 26.29	17.64 19.06	42.67 31.34

7 Mechanical and Electrical Properties of Single Crystal Silicon under External Electric Fields using Nanoindentation

Anthony Wong
Research Associate, Precision Engineering Consortium
Dr. Mark Pankow
Director of the PEC
Assistant Professor
Department of Mechanical and Aerospace Engineering

ABSTRACT

Silicon is widely used for electronics and modern day technology. Phase changes within the silicon structure can reduce machining forces and reduce material springback for electronics manufacturing. Single crystal silicon was tested under electrical contact nanoindentation at voltages between -10 and 10 V. The modulus and hardness of the silicon is measured during indentation and the effects of the voltage is used to determine potential phase changes in the single crystal silicon wafer. Large negative voltages have been shown to increase the reduced modulus of the silicon. The external electric field was found to have no effect on the hardness. Future work can focus on measuring the topography of the indented regions and resistivity while also exploring other materials.

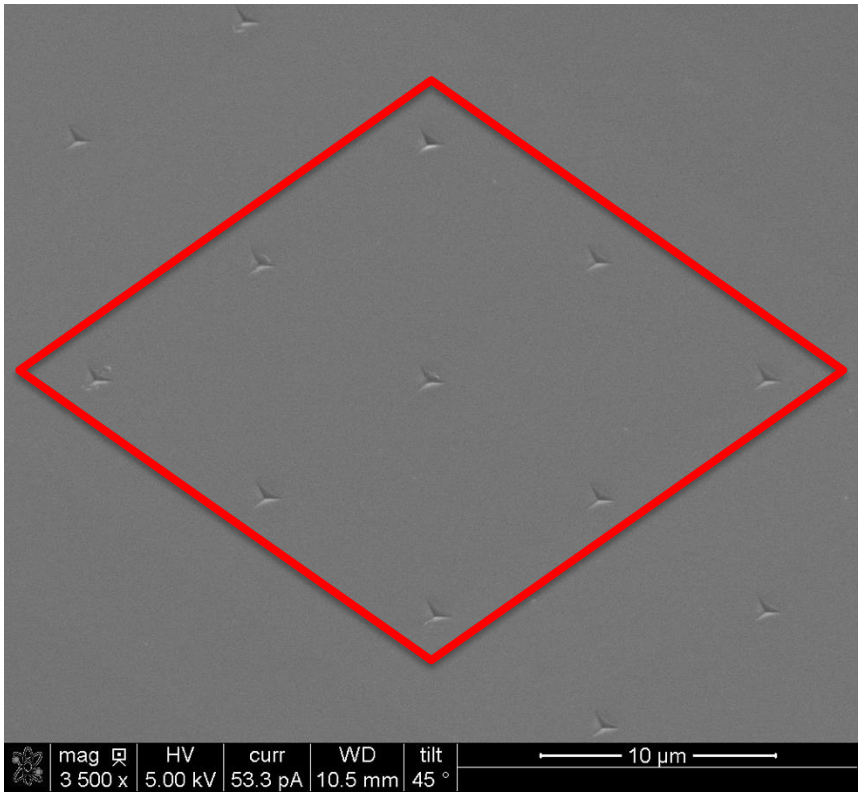

7.1 BACKGROUND

Silicon is an important material in modern society and has a significant role in electronics. Most electronics manufacturing is focused on lithography processes. However, deformation processing may also be useful for other purposes such as silicon molds or optics.

Silicon has historically been viewed as a brittle material. It inherently shows little plasticity and can only handle small strains to failure, 0.3-0.5%. Under nanoscale deformations Silicon is known to change phases under high hydrostatic pressure [1, 2]. At 0-11 GPa, Si is stable in a Si-I (fcc) phase. At 11-15 GPa Si-II forms, a ductile, body-centered tetragonal phase, also known as β-Sn. Si-II will also form at lower pressures when under shear stress. For comparison, Si is reported to have a compressive strength of 120 MPa. This transformation to Si-II is irreversible, and the material will not return to the Si-I phase. Upon unloading, the Si-II phase is unstable and forms amorphous silicon, Si-III or Si-XII phases. The particular phase the silicon transforms into is dependent on the load and unloading rate. This high pressure phase transformation (HPPT) from Si-I to Si-II has been investigated by applying pressure through diamond anvil cells or nanoindentation.

Many researchers have used molecular dynamics models to further understand of the phase change during indentation. Molecular dynamics simulations have shown that for the same indentation depth, a spherical indenter transforms a larger volume of material than a Berkovich (pyramidal) tip while the distribution of Si-III and Si-XII in the unloaded condition remains similar [3].

In scratch tests, the formation of metallic Si-II is thought to be critical for the ductile response that is observed [4]. This phase change and the ductile transition in single point diamond turning of Si has been extensively studied [5-8] as well.

The various lattice structures can be identified through Raman spectroscopy as well as selective area diffraction in cross-sectional transmission electron microscopy. More recently, the change in electrical measurements during nanoindentation has been used to identify the phases formed in-situ [9, 10]. Figure 1a shows a schematic of the nanoindentation experimental apparatus. A voltage is applied across the conductive diamond indenter tip and stage. During indentation, the voltage is swept from -8V to 8V and the resulting current is measured. Figure 2 shows an example of the data collected in this process. The resistivity of the system is calculated by applying a linear fit to the data. The resistance of the various phases of Si are different, so changes in the resistivity are interpreted as changes in the phases under the nanoindentation tip. Bruker has commercialized this experimental setup as the NanoECR module (Electrical Contact Resistance).

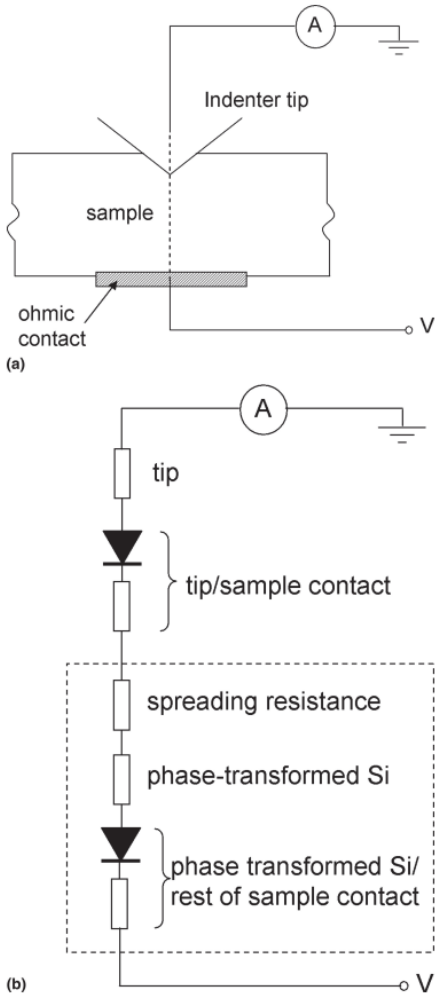

Figure 7-1. (a) Schematic of the electrical contact in a nanoindentation. (b) Circuit diagram of the equivalent circuit [9].

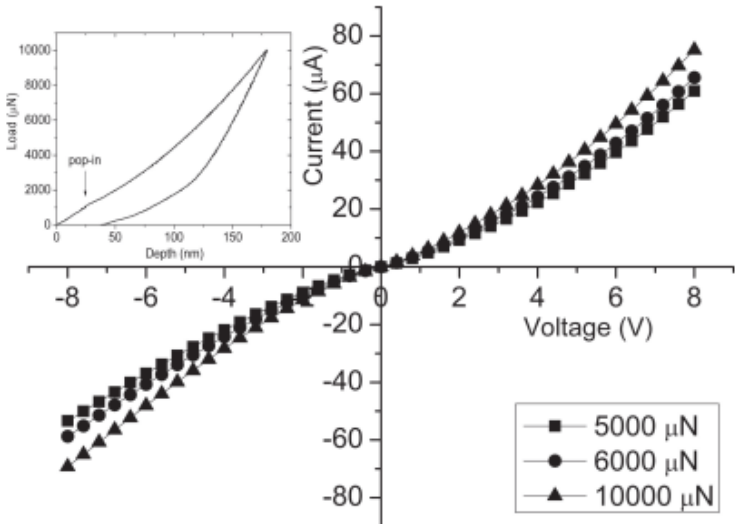

Figure 7-2. I-V curve for an indentation in Si. Load versus depth is shown inset [9].

Other researchers used the NanoECR to investigate the properties of phosphor-doped nano-silicon films. These researchers applied different voltages while indenting silicon and measured both the hardness and elastic modulus and found that they vary with the applied voltage. The results are shown in Figure 3. While the trend is not very clear, the authors speculate that the external electric field induces a rearrangement of the atoms and changes the tribological properties [11].

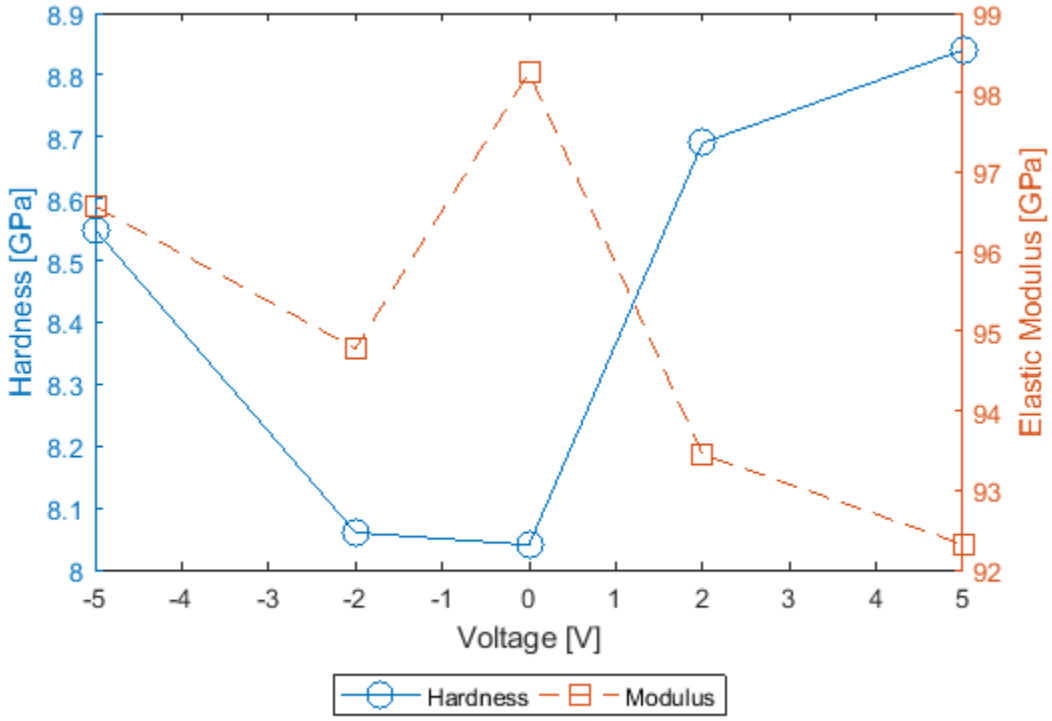

Figure 7-3. Hardness and Elastic Modulus of Si as a function of applied voltage [11]

The same researchers published a study of an alloy of Germanium, Antimony and Tellurium (GST). In this work, they applied a voltage through the NanoECR module during nanoindentation of $GeSb_2Te_4$. The resulting load displacement curves are shown in Figure 4. While the curves for -6V, -5V, and +8V look very similar, the curves for -7V and -8V are significantly different. The authors attribute this change to an external voltage past a critical value driving a phase change in the material [12].

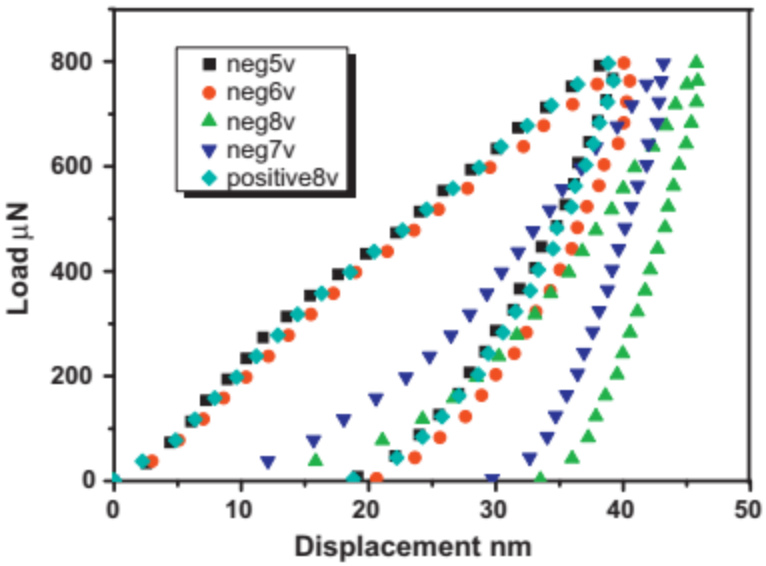

Figure 7-4. Load displacement curves for nanoindentation of $GeSb_2Te_4$ at with an external electrical field [12]

This work investigates whether or not there is a critical voltage that changes the nanoindentation properties of single crystal Si similar to $GeSb_2Te_4$. While there is some indication that the properties of silicon change with voltage as shown in Figure 3, the voltage levels were limited and a more thorough investigation with a NanoECR module may show a critical voltage. Such a phenomenon could facilitate reduced springback, improved plasticity, or reduced forces in tooling in a deformation process.

7.2 EXPERIMENTAL SETUP

A 4 inch silicon wafer sample was purchased from SPI Supplies (PN 4137SC-AB). The P-type silicon has a <100> orientation and is precut into 5 x 7 mm pieces. The vendor advertises the wafer to be 460-530 µm thick with a 2nm polished surface. Figure 6 shows an image of the wafer as received from the vendor.

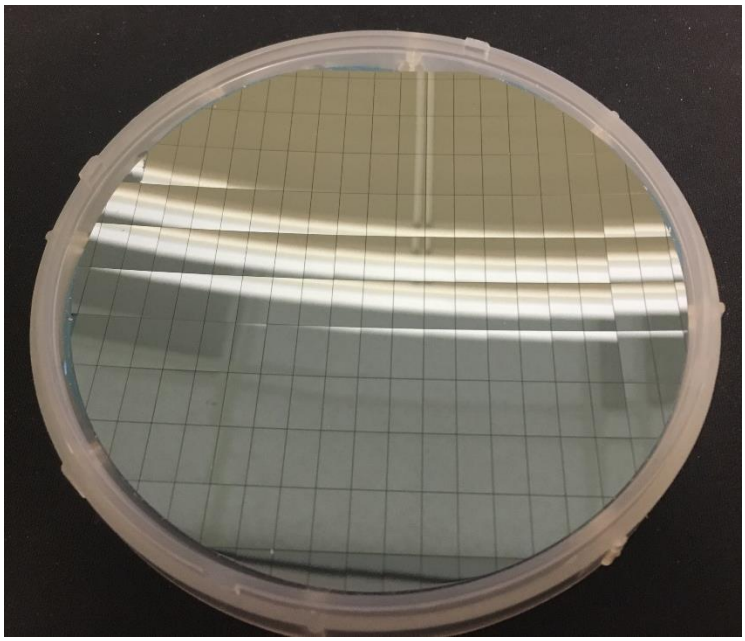

Figure 7-5. Silicon wafer sample

A sample was cleaned by ultrasonicating in methanol and drying with compressed Nitrogen gas. The sample was adhered with silver paint to the conductive plate of a NanoECR module installed on a Bruker Hysitron TI850.

The nanoindenter was programmed to conduct indents with a 10 mN max load. The loading time was 30 s followed by a 30 s hold time and a 30 s unloading time. A plot of a representative load function is shown in Figure 6.

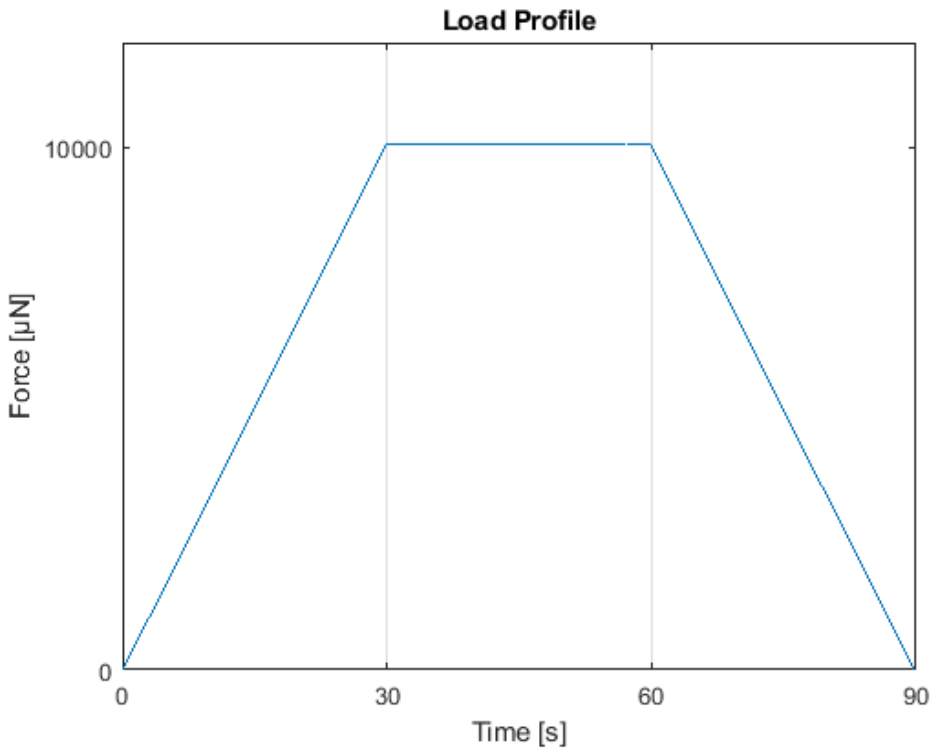

Figure 7-6. Loading function

A standard Berkovich nanoindentation tip was used for all indents. A constant voltage was applied during the indentation process. Voltages from -10 V to 10 V were applied in 2 V increments. Also -0.25, -0.1, 0.1 and 0.25 V were applied as well to investigated effect of small applied external electric fields. For each voltage setting nine indents were programmed to be spaced 10 μm apart in a 3 by 3 grid.

7.3 RESULTS AND DISCUSSION

The reduced modulus and hardness were calculated for each indent. Figure 7 shows the average reduced modulus of the nine indents for each voltage setting. The standard deviation is shown by the error bars. Similarly, Figure 8 shows the hardness results. From the plots, -10V has a clear effect on the reduced modulus, while voltage has little effect on hardness.

Hardness is based on the maximum depth of the indent. The limited effect on hardness suggests that the voltage is not changing the loading phase of the indent to allow the indenter to penetrate deeper into the silicon. As the reduced modulus is calculated from the unloading portion of the force-displacement curve, the voltage influence on reduced modulus suggests the voltage is influencing what the unstable Si-II transforms into upon unloading. These results also show that there is a critical voltage around -8-10 V at which the reduced modulus begins to change.

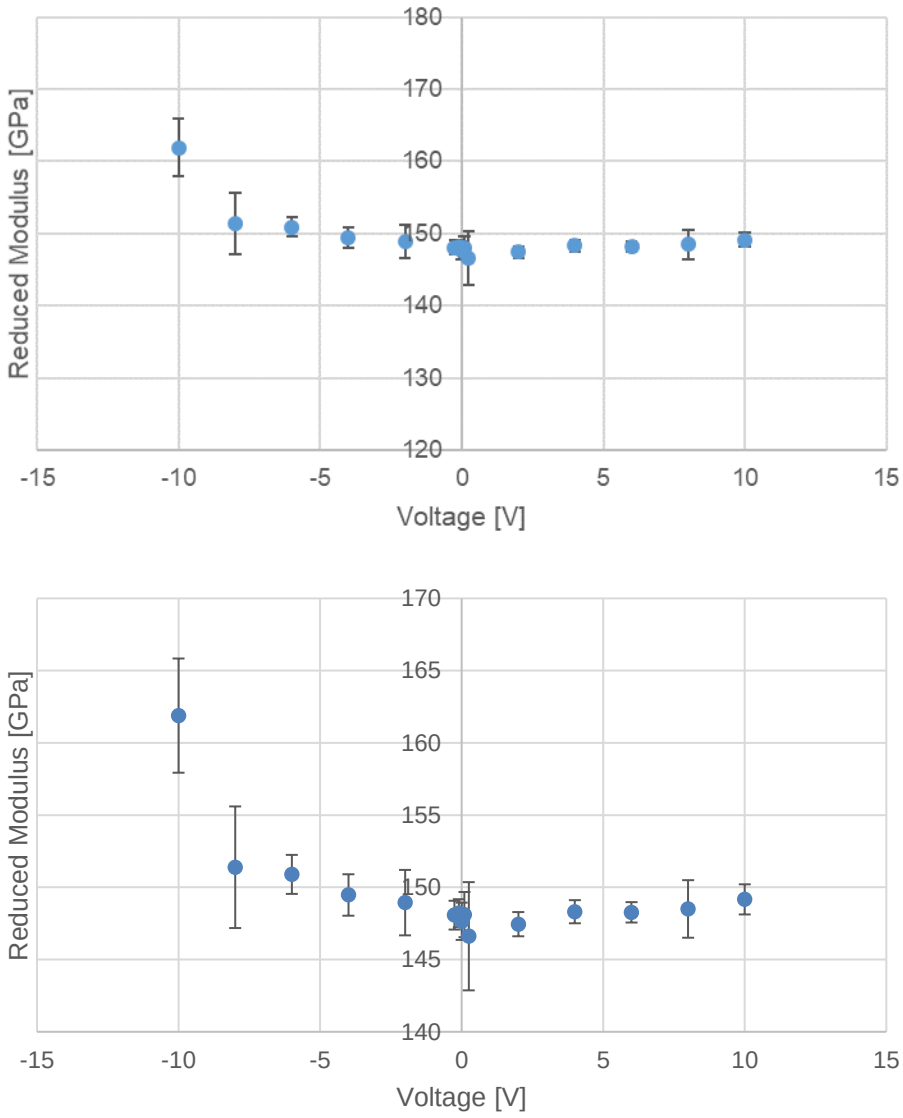

Figure 7-7. The effect of applied voltage on reduced modulus

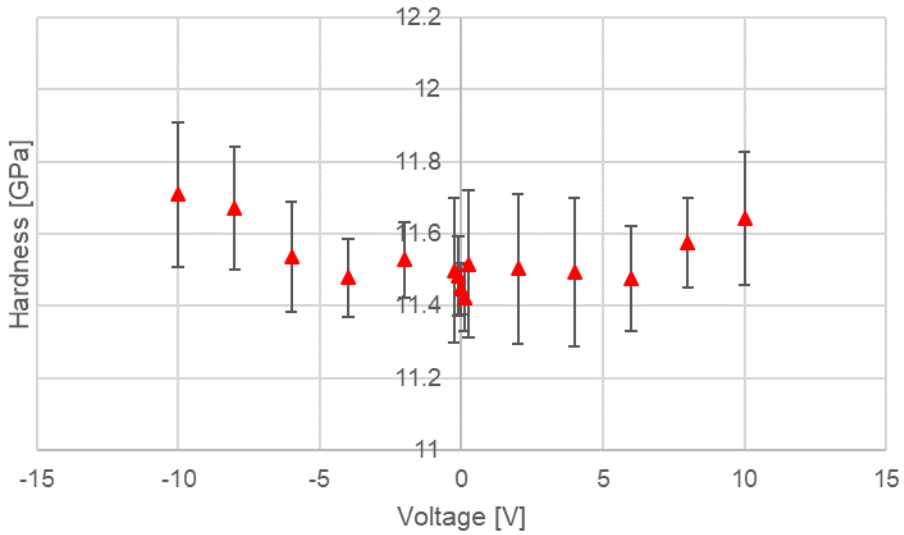

Figure 7-8. The effect of applied voltage on hardness

Figure 9 and Figure 10 shows the same data zoomed in around the origin. The original intention was to investigate whether or not the mere presence of an electric field caused any changes. These figures show that it is only the large negative voltage which has an effect.

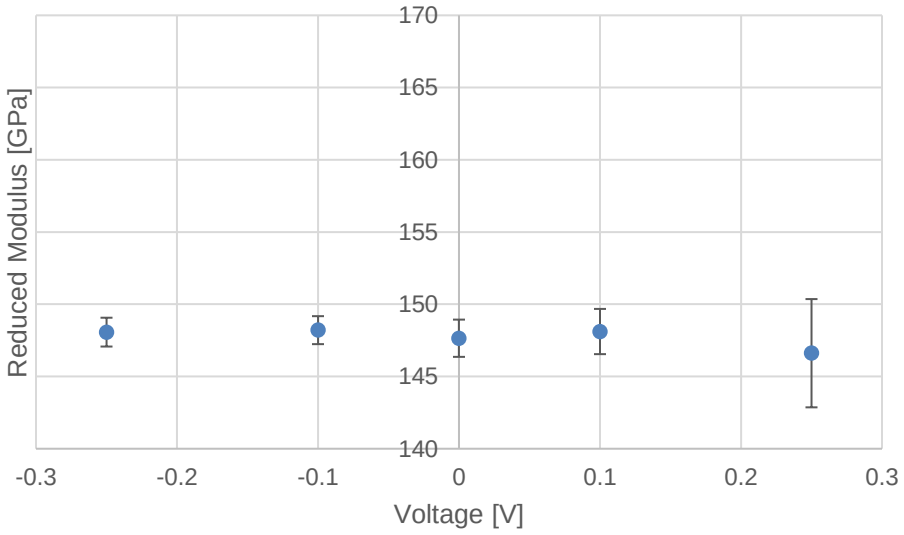

Figure 7-9. The effect of applied voltage on reduced modulus around 0 V

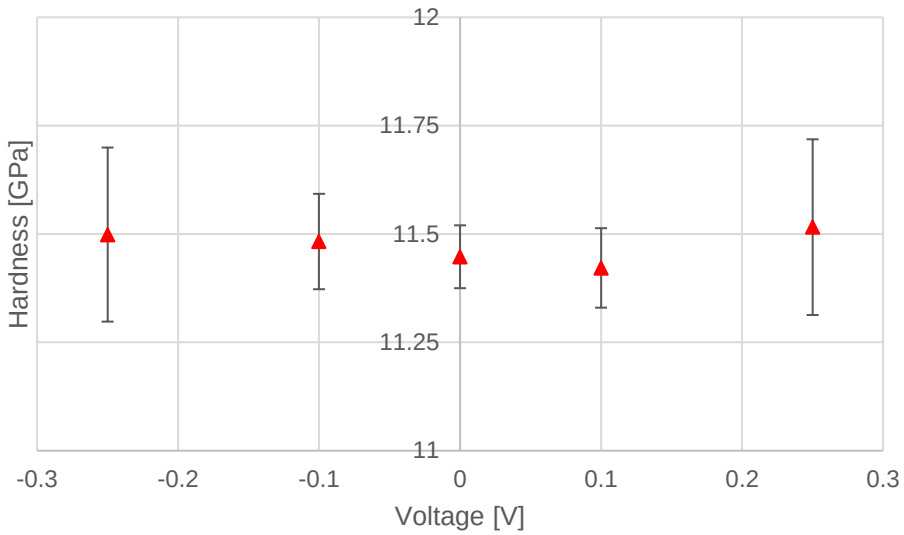

Figure 7-10. The effect of applied voltage on hardness around 0 V

The force-displacement curves are consistent with literature. Figure 11 shows a representative set of force-displacement curves. These plots are for a -10 V applied external electric field. Very little creep occurs during the hold time. Also, some indents, such as Indent 7 in Figure 11, show a distinct pop out event in which the depth changes with no reduction in force during the unloading curve. In literature these pop out events are thought to be related to a transformation from Si-II to Si-XII [2].

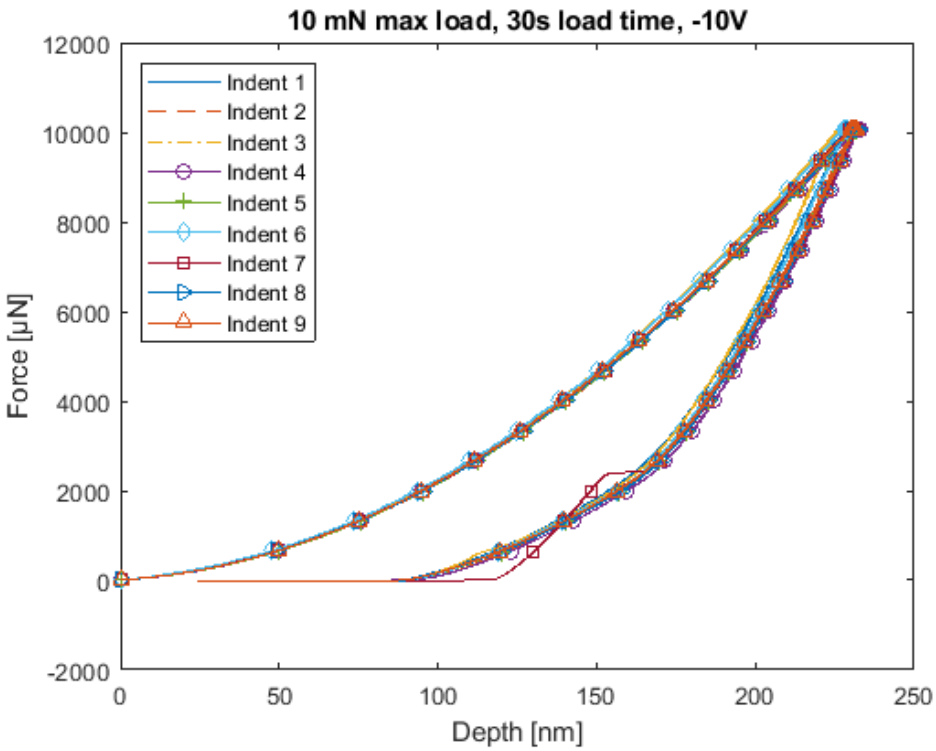

Figure 7-11. Representative force-displacement curves

The indents were also imaged with a scanning electron microscope (SEM). Figure 11, Figure 12, and Figure 13 show SEM images of the indents with -10, 0 and 10 V applied. It is notable that occasionally extruded material similar to machining chips appears at the edges of the indents. Figure 14 shows a close up of the bottom indent in Figure 11. It is unknown why this appears on some indents but not others. This could be the result of machine vibration during the indentation process, but there is no obvious difference in the force-displacement data to indicate that the indenter tip is touching a different surface. Aside from the chips, qualitatively there is no obvious difference between the indents with different voltages applied.

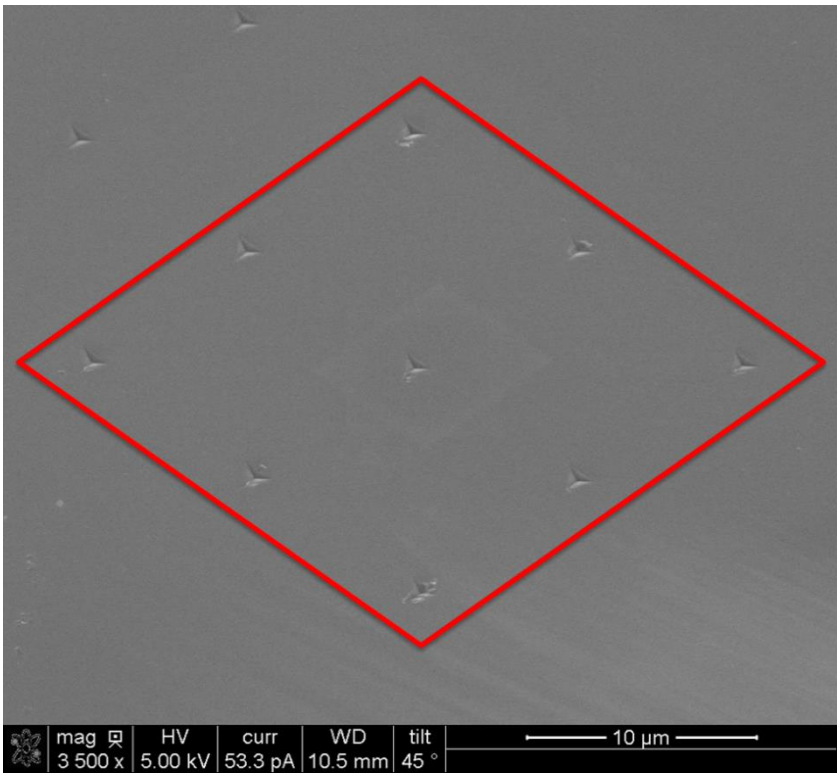

Figure 7-12. SEM image of indents with -10 V applied (highlighted in the red box)

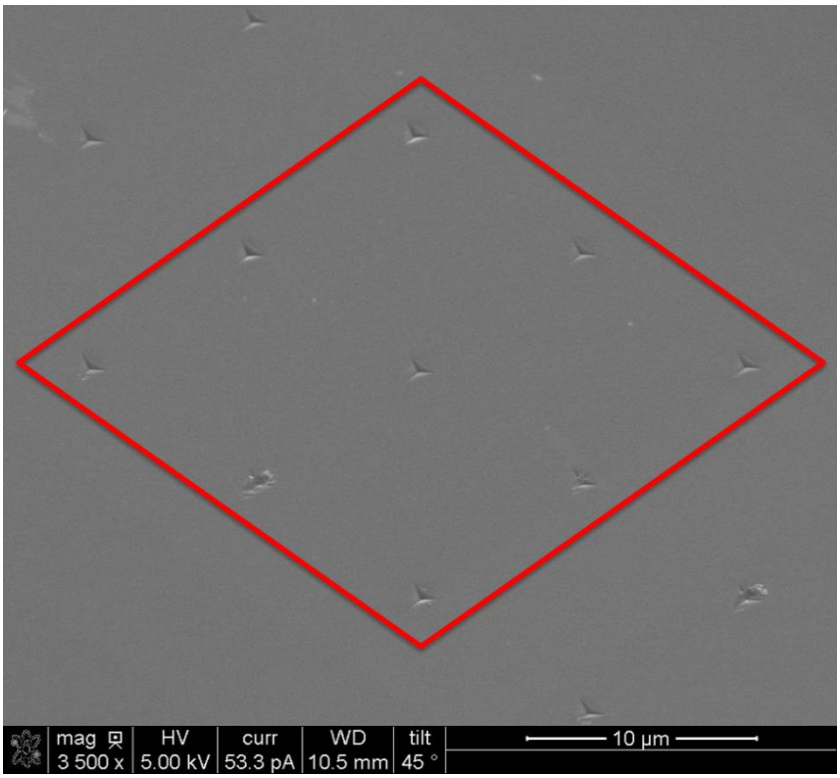

Figure 7-13. SEM image of indents with 0 V applied (highlighted in the red box)

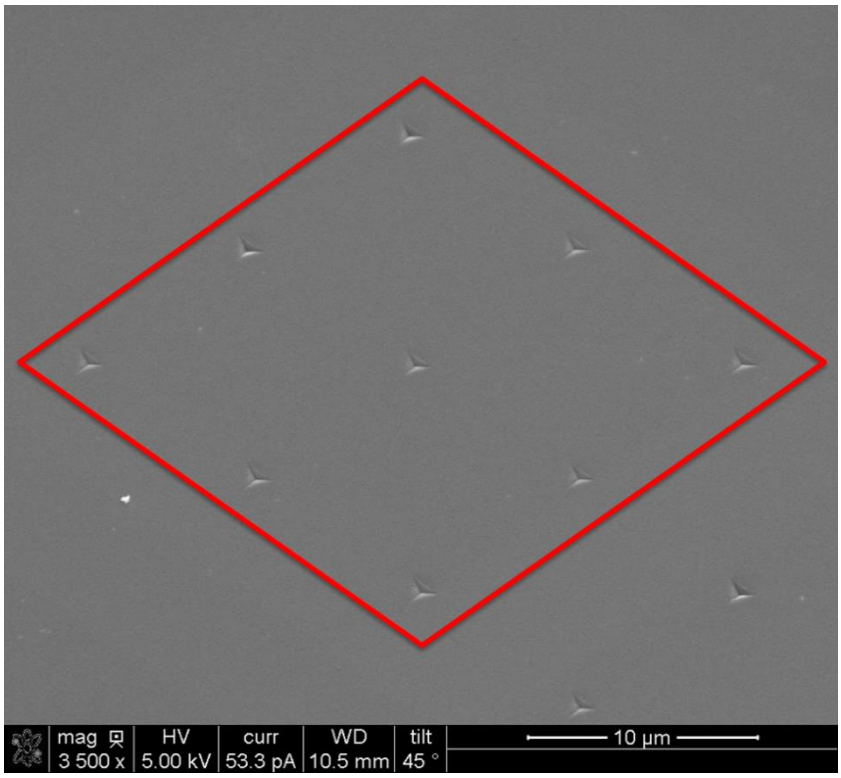

Figure 7-14. SEM image of indents with 10 V applied (highlighted in the red box)

Figure 7-15. Close up image of an indent with -10 V applied

The sign of the applied voltage had a significant effect on the current during the indentations. Figure 16 shows the current during the indents with 10 V applied, while Figure 17 shows the data for the indents with -10 V applied. Figure 18 shows a simpler comparison of Indent 1 from figures Figure 16 and Figure 17 on the same axes. Under both voltage settings the current increases in a similar manner during the loading phase on the indentation. However, the peak current is lower for the positive voltage. There is also much more variability in the peak current under the negative voltage. During the hold, the current under negative voltage drops and then remains steady for the rest of the hold. This behavior is not seen under positive voltages. This behavior in the current during the hold is consistent for all the voltage levels as seen in Figure 19 and Figure 20. During the unloading phase of the indent, the current decreases significantly faster under the negative voltage. Ruffel conducted a similar experiment with 1 and -1 V applied and reported a similar phenomenon while unloading the indenter [10]. These differences in current indicate that different phases with different resistivity are being developed during the indentation.

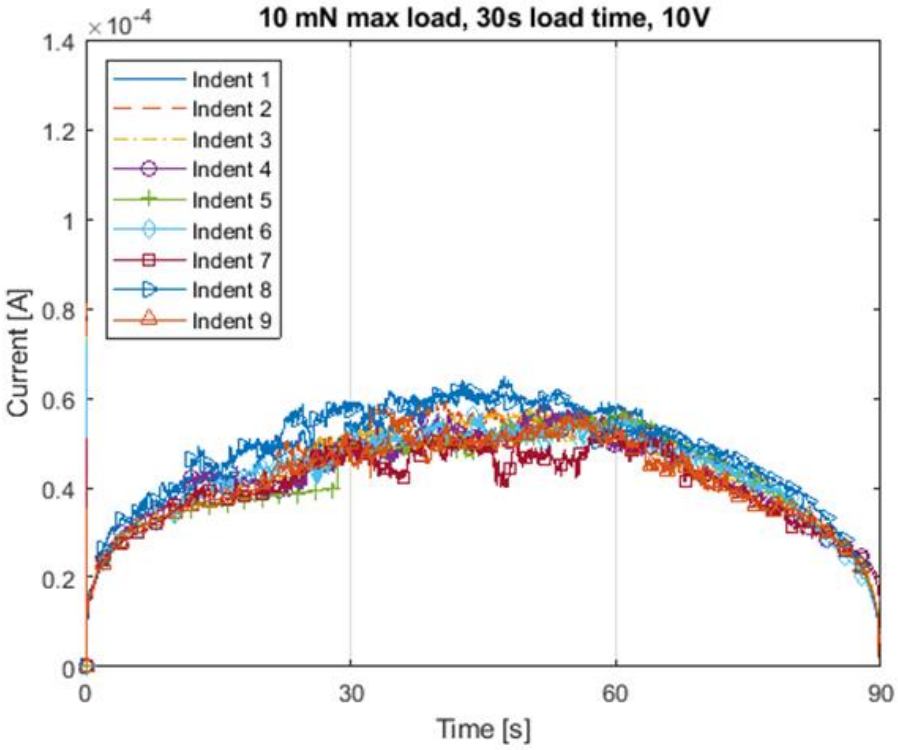

Figure 7-16. Current plots during indentation with 10 V

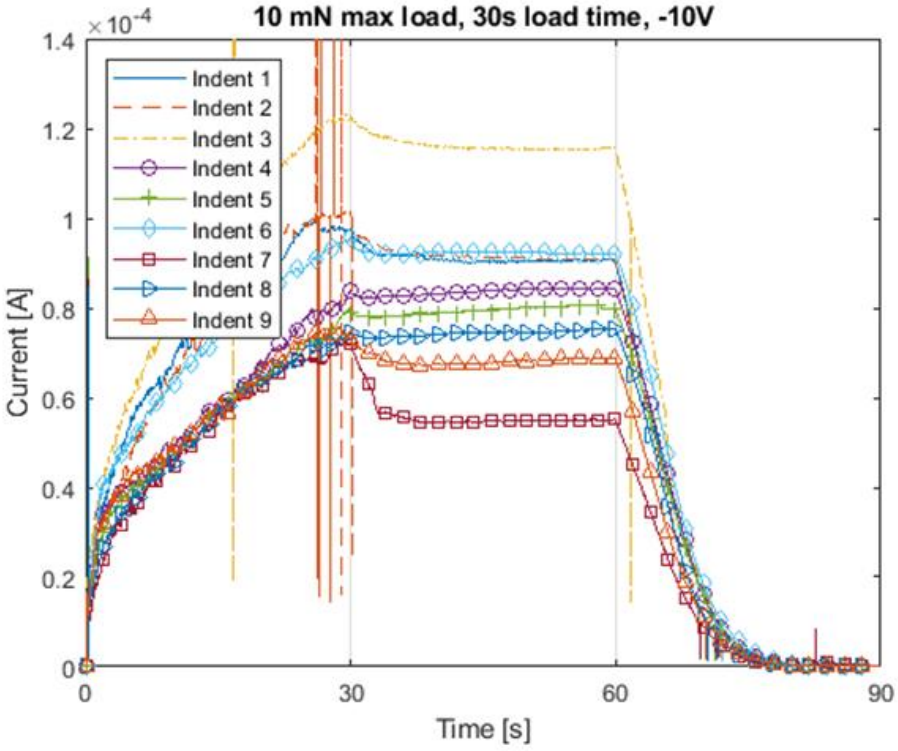

Figure 7-17. Current plots during indentation with -10 V

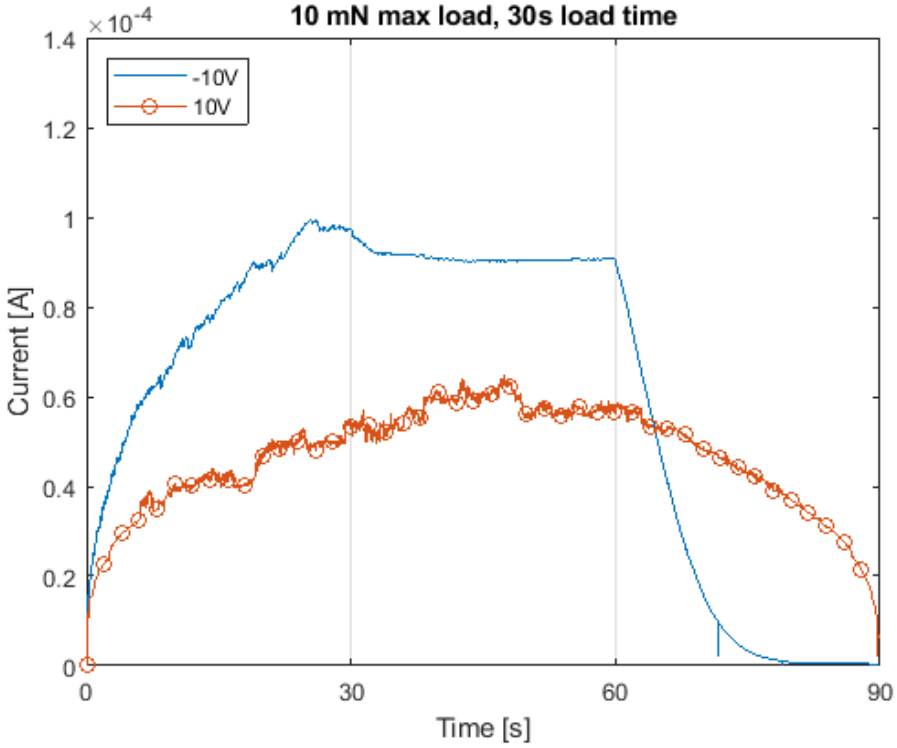

Figure 7-18. Comparison of current with -10 and 10 V

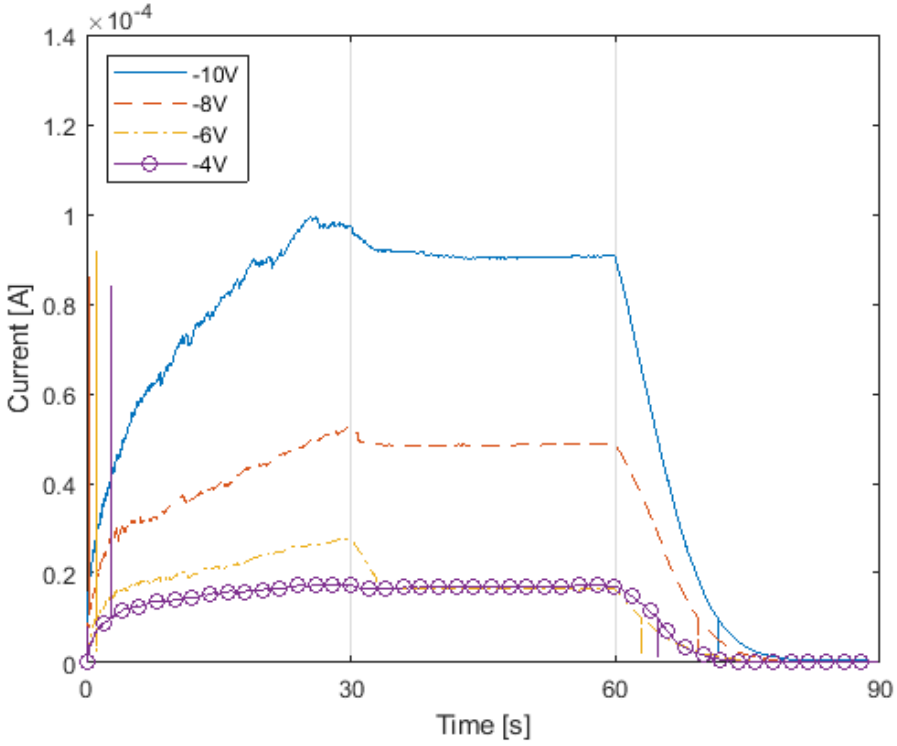

Figure 7-19. Comparison of current with negative voltages

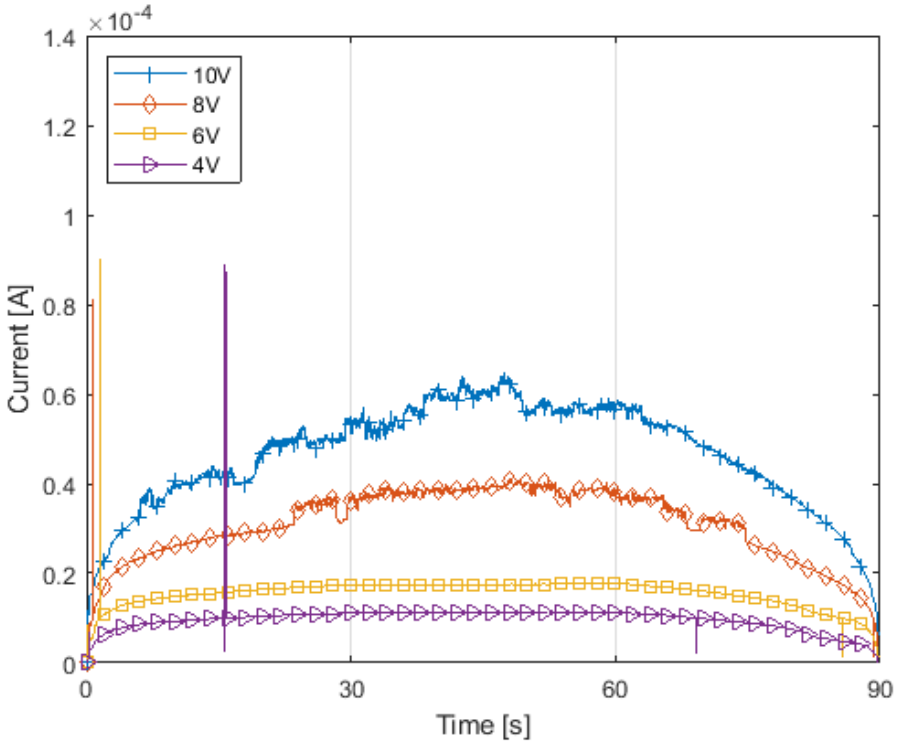

Figure 7-20. Comparison of current with positive voltages

7.4 CONCLUSION

External electric fields have been applied to nanoindents in single crystal silicon. Large negative voltages have been shown to increase the reduced modulus of the silicon. The external electric field has no effect on the hardness. The sign of the voltage leads to very different behaviors in the current as well.

We have shown that the mechanical properties of silicon can be manipulated by applying an external electric field. The differences in electrical response during indentation implies that the external electric field is altering the phases being developed during the high pressure phase transformation as well as during the unloading.

Possible future investigations include measuring the indented surfaces and comparing the resulting surface topographies. Cross sectional transmission electron microscopy can be used to examine the phases in the indented material. The voltage could be swept at various points during the indent to characterize the resistivity of the silicon during the indentation process. Finally, similar materials could be investigated such as Germanium.

REFERENCES

[1] M.M. Khayyat, G.K. Banini, D.G. Hasko and M.M. Chaudhri, "Raman microscopy investigations of structural phase transformations in crystalline and amorphous silicon due to indentation with a Vickers diamond at room temperature and at 77 K," Journal of Physics D: Applied Physics, vol. 36, pp. 1300-1307, Jun 7,. 2003.

[2] V. Domnich and Y. Gogotsi, "Phase transformations in silicon under contact loading," Reviews on Advanced Materials Science, vol. 3, 2002.

[3] Y. Lin, S. Jian, Y. Lai and P. Yang, "Molecular Dynamics Simulation of Nanoindentation-induced Mechanical Deformation and Phase Transformation in Monocrystalline Silicon," Nanoscale Res Lett, vol. 3, pp. 71-75, Feb. 2008.

[4] Y. Gogotsi, G. Zhou, S. Ku and S. Cetinkunt, "Raman microspectroscopy analysis of pressure-induced metallization in scratching of silicon," Semiconductor Science and Technology, vol. 16, pp. 345-352, May 1,. 2001.

[5] P.N. Blake and R.O. Scattergood, "Ductile-regime machining of germanium and silicon," Journal of the American Ceramic Society, vol. 73, pp. 949-957, Apr. 1990.

[6] J.C. Morris, D.L. Callahan, J. Kulik, J.A. Patten and R.O. Scattergood, "Origins of the ductile regime in single-point diamond turning of semiconductors," Journal of the American Ceramic Society, vol. 78, pp. 2015-2020, Aug. 1995.

[7] B.V. Tanikella, A.H. Somasekhar, A.T. Sowers, R.J. Nemanich and R.O. Scattergood, "Phase transformations during microcutting tests on silicon," Applied Physics Letters, vol. 69, pp. 2870-2872, Nov 4,. 1996.

[8] T.J. Randall, "Characterizing the ductile response of brittle semiconductor materials to dynamic contact processes," 2004.

[9] S. Ruffell, J.E. Bradby, J.S. Williams and O.L. Warren, "An in situ electrical measurement technique via a conducting diamond tip for nanoindentation in silicon," Journal of Materials Research, vol. 22, pp. 578-586, Mar 1,. 2007.

[10] S. Ruffell, J.E. Bradby, N. Fujisawa and J.S. Williams, "Identification of nanoindentation-induced phase changes in silicon by in situ electrical characterization," Apr 30,. 2007.

[11] G.G. Cheng, J.N. Ding, G.X. Xie, B. Kan, Z.Y. Ling and Z. Fan, "Mechanical and electrical properties of the phosphor-doped nano-silicon film under an external electric field," Surface and Interface Analysis, vol. 41, pp. 384-388, May. 2009.

[12] G. Cheng, Z. Zhang, J. Ding, Z. Ling and Y. Chen, "Mechanical and electrical properties of GeSb2Te4 film with external voltage applied," Applied Surface Science, vol. 285, pp. 532-537, Nov 15,. 2013.

8 Development of a Novel Monopolar and Bipolar Electrosurgical Forceps

Nehemiah MacDonald
Undergraduate Student
Dr. Mark Pankow
Director of the PEC
Assistant Professor
Department of Mechanical and Aerospace Engineering

Abstract

Electrosurgery devices can offer multi-use capabilities when paired with a surgical forceps design. Such a device can reduce surgical time by limiting the need to transfer between surgical tools. This project is set out to design, manufacture, and test a surgical forceps tool that can act as both a mono- and bipolar electrosurgery tool. Initial ideas were analyzed using a design matrix and with consultation with medical professionals. First steps have been taken to prototype and determine the next steps for material manufacturing and electronics. Future work will include manufacturing, wiring, and testing of the device followed by iterative improvements to the design.

8.1 **BACKGROUND**

Electrosurgery was introduced in the early 1900s and has become essential to modern surgery. The devices used to conduct electrosurgery are typically divided into two subcategories: monopolar and bipolar electrosurgery. The monopolar variety typically takes the form of a cautery pen which is a handheld medical device used to stop bleeding via heat conducted through the tip. The use of a cautery pen is classified as monopolar electrocautery because it directs heat and electricity to the surgical site through a single electrode. The direct electrical current channeled through this electrode can cut and/or cauterize blood vessels and tissue. The current does so by passing through living tissue to a return electrode in the form of a grounding plate that is placed on the patient. Heat is then created by the resistance of the tissue to the current. Monopolar electrosurgery can reach temperatures between 1400°F and 2000°F [1].

Figure 8-1. Covidien Valleylab monopolar electrosurgical pencil [2].

The second type of electrosurgery is bipolar electrosurgery which directs electric current interchangeably through a set of forceps with an electrode on each end of the forceps serving as the active and return electrode, eliminating the need for a grounding plate. When compared to monopolar electrosurgery, this form offers the user more precision. High frequency current of approximately 500,000Hz [3] is supplied to both types of devices through an electrosurgical unit (ESU) which is activated using either a foot pedal or buttons on the device.

Another necessary piece of equipment for surgeons are surgical forceps or scissors which are metal instruments used during surgical procedures to tweeze, clamp, and apply pressure. Surgical scissors have a variety of designs such as curved or straight blades and differing lengths that are adjusted to fit the specific needs of different surgeons. Many bipolar electrosurgical devices take the form of tweezer-like forceps that are able to grab tissue to cauterize.

Electrosurgery is involved in many surgeries, which are often costly and lengthy procedures. A part of this cost can be attributed to the time surgeons take to switch tools during a surgery [4,5]. The development of a device that combines the use of two or more tools would save time as doctors as they are not required to switch tools as often and improve the overall surgical efficiency.

A 2007 study found that each minute of unused operative time cost the University of Rochester Medical Center $60 [4]. As such, the purpose of this project is to propose a multi-use device that works simultaneously as a set of surgical forceps and an electrosurgery tool that could be used in a medical environment.

8.2 EXPERIMENTAL SETUP

In the early stages of this project, numerous design ideas for a product that could simultaneously function as both an electrosurgical device and surgical forceps were created. These designs were then evaluated using a matrix containing seven design criteria of varying weights. The criteria and weight (in parentheses) were as follows: could perform monopolar and bipolar cautery (5), weight (2), cost (2), temperature over time (5), sharpness (3), power requirements (4), ease of use (5). Following this evaluation, the highest rated ideas were presented to an endocrine surgeon at University of North Carolina Medical Center, after which the designs were edited to fit within the parameters given by the surgeon and evaluated using a second matrix. The criterion and weight (in parentheses) of the second matrix are as follows: insulating material used for the device handles (3), connecting method to ensure the instrument can handle monopolar and bipolar cautery (4), ergonomics of activation button/pedal (2), temperature over time (4), and manufacturability (3). The highest rated designs as determined by the second evaluation were made into 3D models that were again assessed by the endocrine surgeon. Further edits were then made to the designs that were more feasible for use by surgeons and carried through to the next stages of prototyping and manufacturing of a device.

8.3 RESULTS & DISCUSSION

Although a working prototype that can be used in surgery has not yet been created, an initial body (see figure 2) has been developed to use for the multi-use device following the second evaluation of design ideas and subsequent feedback from the consulted surgeon, which has led to many crucial realizations as well. To have a tool that can switch between both monopolar and bipolar electrosurgery, there must be one blade that is completely metal with an electrode on the tip that can be used for monopolar electrosurgery. The second blade will be ceramic to ensure it is insulated from the monopolar side of the device as the return electrode for the device will be a grounding plate when monopolar electrosurgery is being used. The ceramic blade will then have a small amount of exposed metal attached to the tip with another electrode that will allow bipolar electrosurgery to be used when the blades are squeezed together. Provided the blades are not squeezed together, this design will ensure the metal blade does not come into contact with the electrode on the opposing blade when monopolar electrosurgery is being used. Proposed methods for achieving such a design are a brazing solution, electrolysis metal plating, or “painting” a ceramic material onto metal. The next steps of this work are to investigate each method of incorporating a metal and ceramic blade while also developing the electronics necessary for electrosurgery function.

This project will take advantage of existing electronics in mono- and bipolar electrosurgery to integrate into this device. A monopolar electrosurgical pencil and a bipolar electrosurgical device

have each been purchased and much of the wiring from these devices such as the plugs for the Bovie machine will be used during the prototyping process. Integrating each of these electronics into one device with a singular activation system either using a foot pedal or buttons placed on the device itself continues to be investigated.

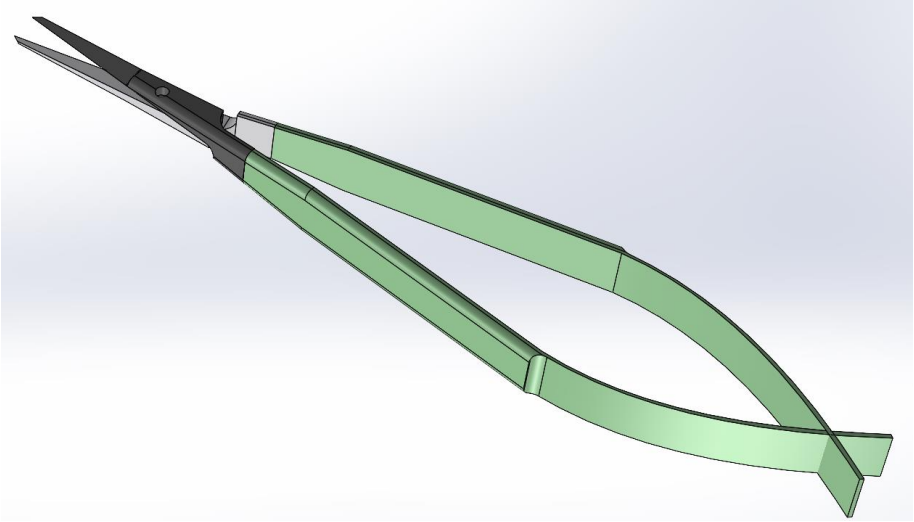

Figure 8-2. CAD Model for the initial design of the device's body with a metal & ceramic blade and plastic handles.

Figure 8-3. Blades of the 3D printed body for the device.

8.4 CONCLUSION AND FUTURE WORK

A multi-use device that can transition from electrosurgery to be used as surgical forceps will save surgeons and hospitals time and money. Initial designs have been modeled for the shell of such a device. The final designs have been settled upon by considering a weighted design matrix and input from medical professionals. Important considerations for the future of this project would be to determine the best method to simultaneously insulate one blade from the other while allowing an electric current to pass through the tips of both blades. Work must also be done to determine the most efficient process for printing a ceramic blade that meets the sharpness standards set for surgical scissors and has high thermal and electrical insulating properties. After establishing the best method for printing the ceramic material, the proposed methods for joining ceramic to metal will be tested to decide which method is the most feasible. In addition, further investigation needs to be done into how the device will be wired so that it can effectively switch between monopolar and bipolar electrosurgery.

REFERENCES

[1.] USA Medical and Surgical Supplies. (2020, April 22). 10 procedures that use a Medical Cautery Pen. Retrieved January 2021, from <https://www.usamedicalsurgical.com/blog/10-procedures-use-medical-cautery-pen/>

[2.] Medtronic. Electrosurgical pencils. Retrieved January 2021, from <https://www.medtronic.com/covidien/en-us/products/electrosurgical-instruments/pencils.html>

[3.] Cordero, Ismael. “Electrosurgical units - how they work and how to use them safely.” *Community eye health* vol. 28,89 (2015): 15-6.

[4.] Girotto JA, Koltz PF, Drugas G. Optimizing your operating room: Or, why large, traditional hospitals don’t work. *Int J Surg* 2010; 8: 359–367. https://doi.org/10.1016/j.ijsu.2010.05.002

[5.] Marsano, L. S., MD. (n.d.). *Principles of Electrocautery*. Lecture presented at University of Louisville. Retrieved from <https://louisville.edu/medicine/departments/medicine/divisions/gimedicine/physician-resources/lectures/procedures/electrocautery>

9 Deployable Structures

Greyson Hodges
Graduate Student
Dr. Mark Pankow
Director of the PEC
Assistant Professor
Mechanical and Aerospace Engineering

ABSTRACT

This report addresses the development of various deployable technologies for aerospace systems and their current status. There are two main research areas: Deployable booms with different mechanisms: both powered and unpowered, and Deployable Composite Origami. This work discusses the manufacturing and testing of each system. Both systems have or have ongoing zero-gravity flight demonstrations to understand their deployment characteristics in a relevant space environment. The Boom project has an ongoing collaboration with NASA Langley.

(a) deployed

(b) stowed

(c) fully deployed boom

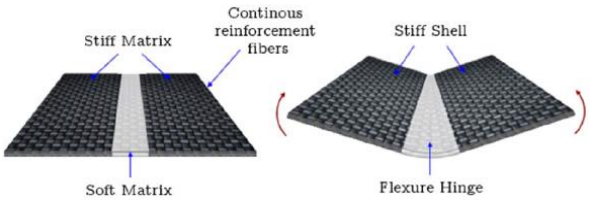

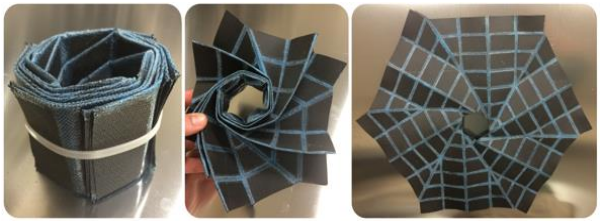

9.1 INTRODUCTION

Space structures are volumetrically limited by the cargo capacity of their launch vehicle. Satellites, antenna, and solar arrays that deploy to many times larger than their launch vehicle require complex packaging or secondary assembly once in orbit. Historically this has been solved by mechanical hinges or modular designs. For efficiency, it is advantageous to launch using the smallest possible cargo volume. Engineering research into structural packaging efficiencies and deployment methods has become crucial to send larger structures into and beyond orbit without relying on larger and larger launch vehicles.

Mechanical hinges are a costly method for deployable structures due to the increased number of high-precision moving parts and their associated mass. This mass also contributes to a dynamic challenge as it is often swung outward from the center of mass. Although mechanical performance and analytical predictions of metallic hinges are well understood there are two major drawbacks. First, they are relatively heavy when comparing strength to weight ratios with fiber reinforced composites. Second, they are thermally expansive and exhibit high deformations when exposed to a thermal gradient [1].

High strain composites (HSC) have been proposed as a light weight and thermally stable solution to replace metallic hinges. HSC are ultra-thin laminates cable of being deformed to a small radius of curvature. These thin fiber reinforced substrates allow coiling or folding for efficient storage of structures while providing the ability for low energy deployment through exploiting elastically stored strain energy. Many applications using HSC in deployable space structures have been proposed as solutions to deploy spacecraft optics, antenna, tension solar sails, or for creating heavy duty hinges [1, 2, 3, 4]. The first deployable structure investigated is a conformal tube mast (CTM) boom and its various release dynamics.

9.2 DEPLOYABLE CONFORMAL TUBE MAST (CTM) BOOMS

CTM booms suffer from weak interfaces which often lead to failure where the two halves of the boom come together. To increase the strength of the tab bond, a single cure cycle was investigated to simultaneously cure together the two halves in their closed form shape. A silicone plug matching the inside geometry of the whole boom would be used to manufacture the closed cross section. This plug was created by pouring a two-part silicone rubber into the cavity made between two negative molds, as shown in Figure 9-1.

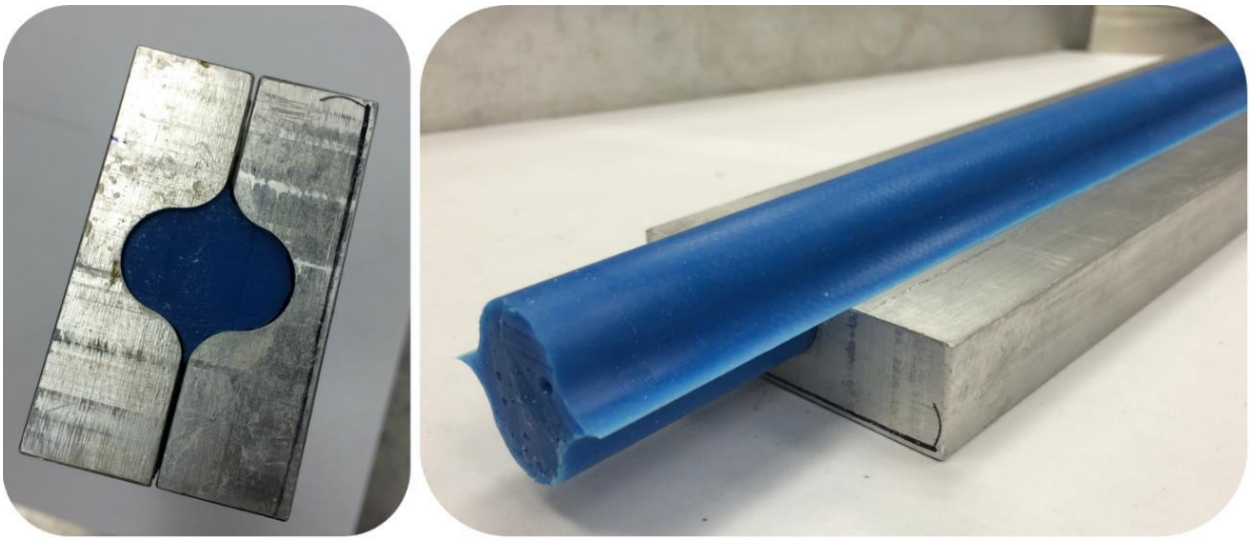

Figure 9-1 Silicone Mold Forming for Whole Boom Fabrication

The plug was then used to lay-up both sides of the boom simultaneously while the entire laminate was vacuum bagged, Figure 9-2.

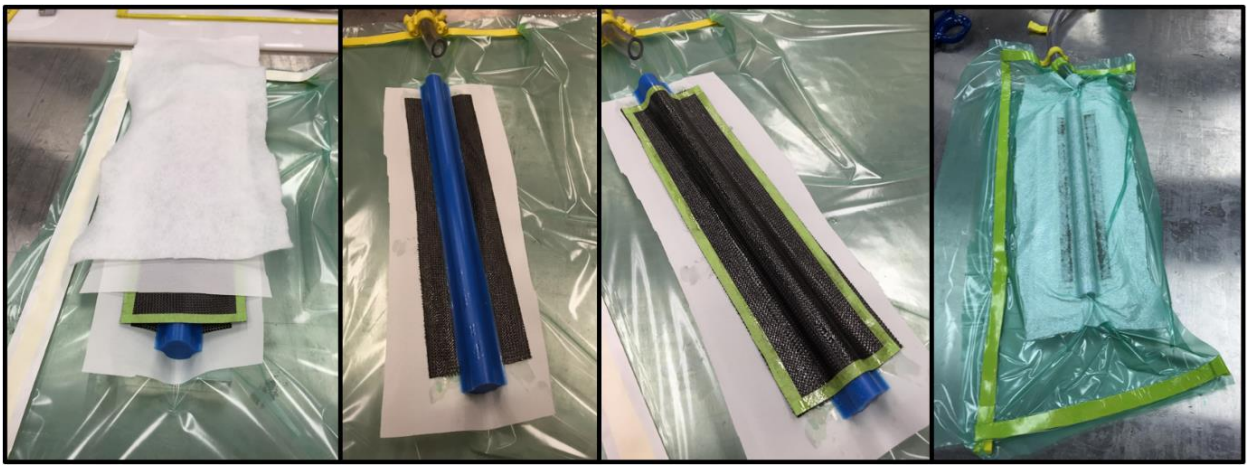

Figure 9-2. Internal Silicone Plug for Whole Boom Fabrication

Easy removal of the plug was possible to due to the smooth, non-stick surface of the silicone and by pulling one exposed end of the plug it would slide out, Figure 9-3.

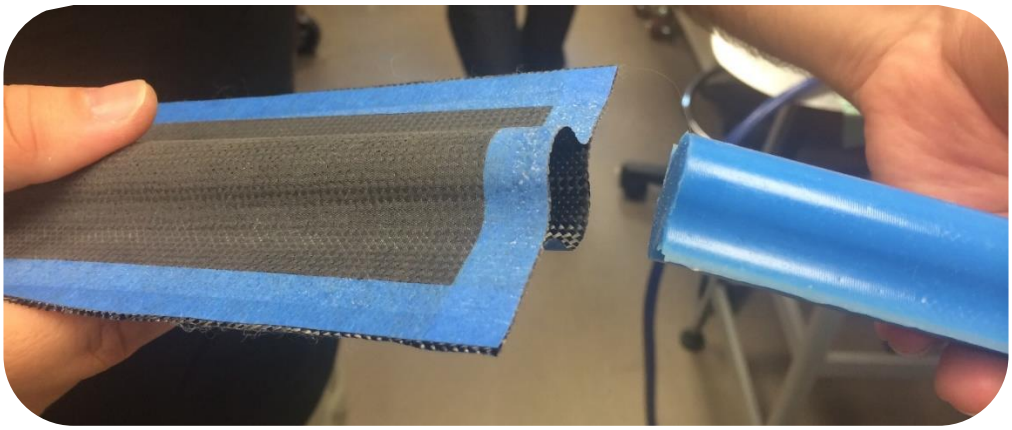

Figure 9-3. Silicone Plug Removal

At the NASA Langley Research Center in Hampton, VA the plug method manufacturing was improved upon by using a spread-tow woven carbon measuring 0.004 inches thick and infused with an out-gassed approved resin film. Six molds designed to connect linearly, as the smaller aluminum molds had, were CNC machined at 4 foot lengths from a high density foam. The molds were then coated in a Teflon sticker to provide a tooling surface and a silicone plug was poured. Cured under vacuum at elevated temperature for several hours in an oven, 4 foot long booms were manufactured to test the process and performance of the new material, Figure 9-4. After curing, the tabs were cut to their appropriate width using a precision straight edge.

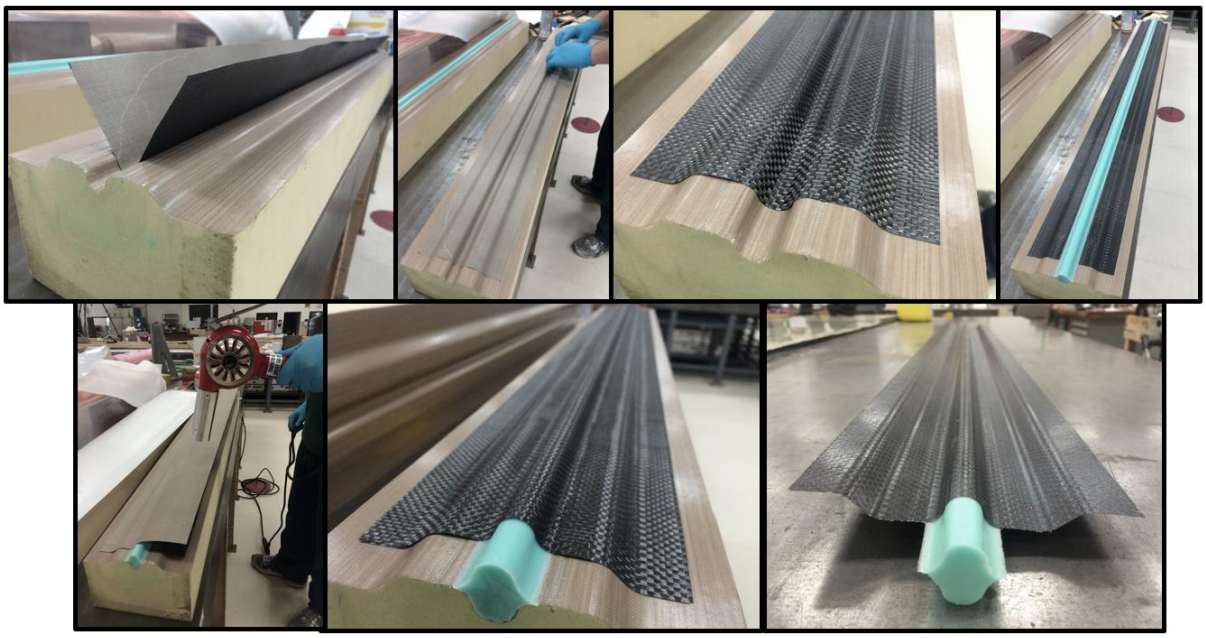

Figure 9-4 Whole boom manufacturing process

The molds were aligned using two rods which fit into channels that had been cut on the underside of the mold. Two sets of three molds were aligned and coated with a Teflon sticker to provide a

continuous 12 foot tooling surface and a 12 foot silicone plug was poured. The same vacuum bagging and lay-up as the 4 foot boom was repeated here and a 12 foot section cured in an autoclave was successfully manufactured in a single cure cycle.

Figure 9-5 12 ft. section of boom

Once manufactured, mechanical characterization of the boom was performed to understand the mechanical response and the means through which strain energy can be stored. Flattening and bending are the two primary mechanisms for energy storage. Figure 9-6 shows some characterization tests and the associated method for calculating the energy stored in the booms during each operation.

$$V_{\text{flattening}} = \int F\,dr$$

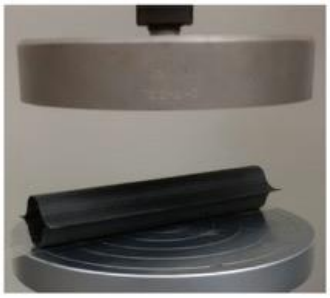

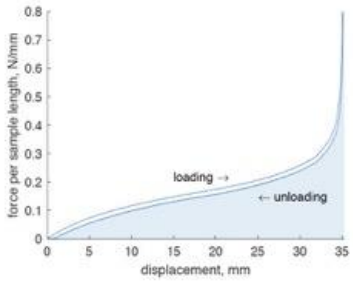

$$V_{\text{bending}} = \int M\,d\theta = s\int M\,d\kappa$$

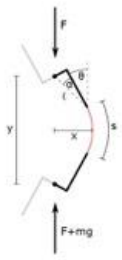

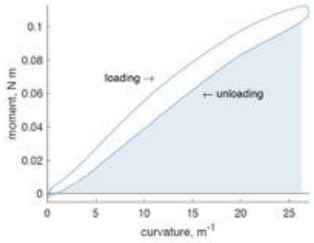

Figure 9-6 Mechanical Characterization of Composite Booms

Higher temperature thermoplastic resins such as PPS and PEKK have been investigated to show the ability to develop more stable creep resistant booms. The tight temperature control during

fabrication is the major hurdle that one needs to overcome. Figure 9-7 shows an example of short sections of booms that were fabricated and tested in bending to understand the structural response, comparing the various resins.

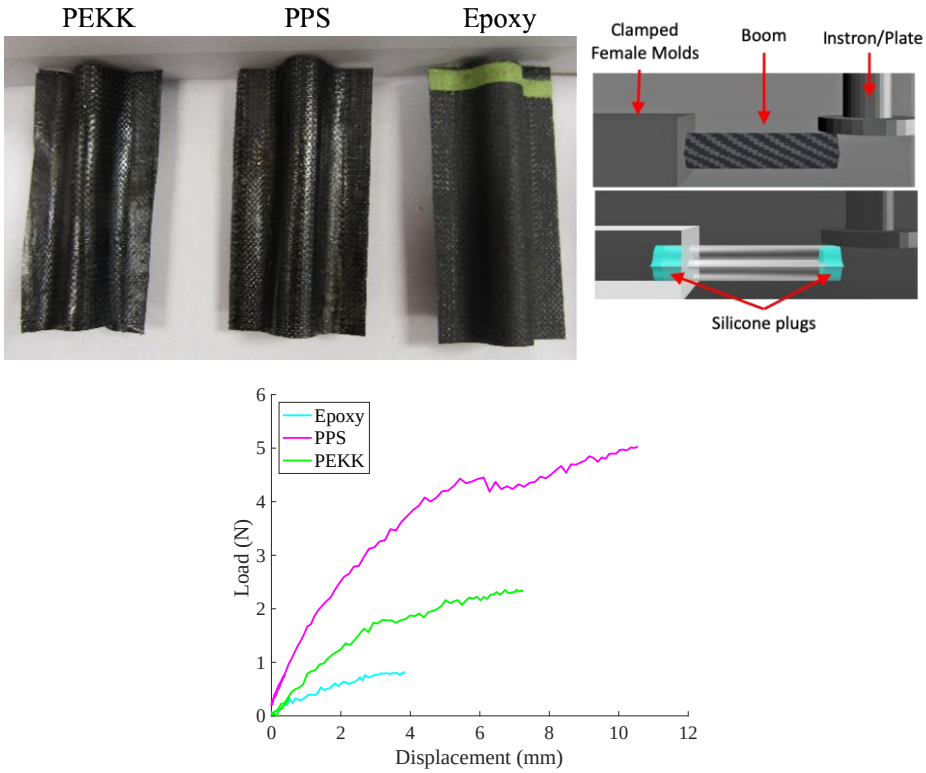

Figure 9-7 Examples of Thermoplastic resin systems.

9.3 DEPLOYABLE BOOMS MECHANISMS

The next step for CTM booms was to determine an appropriate means of deployment. The challenge of designing a boom deployment mechanism is creating a simple and lightweight mechanism that can ensure predictable, reliable, and jam-free operation. There are two main deployment failure modes for rollable booms. The first is uncoiling within the deployment mechanism, known as blossoming, which will lead to the boom becoming irreversibly jammed. The second failure mechanism is chaotic boom deployment, shown in Figure 9-8. Either failure mode can damage the instrument, boom, and/or spacecraft, ultimately ending a mission.

The challenge of storing energy in the boom systems is after long term storage the polymer matrix will relax (creep) over time and release the strain energy. Figure 9-8 shows an extreme example of this with the boom permanently deformed in the coiled configuration. The shown damage would render the device inoperable in orbit. From previous flight tests it has been observed that the booms can experience a reduction in strain energy. It is believed that this loss in energy is due to the relaxation of the boom during storage. Because of these findings, the focus of future tests will

be on characterizing the effects of long-term storage and improving the creep characteristics of the composite.

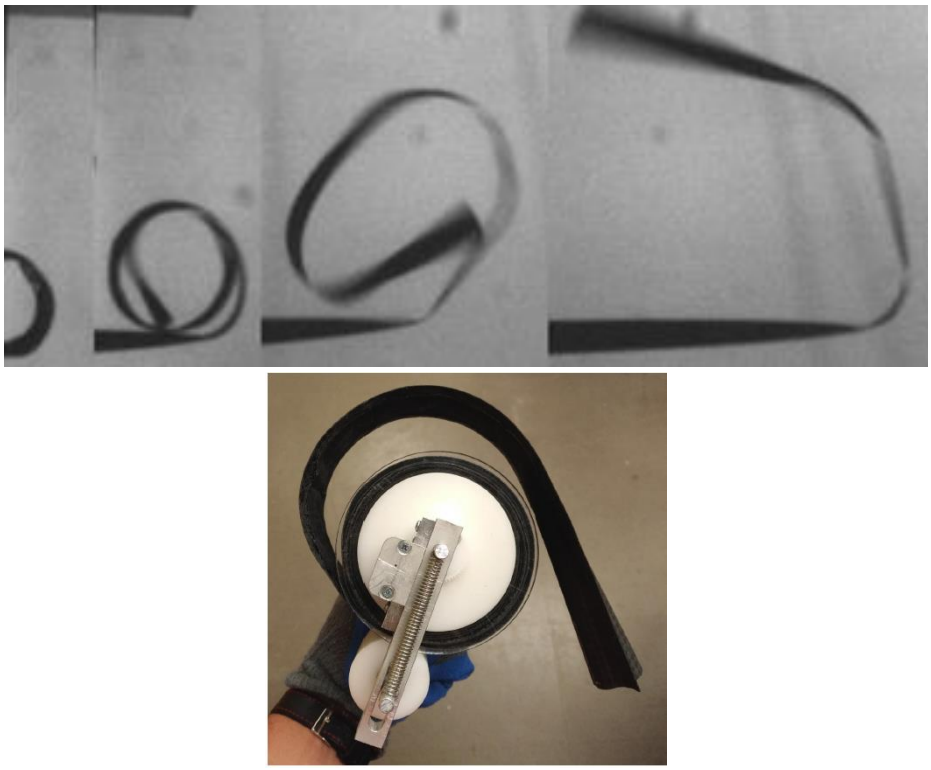

Figure 9-8 NCSU replicated the chaotic nature of a freely deploying boom in a one-G lab environment by suspending a boom vertically (top). Bottom image is a boom that is permanently deformed after long term storage due to creep and relaxation.

9.3.1 **Dual Pull Mechanism**

The first CTM boom deployment mechanism investigated is a dual-pull system. The dual-pull mechanism is named for the tension provided by a Kapton tape, which is co-wound with the boom. This tape is pulled from both ends to maintain tension in the coiled boom, eliminating blossoming to produce a high packing efficiency and reliably jam-free operation in both directions. Because the boom is constrained in a tight coil, the extension distance can be known accurately, which will allow precise deployment and tuning of boom length on orbit. One end of the tape is attached to the deployment motor, and the other end is attached to the central hub. A torsion spring in the hub maintains tension on the tape. This design is conceptually similar to NASA's CS3 spacecraft. However, where CS3 used a low-torque power spring, the dual-pull mechanism uses a high-torque torsion spring. The dual-pull mechanism is shown in Figure 9-9.

A co-wound tape must be thin to avoid wasting unnecessary space in the coiled boom. De-Orbit sail and CS3 used a series of guides to move the tape from the hub to the coaxial spool, which was not in the same plane. The additional drag created by these pulleys required a stronger tape,

up to 43% stronger in the case of De-Orbit sail [5]. De-Orbit sail and CS3 both used a stainless-steel ribbon to satisfy their strength requirements with a tape that was both thin and narrow. The dual-pull mechanism avoids pulleys by using a coplanar spool. This allows the use of a wide tape. The tape was made from Kapton, which is often used in space applications because of its low vacuum outgassing [6]. Kapton is a suitable tape choice because it has a strength-to-weight ratio 2.5 times greater than stainless steel. Furthermore, Kapton is easy to work with and is commercially available in a wide range of widths and thicknesses. Kapton can stretch up to 4% under load at high temperatures and can creep an additional 100% of initial stretch under prolonged loading. However, stretch and creep in the tape can be accommodated by the hub-mounted spring of the dual-pull mechanism.

A small torsion spring cannot accommodate the revolutions required for full boom deployment, and so the spring is attached to a gear instead of directly to the spacecraft. The gear and the hub turn in the same direction during boom deployment, which reduces the compliance required from the spring. The linkage reduces the spring's angular displacement by up to 90% compared to a body-fixed spring. This reduction allows the use of a spring with sufficient stiffness to eliminate blossoming. It also eliminates the motor's requirement to produce a holding torque.

The dual-pull mechanism can be used with any rollable boom. The boom used for this reference design is a CTM-type boom with a subtended angle $\theta 1 = \theta 2 = 75$ deg, radius $r1 = r = 7.62$ mm, and a flattened width of 50 mm. It was made from 1 K plain weave carbon fiber sourced from The Composite Store with 7.5 threads per centimeter and an areal mass of 98 g/cm2. The boom was laid up at an orientation of 45 deg, and Fiberglast's 2000 system epoxy with 2060 hardener was used as the resin system. The complete boom was cured in a single 24 h cycle under vacuum with a small heater maintaining a temperature of approximately 45°C. The mold consists of two identical machined aluminum exterior molds, with a silicone rubber interior plug [7].

This boom configuration is relatively easy to manufacture and works well for the mechanism development work described here. However, it would not be a good choice for use in space. The 45 deg fibers are susceptible to creep, and long-term storage would leave the boom with a significant curve. Moreover, the room temperature epoxy is not intended for use in space. Its glass transition is too low for the space environment, and it is not outgas approved. The two-ply boom used for CS3 would be a good choice for use with this mechanism in space.

A prototype of the dual-pull mechanism was built to support the testing. The reference design for this research is a 2x scale 1U CubeSat (20 x 20 cm). A mechanism sized for a 1x scale 1U CubeSat could accommodate up to four booms with a total length of 5 m. The structure and gears were cut from 5.6 mm acrylic using a Universal Laser Systems VLS 6.60. Spacers and the hub assembly were extruded from Acrylonitrile butadiene styrene using a Flash Forge Creator Pro. The final assembly is shown in Fig. 6. This prototype was used for the functional tests described in this work.

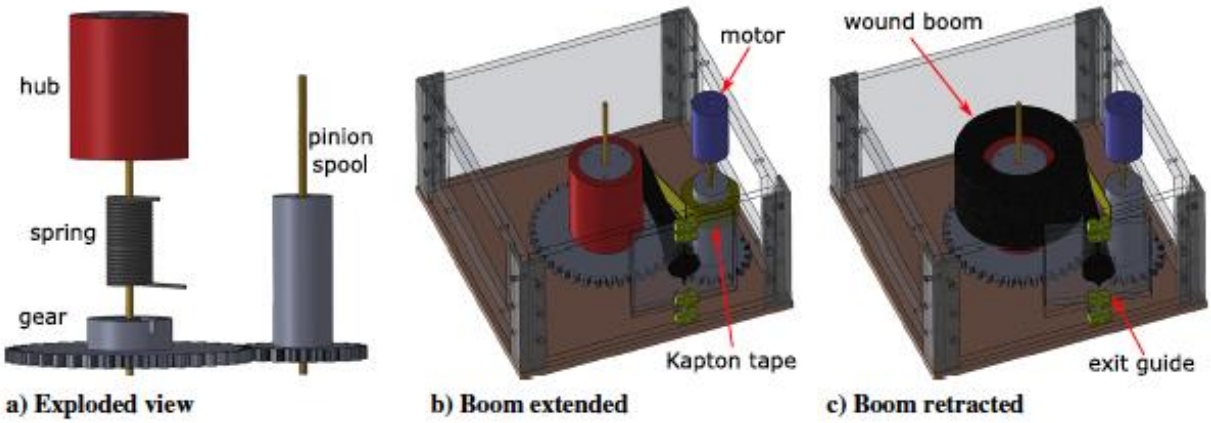

Figure 9-9 Dual- Pull Mechanism

Further details of this can be found in the following publication J. Firth, M. Pankow *Advanced Dual-Pull Mechanism For Deployable Spacecraft Booms* Journal of Spacecraft and Rockets.

The mechanism can be scaled to different sizes and a more refined version has been prototyped as can be seen in Figure 9-10.

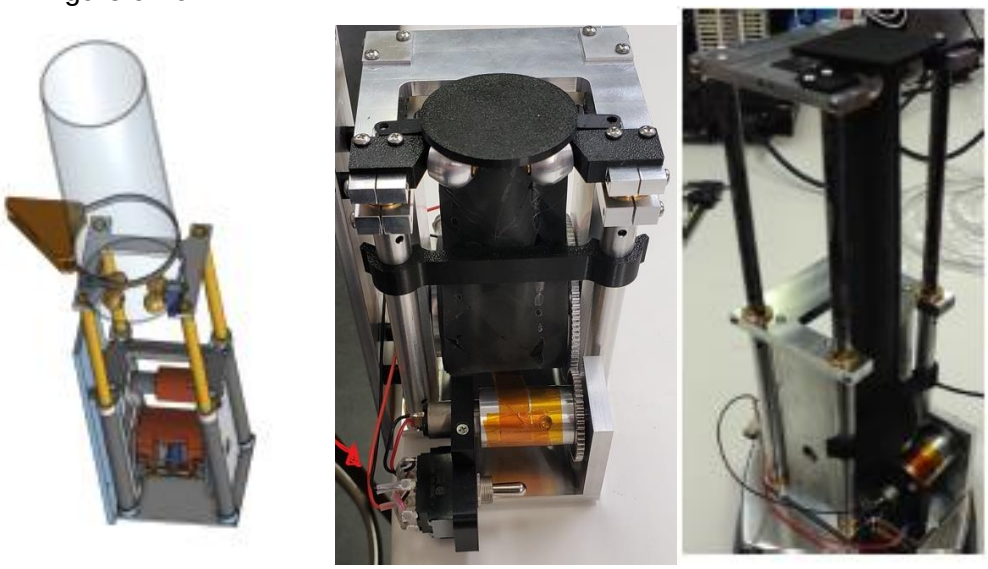

Figure 9-10 More developed Dual-Pull Deployment mechanism

9.3.2 **MUSE Mechanisms**

Other deployment mechanisms can utilize the stored strain energy of the boom through a controlled speed and direction. A minimal unpowered strain-energy mechanism (MUSE) has been built as a means of avoiding additional mechanical components and motors. The MUSE mechanism holds a rollable monostable boom tightly wrapped around its hub. This mechanism controls the boom's deployment rate and speed using an internal rotary dampener. A single roller is connected to the hub with two springs to prevent the boom from unwinding. The springs must

be compliant enough to accommodate the thickness of a fully wound boom and strong enough to prevent blossoming throughout deployment. Bearings ensure that the mechanism does not cause blossoming. A bracket keeps the axles aligned so the boom does not drift off of the rollers and get jammed in the springs. The bracket has a hole on one end and a slot on the other to allow the roller to maintain close contact with the coiled boom throughout deployment. The bracket also holds a rotary damper, which meshes with a hub-fixed gear to limit deployment speed. The mechanism is shown in Figure 9-11. The photograph also shows acrylic guards installed on each side of the hub. These guards ensure that the boom does not slide into the springs, and they make it easier to keep the boom straight as it is rolled onto the hub.

The mechanism relies on inter-layer friction to prevent slip that would lead to blossoming. The sprung roller creates a localized normal force, F_n, in one location on the coiled boom, thereby increasing the force of friction, F_f, between adjacent layers in the coiled boom. This is shown in Figure 9-12.

$$F_n = -kx$$

$$F_f = \mu_s F_n$$

If the boom is used to hold an instrument away from the spacecraft, the instrument can be integrated into the mechanism. If there is no tip-mounted instrument, the mechanism can be retained or jettisoned, depending on debris requirements. If the mechanism is jettisoned, an undamped mechanism may be sufficient. Opening shock will be minimal because only a small portion of the boom is traveling at the end of deployment.

Figure 9-11 MUSE mechanism

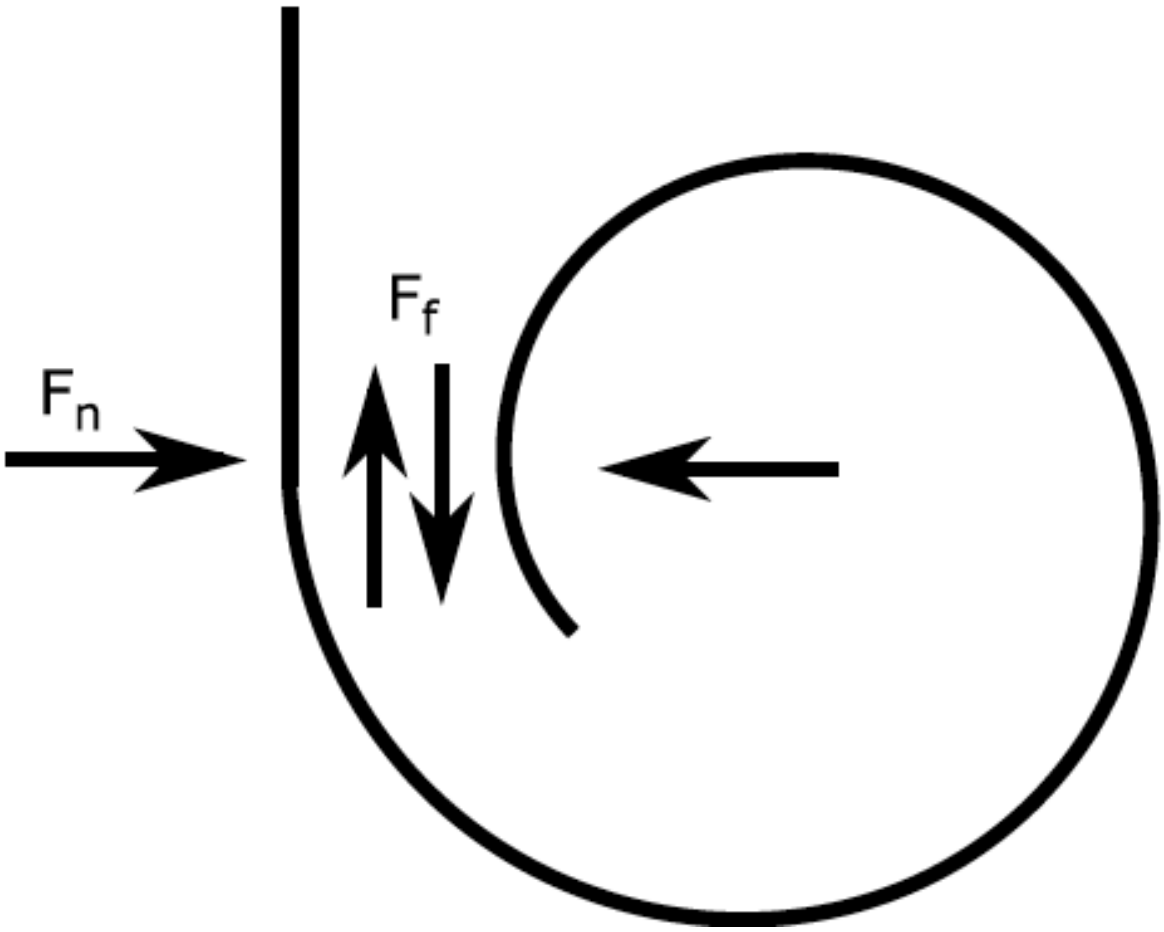

Figure 9-12 Interlayer Friction prevents blossoming

The MUSE mechanism uses a rotary damper to limit deployment speed. An ideal damper for this application would maintain deployment speed at exactly the desired rate. The ideal torque curve would be a step function. Two dampers were used during this test. The first was a commercial viscous fluid damper with a maximum specified torque of 0.8 oz/in (5.65N/mm). This damper was intended for speeds up to 50 rpm. It consists of a rotating paddle that moves through a grease-filled housing. The other damper was a custom centrifugal damper adapted from a music box mechanism. Both dampers are shown in Figure 9-13. The rubber arms of the centrifugal damper experience a centrifugal force as the damper spins.

Below the damper's critical speed, the damper's brake tips deflect outward as damper speed increases. Above the critical speed, the brake tips make contact with the damper's cylindrical walls. The normal force between the brake and the walls increases at faster damper speeds. The friction force between the brake and the damper walls is proportional to the normal force. The

damping torque depends on the friction force and the damper's radius. The forces on the damper's brake are shown in Figure 9-13.

$$M_d = \begin{cases} 0 & \omega \leq \omega_{\text{critical}} \\ \infty & \omega > \omega_{\text{critical}} \end{cases}$$

$$F_{\text{centrifugal}} = mr\omega^2$$

$$F_n = mr(\omega^2 - \omega_{\text{critical}}^2)$$

$$F_f = \mu_k F_n$$

$$M_d = F_f r$$

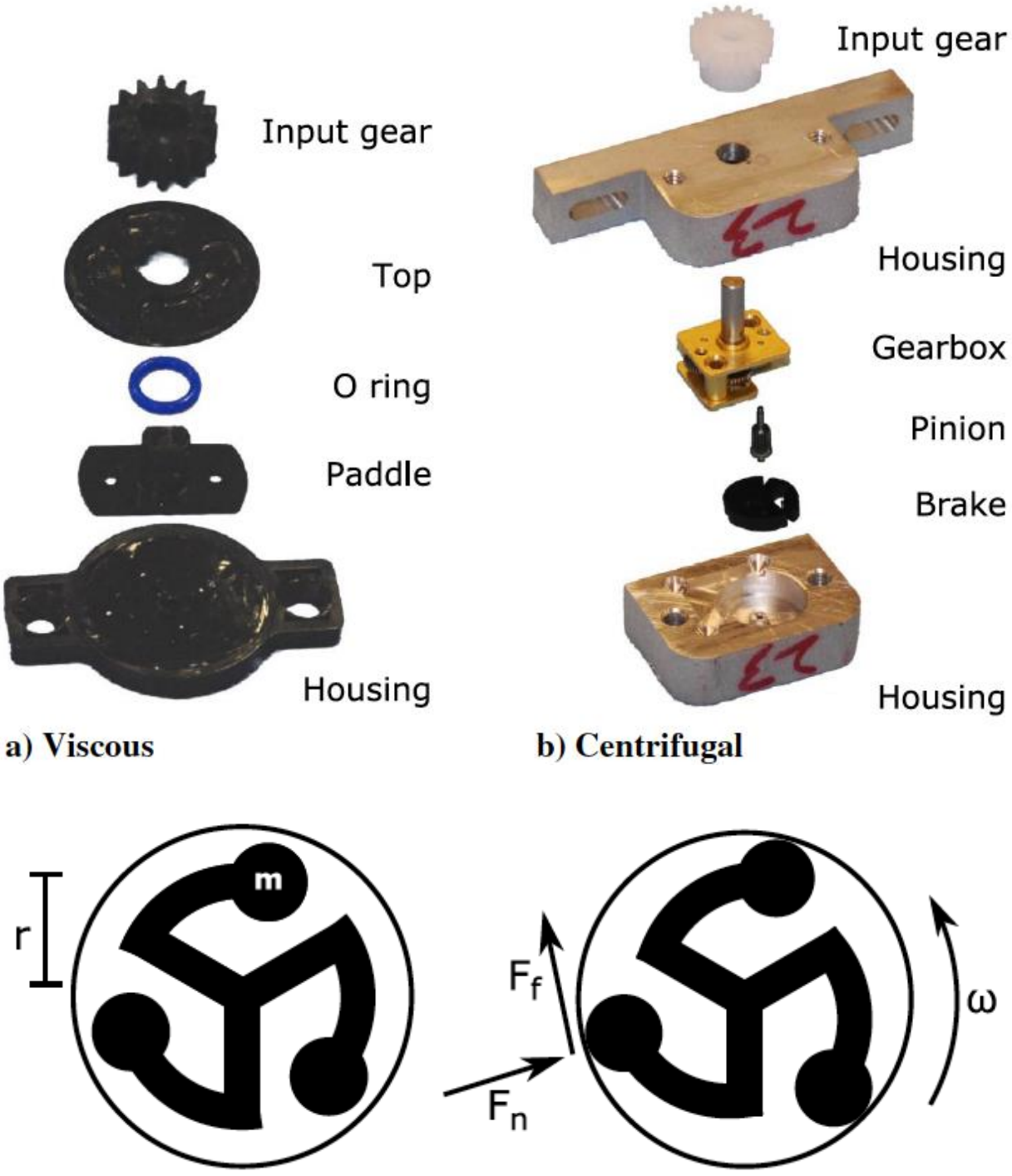

Figure 9-13 Damper Design and friction diagram

Deployment tests were performed to validate the model and ensure that the boom deploys successfully. For each test, the boom was deployed sideways away from a fixed mechanism. An

array of four cameras recorded images throughout deployment. The boom deployed through a transparent tube to ensure that it remained within the field of view of the cameras. Images from the cameras were combined, and the tip was tracked frame-by-frame to determine deployment speed. Figure 9-14 shows a composite image of each boom's deployment along with its position and speed. Each boom was tracked through two deployments. The second deployment had higher image quality and a higher framerate, so the remainder of the paper will use data from the second deployment. Boom deployment was successful with an undamped mechanism and with both types of dampers.

The MUSE mechanism successfully deployed a CTM boom in multiple configurations. In all cases the boom reached full deployment without blossoming. Each deployment was slower than predicted. Observed deployment speeds and times were very close to those predicted for a boom with 50% of nominal strain energy, as shown in Figure 9-15. Multiple strain energy test cycles revealed no progressive damage, and booms tested after deployment exhibited nearly identical strain energy. However, the close fit of the 50% energy model indicates that only half of the boom's energy is harnessed during deployment. The remainder is dissipated through unmodeled effects. Possible means of energy dissipation include friction, viscoelasticity, and imperfect boom rolling. The results of the deployment tests and conclusions for each type of dampening mechanism are discussed below.

9.4 CONCLUSIONS

9.4.1 Deployment Mechanisms

Undamped: The deployment speed of an undamped boom is limited only by boom length. If the mechanism must remain attached to the spacecraft, it will experience severe opening shock when the boom reaches full deployment. In fact, the opening shock was too much during this deployment test. The boom was attached to the hub with tape, and at full deployment the tape peeled off of the hub and the boom kept going at its full speed. A tip-mounted captive deployment would suffer even worse opening shock due to its higher moving mass. However, an undamped mechanism would be suitable for deploying a tip mounted boom if the mechanism could be jettisoned.

Viscous damper: Boom deployment with the viscous damper was slower than deployment using the undamped mechanism the damper successfully limited deployment speed. Opening shock was also lower this boom did not peel the tape from the hub. The viscous damper's relatively at high-speed torque curve makes deployment speed sensitive to small changes in input energy. This could be problematic if the boom's post storage strain energy is unknown. The viscous damper likely produces less torque at higher temperatures as the viscosity decreases. This could cause higher-than-desired deployment speeds. At cold temperatures the increased viscosity could prevent deployment altogether. In fact, less energetic booms used with an earlier version of the MUSE mechanism had trouble deploying because the viscous damper stalled, even at

room temperature. A damper with lower low-speed torque would be more reliable and less likely to prevent deployment.

Centrifugal Damper: Deployment with the centrifugal damper was slower than deployment with the viscous damper and much slower than deployment using the undamped mechanism. After quickly reaching its top speed, the boom continued to deploy at a nearly constant rate. Opening shock was roughly halved compared to the viscous damper. The centrifugal damper will likely produce more torque at higher temperatures. The rubber will be more flexible, which will lower the critical speed at which the brake arms contact the braking surface. Lower temperatures would make the brake stiffer and lower the torque produced. However, both of these effects would only change deployment speed slightly because the torque curve is so steep. The centrifugal damper's relatively steep high-speed torque curve provides a close approximation of the ideal deployment damper described in earlier. This makes deployment speed predictable even with widely varying boom strain energies. Furthermore, the centrifugal damper produces very little torque in the low-speed region. This is beneficial because the damper is less likely to cause stalling. If a damper is required to limit boom deployment speed, a centrifugal damper is better than a viscous damper. It is stiffer at high speeds and less stiff at low speeds, making it less sensitive to variations in strain energy and less likely to prevent deployment initiation. It may also work better in varying temperatures.

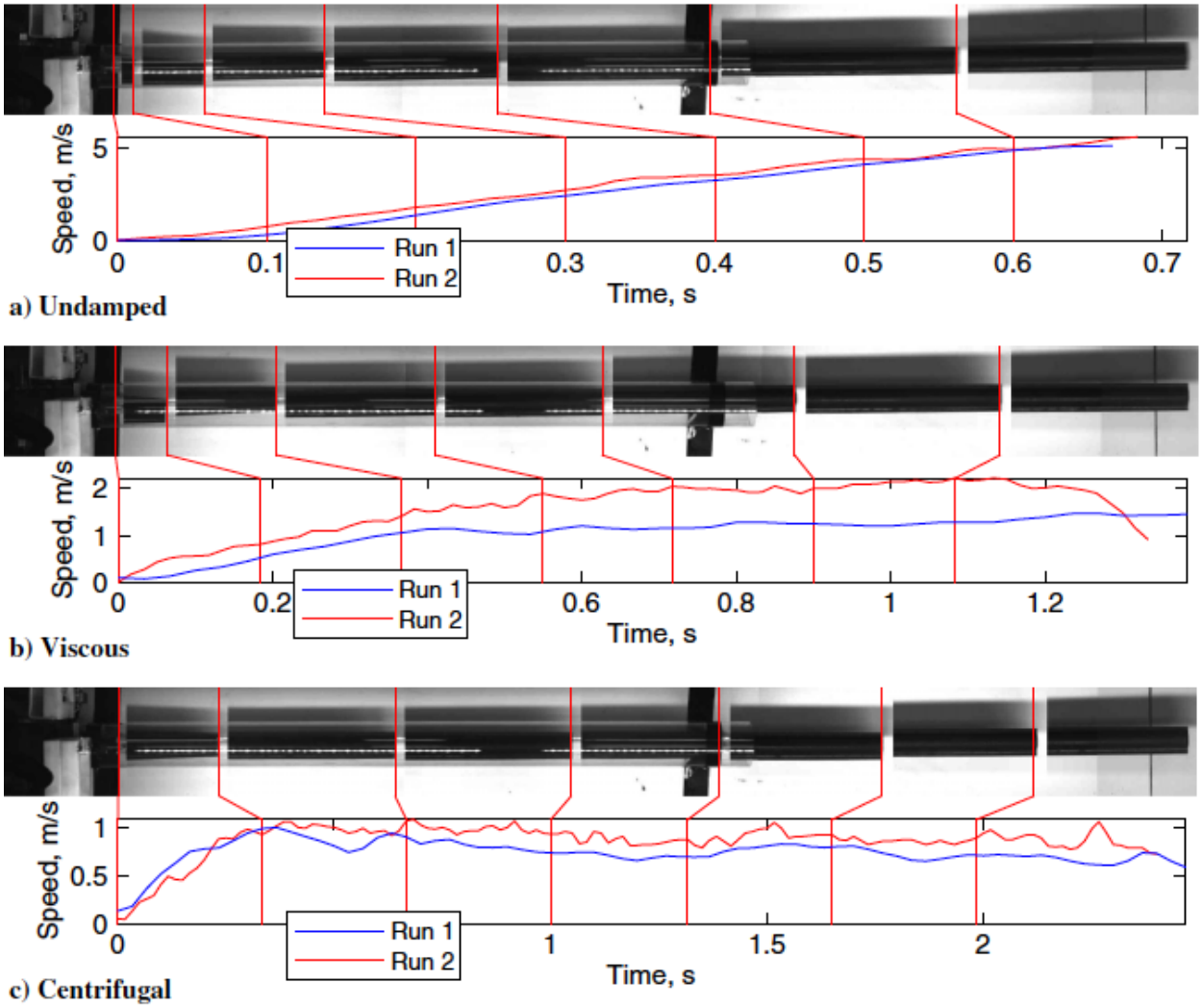

Figure 9-14 Boom Deployment

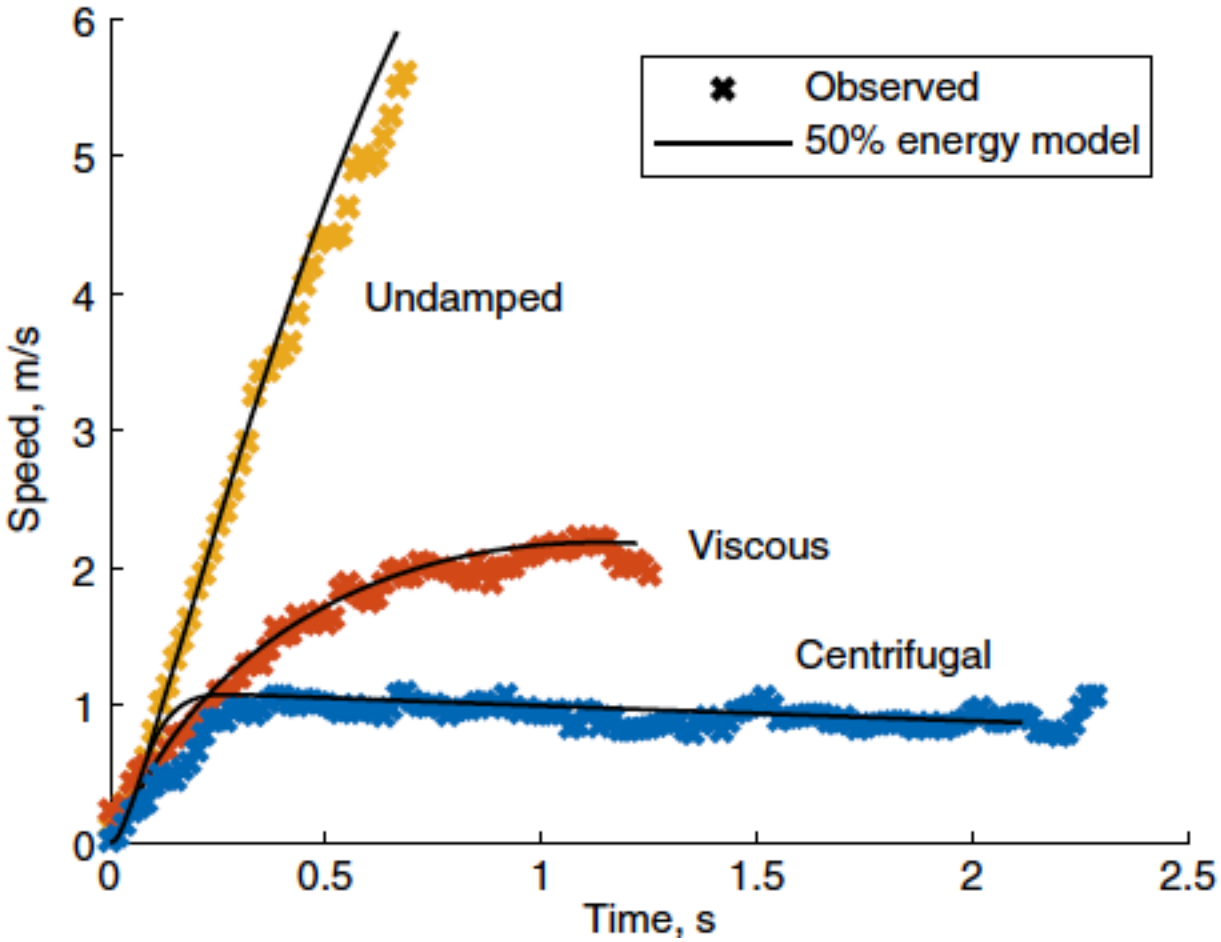

Figure 9-15 Observed Deployment speeds for a 2 m boom.

Previous tests showed the system could easily deploy under controlled circumstances. Figure 9-16 shows deployment of a boom during a flight test along with a tested end of travel mechanism that allowed us to test some integrated electronics that were run down the center of the boom using a flex circuit. Further details about the MUSE mechanism can be found in J. Firth, M. Pankow. *Minimal Unpowered Strain-Energy Deployment Mechanism for Rollable Spacecraft Booms: Ground Test*, Journal of Spacecraft and Rockets 57(2) 2020.

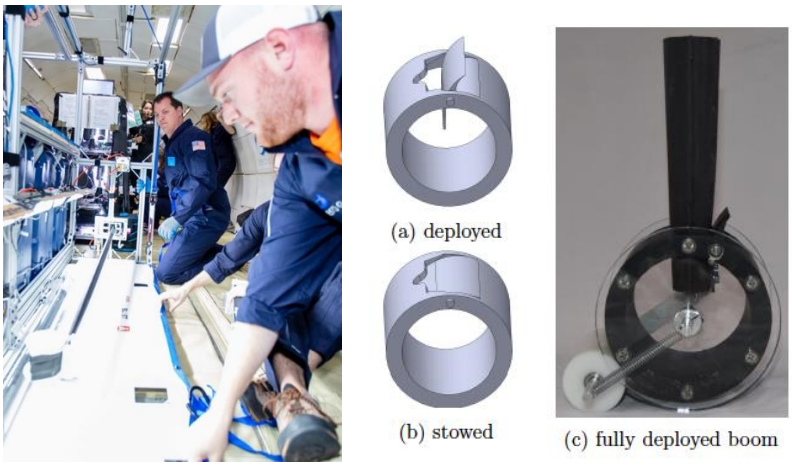

Figure 9-16 NCSU deployment testing from previous funding in Zero-G showing successful deployment. Right is the mechanism that is used for stopping the boom at end of travel.

9.4.2 Composite Origami

Composite Origami offers a new method to be able to efficiently package large structures with integrated hinges that are structurally very efficient and strong due to the integrated carbon fiber. If successful, this technology can replace complex hinged arrays that have many potential failure points and require extensive testing. The scalability of the system enables many possible infusions including large solar arrays and deployable habitats.

The challenge of designing a deployable structure is that it must be structurally strong, ensure predictable, reliable, and jam-free operation, with minimal power input. There are two main deployment failure modes for hinged structures. The first is hinge binding, where the hinge has too much friction and prevents it from achieving full deployment. The second type of failure is where a part fails because of force or deflection incompatibilities.

Figure 9-17 Example of Composite Origami Hinge and The Structures that can be fabricated

Composite Origami offers an integrated structural element that can store energy elastic while also acting as an integrated hinge material, see Figure 9-17 and Figure 9-18. The advantages of this technology extend to benefits associated with: deployment mechanism design (passively deployed integrated hinges), deployability (more predictable and controllable), and strain relaxation over time (reduce creep and less relaxation when stored). In general, this yields more

reliable (capable of reaching a deployment reliability of 0.999), lighter, and less complex designs compared to other array designs or inflatable structures.

Current solar array and deployable technologies usually rely on both a soft flexible material and a separate mechanism for deployment. This adds complexity and affects reliability. This proposal aims to demonstrate that all of these components can be integrated into a single element which will simplify the complexity of systems and increase reliability and structural integrity, using an iterative flight test approach.

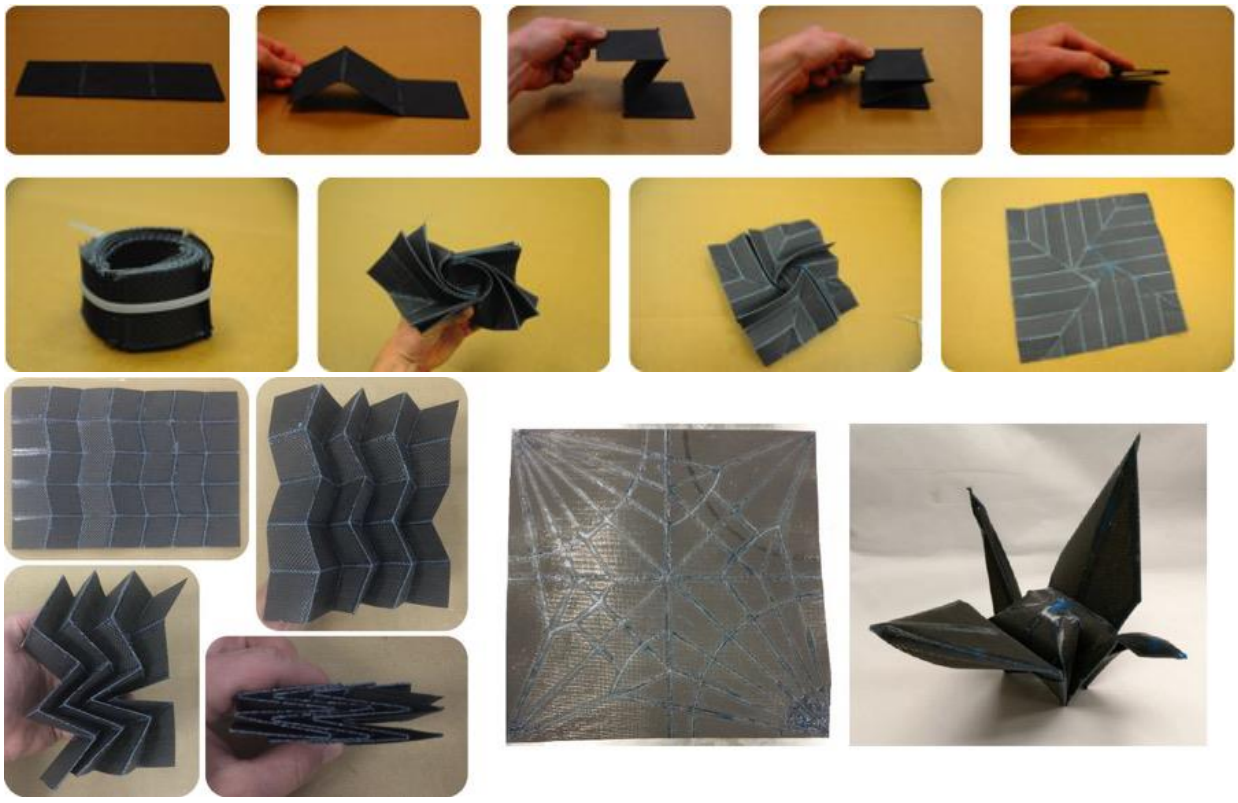

Figure 9-18 Examples of Composite Origami showing the ability to fold and unfold (top), and flasher type model (middle) miura-ori fold (bottom left) and Origami Crane (bottom right) have been fabricated at NCSU.

The current technology is considered a TRL of level 4 based on the fact that NCSU has developed composite origami in the past using High Strain Composites and tested in a lab level setting [8, 9]. Several variations of the composite origami structures have successfully deployed in a one-g environment. The dynamic response of the deploying origami structure now needs to be characterized in a zero-g environment, to understand what the differences are and how it affects the design. By the end of this flight test campaign, the composite origami will be at TRL 5 based on testing in a representative environment. This will be accomplished by conducting deployment tests on an aircraft flying parabolic arcs. A zero-g flight very nearly replicates the space environment for composite origami. For the observed deployment speeds, air resistance in an aircraft cabin will not cause significant dynamic differences from the space environment. We will replicate the thermal environment of space by testing both hot and cold, to understand how this affects the stored strain energy.

We have currently demonstrated manufacturability of these composite and performed mechanical characterization of the joints and impact of the joints on the overall strength of the laminates [8]. We also developed a method to accurately and reliably create the integrated hinges in these composites, through a 3D printer that can lay the traces of the silicone precisely [9]. Mechanical characterization of these composites has been performed and an example can be seen in Figure 9-19.

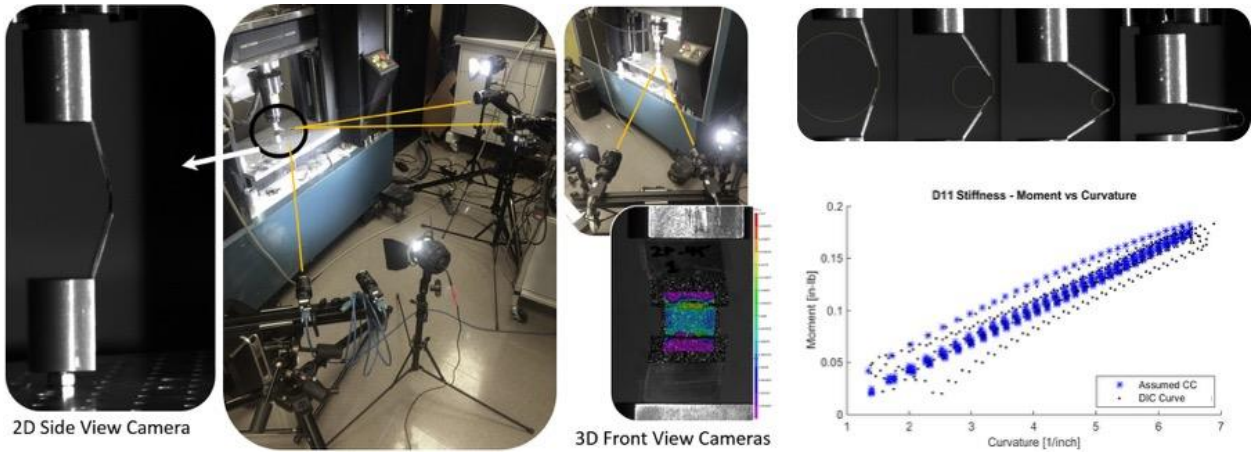

Figure 9-19 Mechanical Characterization of Composite Origami Hinge.

This work will specifically look at validating zero-g deployment along with determining variations that may occur in deployment due to thermal loading. This is especially important since many applications may not be able to control the temperature when deployment occurs.

Flight Tests are scheduled for May 2021.

Before the first test flight relevant non-zero-g data will be gathered to further classify the system prior to each zero-g flight to increase the effectiveness of the science gathered. Ongoing ground testing includes the force available from the hinges strain energy and the dynamics of deployment in 1-g ground testing so that we can compare it to our Zero-G flight.

Round one of zero-g testing will be used to perform verification and validation of the origami along with trials to understand the impact of manufacturing variations on the performance in zero-g and at different temperatures. The results of this testing will enable us to optimize the composite origami in round 2 of testing, which will include the modified origami based on flight 1 testing, along with integrated flexible electronics to simulate the effective integration of solar cells to create solar arrays.

REFERENCES

[1] P. Warren, B. Dobson, J. Hinkle and M. Silver, "Experimental Characterization of Light Weight Strain Energy Deployment Hinges," in *46th AIAA/ASME/ASCE/AHS/ASC Structures, Structural Dynamics & Materials Conference*, Austin, Texas, 2005.

[2] J. Domber, J. Hinkle, L. Peterson and P. Warren, "Dimensional Repeatability of an Elastically Folded Composite Hinge for Deployed Spacecraft Optics," *Journal of Spacecraft and Rockets,* vol. 39, no. 5, 2002.

[3] M. Silver and P. Warren, "The Strain Energy Deployed High Expansion Outer Barrel Assembly," in *2nd AIAA Spacecraft Structures Conference*, 2015.

[4] J. Block, M. Staubel and M. Wiedemann, "Ultralight Deployable Booms for Solar Sails and Other Large Gossamer Structures in Space," *Acta Astronautica,* vol. 68, no. 7-8, pp. 984-992, 2011.

[5] S. Meyer, M. Hillebrandt, M. Straubel and H. Christian, "Design of the De-Orbit Sail Boom Deployment Unit," 13th European Conference on Spacecraft Structures, Materials & Environmental Testing," in *ESA Communications*, Noordwijk, The Netherlands, 2014.

[6] A. Laikhtman, I. Gouzman, R. Verker and E. Grossman, "Contamination Produced by Vacuum Outgassing of Kapton Acrylic Adhesive Tape," *Journal of Spacecraft and Rockets,* vol. 46, no. 2, pp. 236-240, 2009.

[7] S. West, C. White, C. Celestino, S. Philpott and M. Pankow, "Design and Testing of Deployable Carbon Fiber Booms for CubeSat Non-Gossamer Applications.," in *AIAA SciTech*, Kissimmee Florida, 2015.

[8] C. White, "Manufacturing and Structural Characterization of Flexible and Dual-Matrix Deployable Composites for Space Application," North Carolina State University, Raleigh, 2016.

[9] A. Gay, "Fabrication and Classification of Dual-Matrix Composites for Deployable Space Applications," North Carolina State University, Raleigh, 2017.

[10] F. Chen, H. Liu and Q. Yang, "Maskless Fabrication of Concave Microlens Arrays on Silica Glasses by a Femtosecond-Laser-Enhanced Local Wet Etching Method," *Optics Express,* vol. 18, no. 19, pp. 20334-20343, 2010.

[11] R. Syms, E. Yeatman and B. V.M., "Surface Tension-Powered Self-Assembly of Microstructures - the State-of-the-Art," *Journal of Microelectromechanical Systems,* vol. 12, no. 4, pp. 387-417, 2003.

[12] H. Yang, C. Chao and M. Wei, "High Fill-Factor Microlens Array Mold Insert Fabrication using a Thermal Reflow Process," *Journal of Micromechanics and Microengineering,* vol. 14, no. 8, pp. 1197-1204, 2004.

[13] S. Moore, J. Gomez and D. Lek, "Experimental Study of Polymer Microlens Fabrication using Partial-Filling Hot Embossing Technique," *Microelectronic Engineering,* vol. 162, pp. 57-62, 2016.

[14] J. Albero, L. Nieradko and G. C., "Fabrication of Spherical Microlenses by a Combination of Isotropic Wet Etching of Silicon and Molding Techniques," *Optics Express,* vol. 17, no. 8, pp. 6283-6292, 2009.

[15] K. J.Y., N. Brauer and F. V., "Hybrid Polymer Microlens Arrays with High Numerical Apertures Fabricated using Simple Ink-Jet Printing Technique," *Optical Materials Express,* vol. 1, no. 2, p. 259, 2011.

[16] P. Nussbaum, R. Volkel and H. Herzig, "Design, Fabrication and Testing of Microlens Arrays for Sensors and Microsystems," *Pure and Applied Optics: Journa of the European Optical Society Part A,* vol. 6, no. 6, pp. 617-636, 1997.

[17] A. Yi and L. Li, "Design and Fabrication of a Microlens Array by use of a Slow Tool Servo," *Optics Letters,* vol. 30, no. 13, pp. 1707-1709, 2005.

[18] X. Zhang, F. Fang and L. Yu, "Slow Slide Servo Turning of Compound Eye Lens," *Optical Engineering,* vol. 52, no. 2, p. 023401, 2013.

[19] J. Yan, Z. Zhang and T. Kuriyagawa, "Fabricating Micro-Structured Surface by using Single-Crystalline Diamond Endmill," *The International Journal of Advanced Manufacturing Technology,* vol. 51, no. 9, pp. 957-964, 2010.

[20] J. Yan, A. Horikoshi and T. Kuriyagawa, "Manufacturing Structured Surface by Combining Microindentation and Ultraprecision Cutting," *CIRP Journal of Manufacturing Science and Technology,* vol. 5, no. 1, pp. 41-47, 2012.

[21] Y. Bai, X. Wang, T. Zhou, Z. Liang and G. Li, "Compressional Deformation in Indentation Process for Microlens Array Mold," *Journal of Beijing Institute of Technology,* no. 1, pp. 15-21, 2018.

[22] E. Zdanowicz, T. Dow and S. R.O., "Rapid Fabrication of Nanostructured Surfaces using Nanocoining," *Nanotechnology,* vol. 23, no. 41, p. 415303, 2012.

[23] D. T.A., J. Nowak and J. Kessing, "Design of Elliptically-Vibrating Ultrasonic Actuator for Nanocoining," *Precision Engieering,* vol. 45, pp. 301-310, 2016.

[24] A. Karimzadeh, M. Ayatollahi and M. Alizadeh, "Finite Element Simulation of Nano-Indentation Experiment on Aluminum 1100," *Computational Materials Science,* vol. 81, pp. 595-600, 2014.

[25] S. Moore, M. Manzari and Y. Shen, "Nanoindentation in Elastoplastic Materials: Insights from Numerical Simulations," *International Journal of Smart and Nano Materials,* vol. 1, no. 2, pp. 95-114, 2010.

[26] A. Warren and Y. Guo, "Machined Surface Properties Determined by Nanoindentation: Experimental and FEA Studies on the Effects of Surface Integrity and Tip Geometry," *Surface & Coatings Technology ,* vol. 201, no. 1, pp. 423-433, 2006.

[27] Anonymous, ABAQUS/Standard User's Manual, Version 6.9, Providence, RI: Simulia, 2016.

FACULTY

MARK R. PANKOW

Director, Precision Engineering Center
Director, Ballistic Loading and Structural Testing Laboratory
Assistant Professor, Department of Mechanical and Aerospace Engineering

BS, Mechanical Engineering, California Polytechnic State University, San Luis Obispo, 2005
MS, Mechanical Engineering, University of Michigan, 2007
PhD, Mechanical Engineering, University of Michigan, 2010

After receiving his PhD degree from the University of Michigan in 2010, Dr. Pankow joined the Army Research Laboratories and worked there for two years. His research interests were in the areas of dynamic failure of composite materials. His work was both experimental and computational in nature. Dr. Pankow joined the faculty at North Carolina State University in 2012. His current research interests include dynamic testing (ballistic, blast, impact), computational modeling of composites, and deployable structures. He is the editor for the American Society for Composites.

DAVID C. MUDDIMAN

Jacob and Betty Belin Distinguished Professor of Chemistry
Founder and Director of the W.M. Keck FTMS Laboratory for Human Health Research

B.S., Chemistry, Gannon University, 1990
Ph.D., Analytical Chemistry, University of Pittsburgh, 1995

Prior to moving his research group to North Carolina State University in 2006, David was a Professor of Biochemistry and Molecular Biology and Founder and Director of the Proteomics Research Center at the Mayo Clinic College of Medicine in Rochester, MN. Prior to this appointment, David was an Associate Professor of Chemistry at Virginia Commonwealth University. It was there that he began his professional career as an assistant professor with an adjunct appointment in the Department of Biochemistry and Molecular Biophysics and as a member of the Massey Cancer Center in 1997. These academic appointments followed a postdoctoral fellowship at Pacific Northwest National Laboratory in the Environmental Molecular Sciences Laboratory under Richard D. Smith from 1995-1997. David was born in Long Beach, CA in 1967 but spent most of his formative years in a small town in Pennsylvania. Dr. Muddiman is Editor of *Analytical and Biological Chemistry* and Associate Editor of the *Encyclopedia of Analytical Chemistry* as well as on the Editorial Advisory Board of *Mass Spectrometry Reviews*, *Molecular and Cellular Proteomics*, *Rapid Communications in Mass Spectrometry*, and the *Journal of Chromatography B*. He also serves on the advisory board of the NIH Funded Complex Carbohydrate Research Center, University of Georgia and the Yale/NIDA Neuroproteomics Center, Yale University. Dr. Muddiman has served as a member of the ASMS Board of Directors and Treasurer of US-HUPO, and he is currently the President of US HUPO. His group has presented over 500 invited lectures and presentations at national and international meetings including 20 plenary/keynote lectures. His group has published over 250 peer-reviewed papers and has received four US patents in addition to two patents pending. He is the recipient of the 2015 ACS Award in Chemical Instrumentation, 2010 Biemann Medal (American Society for Mass Spectrometry), 2009 NCSU Alumni Outstanding Research Award, the 2004 ACS Arthur F. Findeis Award, the 1999 American Society for Mass Spectrometry Research Award, and the 1990-1991 Safford Award for Excellence in Teaching (University of Pittsburgh). Dr. Muddiman's research is at the intersection of innovative mass spectrometry technologies, systems biology, and model organisms for diseases and bioenergy, and is funded by the National Institutes of Health, the National Science Foundation, the Department of Energy, and The United States Department of Agriculture.

BRENDAN T. O'CONNOR

Associate Professor
Department of Mechanical and Aerospace Engineering

BS, Mechanical Engineering, Marquette University, 2000
MS, Mechanical Engineering, University of Massachusetts, 2004
PhD, Mechanical Engineering, University of Michigan, 2009

After receiving his BS from Marquette University, Dr. O'Connor joined Norian/Siani Engineering, an engineering consulting firm in Boston MA. He then returned to the University of Massachusetts and joined the Industrial Assessment Center, conducting energy audits of industrial facilities. During his PhD, Dr. O'Connor turned his research towards solar power, with a focus on organic electronic materials processing. After his graduation, Dr. O'Connor joined the Polymers Division at the National Institute of Science and Technology as an NRC-NIST Postdoctoral Fellow. At NIST, Dr. O'Connor conducted research on processing and mechanical properties of organic electronic films, primarily for flexible transistor applications. He then joined NC State University in 2011. At NC State, Dr. O'Connor's research interests are focused on polymer semiconductor device processing and characterization. His research efforts include developing plastic solar cells with unique optoelectronic characteristics and developing mechanically robust flexible and stretchable electronic devices.

RONALD O. SCATTERGOOD

Professor
Materials Science and Engineering Department

BS, Metallurgical Engineering, Lehigh University, 1961
MS, Metallurgy, Massachusetts Institute of Technology, 1963
PhD, Metallurgy, Massachusetts Institute of Technology, 1968

R.O. Scattergood is a Professor in the Department of Materials Science and Engineering. He received BS degrees in Mining Engineering and Metallurgical Engineering from Lehigh University. His MS and PhD degrees were obtained in Metallurgy from M.I.T. In 1968 he became a member of the basic research staff in the Materials Science Division at the Argonne National Laboratory. In 1981, he joined the faculty as a Professor of Materials Engineering at North Carolina State University.

Professor Scattergood's major research interests have been focused on the mechanical behavior of solids. He has worked in the areas of strengthening mechanisms in solids, mechanical testing, fracture and toughening in ceramics, tribology, processing, properties and thermal stability of nanocrystaline materials and precision machining processes. He has published over 250 papers.

STAFF

KENNETH P. GARRARD

Senior Research Scholar
Precision Engineering Consortium and
FTMS Laboratory for Human Health Research

BS, Computer Science, North Carolina State University, 1979
MS, Computer Studies, North Carolina State University, 1983

As a full-time researcher at the Precision Engineering Consortium for over 32 years, Mr. Garrard's interests and duties have included the development of high performance control systems for ultraprecision machines and software for custom, multiprocessor computer systems. He participated in the development of the original PEC fast tool servo as well as three other fast tool servo systems that have been delivered to commercial and government sponsors. One of these systems was built specifically for the machining of off-axis segments of conic surfaces of revolution and another was used for the fabrication of inertial confinement fusion targets. He has performed numerous prototype fabrication projects that required unique machine configurations and controller software. He is also co-inventor of the spherical coordinate measurement machine, *Polaris3D*, and was the developer of algorithms for its control and for the analysis of measurement data.

Since 2012 he has collaborated with the FTMS Laboratory for Human Health Research to assist with the implementation of video system directed sample stage motion control, region of interest selection, laser optics and instrument synchronization for IR-MALDESI imaging. This led to the development of the widely-used, open-source *MSiReader* software package for analysis and visualization of Mass Spectrometry Imaging data sets.

Mr. Garrard has a long-standing interest in the analysis of scientific data, computational geometry, signal processing, programming language structures, sorting and searching algorithms, multiprocessor computer architecture and the design and implementation of hard real-time systems. He is a regular contributor to the Mathworks user community web site.

ANTHONY R. WONG

Research Associate

BS, Mechanical Engineering, NC State University, 2005
MS, Mechanical Engineering, Massachusetts Institute of Technology, 2012

Mr. Wong joined the Precision Engineering Consortium in 2017 as a member of the technical staff. His current research interests include machine design and metrology. Prior to coming to the PEC, he had 7 years of industry experience including positions at Caterpillar, AKG of America, ShopBot Tools and Keystone Tower Systems.

JACOB MARX

Research Associate

BA, Physics, Case Western Reserve University, 2013
ME, Nuclear Engineering, North Carolina State University, 2015
PhD, Mechanical Engineering, North Carolina State University, 2020

Dr. Marx joined the Precision Engineering Consortium as a member of the technical staff after graduating with his doctorate degree. During his PhD he worked on manufacturing and testing of metal foam technologies for a variety of engineering applications. He has helped develop composite metal foam armors to protect against ballistic threats and blast and fragment impact as well as investigate their use for aerospace and tank car applications. He joins the PEC with an interest in material manufacturing and testing. Outside of work he enjoys hiking with his wife, daughter, and dog.

GRADUATE STUDENTS

USAMA DINGANKAR obtained his Bachelor's in Mechanical Engineering from SRM University, Chennai, India. He is currently pursuing his M.S. degree in Mechanical Engineering at North Carolina State University at Raleigh. Outside of work Usama is actively involved in the Fantasy Football (Soccer) setup, as he is a huge Football (Soccer) fan. Usama joined the PEC as a graduate researcher in July 2019.

SUMIT GUNDYAL obtained his B.S. degree in Mechanical Engineering at University of Pune, Pune, India. He worked for 2 years at Dassault Systèmes, Pune, India before starting as a graduate student at NC State University. Sumit joined the BLAST lab in February 2018, working on the modeling and the simulation aspect of the microlens array project. He enjoys swimming, basketball, and tennis outside of the lab.

JACOB GUYMON received his B.S. degree in Mechanical Engineering from Utah State University in Logan Utah. He received his MBA from Weber State University in Ogden Utah. He has worked in manufacturing and mechanical design for over 8 years. Jacob joined the PEC in December of 2019, working on the sub-aperture polishing project. Outside of the PEC he enjoys soccer, sailing and spending time with his wife and daughter.

PARKER EATON received his B.S. in Mechanical Engineering from North Carolina State University in May 2020. He is currently pursuing his M.S. degree in Mechanical Engineering at North Carolina State University. Parker joined the PEC in August of 2020, working on minimizing form error in the high-frequency manufacturing of microlens array molds. Outside of the lab, Parker is an avid fan of motorsports, having spent his college career competing with NCSU's Formula SAE team and participating in autocross events.

GRADUATES OF THE PRECISION ENGINEERING CONSORTIUM

2019
Noa Mcnutt

2018
Charan Bodlapati

2016
Brandon Suit

2014
David Gebb
Sean Gunning
David Brehl
John Nowak

2012
Brandon Lane
Zachary Marston

2010
Meirong Shi

2009
Qunyi Chen
Erik Zdanowicz

2008
Lucas Lamonds
Stephen Furst

2006
Nadim Wanna
Robert Woodside

2005
Brett Brocato
Nathan Buescher
Karalyn Folkert

2004
Karl P. Freitag
Simon Halbur
Witoon Panusittikorn
Travis Randall

2003
Stuart Clayton
David Hood
Patrick Morrissey
Nobu Negishi
Tao Wu

2002
David Gill
David Kametz

2001
Markus Bauer
Matthew Cerniway
Matias Heinrich
Bryan Love

2000
Brad Austin
Byoung Loh
Michael Long
Edward Miller
Wonbo Shim

1999
Konrad Jarausch
Bradley Jared
Edward Marino

1998
Robert Day
John Fasick
Paul Minor
Keith Sharp

1997
Eugenio Decrescenzo
Hector Gutierrez
Ayodele Oyewole
John Richards
Robert Skolnick

1996
Chris Arcona
Christian Haeuber
Bradley Jared
Quan Ma
Alex Ruxton
Anthony Santavy
Brent Stancil
Anand Tanikella
Donna Thaus

1995
Konrad Jarausch
Charles Mooney
Keith Sharp
John Tyner

1994
Jeffrey Abler
William Allen
James Cuttino
Michele Miller
Ganesh Rao

1990
Scott Blackley
Byron Knight
John Pellerin
Mary Beth Smith

1989
Joseph Drescher
Karl Falter
David Grigg
Michael Luh
Hakan Ozisik
Denise Skroch
Elizabeth Smith

1988
Thomas Bifano
Peter Blake
Steven Fawcett
Michael Loewenthal

1987
John Carroll
Dan Luttrell
Gary Mitchum
Larry Mosley

1986
Mark Cagle
James Gleeson
Jerry Kannel
Mark Landy

1985
Damon Christenbury

ACADEMIC PROGRAMS

Problems and limitations associated with precision manufacturing can originate in the machine, the process, or the material. In fact, most problems will probably be caused by a combination of these factors. Therefore, improvement of current processes and development of new manufacturing methods will require knowledge of a multi-disciplinary array of subjects. The educational goal of the Precision Engineering Consortium is to develop an academic program which will educate scientists and engineers in metrology, control, materials, and the manufacturing methods of precision engineering.

The graduate students involved in the Precision Engineering Consortium have an annual stipend as research assistants. They can take up to 3 classes each semester while spending about 20 hours per week on their research projects. These students also work in the Consortium full-time during the summer months.

The Precision Engineering Consortium began in 1982 with an emphasis on the mechanical engineering problems associated with precision engineering. As a result, the original academic program proposed was biased toward courses related to mechanical design and analysis. However, as the research program has developed, the need for complementary research in sensors, materials, and computers has become obvious. A graduate student capable of making valuable contributions in the computer area, for example, will require a significantly different academic program than in mechanical engineering. For this reason, the Consortium faculty has set a core curriculum and each student in the program is required to take at least 2 of these core courses. The remainder of the courses for the MS or the PhD degree are determined by the university or department requirements and the faculty committee of the student.

The core courses are:

MAE 545 Metrology in Precision Manufacturing
PY 516 Physical Optics
MSE 500 Modern Concepts in Materials Science
CSC (ECE) 714 Real Time Computer Systems

PHD DEGREE PROGRAM

The PhD program in Precision Engineering has been set up as a multi-disciplinary program, drawing upon courses throughout the University to provide background and expertise for the students. It should contain required courses to ensure solid grounding in the fundamentals plus electives to prepare the student in his area of specialization. Because Precision Engineering is concerned with an integrated manufacturing process, students interested in computer control, materials, machine structure, and measurement and actuation systems are involved in the program. Student research projects include the wide variety of topics addressed in this report. Each student's thesis should have an experimental component because Precision Engineering is basically a hands-on technology.

MS DEGREE PROGRAM

The Master of Science degree will have a higher percentage of application courses than the PhD degree. The emphasis will be to develop the foundation for involvement in precision engineering research and development. A total of 30 credits, including 6 credits for the MS thesis, are required. The thesis, while less comprehensive than the PhD dissertation, will be directed at important problems in Precision Engineering. Typically, the MS program will take four semesters plus one summer.

UNDERGRADUATE PROGRAM

The undergraduate degree broadly prepares an engineering student for industrial activities ranging from product design and engineering sales to production implementation. Because a large share of engineers only have the BS degree, these will be the people who must implement the new technology developed in research programs like the Precision Engineering Consortium. Therefore, a way must be found to acquaint engineers at the BS level with the techniques, problems, and potential of precision manufacturing.

In most undergraduate degree programs only limited time is available for technical electives. However, these electives offer the student the opportunity to expand his knowledge in many different directions. Beginning graduate courses (such as metrology) can be used as undergraduate electives.

FACT SHEET – PRECISION ENGINEERING CONSORTIUM (PEC)

HISTORY

1982-1985 ONR Selected Research Opportunity

Based on several years of evaluation of the state of the field known as precision engineering in Europe and Japan, the Office of Naval Research decided to ask for proposals in this area. Ralph Burton, the head of Mechanical and Aerospace Engineering at NC State, and Thomas Dow, who had just joined the University from the Battelle Research Labs, headed a proposal team consisting of faculty from NC State and the Research Triangle Institute. The proposal involved research in the areas of metrology, fabrication and controls. The proposal from NCSU was funded along with proposals from Purdue, Stanford and Maryland.

1985 PEC Affiliate Meeting

Buoyed by the success of the SRO project and interactions with precision engineering industries across the country, a meeting was held in Raleigh with 31 representatives from 26 potential industrial affiliates of the PEC. At the end of this meeting, the 5 original members - Kodak, Moore, General Motors, Texas Instruments and Livermore National Labs - signed up to provided $25K each to help support the Center. Support from these and other Affiliates, along with new projects funded by ONR, NSF and others, has allowed the PEC to educate a new generation of precision engineers and scientists. Our web site is www.pec.ncsu.edu

1986 ASPE Founded

The success of the PEC and the need to provide a forum for communication within this broad field led to the formation of the American Society for Precision Engineering in 1986. The impetus was a meeting held one year earlier in Raleigh that was jointly organized by Lawrence Livermore Labs and the PEC. There were about 60 attendees at that meeting and the question was posed - should a new society be created to serve the field? A majority of the attendees indicated “yes” and a notfor-profit corporation was chartered in North Carolina by Tom Dow, Ron Scattergood and John Strenkowski. The first meeting was held in Dallas, Texas in the fall of 1886 with Tom’s wife as a voluntary staff member. Currently the ASPE has offices in Raleigh and a worldwide membership of 800. ASPE headquarters will be relocating to Charlotte in 2019. The 2018 Annual Meeting was held in Las Vegas, Nevada and had more than 225 attendees and over 40 exhibiting companies. Web site: www.aspe.net

1986-1991 University Research Initiative

In 1986, a new DOD initiative was announced and NC State submitted a multi-disciplinary proposal with faculty from mechanical engineering, materials science, physics, computer science, and electrical engineering. There were 35 proposals submitted in the manufacturing area and only the NC State concept was funded. This project was funded at $1M per year for 5 years.

1988 First Building on Centennial Campus

The $5M URI grant to the PEC was the largest single research grant received by the University up to that time. This grant came at a time when the University acquired a 1000 acre research campus from the state named Centennial Campus. Based on the space need for this program as well as the desire to begin development of the CC, a building for the PEC was started in April of 1987 and the Center was moved to Centennial Campus in February of 1988. This building was inaugurated in April of 1988 with Dr. Saalfeld, Technical Director of ONR, as one of the guest speakers.

PEC Affiliates

Numerous companies and government organizations have been members of the PEC and supported specific research projects with additional support. Membership fees partially support the administrative staff as well as the two research engineers.

1. Aerotech, Inc
2. Biomachines
3. Burleigh Instruments
4. Chardon Tool
5. Corning, Inc
6. Cummins Engine Co.
7. Department of Energy
8. Digital Instruments
9. Eastman Kodak
10. Electro-Optics Center
11. General Motors
12. Hughes Danbury
13. IBM
14. Johnson & Johnson
15. Lexmark
16. Livermore National Labs
17. Lockheed Martin
18. Los Alamos National Labs
19. 3M Company
20. Martin Marietta
21. Materials Analytical Services
22. Missile Defense Agency
23. Moore Special Tool
24. NASA National Institutes of Health
25. National Institute of Justice
26. National Institute of Standards and Technology
27. National Science Foundation
28. Oak Ridge National Labs
29. Optical Research Associates
30. Facebook VR
31. Office of Naval Research
32. Panasonic
33. Precitech
34. Pneumo Precision Inc
35. Rank Taylor Hobson , Inc.
36. Sandia National Labs
37. StorageTek
38. Teledyne, Inc.
39. Texas Instruments